

UNIVERSITY OF TURIN
and
NATIONAL RESEARCH TOMSK POLYTECHNIC UNIVERSITY

Alexandr Chumakov

**STUDY OF NUCLEON SPIN (IN)DEPENDENT AZIMUTHAL
ASYMMETRIES IN PION INDUCED DRELL-YAN PROCESS AT COMPASS**

Jointly-supervised doctoral thesis

Supervisors of the thesis:

Tübingen University and Tomsk Polytechnic University: prof. Valery Lyubovitskij

University of Turin: prof. M. Chiosso and dr. B. Parsamyan

Turin 2022

Jointly-supervised doctoral thesis

Title: Study of nucleon spin (in)dependent azimuthal asymmetries in pion induced Drell-Yan process at COMPASS

Author: Alexandr Chumakov

Abstract:

The thesis concerns the study of the nucleon spin structure. In the beginning a concise summary of the thought flow on the nucleon structure is given. Then the basic theoretical concepts of two processes, semi-inclusive deeply inelastic scattering (SIDIS) and Drell–Yan (DY), accessing the internal spin structure of hadrons are overviewed, and the corresponding experimental observables in terms of asymmetries are presented. The relations of the SIDIS and DY processes are briefly discussed including the well-known sign-change law in the Sivers and Boer-Mulders transverse momentum dependent (TMD) parton distribution functions (PDFs). The main part of the work is devoted to an analysis of the transverse spin (in)dependent azimuthal modulations in the DY process from data collected by the COMPASS experiment (CERN) in 2015 and in 2018 years using the π^- beam at energy of 190 GeV/c, which is scattered off a proton polarized target. The transverse spin asymmetries are extracted in two ranges of invariant dimuon mass (“ J/ψ -production range”: $2.85 < M_{\mu^+\mu^-}/(\text{GeV}/c^2) < 3.4$ and “High Mass” (HM) range $4.3 < M_{\mu^+\mu^-}/(\text{GeV}/c^2) < 8.5$) as functions of five kinematic variables: x_N , x_b , x_F , q_T , $M_{\mu^+\mu^-}$. The spin-independent azimuthal modulations from the NH_3 and tungsten target in the HM range are also obtained. The model-independent Lam–Tung relation between hadronic structure functions is tested.

Keywords:

Nucleon spin structure, hadron structure, quantum chromodynamics (QCD), spin asymmetries, parton distribution functions (PDFs), non-perturbative QCD, transverse momentum dependent distribution functions (TMDs), COMPASS experiment, Drell-Yan and SIDIS processes.

Acknowledgements

First of all, I would like to thank to all my supervisors. Their teaching and work with me has played a crucial role for my education, professional skills and human qualities as well. A special deepest grateful to Dr. Bakur Parsamyan for his training, wise advices, fruitful ideas, for his willingness to dedicate time for me despite his tight and busy schedule. He could teach me data analysis almost from scratch to complete my PhD thesis. I really appreciate work with him, especially our close collaboration during the most difficult time of my PhD study this year. I express a huge gratitude to Prof. Valery Lyubovitskij, thanks to him a Tomsk group of elementary particle physics has been formed. Prof. Lyubovitskij expands my interests in physics by sharing his horizons and ideas, he demonstrates hard work and life optimism, which is very inspiring and which serves as a great example to follow. I am grateful to Prof. Michela Chiosso for her support and organization of my PhD study at University of Turin.

I thank all the COMPASS collaboration, which members are impressive with their hard work, dedication and fanaticism for the common cause. A special thought goes to the DY analysis group for all the efforts, which made to be possible final analyses of the collected data. Thanks to April Townsend for the final data productions in tight time and collaborative work on TSAs analysis. I am very thankful to Yu-Hsiang Lien, with whom I have done the analysis on unpolarized asymmetries. I remember and appreciate Yu-Hsiang's kind responsiveness during sleepless nights in order to successfully perform the cross-check of our analysis on time. Also I would like to express my thanks to referees of my thesis, Prof. Andrea Bressan and Dr. Stephane Platchkov, whose fair remarks helped me to improve my manuscript.

I gratefully acknowledge all the Tomsk group. A special grateful thought goes to Renat Dusaev for his self-sacrificing and enduring work on the alignment, for his advices and deep thoughts, and for sharing his huge expertise in software development. Thanks to Alexey Shevelev, who is doing a lot for the support and the development of our group. I would also

like to thank my colleague Konstantin Sharko for our fruitful and interesting conversations on physics and not only on it. A posthumous gratitude to Prof. Andrey Trifonov, who supported me all the time of my PhD. He helped our group with a lot of organizational matters, education and work processes. He was a real leader, scientist and teacher, in one word, a truly Professor!

I thank my parents, my way to science would be impossible without their care. They supported me all the time, despite that in the beginning they did not agree with my choice to become a physicist. I would also like to posthumously acknowledge my uncle Yakov Plyusnin who passed away just a month before the submission of this manuscript. I thank him and his family for their help particularly in the early times after my arrival in Tomsk.

Finally, I am very grateful to my lovely wife Tatiana, who was there all the way of my study and work; thanks for the support, care and patience.

Contents

1	Introduction	3
1.1	Experimental Overview	6
1.2	Brief overview of results on TMD PDFs	8
1.3	Spin independent effects in Drell-Yan process	16
1.4	TMD effects in J/ψ production	19
2	Theoretical basis	25
2.1	Drell-Yan cross section	25
2.2	Reference frames	26
2.3	Kinematics in the DY process	28
2.4	Angular distribution of the DY cross section	29
2.5	Parton model and parton distribution functions	32
2.6	Deeply inelastic and semi-inclusive deeply inelastic scattering	35
3	The COMPASS experiment	43
3.1	Beam	45
3.2	Polarized target	49
3.3	Hadron absorber	51
3.4	Scintillating fibers	52
3.5	Pixel Micromegas	53
3.6	GEM	54
3.7	RICH Wall	55
3.8	MWPC	56
3.9	Drift Chambers	57

3.10	Straw	58
3.11	Large area drift chambers (W45)	60
3.12	Muon walls	60
3.13	Hadronic calorimeters	62
3.14	Trigger system	63
3.15	Data acquisition system	64
3.16	Future upgrade of the setup	67
4	Data processing	69
4.1	Reconstruction	69
4.2	Alignment	71
4.2.1	Overview	71
4.2.2	Procedure	74
4.2.3	Quality criteria	75
4.2.4	Alignment with constraints	80
5	Analysis	85
5.1	Data sample	86
5.2	Analysis of transverse spin asymmetries	87
5.2.1	Event selection	88
5.2.2	Kinematic binning	95
5.2.3	Data stability checks	97
5.2.4	Data productions	100
5.2.5	Monte-Carlo studies: resolutions, target event mixing	108
5.2.6	Target polarization	110
5.2.7	Dilution factor	113
5.2.8	Depolarization factors	116
5.3	One-dimensional double ratio	117
5.4	Extended Weighted Unbinned Maximum Likelihood	120
5.5	Systematic studies	123
5.5.1	Compatibility of asymmetries from different periods	124
5.5.2	Right-Left-Top-Bottom (RLTB) test	128

5.5.3	False-asymmetries	132
5.5.4	The total systematic uncertainty	133
5.6	Results	137
5.7	Analysis of spin-independent azimuthal asymmetries	142
5.7.1	Monte-Carlo production	142
5.7.2	Event selection	150
5.7.3	Kinematic binning	151
5.7.4	Evaluation of the Angular Acceptance	151
5.7.5	Extraction of Drell-Yan Unpolarized Asymmetries	154
5.7.6	Systematic studies	157
5.7.7	Extraction of J/ψ Unpolarized Asymmetries	162
5.7.8	Results	163
Conclusion and discussion		173
Appendix A. Details on the DY cross-section		183
Appendix B. Structure functions in parton model		189
5.8	DY case	189
5.9	SIDIS case	191
Appendix C. Statistics summary		193
References		214

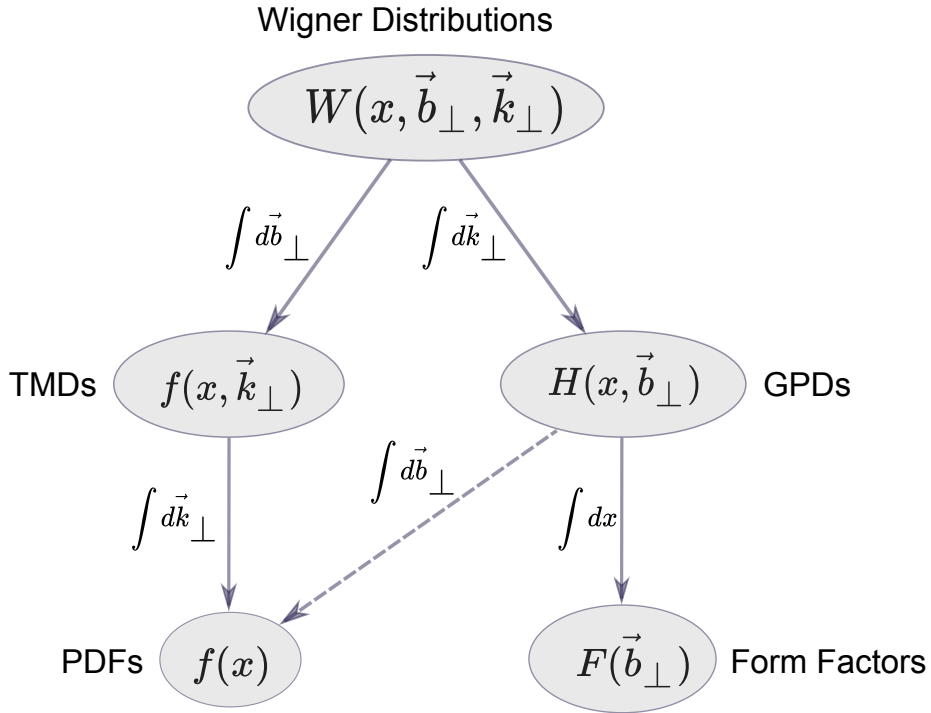
Chapter 1

Introduction

Nucleons are fundamental particles forming nuclei, which are the basic blocks of surrounding matter. They belong to the hadron family – particles bound by the strong force. Hadrons are not elementary particles and are composed of quarks. First idea on quark content of hadrons was elegantly proposed by M. Gell-Mann [1] and G. Zweig [2,3] to explain a classification of light hadrons using the irreducible representations of the unitary flavor group $SU_f(3)$. In 1969, the parton model was formulated by R. Feynman [4], J. Bjorken and E. Paschos [5]. At that time it became possible to experimentally probe constituents (partons) inside a proton using deep inelastic electron-proton scattering at linear colliders. So, in 1969, after a series of experiments at Stanford Linear Accelerator Center (SLAC) in USA [6, 7], the quark structure of hadrons was finally confirmed. Subsequently, this led to formulation of the Quantum Chromodynamics (QCD), the gauge theory of the strong interactions, based on the color $SU_c(3)$ invariance, in which gluons are gauge vector bosons. However, the study of strong force sector are complicated by the fact that quarks are not observable as free states due to their color confinement. Thereby, processes governed by strong interactions at small momenta can not be described by a perturbative approach (where initial and final states are supposed to be free). In 1979-1989, S. Brodsky and P. Lepage [8], A. Efremov and A. Radyushkin [9], J. Collins, D. Soper, and G. Sterman [10] proposed and developed an idea of factorization theorem for application of QCD to hadron processes, which states that one can isolate effects of strong interactions at small distances described by the perturbative QCD from the ones at large distances (or at small momenta), which have a non-perturbative origin. The perturbative part consists of sub-processes of QCD constituents (quarks and gluons), which describe hadronic collisions at microscopic

level including their interactions with the electroweak sector of Standard Model (SM). On the other hand, the non-perturbative part describes interaction effects of partons inside a hadron, which are parameterized by different *distribution functions*.

From a modern point of view, parton distributions giving full information about the intrinsic hadron structure are the so-called *Wigner functions* [11–13], which depend on five variables of the parton: longitudinal coordinate x , 2-vector in transverse coordinate space \vec{b}_\perp , and 2-vector in transverse momentum space \vec{k}_\perp . In total, there are 16 Wigner distribution functions at the leading twist-2 expansion, since both hadron and quark have four spin degrees of freedom: one unpolarized and three polarized states. Integration or Fourier transform of the Wigner functions leads to other well-known and important distribution functions: Transverse Momentum Dependent Parton Distribution Functions (TMD PDFs), Generalized Parton Distributions (GPDs), Parton Distribution Functions (PDFs), elastic form factors, and charges (see Fig. 1.1).


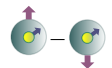
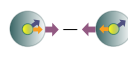
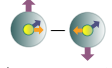



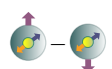


The main objective of the Thesis is a study of effects related to TMD PDFs measured from experimental data collected in Drell-Yan (DY) process, *i.e.* in massive dilepton-pair production in hadron-nucleon collisions ($hN \rightarrow l\bar{l}X^1$). The DY process was first described by Drell and Yan

¹Here the notations for states read as follow: h – hadron, N – nucleon, l, l', \bar{l} – leptons, X – inclusive hadrons.

in their work [14], in 1970. Seven years later Collins and Soper formulated a model independent approach to the unpolarized DY processes in [15]. Their work is based on a representation of the differential cross section in terms of hadronic structure functions. Then Lam and Tung in [16,17] came to the same result introducing a set of three ratios of structure functions λ , μ , ν , which were nothing more than azimuthal modulation coefficients of angular amplitudes. Lam and Tung also obtained the model independent relation: $\lambda + 2\nu = 1$ (hereinafter it received their name – Lam-Tung sum rule). The state of the art of the DY process description can be found in reviews [18, 19]. It is important to point out, that experimental study of TMD PDFs are being also done in Semi-Inclusive Deeply Inelastic Scattering (SIDIS) [20–22], *i.e.* a scattering off a lepton on a nucleon target producing new hadron states, part of which can be identified ($lN \rightarrow l'Xh$).

TMD PDFs are obtained from the Wigner distribution functions by integration over \vec{b}_T . In the next Chapter we will demonstrate their derivation from a decomposition of a quark correlator. Eight TMD PDFs emerge at the leading order (twist-2) expansion of hadron correlation tensor function. Six of them are T-even (time reversal invariants): $f_1(x, \vec{k}_T)$, $g_{1L}(x, \vec{k}_T)$, $g_{1T}(x, \vec{k}_T)$, $h_{1T}(x, \vec{k}_T)$, $h_{1L}^\perp(x, \vec{k}_T)$, $h_{1T}^\perp(x, \vec{k}_T)$; while two of them are T-odd (changing sign under the time reversal transformation): Sivers function $f_T^1(x, \vec{k}_T)$ and Boer-Mulders function $h_1^\perp(x, \vec{k}_T)$. Integration of $f_1(x, \vec{k}_T)$, $g_{1L}(x, \vec{k}_T)$ and $h_{1T}(x, \vec{k}_T)$ over \vec{k}_T gives three collinear PDFs $f_1(x)$, $g_{1L}(x)$ and $h_{1T}(x)$. Distribution functions characterize the distribution of a parton with a certain flavour inside a hadron, over variables x and \vec{k}_T (TMD distributions) according to the Fig. 1.2, or only over x (PDF distributions). One of the key features of the T-even TMD PDFs is their predicted process independence. Within the concept of generalized universality of TMD PDFs, nucleon parton distribution functions accessed via measurements of azimuthal asymmetries in SIDIS and Drell-Yan are expected to be process independent. While one of the key features of the T-odd TMD distributions (Sivers $f_T^1(x, \vec{k}_T)$ and Boer-Mulders $h_1^\perp(x, \vec{k}_T)$) is the predicted sign-change between SIDIS and DY [23, 24]. Thus, in case of the DY process there are “mirrored” observables w.r.t. the SIDIS process, that defines a “bridge” between measurements in these reactions. It should be noted, all types of the parton distributions are scale-dependent quantities. This dependence is defined by the Dokshitzer-Gribov-Lipatov-Altarelli-Parisi (DGLAP) equations [25–27] in case of PDFs (by resummation of leading logarithms) and by the Collins-Soper (CS) equations [28] in case of TMDs (by resummation of contribution of

		Nucleon polarization		
		unpolarized	longitudinal	transverse
Quark polarization	unpolarized	 $f_1(x, \mathbf{k}_T^2)$ Number Density		 $f_{1T}^\perp(x, \mathbf{k}_T^2)$ Sivers
			 $g_{1L}^\perp(x, \mathbf{k}_T^2)$ Helicity	 $g_{1T}^\perp(x, \mathbf{k}_T^2)$ Kotzinian-Mulders Worm-Gear T
	transverse	 $h_1^\perp(x, \mathbf{k}_T^2)$ Boer-Mulders	 $h_{1L}^\perp(x, \mathbf{k}_T^2)$ Worm-Gear L	 $h_1(x, \mathbf{k}_T^2)$ Transversity
				 $h_{1T}^\perp(x, \mathbf{k}_T^2)$ Pretzelosity

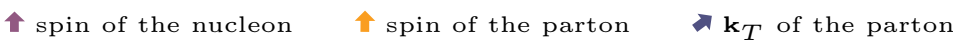


Figure 1.2: The eight leading 2-twist TMD PDFs.

the double logarithms caused by the gluon radiation of the active partons).

In general, to probe the nucleon structure in the transverse momentum space, it is important to prepare polarized initial states. Only unpolarized $f_1(x, \vec{k}_T)$ and Boer-Mulders $h_1^\perp(x, \vec{k}_T)$ distributions can be accessed in unpolarized processes.

1.1 Experimental Overview

The first polarized proton beams were used at the Argonne National Laboratory (ANL) in 1973, where large Single Spin Asymmetries (SSAs) were observed in polarized proton-proton collisions [29, 30].

In the same years the SLAC experiments E80 and E130 dealt with deep inelastic scattering of longitudinally polarized electrons on longitudinally polarized protons [31–34]. Other experiments followed able to perform higher precision measurements: E142 [35], E143 [36], E154 [37], E155 [38, 39].

At the end of '80s the European Muon Collaboration (EMC) measured quark spin effects for a proton [40]. One of the main and famous EMC results was a measurement of the average spin of quarks inside proton $\Delta\Sigma$. The obtained value was $\Delta\Sigma \approx 0.12$, which is unexpected w.r.t. the naive quark model, where it is predicted to be $\Delta\Sigma = 1$. This phenomenon got a name “spin crisis” (also “EMC effect” or “spin puzzle”), that has strongly spurred further experimental and theoretical research on the spin nucleon structure. In the '90s the EMC experiment was followed by the Spin Muon Collaboration (SMC) [41], which was the first one to measure spin effects from the semi-inclusive reaction [42,43] detecting pions and kaons in the final state. These SIDIS measurements gave access to the determination of various quark spin distributions. Then a lot of experimental studies on the spin structure were done by the HERMES collaboration [44] at DESY. The HERMES experiment has provided data for the neutron, proton and deuteron structure functions [45–47]. During the second phase of the HERMES data taking, the COMPASS experiment at CERN had been started [48], which has been vastly contributing to the knowledge of the nucleon structure. A series of corresponding experiments was also carried out at JLab in three halls: HALL A [49–51], HALL B with Continuous Electron Beam Accelerator Facility (CEBAF) Large Acceptance Spectrometer (CLAS) [52, 53] and HALL C [54–56].

A first collider where polarized protons can collide was the Relativistic Ion Collider (RHIC) at Brookhaven National Laboratory (BNL), which was started in 2002. Three experiments on the RHIC ring worked on the proton spin physics: Broad RAnge Hadron Magnetic Spectrometers (BRAHMS) [57], Pioneering High Energy Nuclear Interaction eXperiment (PHENIX) [58] and Solenoidal Tracker at RHIC (STAR) [59, 60]. The BRAHMS and PHENIX collaborations have finished their data taking in 2006 and in 2016, respectively. STAR is a running experiment and has been collecting data. The COMPASS experiment is also in an active stage now. Data collected from DY runs of 2015 and 2018, Deeply Virtual Compton Scattering (DVCS) and SIDIS runs of 2016 and 2017 are being actively analyzed. Some results from STAR and COMPASS have been already obtained and published (see next Section).

There are many proposals for future experiments performing polarization measurements. On basis of the COMPASS experiment “A New QCD facility at the M2 beam line of the CERN SPS” (AMBER collaboration) [61] is planned to be launched in 2022 [62]. Spin Physics Detector (SPD) at Nuclotron-based Ion Collider fAcility (NICA) is currently being designed [63] at Joint Institute for Nuclear Research (JINR). There are plans to extend the LHCb physics

programme with the so-called LHCSpin project [64, 65]. Concerning the long-term future an Electron-Ion Collider (EIC) [66] is widely discussed with its large QCD physics programme (*e.g.* see review [67]).

1.2 Brief overview of results on TMD PDFs

Phenomenological inputs for the TMDs are the measurements of the corresponding asymmetries – Transverse Spin Asymmetries (TSAs), and Unpolarized Asymmetries (UAs) for a study of the unpolarized distributions. The asymmetries are related to the distribution functions and allow thus to fit and extract them. The main objective of the Thesis is an analysis of DY data from the COMPASS experiment collected in 2015 and in 2018 years operating with a pion beam scattering on a transversely polarized proton target [68]. These data allow to extract TSAs, which give access to 5 proton TMD PDFs: unpolarized distribution $f_{1,p}^a(x, k_T)$, transversity distribution $h_{1,p}^a(x, k_T)$, Sivers distribution $f_{1T,p}^{\perp a}(x, k_T)$, Boer-Mulders distribution $h_{1,p}^{\perp a}(x, k_T)$, pretzelosity distribution $h_{1T,p}^{\perp a}$, and two pion TMDs: unpolarized distribution $f_{1,\pi}^a(x, k_T)$, Boer-Mulders distribution $h_{1,\pi}^{\perp a}(x, k_T)$.

The Sivers TSAs for proton and deuteron targets measured in SIDIS have been published by HERMES [69, 70] and COMPASS [71–79]. The Sivers asymmetry was also extracted from the JLab experiments in charged pion and kaon productions in SIDIS on a transversely polarized ^3He target [80, 81]. There are also published results [82] on the Sivers TSA from collider data measured by the STAR collaboration at RHIC using a proton-proton process with weak bosons production $p^\uparrow + p \rightarrow W^\pm/Z^0$ (Fig. 1.6), and the analysis was recently updated and presented at the 22nd Particles and Nuclei International Conference [83]. The new STAR preliminary results are shown in Fig. 1.7, where the uncertainties were decreased and the Sivers asymmetry has been found around zero. Results from the COMPASS 2015 DY data taking were published in 2017 [84], which include extractions of the Sivers, transversity, pretzelosity, and two higher-twist TSAs (Fig. 1.3). The DY COMPASS measurements have also allowed to test the sign-change law for the Sivers functions, that is presented in Fig. 1.4. Recently, the HERMES experiment has published a comprehensive analysis on various azimuthal single-spin and double-spin asymmetries with an interpretation of them as signals related to corresponding TMDs [85] (an example on the Sivers asymmetry is shown in Fig. 1.5). Overview of the results, which are

related to further analyses discussed in this Thesis, is presented in Tab. 1.1.

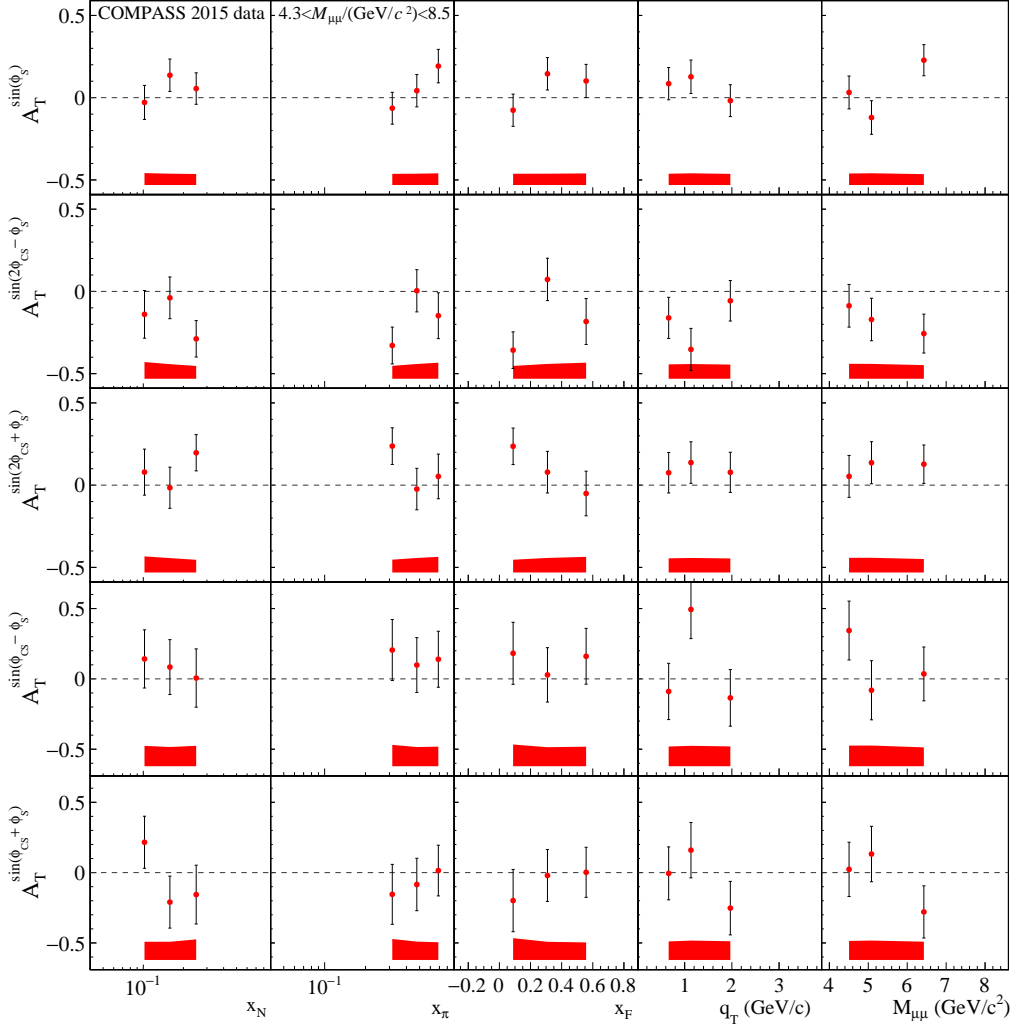


Figure 1.3: Results on Drell-Yan TSAs as functions of x_N , x_π , x_F , q_T , $M_{\mu\mu}$ extracted by COMPASS collaboration from 2015 data.

The most studied object among the distribution functions is the unpolarized distribution for a proton $f_{1,p}^a(x, k_T)$ [92–102]. The Sivers TMD function for a proton $f_{1T,p}^{\perp a}(x, k_T)$ was studied in various global QCD analyses [90, 91, 103–106]. Also there are many results for the pion Sivers distribution $f_{1T,\pi}^{\perp a}(x, k_T)$ [107–112]. A parameterization of the proton pretzelosity distribution $h_{1T,p}^{\perp a}(x, k_T)$ can be found in [113], while an extraction of the proton transversity function $h_{1,p}^a(x, k_T)$ is done in the recent work [105]. As far as the Boer-Mulders function is concerned, there are results for a proton [114], however the pion $h_{1,\pi}^{\perp a}(x, k_T)$ Boer-Mulders TMD has not yet been extracted. References of these studies are also summarized in Tab. 1.1. Based on these data various groups of phenomenologists perform global analyses to extract the corresponding

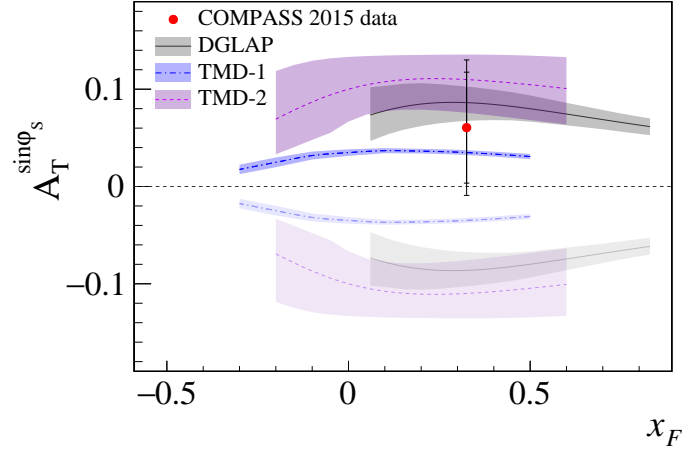


Figure 1.4: Sivers sign-change test from the COMPASS Drell-Yan data [84] compared to the theoretical predictions for different Q^2 evolution schemes from [86] (DGLAP), [87] (TMD-1) and [88] (TMD-2). The dark-shaded (light-shaded) predictions are evaluated with (without) the sign-change hypothesis.

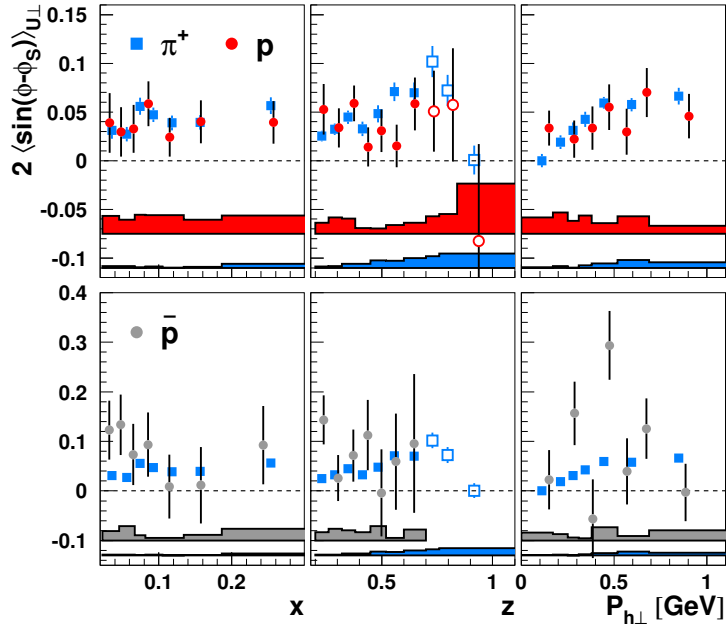


Figure 1.5: Results on the Sivers asymmetry for pions, protons (upper plot) and antiprotons (lower plot) from the HERMES experiment at DESY [85].

TMDs. There are also theoretical model predictions. In Fig. 1.8 calculations for u- and d-quark TMD PDFs in nucleon done by T. Gutsche, V. Lyubovitskij and I. Schmidt in a light-front quark model motivated by soft-wall AdS/QCD are presented [130]. One should stress that results obtained in Ref. [130] are consistent with constituent quark counting rules [131, 132] and

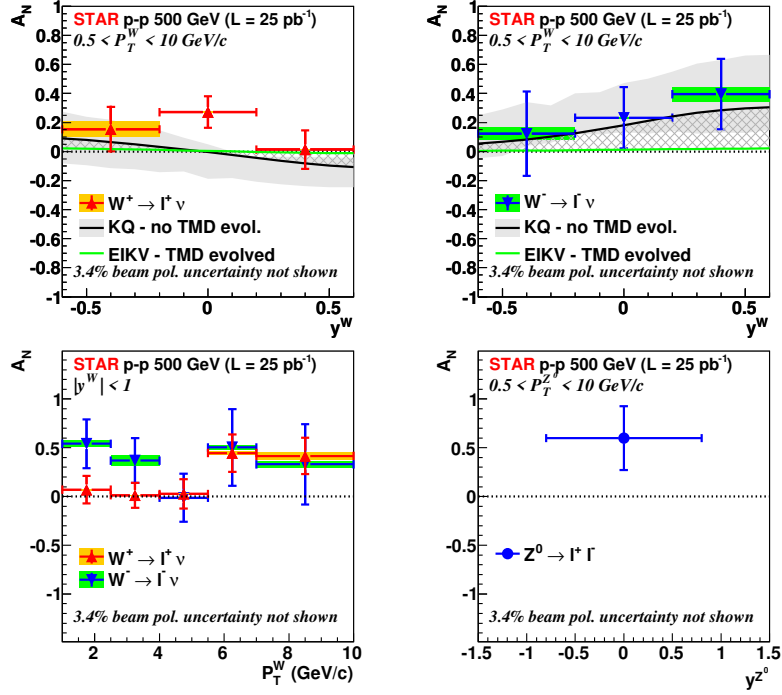


Figure 1.6: Results from the STAR collaboration at BNL [82], the plots show the Siverts asymmetry as a function of rapidity y^W and transverse momentum P_T^W from the W^\pm -boson production compared to the KQ [89] and to the EIKV [87] models; the Siverts asymmetry as a function of rapidity of the Z^0 -boson from DY process is shown on the bottom right panel.

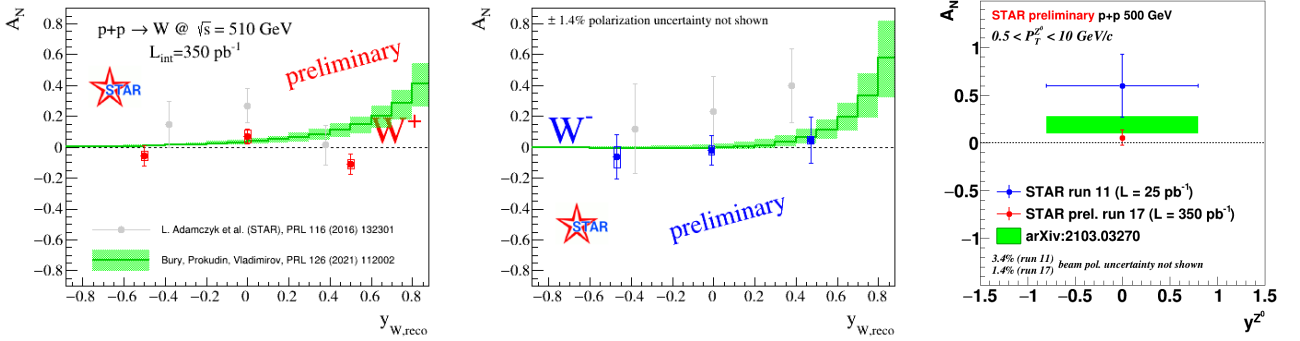


Figure 1.7: New preliminary results from the STAR collaboration given at the PANIC conference in 2021 [83]. Two left plots: the Siverts asymmetry as a function of rapidity y^W from the W^\pm -boson production compared to the previous results [82] (gray points) and a theoretical prediction from Ref. [90] (in green). Right plot: the Siverts asymmetry from the DY-like $Z^0 \rightarrow l^+ l^-$ production as a function of rapidity y^{Z^0} compared to the previous results [82] (blue point) and to a theoretical prediction from Ref. [91] (in green).

TMD PDF	Observable	Data	Global fits
Sivers $f_{1T,p}^{\perp a}(x, k_T)$	SIDIS: $A_{UT}^{\sin(\phi_h - \phi_S)}$	HERMES: [69, 70, 85, 115] COMPASS: [71–79] JLab: [80, 81]	[90, 91, 103–106]
	DY: $A_{UT}^{\sin\varphi_S}$	STAR: [82] COMPASS: [84]	
Transversity $h_{1,p}(x, k_T)$	SIDIS: $A_{UT}^{\sin(\phi_h + \phi_S)}$	HERMES: [69, 70, 85, 115] COMPASS: [72–74, 79] JLab: [80, 81]	[105, 116, 117]
	DY: $A_{UT}^{\sin(2\varphi_{CS} - \varphi_S)}$	COMPASS: [84]	
Pretzelosity $h_{1T,p}^{\perp a}(x, k_T)$	SIDIS: $A_{UT}^{\sin(3\phi_h - \phi_S)}$	HERMES: [118] COMPASS: [79, 119–121] JLab: [122]	[113]
	DY: $A_{UT}^{\sin(2\varphi_{CS} + \varphi_S)}$	COMPASS: [84]	
Boer-Mulders $h_{1,p}^{\perp a}(x, k_T)$	SIDIS: $A_{UU}^{\cos(2\phi_h)}$	COMPASS: [123, 124] HERMES: [125] JLab (CLAS): [126]	[114]
Boer-Mulders $h_{1,\pi}^{\perp a}(x, k_T)$	DY: $A_{UU}^{\cos(2\varphi_{CS})}$	NA10: [127] E615 (FermiLab): [128] COMPASS: [129]	<i>not yet extracted</i>

Table 1.1: World-wide results and extraction of a part of TMD PDFs. The table concerns only observables, which are related to an TSAs analyses of pion-induced DY data from COMPASS, and, therefore here the helicity $g_1^a(x, k_T)$, the Kotzinian-Mulders (transerve worm-gear) $g_{1T}^{\perp a}(x, k_T)$ and the longitudinal worm-gear $h_{1L}^{\perp a}(x, k_T)$ functions are skipped.

Drell-Yan-West duality [133–135] occuring at large x and are very important for the current and future program of the COMPASS and AMBER experiments. Some available model predictions and global fits were comprehensively discussed for the COMPASS kinematic region in the recent work [136], results on TMDs of u and d quarks from this publication are shown in Fig. 1.10 and in Fig. 1.9, where predictions from a light-front constituent quark model (LFCQM) [137–139] and a spectator model (SPM) [140] are compared to phenomenological

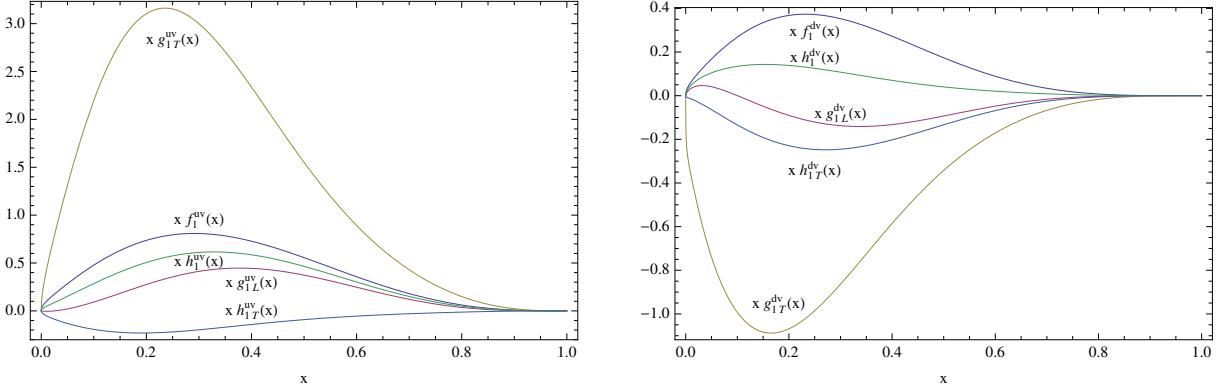


Figure 1.8: TMDs in a light-front quark model multiplied with x (left: up quark distributions; right: for down quark distributions). Plots are taken from [130].

extractions (if available) done by: Jefferson Lab angular momentum (JAM) collaboration [141] for $f_{1T,p}^{\perp(1)a}(x, k_T)$ [105] and for $h_{1,p}^a(x, k_T)$ [105]; “Torino” group for $f_{1T,p}^{\perp(1)a}(x, k_T)$ [103] and for $h_{1,p}^a(x, k_T)$ [104]; A. D. Martin, W. J. Stirling, R. S. Thorne, and G. Watt (MSTW) [95] for $f_{1,p}(x, k_T)$; V. Barone, S. Melis, and A. Prokudin (BMP) for $h_{1,p}^{\perp(1)a}(x, k_T)$ [114]; C. Lefky and A. Prokudin (LP) for $h_{1T,p}^{\perp(2)a}(x, k_T)$ [113]. Also, in the Ref. [136], the corresponding asymmetries were calculated and compared to the COMPASS results [84], the comparison is shown in Fig. 1.11. The fits and model predictions, shown in Fig. 1.11, have a non-zero positive value for the Sivers asymmetry $A_{UT}^{\sin\varphi_S}$ while the transversity $A_{UT}^{\sin(2\varphi_{CS}-\varphi_S)}$ lies in a negative region. As far as the pretzelosity value $A_{UT}^{\sin(2\varphi_{CS}+\varphi_S)}$ is concerned, there is no clear evidence on the behavior of this quantity and the corresponding TMD distribution function $h_{1T,p}^{\perp a}(x, k_T)$, and the available fit has large errors [113]. For today the pretzelosity is the least known function among the proton TMD PDFs.

An analysis on the extraction of the TSAs from pion-induced DY data of the COMPASS experiment will be presented in Chapter 5, which is a continuation of the study published in [84] where 2015 data were used. The work in this Thesis is carried out on a new data-set collected in 2018 and on a recent re-production of 2015 data.

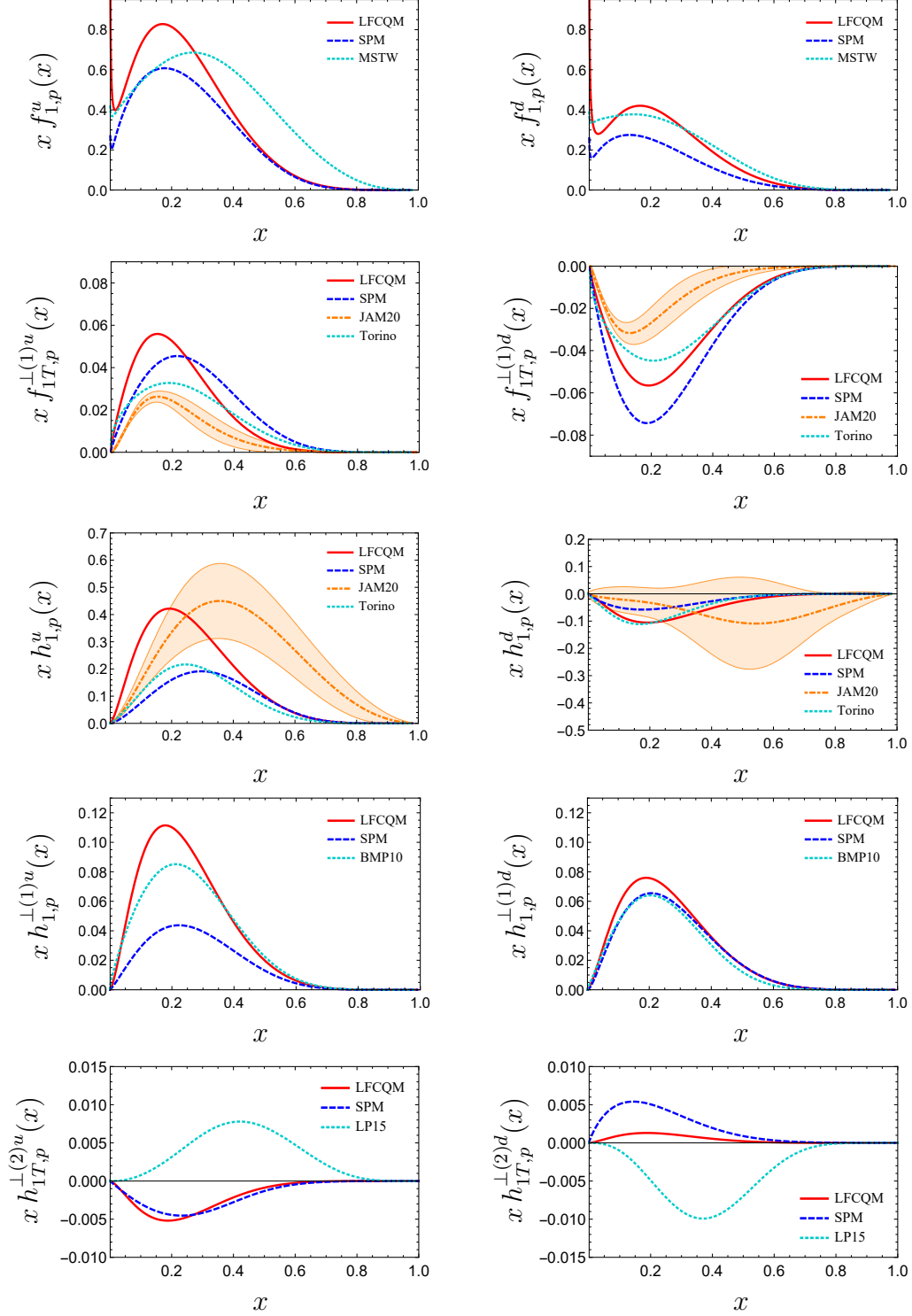


Figure 1.9: The proton TMDs of u and d quarks in LFCQM [137–139] and SPM [142] at the scale $Q_0^2 = 2.4 \text{ GeV}^2$ compared to phenomenological fits for $f_{1,p}(x)$ from MSTW2008(LO) [95], $f_{1T,p}^{\perp(1)a}(x)$ from JAM20 [105] and Torino [103], $h_{1,p}^a(x)$ from JAM20 [105] and Torino [104], $h_{1,p}^{\perp(1)a}(x)$ from BMP10 [114], $h_{1T,p}^{\perp(2)a}(x)$ from LP15 [113]. Siverts and Boer-Mulders TMDs are shown with the sign for DY process. The error bands show the $1\text{-}\sigma$ uncertainty of the JAM20 extractions [105]. Plots are taken from Ref. [136].

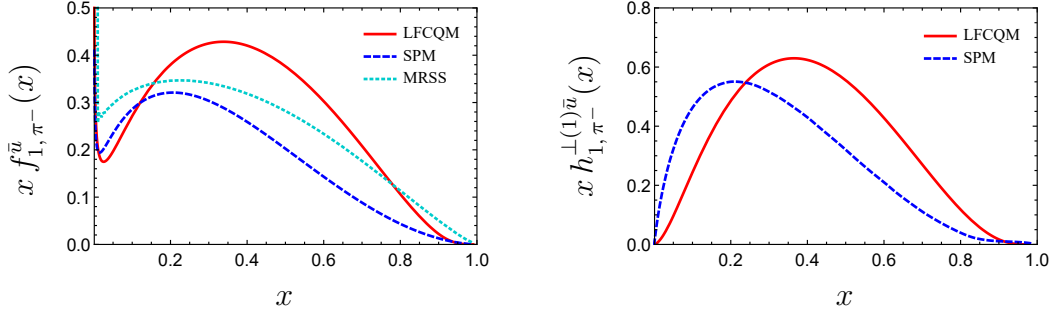


Figure 1.10: Left: $f_{1,\pi^-}^{\bar{u}}(x)$ from LFCQM [143] and SPM [140] LO-evolved to the scale $Q_0^2 = 2.4$ GeV² in comparison to MRSS parameterization [108]. Right: Predictions from LFCQM [143] and SPM [140] for the pion Boer-Mulders function (with the sign for DY) for which no parameterizations are currently available. Plots are taken from Ref. [136].

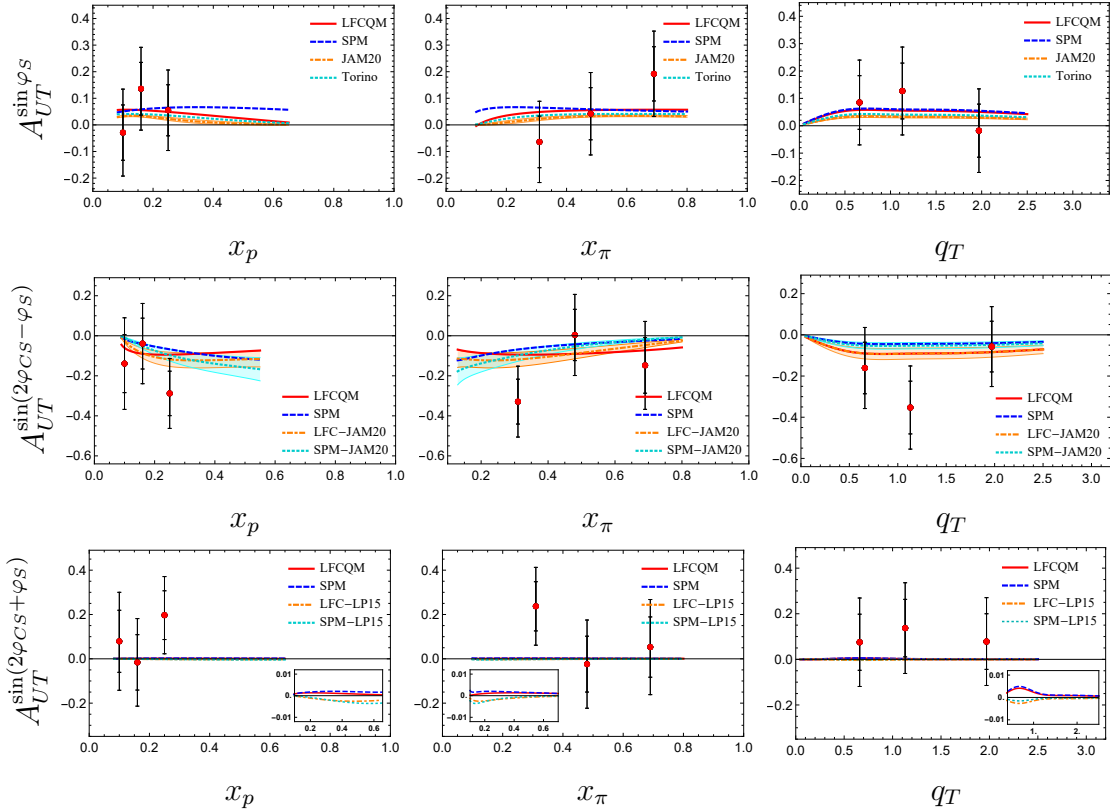


Figure 1.11: Leading-twist TSAs as a function of x_p (left), x_π (middle) and q_T (right) compared to COMPASS results [84]. Plots are taken from Ref. [136].

1.3 Spin independent effects in Drell-Yan process

In this section we briefly review unpolarized DY measurements, which also provide interesting physics on the nucleon structure. Intriguing results were obtained with DY measurements of the angular effects of the unpolarized amplitudes. In 1986, the NA10 experiment at CERN measured the spin-independent azimuthal asymmetries in the Drell-Yan process using a pion beam (with different energies 140, 194 and 286 GeV/c) scattered on tungsten and deuterium targets [127]. The collaboration obtained an unexpected result, which was violating the Lam-Tung relation in the high q_T region [144]. Later a larger violation of the Lam-Tung sum rule was observed by the E615 collaboration at Fermilab [128], where a pion beam was scattered on a tungsten target at energy of 252 GeV/c. After that Fermilab studied this effect in its new experiment E866 with a proton beam scattering on hydrogen and deuterium targets, where the DY asymmetries were measured using proton-proton and proton-deuteron initial states [145]. The results obtained from the aforementioned experiments are summarized in Fig. 1.12 and in Tab. 1.2. Note that the results from E615 experiment are clearly violating the Lam-Tung relation, which is mainly driven by large measured values of ν .

Experiment	NA10 [127]	E615 [128]	E866 [145]
Interaction	$\pi^- + W$	$\pi^- + W$	$p + d$
Beam Energy	194 GeV/c	252 GeV/c	800 GeV/c
x_1 range	0.2 \rightarrow 1.0	0.2 \rightarrow 1.0	0.15 \rightarrow 0.85
x_2 range	0.1 \rightarrow 0.4	0.04 \rightarrow 0.38	0.02 \rightarrow 0.24
$\langle \lambda \rangle$	0.83 ± 0.04	1.17 ± 0.06	1.07 ± 0.07
$\langle \mu \rangle$	0.008 ± 0.010	0.09 ± 0.02	0.003 ± 0.013
$\langle \nu \rangle$	0.091 ± 0.009	0.169 ± 0.019	0.027 ± 0.010
$\langle 2\nu - (1 - \lambda) \rangle$	0.01 ± 0.04	0.51 ± 0.07	0.12 ± 0.07

Table 1.2: Mean value results on spin-independent azimuthal asymmetries from the NA10, E615 and E866 experiments.

Later corresponding measurements were carried out by collider experiments: the Collider Detector at Fermilab (CDF) at Tevatron [146] in proton-antiproton collisions and the Compact Muon Solenoid (CMS) at LHC [147] in proton-proton collisions. The results from the colliders

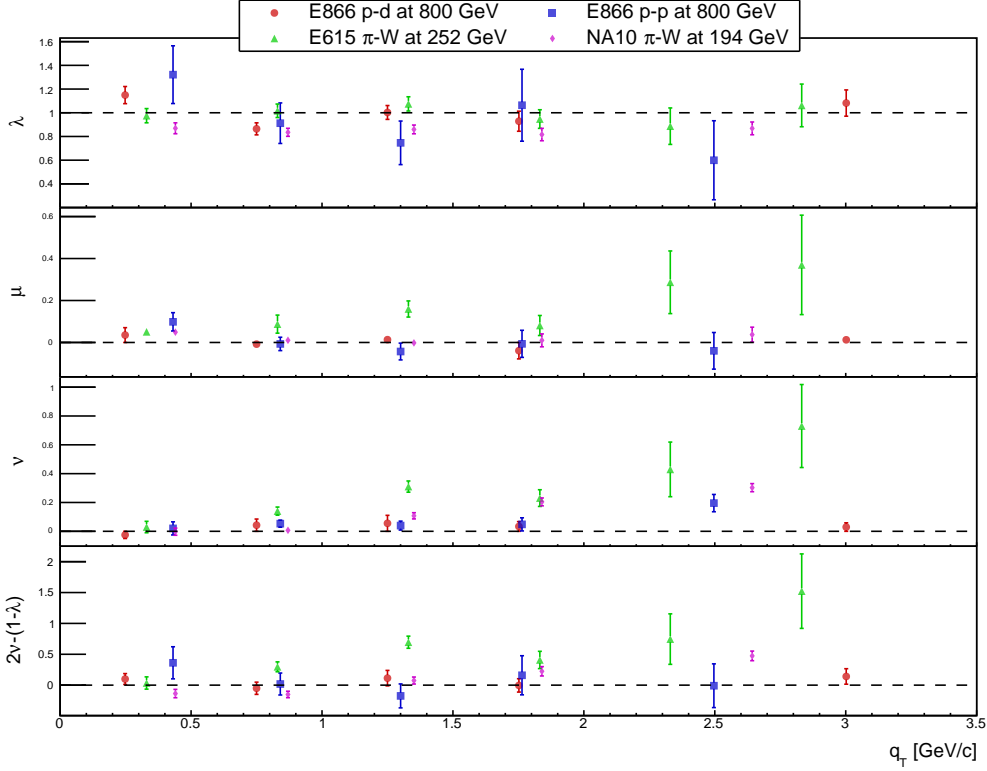


Figure 1.12: Results on λ , ν , μ asymmetries from CERN (NA10 [144]) and FermiLab (E615 [128], E866 [145]) experiments. The asymmetries are presented in the CS frame and only statistical uncertainties are drawn.

have added to the intrigue in understanding of global picture of the spin-independent azimuthal effects. The CDF data were found in good agreement with the Lam-Tung relation, while CMS has observed a noticeable violation. The results from the CDF and CMS on λ and ν asymmetries are illustrated in Fig. 1.13 comparing to pQCD NLO at NNLO calculations from [148], which are found in a good agreement with the data (except a little deviation at large q_T for ν). However, later in Ref. [149] the theoretical estimations has been done for a pion-induced fixed target DY process and the comparison to available data showed a discrepancy (see Fig. 1.14).

The pQCD calculation can not explain the obtained values [16, 149], despite of the NNLO calculation in [149] predicts a slight violation of the Lam-Tung rule, but experimental points place mostly out the perturbative curve (Fig. 1.14). One of the explanations of this result could be non-perturbative effects, *e.g.* a non-zero Boer-Mulders effect, which is described by the corresponding TMD PDF [150] accessing by the $\nu = 2A_{UU}^{\cos(2\varphi_{CS})}$ asymmetry.

One can notice from the plot in Fig. 1.12 the ν value is larger for the pion-induced DY

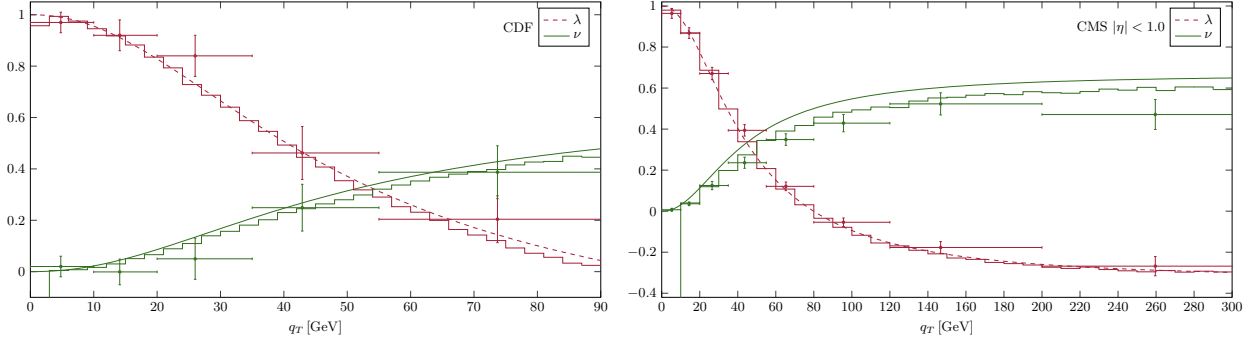


Figure 1.13: Results on λ and ν asymmetries from CDF (left) and CMS (right) experiments with a comparison to LO (line) and NLO (histogram) pQCD calculations [148]. Plots are taken from Ref. [148].

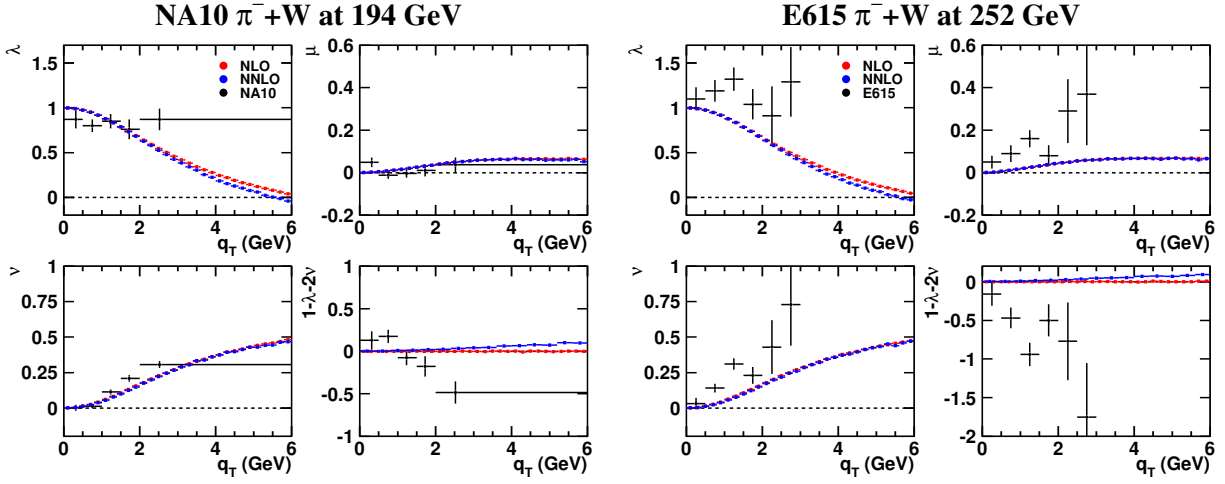


Figure 1.14: Results on spin-independent azimuthal asymmetries λ , ν , μ experiments with a comparison to NLO (red line) and NNLO (blue line) pQCD calculations [149]. Plots are taken from Ref. [149].

reaction (NA10 and E615 results) w.r.t. the proton-induced case (E866 results). The picture is due to the fact that the pion-induced Drell-Yan cross section is dominated by a valence antiquark in the pion annihilating a valence quark in the nucleon, while the proton-induced Drell-Yan process must involve a sea antiquark in the nucleon. Therefore, the p+d and p+p results that proton Boer-Mulders functions for sea quarks are smaller than those for valence quarks [151]. It is also confirmed by empirical parameterizations done in [152, 153], which are presented in Fig. 1.15. Thus, the comparison of the data leads that the sea-quark Boer-Mulders function has a sign opposite to that of the valence Boer-Mulders function in the proton. As far as a pion case is concerned, it is supposed that valence-quark Boer-Mulders functions have the same signs and also similar in magnitude (see *e.g.* Refs. [154, 155]).

Here it has to be noted, that the existence of non-trivial Boer-Mulders effect is also indicated by the measurements of the $\langle \cos 2\phi \rangle$ modulation carried out by a lot of SIDIS experiments, historically first by the EMC Collaboration [156, 157] and then at FNAL [158] and at higher energies by the ZEUS experiment at HERA [159]. There are also results from the HERMES [125] and CLAS [126] experiments. In one of the recent COMPASS results [123] the $A_{UU}^{\cos 2\phi}$ shows strong kinematic dependencies both for positive and negative hadrons.

The current knowledge on the proton and pion Boer-Mulders functions are presented in Tab. 1.1. There are also estimations of the Boer-Mulders effect for the ν asymmetry [136, 160], which are shown in Fig. 1.16.

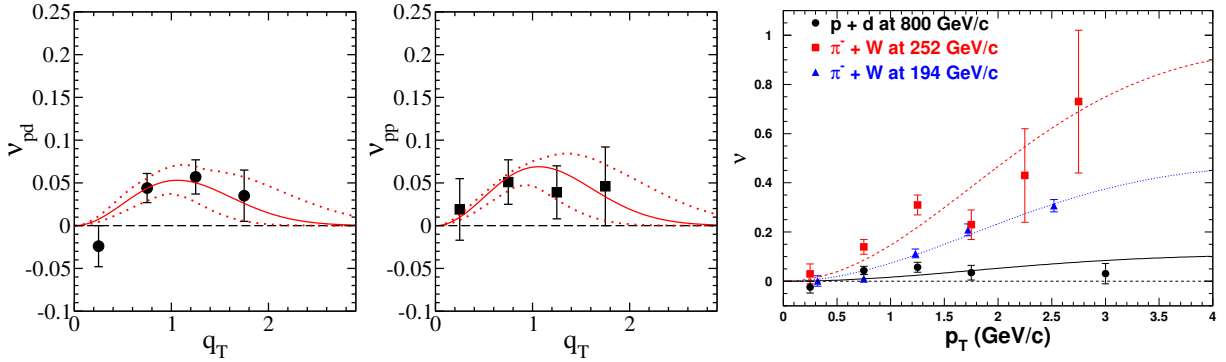


Figure 1.15: Results on phenomenological extractions of the ν asymmetry. Two left plots: extracted results from the Ref. [153] based on data of the E866 experiments, the red solid line is the fit curve, while the dotted red lines represent the corresponding errors. Right plot: extracted results from Ref. [152].

To this day there are no conclusive results on the Boer-Mulders effect that motivates further experimental and theoretical studies. COMPASS is one of the experiments that has corresponding Drell-Yan data and the extraction of the spin-independent azimuthal asymmetries is one of the analyses presented in this Thesis.

1.4 TMD effects in J/ψ production

Apart from the Drell-Yan process the signature of dimuon pair is one of the signals for J/ψ meson production. For example, dimuon mass spectrum from the COMPASS data collected during Drell-Yan runs has a clear peak around the J/ψ mass region, so, it is possible to extract valuable information about J/ψ physics. Among the studies of J/ψ physics there are

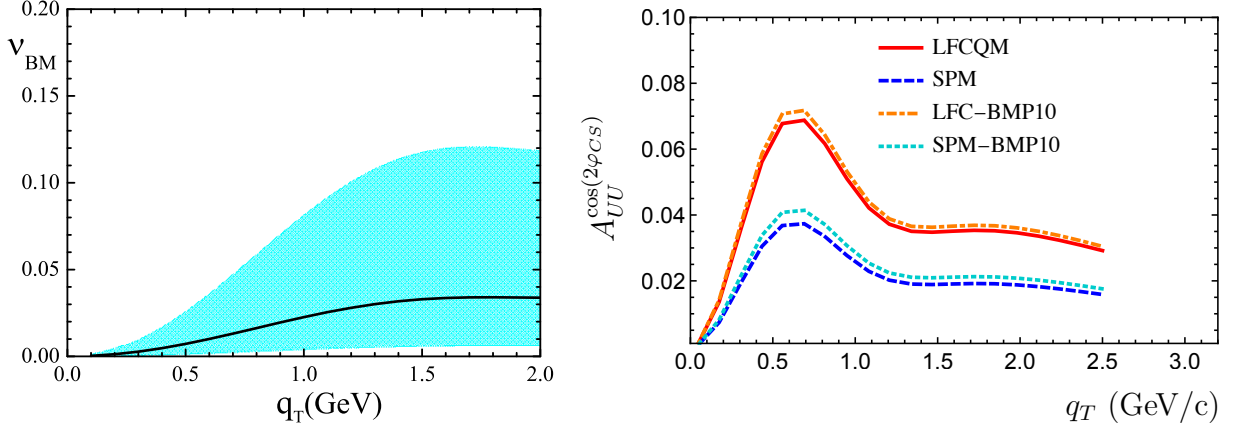


Figure 1.16: Predictions in the COMPASS kinematics for the asymmetry as a function of q_T related to the non-perturbative Boer-Mulders effect. Left: a prediction from Ref. [160]. Right: model predictions for the $A_{UU}^{\cos(2\varphi_{CS})} = \nu/2$ from Ref. [136].

measurements of spin (in)dependent azimuthal asymmetries, which are similar to the UAs and the TSAs of the Drell-Yan process.

Interpretations of the J/ψ azimuthal asymmetries are related to the nature of the J/ψ production mechanism, which is still poorly understood. According to the QCD factorization, J/ψ production is described by two parts: first is the production of partons, which is described by pQCD framework; second is the hadronization from partons into the J/ψ bound state. The hadronization is non-perturbative part of the factorization, which can be determined by various competing theoretical models, such as: Color Evaporation Model (CEM) [161, 162], Color-Singlet Model (CSM) [163, 164] and Non-Relativistic QCD (NRQCD) [165].

There are two pQCD subprocesses contributing to J/ψ production at the LO. One of them is quark-antiquark ($q\bar{q}$) -annihilation, which has an impact on quark TMD PDFs, while another subprocess is gluon-gluon (gg) -fusion, which is sensitive to gluon TMD PDFs. Depending on which of these two subprocesses is dominant one can get various interpretation on the Sivers asymmetry. In case of dominance of the $q\bar{q}$ -annihilation subprocess, measurements of J/ψ TSAs can be considered as an alternative way to access quark TMD PDFs. On the other hand, if one considers the gg -fusion as a dominant subprocess, the study of J/ψ TSAs may serve as a unique and complementary source of information about gluon PDFs and J/ψ -production mechanisms.

For the COMPASS kinematics, in Ref. [166] there is a prediction of a significant non-zero

value for the Siverson J/ψ TSA (see Fig. 1.18) assuming that the $q\bar{q}$ - annihilation mainly contributes to the asymmetry. Other production mechanisms of J/ψ might affect, but the authors in Ref. [166] consider it very unlikely that the other contributions can affect the numerator of the Siverson asymmetry. Another study at the COMPASS kinematics has been recently published in Ref. [167]. Based on the CEM approach the authors suggested that the gg -fusion contribution can be high and can even play a dominant role in COMPASS, that makes more elaborate the interpretation of the TSAs from the COMPASS J/ψ -production data. For example, in case of the dominance of gg -fusion, the J/ψ TSA measurements can constrain gluon TMD PDFs, which are still poorly studied. A few experimental results accessing gluon Siverson function have been provided from COMPASS SIDIS [221] data and from PHENIX $p+p$ collisions [222] (Fig. 1.17). The COMPASS gluon Siverson asymmetry was found to be non-zero with more than two standard deviations, while the PHENIX result is compatible with zero. The PHENIX measurements were done at quite different kinematics w.r.t. COMPASS, that can possibly explain the observed discrepancy between two experiments.

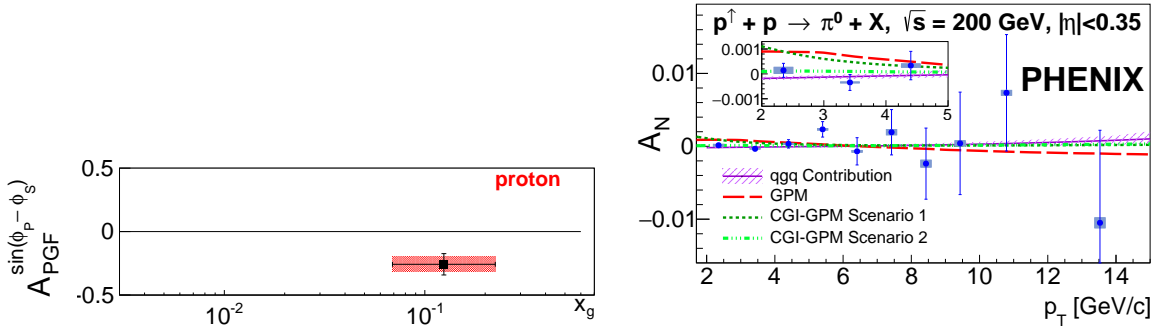


Figure 1.17: Experimental results on gluon Siverson asymmetry. Left: COMPASS results at high- p_T in hadron pair production in SIDIS data collected transversely polarized deuterons and protons [221]. Right: PHENIX results in π^0 and η meson productions in polarized $p+p$ collisions (pseudorapidity range $|\eta| < 0.35$, center-of-mass energy of 200 GeV) compared to theoretical predictions (see details and references in Ref. [222]).

A set of spin independent azimuthal asymmetries λ , μ and ν can provide information on the direction of the spin-alignment of the decaying J/ψ meson and, therefore, on the topological properties of the dominant production mechanism [168]. For example, the CEM predicts unpolarized production of J/ψ , *i.e.* the λ asymmetry should be comparable with zero. In the

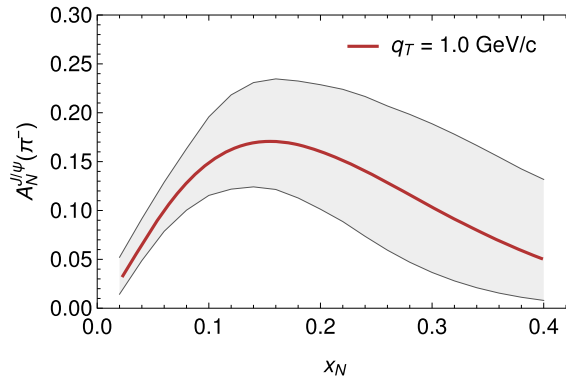


Figure 1.18: The Siverts asymmetry from J/ψ production predicted in Ref. [166] at COMPASS kinematics.

specific dilepton rest frame, in the Collins-Soper frame², J/ψ is produced with the transverse polarization ($\lambda > 0$) within the CSM approach, while the NRQCD assumed the production of longitudinally polarized J/ψ ($\lambda < 0$) [169, 171, 172].

A lot of experiments measured the λ asymmetry in J/ψ production at low p_T at fixed targets (Fig. 1.19) and at high p_T at colliders as well (Fig. 1.20). First collider results (left plot in Fig. 1.20) demonstrated discrepancies between various experimental results, even between two CDF runs at Tevatron. Later, in Ref. [168] a possible difference in the choice of axis in the reference frame was pointed out as a reason of the inconsistencies, and a common approach has been suggested, which was adopted in new LHC analyses (right plot in Fig. 1.20). The new LHC results were found more consistent within the uncertainties, but theoretical predictions are still not in satisfactory agreement with the data [173]. More accurate inputs are needed from both experimental and theoretical sides. Here, COMPASS can valuably contribute extracting the UAs from J/ψ production in the low p_T region.

²In the another specific dilepton rest frame, in the Helicity frame, the situation is inverted [169, 170].

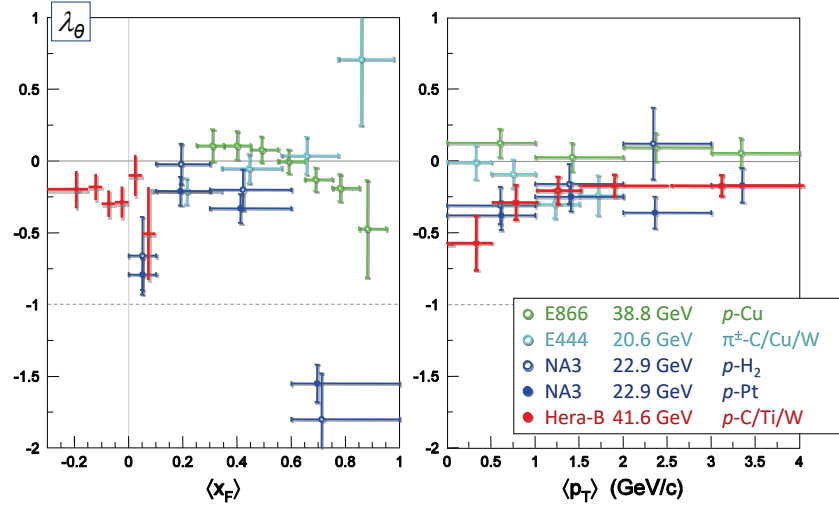


Figure 1.19: Results on the λ asymmetry in J/ψ production from various fixed target experiments [174]. The data are presented in the Collins-Soper frame.

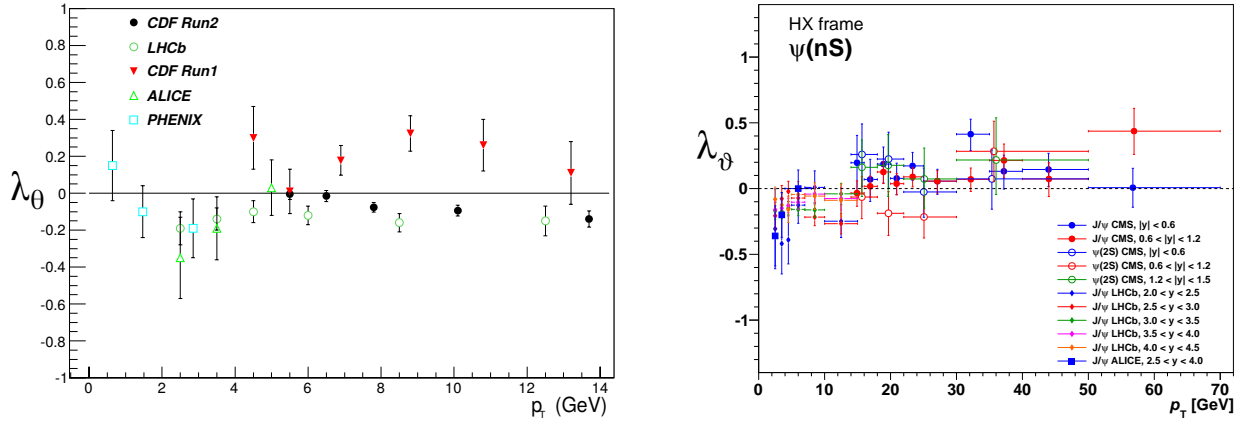


Figure 1.20: Results on the λ asymmetry in J/ψ production from collider experiments [168, 175]. The data are presented in Helicity frame.

Nucleon (and hadron in general) structure is a very rich field for physics phenomena. Only a part of active studies was mentioned in the present introduction. All available experimental results are being actively used for global fits in order to describe the 3D structure of hadrons. Measurements with polarized states provide a tool to look at the 3D picture of hadrons. In this regard, new results from the COMPASS polarized measurements are highly anticipated by the community.

Chapter 2

Theoretical basis

Deep Inelastic Scattering (DIS), Semi Inclusive Deep Inelastic Scattering (SIDIS), Drell-Yan (DY) and Deeply Virtual Compton Scattering (DVCS) processes are very powerful experimental tools to study the nucleon structure. DIS gives access to the Parton Distribution Functions (PDFs), exploring the momentum structure of the nucleon in the collinear approximation, *i.e.* neglecting transverse degrees of freedom. PDFs were investigated independently from nucleon electromagnetic form factors that are related to ratios of the observed elastic electron-nucleon scattering cross section to that predicted for a structureless nucleon. The recently developed theoretical framework of Generalized Parton Distributions (GPDs) embodies both form factors and PDFs, such that GPDs can be considered as momentum dissected form factors which provide information on the transverse localisation of a parton as a function of the fraction it carries of the nucleon's longitudinal momentum. In a complementary approach, the subtle effects of intrinsic transverse parton momenta are described by Transverse-Momentum-Dependent PDFs (TMDs). These effects become visible in hadronic Drell-Yan (DY) and Semi-Inclusive DIS (SIDIS) processes.

In this Chapter on the DY process we discuss its interplay and complementarity with the SIDIS process.

2.1 Drell-Yan cross section

DY process is a hadron-hadron scattering when a quark of one hadron and an antiquark of another hadron annihilate, creating a virtual photon (or Z^0 boson), which produces then a

dilepton pair: $H_a + H_b \rightarrow X_a + X_b + (\gamma^*(Z^{0*}) \rightarrow l^+ + l^-)$. The Feynman diagrams at tree-level corresponding QCD subprocess $q + \bar{q} \rightarrow \gamma(Z^{0*}) \rightarrow l^+ + l^-$ are presented in Fig. 2.1.

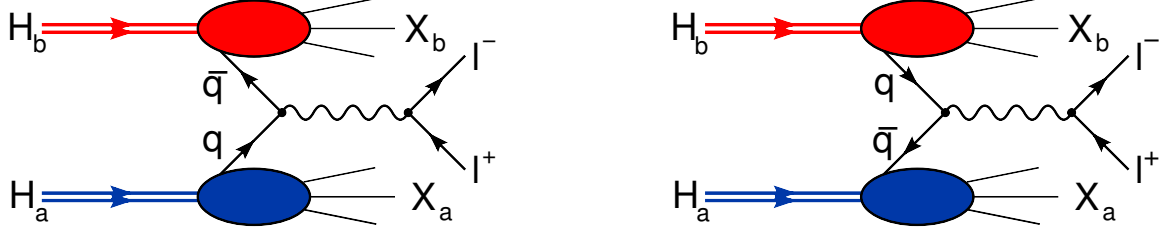


Figure 2.1: Diagram of the DY process at tree level.

We neglect Z^0 boson exchange in our consideration. In this case, following the work [176], the general formula for the differential cross section in any dilepton rest frame is

$$\frac{d\sigma}{d\Omega d^4q} = \frac{\alpha_{em}^2}{2Fq^4} L_{\mu\nu} W^{\mu\nu}, \quad (2.1)$$

where

$$F = 4\sqrt{(P_a \cdot P_b)^2 - M_a^2 M_b^2} \quad (2.2)$$

is the invariant Møller flux factor of incoming hadrons.

The cross section (2.1) can be conventionally rewritten in terms of *structure functions*, which arise as coefficient basis functions in a decomposition of the hadronic tensor $W^{\mu\nu}$. Herewith the basis Lorentz elements, due to the fact that they are composed of initial and final states, are derived in terms of simple kinematical quantities in the specified reference frame. The details are given in Appendix A.

2.2 Reference frames

For purposes of analysis and interpretation of experimental results it is convenient to use special reference frames. One of them is target rest frame (TF) where one of the hadrons is supposed to belong to the target and to have zero 3-momentum (Fig. 2.2). Wherein the momentum of another hadron is aligned along Z -axis and the virtual photon vector q is put on the (XZ) -plane in direction of the X -axis. Note that there are observable kinematic variables in this frame: azimuthal angle of the target spin vector φ_S and transverse component of the virtual photon momentum q_T .

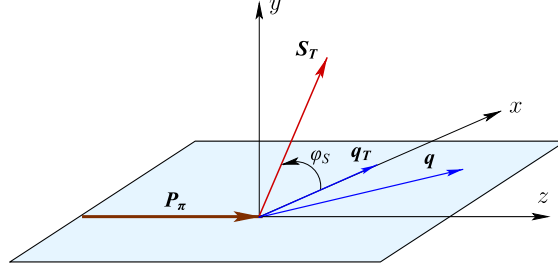


Figure 2.2: Target rest frame definition for proton-pion interaction where the proton belongs to the target and has zero 3-momentum. S_T — target (proton) spin vector.

Another commonly used reference frame is so-called *Collins-Soper frame* (CS) [15], which is one of the dilepton pair rest frames where the 3-momentum of the virtual photon \vec{q} is zero 3-vector, *i.e.* lepton vectors (l, \bar{l}) are opposite and have the same modulus, Fig. 2.3. In the dilepton rest frames the angular distribution of the DY process contracts the most convenient form (as it will be shown in the next subsection for the CS frame). Dilepton rest frame is not unique, there is an ambiguity in the position of the hadron vectors P_a, P_b since they can rotate around the lepton \vec{l} (or antilepton $\vec{\bar{l}}$) vector. In the case of the CS frame one fixes the X -axis in antiparallel direction of bisector of the hadron vectors P_a, P_b and Z -axis is chosen by the right hand rule.

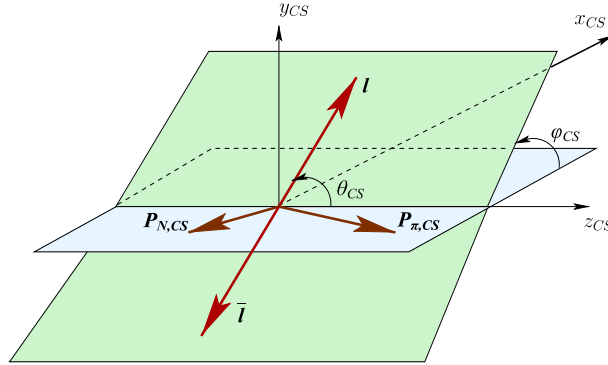


Figure 2.3: Collins-Soper frame definition for a proton-pion interaction.

Other dilepton rest frames using in literature:

- *t-channel helicity* or *Gottfried-Jackson* frame (GJ) [177], which is specified by direction of Z -axis along beam momentum \vec{P}_b ;
- *u-channel* (UC) frame [178], which is specified by antiparallel direction to the target momentum \vec{P}_a .

- *s-helicity* (SH) frame [179], which is specified by antiparallel direction to the sum of target and beam momenta $\vec{P}_a + \vec{P}_b$;

One defines two angles in the CS frame θ_{CS} and φ_{CS} , as it is shown in Fig. 2.3. θ_{CS} is a polar angle between Z -axis and lepton momentum \vec{l} , and φ_{CS} is an azimuthal angle between (XY) -plane and a plane formed by Z -axis and lepton momentum.

2.3 Kinematics in the DY process

In this subsection we collect often used kinematical expressions in the DY process, Tab. 2.1.

P_a, P_b	Lorentz 4-vectors for hadron momenta. For fixed target experiments index a corresponds to hadron from beam and index b corresponds to hadron from target.
l, l'	Lorentz 4-vectors for lepton and antilepton momenta
$q = l + l'$	virtual photon momentum
$q_T \equiv Q_T = \vec{q}_T $	transverse component of the virtual photon momentum
$Q^2 = M_{ll'}^2 = q^2$	virtuality of the photon, dilepton invariant mass
$\vec{h} \equiv \vec{q}_T / q_T$	unit vector for \vec{q}_T
$x_{1,2} = \frac{Q^2}{2(P_{b,a} \cdot q)}$	Bjorken variables
$x_F = x_1 - x_2$	Feynman variable
$\tau = x_1 x_2$	τ -variable - the product of the momentum fractions carried by the partons
$y = \frac{1}{2} \log(x_1/x_2)$	rapidity of the virtual photon
$\rho = \frac{Q_T}{Q}$	ratio of transversity
$S_T = \vec{S}_T $	transverse (w.r.t. Z -axis in TF) part of the b hadron (target in fixed target experiments) polarization
φ_S	angle between q_T and S_T vectors
$\theta_{CS}, \varphi_{CS}$	polar and azimuthal angle of lepton l in CS frame

Table 2.1: Common used notations in kinematics of the DY process

For the next we describe 4-vectors of the DY process in the CS frame. We will neglect

masses of particles in our consideration, *i.e.* $P_a^2 = P_b^2 = l^2 = l'^2 = 0$. For leptons we have

$$l_{CS}^\mu = \frac{Q}{2} \left(1, \sin \theta_{CS} \cos \varphi_{CS}, \sin \theta_{CS} \sin \varphi_{CS}, \cos \theta_{CS} \right), \quad (2.3)$$

$$l'_{CS}^\mu = \frac{Q}{2} \left(1, -\sin \theta_{CS} \cos \varphi_{CS}, -\sin \theta_{CS} \sin \varphi_{CS}, -\cos \theta_{CS} \right) \quad (2.4)$$

and for hadronic vectors

$$P_{a,CS}^\mu = \left(P_{a,CS}^0, -\sin \bar{\alpha} |\vec{P}_{a,CS}|, 0, \cos \bar{\alpha} |\vec{P}_{a,CS}| \right) \quad (2.5)$$

$$\approx P_{a,CS}^0 (1, -\sin \alpha, 0, \cos \alpha),$$

$$P_{b,CS}^\mu = \left(P_{b,CS}^0, -\sin \bar{\alpha} |\vec{P}_{b,CS}|, 0, -\cos \bar{\alpha} |\vec{P}_{b,CS}| \right) \quad (2.6)$$

$$\approx P_{b,CS}^0 (1, -\sin \alpha, 0, -\cos \alpha),$$

where α and $\bar{\alpha}$ are angles between the Z -axis and hadron momenta. The photon momentum $q = l + l'$ in the CS frame is

$$q_{CS}^\mu = (Q, 0, 0, 0), \quad (2.7)$$

which coincides with photon or dilepton rest frame. In terms of the rapidity y and the ratio $\rho = Q_T/Q$ introduced before hadron momenta can expressed as:

$$P_{a,CS}^\mu = e^{-y} \frac{\sqrt{s}}{2} \left(\sqrt{1 + \rho^2}, -\rho, 0, 1 \right), \quad (2.8)$$

$$P_{b,CS}^\mu = e^y \frac{\sqrt{s}}{2} \left(\sqrt{1 + \rho^2}, -\rho, 0, -1 \right). \quad (2.9)$$

2.4 Angular distribution of the DY cross section

The mostly used expression for the angular distribution of the DY cross section in the dilepton rest frame has the following form

$$\frac{d\sigma}{d^4q d\Omega} = \frac{\alpha_{em}^2}{F q^2} \times$$

$$\left\{ \left((1 + \cos^2 \theta) F_{UU}^1 + (1 - \cos^2 \theta) F_{UU}^2 + \sin 2\theta \cos \varphi F_{UU}^{\cos \varphi} + \sin^2 \theta \cos 2\varphi F_{UU}^{\cos 2\varphi} \right) \right.$$

$$+ S_{aL} \left(\sin 2\theta \sin \varphi F_{LU}^{\sin \varphi} + \sin^2 \theta \sin 2\varphi F_{LU}^{\sin 2\varphi} \right)$$

$$+ S_{bL} \left(\sin 2\theta \sin \varphi F_{UL}^{\sin \varphi} + \sin^2 \theta \sin 2\varphi F_{UL}^{\sin 2\varphi} \right)$$

$$+ |\vec{S}_{aT}| \left[\sin \varphi_a \left((1 + \cos^2 \theta) F_{TU}^1 + (1 - \cos^2 \theta) F_{TU}^2 + \sin 2\theta \cos \varphi F_{TU}^{\cos \varphi} + \sin^2 \theta \cos 2\varphi F_{TU}^{\cos 2\varphi} \right) \right.$$

$$\left. \left. + \cos \varphi_a \left(\sin 2\theta \sin \varphi F_{TU}^{\sin \varphi} + \sin^2 \theta \sin 2\varphi F_{TU}^{\sin 2\varphi} \right) \right] \right\}$$

$$\begin{aligned}
 & + |\vec{S}_{bT}| \left[\sin \varphi_b \left((1 + \cos^2 \theta) F_{UT}^1 + (1 - \cos^2 \theta) F_{UT}^2 + \sin 2\theta \cos \varphi F_{UT}^{\cos \varphi} + \sin^2 \theta \cos 2\varphi F_{UT}^{\cos 2\varphi} \right) \right. \\
 & \quad \left. + \cos \varphi_b \left(\sin 2\theta \sin \varphi F_{UT}^{\sin \varphi} + \sin^2 \theta \sin 2\varphi F_{UT}^{\sin 2\varphi} \right) \right] \\
 & + S_{aL} S_{bL} \left((1 + \cos^2 \theta) F_{LL}^1 + (1 - \cos^2 \theta) F_{LL}^2 + \sin 2\theta \cos \varphi F_{LL}^{\cos \varphi} + \sin^2 \theta \cos 2\varphi F_{LL}^{\cos 2\varphi} \right) \\
 & + S_{aL} |\vec{S}_{bT}| \left[\cos \varphi_b \left((1 + \cos^2 \theta) F_{LT}^1 + (1 - \cos^2 \theta) F_{LT}^2 + \sin 2\theta \cos \varphi F_{LT}^{\cos \varphi} + \sin^2 \theta \cos 2\varphi F_{LT}^{\cos 2\varphi} \right) \right. \\
 & \quad \left. + \sin \varphi_b \left(\sin 2\theta \sin \varphi F_{LT}^{\sin \varphi} + \sin^2 \theta \sin 2\varphi F_{LT}^{\sin 2\varphi} \right) \right] \\
 & + |\vec{S}_{aT}| S_{bL} \left[\cos \varphi_a \left((1 + \cos^2 \theta) F_{TL}^1 + (1 - \cos^2 \theta) F_{TL}^2 + \sin 2\theta \cos \varphi F_{TL}^{\cos \varphi} + \sin^2 \theta \cos 2\varphi F_{TL}^{\cos 2\varphi} \right) \right. \\
 & \quad \left. + \sin \varphi_a \left(\sin 2\theta \sin \varphi F_{TL}^{\sin \varphi} + \sin^2 \theta \sin 2\varphi F_{TL}^{\sin 2\varphi} \right) \right] \\
 & + |\vec{S}_{aT}| |\vec{S}_{bT}| \left[\cos(\varphi_a + \varphi_b) \left((1 + \cos^2 \theta) F_{TT}^1 + (1 - \cos^2 \theta) F_{TT}^2 \right. \right. \\
 & \quad \left. \left. + \sin 2\theta \cos \varphi F_{TT}^{\cos \varphi} + \sin^2 \theta \cos 2\varphi F_{TT}^{\cos 2\varphi} \right) \right. \\
 & \quad \left. + \cos(\varphi_a - \varphi_b) \left((1 + \cos^2 \theta) \bar{F}_{TT}^1 + (1 - \cos^2 \theta) \bar{F}_{TT}^2 \right. \right. \\
 & \quad \left. \left. + \sin 2\theta \cos \varphi \bar{F}_{TT}^{\cos \varphi} + \sin^2 \theta \cos 2\varphi \bar{F}_{TT}^{\cos 2\varphi} \right) \right. \\
 & \quad \left. + \sin(\varphi_a + \varphi_b) \left(\sin 2\theta \sin \varphi F_{TT}^{\sin \varphi} + \sin^2 \theta \sin 2\varphi F_{TT}^{\sin 2\varphi} \right) \right. \\
 & \quad \left. + \sin(\varphi_a - \varphi_b) \left(\sin 2\theta \sin \varphi \bar{F}_{TT}^{\sin \varphi} + \sin^2 \theta \sin 2\varphi \bar{F}_{TT}^{\sin 2\varphi} \right) \right] \Bigg\}, \tag{2.10}
 \end{aligned}$$

where another set of structure functions $F(q^2, (P_a \cdot q), (P_b \cdot q))$ is used are used. In order to reveal the relations between the invariant structure functions $U(q^2, (P_a \cdot q), (P_b \cdot q))$ and the structure functions $F(q^2, (P_a \cdot q), (P_b \cdot q))$ from the angular distribution in dilepton rest frame (2.10) we make a convolution of the hadronic tensor $W^{\mu\nu}$ with the leptonic tensor $L_{\mu\nu}$ substituting 4-vectors of momenta derived in the CS frame (2.4), (2.4), (2.8), (2.9). For brevity we consider only the unpolarized case, other cases are similar with additional complexity of taking into account the spin vectors S_{aT}, S_{bT} . So one has

$$\begin{aligned}
 W_u^{\mu\nu} L_{\mu\nu} & = (t_{u,1}^{\mu\nu} U_{u,1} + t_{u,2}^{\mu\nu} U_{u,2} + t_{u,3}^{\mu\nu} U_{u,3} + t_{u,4}^{\mu\nu} U_{u,4}) L_{\mu\nu} = \\
 & \quad \frac{1}{16} s \left(\frac{U_{u,1}}{s} + (1 + \rho^2) (e^{-2y} U_{u,2} + e^{2y} U_{u,3} + 2U_{u,4}) \right. \\
 & \quad \left. - (\cos^2 \theta - 2\rho \cos \theta \sin \theta \cos \varphi + \rho^2 \sin^2 \theta \cos^2 \varphi) e^{-2y} U_{u,2} \right. \\
 & \quad \left. - (\cos^2 \theta + 2\rho \cos \theta \sin \theta \cos \varphi + \rho^2 \sin^2 \theta \cos^2 \varphi) e^{2y} U_{u,3} \right. \\
 & \quad \left. + 2(\cos^2 \theta - \rho^2 \sin^2 \theta \cos^2 \varphi + \rho \sqrt{1 + \rho^2} \cos \varphi \sin \theta) U_{u,4} \right). \tag{2.11}
 \end{aligned}$$

Our goal is to obtain the same angular coefficients as at the structure functions in (2.10). For this we use the following trigonometric identities

$$\cos \theta \sin \theta = \frac{1}{2} \sin 2\theta, \quad (2.12)$$

$$\cos^2 \varphi = \frac{1}{2} + \frac{1}{2} \cos 2\varphi, \quad (2.13)$$

so, we get

$$\begin{aligned} W_u^{\mu\nu} L_{\mu\nu} = & \frac{1}{16} s \left(\frac{U_{u,1}}{s} + (1 + \rho^2)(e^{-2y}U_{u,2} + e^{2y}U_{u,3} + 2U_{u,4}) \right. \\ & + \cos^2 \theta (-e^{-2y}U_{u,2} - e^{2y}U_{u,3} + 2U_{u,4}) \\ & - \sin 2\theta \cos \varphi \rho (e^{-2y}U_{u,2} + e^{2y}U_{u,3}) \\ & \left. + \sin^2 \theta \left(\frac{1}{2} + \frac{1}{2} \cos 2\varphi \right) \rho^2 (-e^{-2y}U_{u,2} - e^{2y}U_{u,3} + 2U_{u,4}) \right). \end{aligned} \quad (2.14)$$

Further, deriving $\sin^2 \theta$ as $1 - \cos^2 \theta$ and collecting similar terms at $1 \pm \cos^2 \theta$, $\sin 2\theta \sin \varphi$, and $\sin^2 \theta \cos 2\varphi$, we can write down the relations between the invariant structure functions $U_{u,i}$ and the F functions:

$$F_{UU}^1 = \left(1 + \frac{1}{2} \rho^2 \right) \left(2e^{2y}U_{u,4} - e^{4y}U_{u,3} - U_{u,2} \right) + e^{4y}U_{u,3} + U_{u,2}, \quad (2.15)$$

$$F_{UU}^2 = 4e^{2y}U_{u,4} + \frac{2}{\rho^2} \left(e^{4y}U_{u,3} + U_{u,2} \right), \quad (2.16)$$

$$F_{UU}^{\cos \varphi} = \frac{\rho}{2} \left(e^{-2y}U_{u,2} + 2U_{u,3} \right), \quad (2.17)$$

$$F_{UU}^{\cos 2\varphi} = \frac{\rho^2}{2} \left(\frac{1}{2} e^{-2y}U_{u,2} + e^{2y}U_{u,3} + U_{u,4} \right). \quad (2.18)$$

For the unpolarized process also the following notations are used

$$\lambda = \frac{F_{UU}^1 - F_{UU}^2}{F_{UU}^1 + F_{UU}^2}, \quad \mu = \frac{F_{UU}^{\cos \varphi}}{F_{UU}^1 + F_{UU}^2}, \quad \nu = \frac{2 F_{UU}^{\cos 2\varphi}}{F_{UU}^1 + F_{UU}^2}. \quad (2.19)$$

In these notations the Lam-Tung relation ([16, 17]) reads as

$$\lambda + 2\nu = 1. \quad (2.20)$$

For the DY measurements at the COMPASS experiment we are interested in the case when the only target is polarized. So, further we will not consider parts of formulas containing the beam polarization. For the presentment in Chapter 5 one has to define the asymmetries $A_{U,L,T}^{f(\varphi, \varphi_S)}$

(where $f(\varphi, \varphi_S)$ is modulations in the cross section):

$$A_U^1 = \frac{F_{UU}^1 - F_{UU}^2}{F_{UU}^1 + F_{UU}^2}, \quad A_U^{\cos \varphi} = \frac{F_{UU}^{\cos \varphi}}{F_{UU}^1 + F_{UU}^2}, \quad A_U^{\cos 2\varphi} = \frac{F_{UU}^{\cos 2\varphi}}{F_{UU}^1 + F_{UU}^2}, \quad (2.21)$$

$$A_L^{\sin \varphi} = \frac{F_{UL}^{\sin \varphi}}{F_{UU}^1 + F_{UU}^2}, \quad A_L^{\sin 2\varphi} = \frac{F_{UL}^{\sin 2\varphi}}{F_{UU}^1 + F_{UU}^2}, \quad (2.22)$$

$$A_T^{\sin \varphi_S} = \frac{F_{UT}^1 + F_{UT}^2}{F_{UU}^1 + F_{UU}^2}, \quad \tilde{A}_T^{\sin \varphi_S} = \frac{F_{UT}^1 - F_{UT}^2}{F_{UU}^1 + F_{UU}^2},$$

$$A_T^{\sin(\varphi+\varphi_S)} = \frac{F_{UT}^{\sin \varphi} + F_{UT}^{\cos \varphi}}{2(F_{UU}^1 + F_{UU}^2)}, \quad A_T^{\sin(\varphi-\varphi_S)} = \frac{F_{UT}^{\sin \varphi} - F_{UT}^{\cos \varphi}}{2(F_{UU}^1 + F_{UU}^2)}, \quad (2.23)$$

$$A_T^{\sin(2\varphi+\varphi_S)} = \frac{F_{UT}^{\sin 2\varphi} + F_{UT}^{\cos 2\varphi}}{2(F_{UU}^1 + F_{UU}^2)}, \quad A_T^{\sin(2\varphi-\varphi_S)} = \frac{F_{UT}^{\sin 2\varphi} - F_{UT}^{\cos 2\varphi}}{2(F_{UU}^1 + F_{UU}^2)}.$$

In terms of asymmetries the angular distribution for an unpolarized beam and a polarized target case has a form

$$\begin{aligned} \frac{d\sigma}{d^4q d\Omega} = & \frac{\alpha_{em}^2}{Fq^2} \hat{\sigma}_U \left\{ (1 + D_{[\sin 2\theta]} A_U^{\cos \varphi} \cos \varphi + D_{[\sin^2 \theta]} A_U^{\cos 2\varphi} \cos 2\varphi) \right. \\ & + S_L (D_{[\sin 2\theta]} A_L^{\sin \varphi} \sin \varphi + D_{[\sin^2 \theta]} A_L^{\sin 2\varphi} \sin 2\varphi) \\ & + |\vec{S}_T| \left[(D_{[1]} A_L^{\sin \varphi} \sin \varphi + D_{\sin^2 \theta} A_L^{\sin 2\varphi} \sin 2\varphi) \sin \varphi_S \right. \\ & + D_{[\sin 2\theta]} \left(A_T^{\sin(\varphi+\varphi_S)} \sin(\varphi + \varphi_S) + A_T^{\sin(\varphi-\varphi_S)} \sin(\varphi - \varphi_S) \right) \\ & \left. \left. + D_{[\sin^2 \theta]} \left(A_T^{\sin(2\varphi+\varphi_S)} \sin(2\varphi + \varphi_S) + A_T^{\sin(2\varphi-\varphi_S)} \sin(2\varphi - \varphi_S) \right) \right] \right\}, \end{aligned} \quad (2.24)$$

where $\hat{\sigma}_U = (F_{UU}^1 + F_{UU}^2)(1 + A_U^1 \cos^2 \theta)$ — the part of the cross-section, which survives after integration over azimuthal angles φ and φ_S . Here *depolarization factor* was introduced:

$$D_{[f(\theta)]} = \frac{f(\theta)}{1 + A_U^1 \cos^2 \theta}. \quad (2.25)$$

2.5 Parton model and parton distribution functions

According to the parton model the hadronic tensor can be written as

$$W^{\mu\nu} = \frac{1}{3} \sum_q e_q^2 \int d^4k_a d^4k_b \delta^{(4)}(q - k_a - k_b) \times \quad (2.26)$$

$$\text{Tr}[\gamma^\mu \Phi^q(k_a, P_a, S_a | n_a) \gamma^\nu \bar{\Phi}^q(k_b, P_b, S_b | n_b)] + \{\Phi \leftrightarrow \bar{\Phi}\},$$

where index q denotes quark flavor and $\Phi_{ij}^q(\bar{\Phi}_{ij}^q)$ are quark-quark correlators, which are defined as

$$\Phi_{ij}^q(k_a, P_a, S_a | n_a) = \int \frac{d^4 z}{(2\pi)^4} e^{ik_a \cdot z} \langle P_a, S_a | \bar{\psi}_j^q(0) \mathcal{W}[0, z | n_a] \psi_i^q(z) | P_a, S_a \rangle, \quad (2.27)$$

$$\bar{\Phi}_{ij}^q(k_b, P_b, S_b | n_b) = \int \frac{d^4 z}{(2\pi)^4} e^{ik_b \cdot z} \langle P_b, S_b | \psi_i^q(0) \mathcal{W}[0, z | n_b] \bar{\psi}_j^q(z) | P_b, S_b \rangle. \quad (2.28)$$

Here we introduce the following notations:

- the light-cone vectors

$$n_a^\mu = \frac{1}{\sqrt{2}} (1, 0, 0, -1), \quad (2.29)$$

$$n_b^\mu = \frac{1}{\sqrt{2}} (1, 0, 0, 1); \quad (2.30)$$

- $\mathcal{W}[0, z | n_{a/b}]$ — Wilson line (color gauge link operator);
- i, j denote spinor indices.

The correlators (2.29), (2.30) are Dirac spinors and, consequently, they can be decomposed using the basis of the Dirac matrices in the spinor space $\Gamma = \{\mathbb{1}_{4 \times 4}, \gamma^\mu, \gamma^\mu \gamma_5, i\sigma^{\mu\nu} \gamma_5, i\gamma_5\}$. Due to hermiticity and parity constraints with identity (5.55) the decomposition ends up with 32 terms – matrix structures multiplied by scalar functions. We do not write down the full expression here, one can find it in Ref. [180], (see Eq. (7)). Our main quantity of interest is the trace of correlator, which is parameterized in terms of TMD functions [180–185]

$$\Phi^q[\Gamma] \equiv \frac{1}{2} \text{Tr} [\Phi^q \Gamma]. \quad (2.31)$$

After expansion of the operator in Eq. (2.31) and restricting to the leading order (twist-2) we have

$$\Phi^q[\gamma^+] = f_1^q(x_a, \vec{k}_{aT}^2) - \frac{\varepsilon_T^{ij} k_{aT}^i S_{aT}^j}{M_a} f_{1T}^{\perp q}(x_a, \vec{k}_{aT}^2), \quad (2.32)$$

$$\Phi^q[\gamma^+ \gamma_5] = S_{aL} g_{1L}^q(x_a, \vec{k}_{aT}^2) + \frac{\vec{k}_{aT} \cdot \vec{S}_{aT}}{M_a} g_{1T}^q(x_a, \vec{k}_{aT}^2), \quad (2.33)$$

$$\begin{aligned} \Phi^q[i\sigma^{i+} \gamma_5] &= S_{aT}^i h_1^q(x_a, \vec{k}_{aT}^2) + \frac{k_{aT}^i (\vec{k}_{aT} \cdot \vec{S}_{aT}) - \frac{1}{2} \vec{k}_{aT}^2 S_{aT}^i}{M_a^2} h_{1T}^{\perp q}(x_a, \vec{k}_{aT}^2) \\ &+ S_{aL} \frac{k_{aT}^i}{M_a} h_{1L}^{\perp q}(x_a, \vec{k}_{aT}^2) + \frac{\varepsilon_T^{ij} k_{aT}^j}{M_a} h_1^{\perp q}(x_a, \vec{k}_{aT}^2), \end{aligned} \quad (2.34)$$

where ε_T^{ij} abbreviates the transverse antisymmetric Levi-Cevita tensor ε^{-+ij} , and we use the convention $\varepsilon^{-+12} = 1$. Similarly for the $\bar{\Phi}$ correlator we have

$$\bar{\Phi}^q[\gamma^-] = f_1^{\bar{q}}(x_b, \vec{k}_{bT}^2) + \frac{\varepsilon_T^{ij} k_{bT}^i S_{bT}^j}{M_b} f_{1T}^{\perp\bar{q}}(x_b, \vec{k}_{bT}^2), \quad (2.35)$$

$$\bar{\Phi}^q[\gamma^- \gamma_5] = -S_{bL} g_{1L}^{\bar{q}}(x_b, \vec{k}_{bT}^2) - \frac{\vec{k}_{bT} \cdot \vec{S}_{bT}}{M_b} g_{1T}^{\bar{q}}(x_b, \vec{k}_{bT}^2), \quad (2.36)$$

$$\begin{aligned} \bar{\Phi}^q[i\sigma^i \gamma_5] &= S_{bT}^i h_1^{\bar{q}}(x_b, \vec{k}_{bT}^2) + \frac{k_{bT}^i (\vec{k}_{bT} \cdot \vec{S}_{bT}) - \frac{1}{2} \vec{k}_{bT}^2 S_{bT}^i}{M_b^2} h_{1T}^{\perp\bar{q}}(x_b, \vec{k}_{bT}^2) \\ &+ S_{bL} \frac{k_{bT}^i}{M_b} h_{1L}^{\perp\bar{q}}(x_b, \vec{k}_{bT}^2) - \frac{\varepsilon_T^{ij} k_{bT}^j}{M_b} h_1^{\perp\bar{q}}(x_b, \vec{k}_{bT}^2). \end{aligned} \quad (2.37)$$

Thus, it results in the eight leading 2-twist TMD PDFs:

$f_1(x, \vec{k}_T^2)$ — unpolarized distribution;

$g_{1L}(x, \vec{k}_T^2)$ — helicity distribution;

$g_{1T}(x, \vec{k}_T^2)$ — distribution of longitudinally polarised quarks in transversely polarized nucleon;

$f_{1T}^{\perp}(x, \vec{k}_T^2)$ — Sivers distribution: distribution of quarks in a transversely polarized nucleon;

$h_{1T}(x, \vec{k}_T^2)$ — quark transverse polarization along nucleon transverse polarisation;

$h_{1L}^{\perp}(x, \vec{k}_T^2)$ — quark transverse polarization in a longitudinally polarised nucleon;

$h_{1T}^{\perp}(x, \vec{k}_T^2)$ — quark transverse polarization in a transversely polarised nucleon;

$h_1^{\perp}(x, \vec{k}_T^2)$ — Boer-Mulders distribution: quark transverse polarization in an unpolarized nucleon.

Note that six of them are T-even: $f_1(x, \vec{k}_T^2)$, $g_{1L}(x, \vec{k}_T^2)$, $g_{1T}(x, \vec{k}_T^2)$, $h_{1T}(x, \vec{k}_T^2)$, $h_{1L}^{\perp}(x, \vec{k}_T^2)$, $h_{1T}^{\perp}(x, \vec{k}_T^2)$. And the rest two TMDs are T-odd: Sivers $f_{1T}^{\perp}(x, \vec{k}_T^2)$ and Boer-Mulders $h_1^{\perp}(x, \vec{k}_T^2)$ distributions.

In the next leading order (3-twist) 16 TMD PDFs arise but they will not be considered in the Thesis (3-twist and 4-twist results can be found in Ref. [180]).

So we have two types of the decomposition of the hadronic tensor $W^{\mu\nu}$: one in basis of Lorentz space (5.63) and second is in spinor basis of Dirac matrices (2.26). The first one leads to the structure functions, while the second one deals with the distribution functions. In order to establish the relation between two decompositions the following convolution operation is

introduced

$$\begin{aligned} \mathcal{C} [w f_1 \bar{f}_2] &\equiv \frac{1}{3} \sum_q e_q^2 \int d^2 \vec{k}_{aT} d^2 \vec{k}_{bT} \delta^{(2)}(\vec{q}_T - \vec{k}_{aT} - \vec{k}_{bT}) \times \\ &w \left[f_1^q(x_a, \vec{k}_{aT}^2) f_2^{\bar{q}}(x_b, \vec{k}_{bT}^2) + f_1^{\bar{q}}(x_a, \vec{k}_{aT}^2) f_2^q(x_b, \vec{k}_{bT}^2) \right]. \end{aligned} \quad (2.38)$$

Using the convolution one finds leading order structure functions in terms of distribution functions in the CS frame. The list of expressions is placed in Appendix B.

At the leading order the functions F_{UU}^2 , F_{UT}^2 , $F_{UL}^{\sin \varphi}$, $F_{UU}^{\cos \varphi}$, $F_{UT}^{\sin(\varphi+\varphi_S)}$, $F_{UT}^{\sin(\varphi-\varphi_S)}$ vanish and, consequently, $A_U^1 = 1$, $A_L^{\sin \varphi} = 0$, $A_T^{\sin \varphi_S} = 1$, $\tilde{A}_T^{\sin \varphi_S} = 1$. Thus, at leading order the Eq. (2.24) simplifies [186]:

$$\begin{aligned} \frac{d\sigma}{dq^4 d\Omega} &= \frac{\alpha^2}{Fq^2} \hat{\sigma}'_U \left\{ 1 + D_{[\sin 2\theta_{CS}]} A_U^{\cos \varphi_{CS}} \cos \varphi_{CS} + D_{[\sin^2 \theta_{CS}]} A_U^{\cos 2\varphi_{CS}} \cos 2\varphi_{CS} \right. \\ &+ |S_T| \left[A_T^{\sin \varphi_S} \sin \varphi_S \right. \\ &+ D_{[\sin 2\theta_{CS}]} \left(A_T^{\sin(\varphi_{CS}+\varphi_S)} \sin(\varphi_{CS} + \varphi_S) + A_T^{\sin(\varphi_{CS}-\varphi_S)} \sin(\varphi_{CS} - \varphi_S) \right) \\ &\left. \left. + D_{[\sin^2 \theta_{CS}]} \sin^2 \theta_{CS} \left(A_T^{\sin(2\varphi_{CS}+\varphi_S)} \sin(2\varphi_{CS} + \varphi_S) + A_T^{\sin(2\varphi_{CS}-\varphi_S)} \sin(2\varphi_{CS} - \varphi_S) \right) \right] \right\} \end{aligned} \quad (2.39)$$

with the simplified unpolarized part of the cross section $\hat{\sigma}_U^{LO}$ and depolarization factor D^{LO} :

$$\hat{\sigma}_U^{LO} = F_{UU}^1 (1 + \cos^2 \theta), \quad (2.40)$$

$$D_{[\sin^2 \theta]}^{LO} = \frac{\sin^2 \theta}{1 + \cos^2 \theta}. \quad (2.41)$$

Note that the LO angular distribution (2.39) will be used for asymmetries extraction in the analysis in Chapter 5.

2.6 Deeply inelastic and semi-inclusive deeply inelastic scattering

Another important, and historically first, process accessing the TMD PDFs is Semi-Inclusive Deeply Inelastic Scattering (SIDIS), which is a Deeply Inelastic Scattering (DIS) with a detected hadron state. In this section we also describe this process since DY and SIDIS complement each other and have relation through distribution functions due to assumption of their universality (process independence). The reaction deals with scattering of lepton on a nucleon. The high

energetic lepton breaks up the nucleon that leads to a final hadronic state X . We focus on the scattering of polarized lepton l on proton P . The reactions are

$$l + P \rightarrow l' + X, \quad \text{DIS} \quad (2.42)$$

$$l + P \rightarrow l' + P_h + X, \quad \text{SIDIS} \quad (2.43)$$

In full-inclusive case *i.e.* in DIS, only the lepton l' is detected in the final state and X is unknown (Eq. (2.42)). In semi-inclusive (SIDIS) process a part of hadronic state is also detected in the final state (P_h in Eq. (2.43)), see Fig. 2.4. Analogously to the DY case, the SIDIS cross section

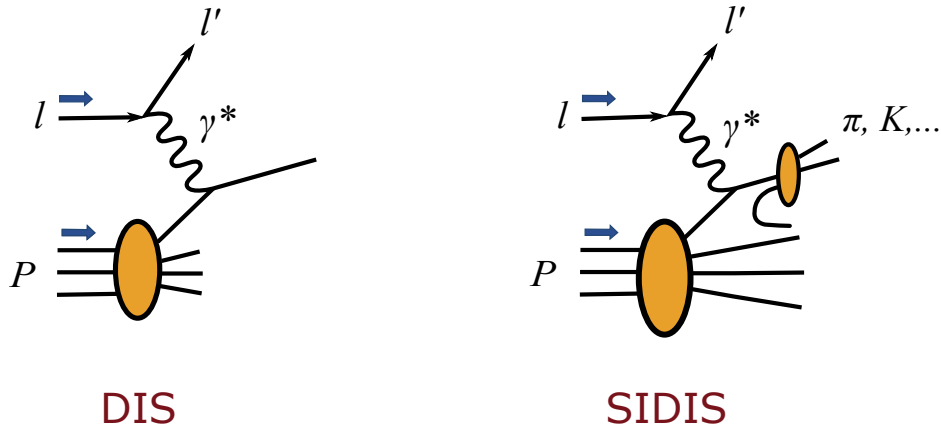


Figure 2.4: Diagrams of DIS and SIDIS processes.

can be also decomposed on the basis with coefficients as structure functions in a certain reference frame. Such treatment can be found *e.g.* in Ref. [22]. The definitions of kinematic variables and the choice of a reference frame have been agreed at the Transversity workshop in Trento in 2004 [187]. The specified reference frame is a target rest frame where the Z axis is directed along the momentum of virtual photon, the X axis is collinear with the lepton scattering plane, the Y axis is chosen to be perpendicular to the (XY) plane as shown in Fig. 2.5. Commonly used kinematic variables and their notations for description of the SIDIS process are given in Tab. 2.2. Applying the parton model for the hadronic tensor, one obtains

$$W^{\mu\nu} = \sum_{quarks} e_i^2 \int \frac{d^2p}{(2\pi)^4} \delta[(p+q)^2] \text{Tr}(\Phi \gamma^\mu(p+\not{q}) \gamma^\nu), \quad (2.44)$$

in the DIS case and

$$W^{\mu\nu} = \frac{z}{M} \sum_{quarks} e_i^2 \int d^3\vec{p}_T \text{Tr}[\Phi^q(x, p_T) \gamma^\mu \Delta^q(z, k_T) \gamma^\nu] \quad (2.45)$$

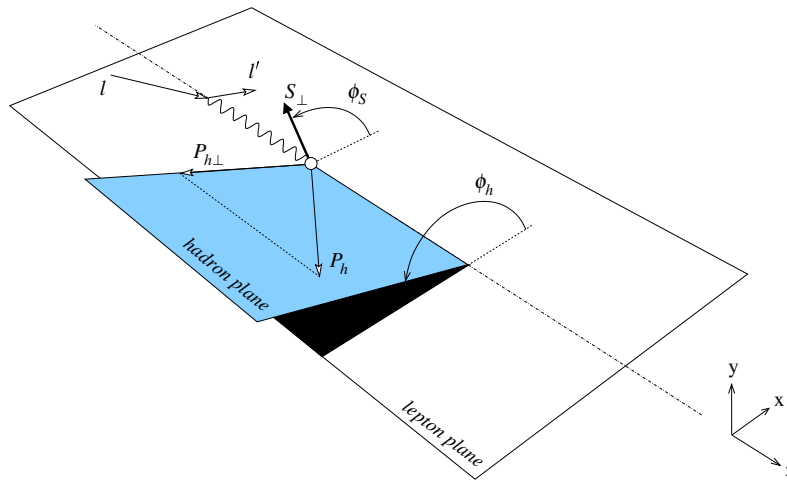


Figure 2.5: Lepton and hadron planes in semi-inclusive deep inelastic scattering.

$x = \frac{Q^2}{2(P,q)}$	the fraction of the nucleon momentum transferred by the quark
$y = \frac{(P,q)}{(P,l)}$	the fraction of the energy transfer to the nucleon
$z = \frac{(P,P_h)}{(P,q)}$	the fraction of the struck quark energy transferred by the detected hadron after fragmentation
$q = l - l'$	4-momentum transferred by the lepton to the target
$Q^2 \equiv -q^2$	virtuality of the photon, dilepton invariant mass, defines the resolution power of the measurement
$W^2 = (\vec{P} + \vec{q})^2$	squared mass of X
$\nu = \frac{(P,q)}{M}$	energy transfer from lepton to nucleon in the laboratory frame
θ	the lepton scattering angle in the laboratory frame
ϕ_h	angle between lepton and hadron planes
ϕ_S	angle between spin vector and lepton plane
λ	the initial lepton helicity ($ \lambda \leq 1$)

Table 2.2: Commonly used notations in kinematics of the SIDIS process.

for the SIDIS process. Note, that here a new type of the correlator $\Delta^q(x, k_T)$ arises, which corresponds to a description of hadronization of the final state X in terms of *fragmentation functions*. Also here the hermitian conjugate terms (with $\bar{\Phi}$ and $\bar{\Delta}$) in (2.42) and (2.43) are omitted, but can be written analogously to the DY case. Similarly to $\Phi^q(x, p_T)$, the “ Δ -correlators” expands at the leading order in the following way:

$$\Delta^{q[\gamma^-]}(z, k_T) = D_1(z, k_T^2) + \frac{\epsilon_{Tij} k_T^i S_{hT}^j}{z M_h} D_{1T}^\perp(z, k_T^2), \quad (2.46)$$

$$\Delta^{q[\gamma^- \gamma_5]} = S_L G_{1L}^q(z, k_T^2) + \frac{k_T \cdot \vec{S}_T}{M_h} G_{1T}^q(z, k_T^2), \quad (2.47)$$

$$\Delta^{q[i\sigma^{i-} \gamma_5]}(z, k_T) = S_{hT}^i H_1(z, k_T^2) + \frac{\epsilon_T^{ij} k_{Tj}}{z M_h} H_1^\perp(z, k_T^2) + \dots \quad (2.48)$$

Here $D_1(z, k_T^2)$, $G_{1L}^q(z, k_T^2)$, and $H_1^\perp(z, k_T^2)$ are the fragmentaion functions.

In the SIDIS case the convolution operation is defined with a fragmentation function D for the third argument¹ (instead of another PDF as it is in the convolution in DY):

$$\begin{aligned} C[\omega f D] = & x \sum_a e_a^2 \int d^2 \vec{k}_T d^2 \vec{p}_T \delta^2 \left(\vec{k}_T - \vec{p}_T - \frac{\vec{P}_T^h}{z} \right) \times \\ & \omega \left(\vec{P}_T, \vec{k}_T \right) f_a(x, k_T^2) D_a(z, p_T^2). \end{aligned} \quad (2.49)$$

The structure functions expressed in terms of TMD PDFs and TMD FFs through convolution are listed in Appendix B

The SIDIS differential cross-section in terms of the structure functions reads

$$\begin{aligned} \frac{d\sigma}{dx dy d\psi dz d\phi_h dP_{h\perp}^2} = & \frac{\alpha^2}{xyQ^2} \frac{y^2}{2(1-\varepsilon)} \left(1 + \frac{\gamma^2}{2x} \right) \times \\ & \left\{ F_{UU,T} + \varepsilon F_{UU,L} + \sqrt{2\varepsilon(1+\varepsilon)} \cos \phi_h F_{UU}^{\cos \phi_h} \right. \\ & + \varepsilon \cos(2\phi_h) F_{UU}^{\cos 2\phi_h} + \lambda_e \sqrt{2\varepsilon(1-\varepsilon)} \sin \phi_h F_{LU}^{\sin \phi_h} \\ & + S_{\parallel} \left[\sqrt{2\varepsilon(1+\varepsilon)} \sin \phi_h F_{UL}^{\sin \phi_h} + \varepsilon \sin(2\phi_h) F_{UL}^{\sin 2\phi_h} \right] \\ & + S_{\parallel} \lambda_e \left[\sqrt{1-\varepsilon^2} F_{LL} + \sqrt{2\varepsilon(1-\varepsilon)} \cos \phi_h F_{LL}^{\cos \phi_h} \right] \\ & \left. + |\vec{S}_{\perp}| \left[\sin(\phi_h - \phi_S) \left(F_{UT,T}^{\sin(\phi_h - \phi_S)} + \varepsilon F_{UT,L}^{\sin(\phi_h - \phi_S)} \right) \right] \right\} \end{aligned}$$

¹Here D is a general notation for all types of FFs ($D_1(z, k_T^2)$, $G_{1L}^q(z, k_T^2)$, and $H_1^\perp(z, k_T^2)$).

$$\begin{aligned}
 & + \varepsilon \sin(\phi_h + \phi_S) F_{UT}^{\sin(\phi_h + \phi_S)} + \varepsilon \sin(3\phi_h - \phi_S) F_{UT}^{\sin(3\phi_h - \phi_S)} \\
 & + \sqrt{2\varepsilon(1+\varepsilon)} \sin\phi_S F_{UT}^{\sin\phi_S} + \sqrt{2\varepsilon(1+\varepsilon)} \sin(2\phi_h - \phi_S) F_{UT}^{\sin(2\phi_h - \phi_S)} \Big] \\
 & + |\vec{S}_\perp| \lambda_e \left[\sqrt{1-\varepsilon^2} \cos(\phi_h - \phi_S) F_{LT}^{\cos(\phi_h - \phi_S)} + \sqrt{2\varepsilon(1-\varepsilon)} \cos\phi_S F_{LT}^{\cos\phi_S} \right. \\
 & \left. + \sqrt{2\varepsilon(1-\varepsilon)} \cos(2\phi_h - \phi_S) F_{LT}^{\cos(2\phi_h - \phi_S)} \right] \Big\}, \tag{2.50}
 \end{aligned}$$

where for a compact view the following notations have been introduced

$$\varepsilon = \frac{1 - y - \frac{1}{4}\gamma^2 y^2}{1 - y + \frac{1}{2}y^2 + \frac{1}{4}\gamma^2 y^2}, \tag{2.51}$$

which represents the ratio of the longitudinal to the transverse photon flux, and

$$\gamma = \frac{2Mx}{Q}. \tag{2.52}$$

In terms of the asymmetries, which are defined as

$$A_{U(L),T}^{w(\phi_h, \phi_S)} = \frac{F_{U(L),T}^{w(\phi_h, \phi_S)}}{F_{UU,T} + \varepsilon F_{UU,L}}, \tag{2.53}$$

the SIDIS single-polarized cross-section takes the form [182, 188, 189]:

$$\begin{aligned}
 \frac{d\sigma}{dx dy dz dp_T^2 d\phi_h d\phi_S} &= \left[\frac{\alpha^2}{xyQ^2} \frac{y^2}{2(1-\varepsilon)} \left(1 + \frac{\gamma^2}{2x} \right) (F_{UU,T} + \varepsilon F_{UU,L}) \times \right. \\
 & \left(1 + \sqrt{2\varepsilon(1+\varepsilon)} A_{UU}^{\cos\phi_h} \cos\phi_h + \varepsilon A_{UU}^{\cos 2\phi_h} \cos 2\phi_h \right. \\
 & + \lambda \sqrt{2\varepsilon(1-\varepsilon)} A_{LU}^{\sin\phi_h} \sin\phi_h \\
 & + S_L [\sqrt{2\varepsilon(1+\varepsilon)} A_{UL}^{\sin\phi_h} \sin\phi_h + \varepsilon A_{UL}^{\sin 2\phi_h} \sin 2\phi_h] \\
 & + S_L \lambda [\sqrt{1-\varepsilon^2} A_{LL} + \sqrt{2\varepsilon(1-\varepsilon)} A_{LL}^{\cos\phi_h} \cos\phi_h] \\
 & + S_T [A_{UT}^{\sin(\phi_h - \phi_S)} \sin(\phi_h - \phi_S) \\
 & + \varepsilon A_{UT}^{\sin(\phi_h + \phi_S)} \sin(\phi_h + \phi_S) + \varepsilon A_{UT}^{\sin(3\phi_h - \phi_S)} \sin(3\phi_h - \phi_S) \\
 & + \sqrt{2\varepsilon(1+\varepsilon)} A_{UT}^{\sin\phi_S} \sin\phi_S + \sqrt{2\varepsilon(1+\varepsilon)} A_{UT}^{\sin(2\phi_h - \phi_S)} \sin(2\phi_h - \phi_S)] \\
 & + S_T \lambda [\sqrt{1-\varepsilon^2} A_{LT}^{\cos(\phi_h - \phi_S)} \cos(\phi_h - \phi_S) \\
 & \left. + \sqrt{2\varepsilon(1-\varepsilon)} A_{LT}^{\cos\phi_S} \cos\phi_S + \sqrt{2\varepsilon(1-\varepsilon)} A_{LT}^{\cos(2\phi_h - \phi_S)} \cos(2\phi_h - \phi_S) \right] \Big], \tag{2.54}
 \end{aligned}$$

SIDIS asymmetry	DY asymmetry
$A_{UU}^{\cos 2\phi_h} \propto \mathbf{h}_1^{\perp\mathbf{q}} \otimes H_{1q}^{\perp h} + \dots$	$A_{UU}^{\cos 2\varphi_{CS}} \propto h_{1,\pi}^{\perp q} \otimes \mathbf{h}_{1,\mathbf{p}}^{\perp\mathbf{q}}$
$A_{UT}^{\sin(\phi_h - \phi_s)} \propto \mathbf{f}_{1\mathbf{T}}^{\perp\mathbf{q}} \otimes D_{1q}^h$	$A_{UT}^{\sin \varphi_S} \propto f_{1,\pi}^q \otimes \mathbf{f}_{1\mathbf{T},\mathbf{p}}^{\perp\mathbf{q}}$
$A_{UT}^{\sin(\phi_h + \phi_s)} \propto \mathbf{h}_1^{\mathbf{q}} \otimes H_{1q}^{\perp h}$	$A_{UT}^{\sin(2\varphi_{CS} - \varphi_S)} \propto h_{1,\pi}^{\perp q} \otimes \mathbf{h}_{1,\mathbf{p}}^{\mathbf{q}}$
$A_{UT}^{\sin(3\phi_h - \phi_s)} \propto \mathbf{h}_{1\mathbf{T}}^{\perp\mathbf{q}} \otimes H_{1q}^{\perp h}$	$A_{UT}^{\sin(2\varphi_{CS} + \varphi_S)} \propto h_{1,\pi}^{\perp q} \otimes \mathbf{h}_{1\mathbf{T},\mathbf{p}}^{\perp\mathbf{q}}$
$A_{UL}^{\sin 2\phi_h} \propto \mathbf{h}_{1\mathbf{L}}^{\perp\mathbf{q}} \otimes H_{1q}^{\perp h}$	$A_{UL}^{\sin 2\varphi_{CS}} \propto h_{1,\pi}^{\perp q} \otimes \mathbf{h}_{1\mathbf{L},\mathbf{p}}^{\perp\mathbf{q}}$
$A_{LL} \propto g_{1L}^q \otimes D_{1q}^h$	Double polarized DY only
$A_{LT}^{\cos(\phi_h - \phi_s)} \propto g_{1T}^q \otimes D_{1q}^h$	

Table 2.3: Relations in measurements between the SIDIS and DY processes.

Hereby, with assumption of the universality of PDFs there is a bridge between the SIDIS and DY measurements. The Tab. 2.3 shows the corresponding relations between asymmetries, which can be experimentally extracted.

Particularly, for the Sivers and Boer-Mulders TMD PDFs we have time-reversal odd properties that gives sign-change with respect to the DY and SIDIS processes:

$$f_{1T}^{\perp}(DY) = -f_{1T}^{\perp}(SIDIS), \quad (2.55)$$

$$h_1^{\perp}(DY) = -h_1^{\perp}(SIDIS). \quad (2.56)$$

The experimental confirmation of (2.55) and (2.56) with comparison to the amplitude shape of the corresponding TMDs is considered as an universality test of non-perturbative QCD.

Concluding this Section, it has to be noted that the COMPASS experiment is presently the only place to perform the measurements in either SIDIS or DY processes, using a similar setup and a similar transversely polarized proton target. This opens a unique opportunity, when comparing results obtained from the two alternative experimental approaches, to test the opposite sign prediction for the T-odd TMD functions, to confirm (pseduo)universality of TMD PDFs at practically the same hard scale, thereby minimising possible bias introduced by TMD evolution. Corresponding TSAs extracted from SIDIS data at the hard scales similar to the DY mass ranges² at COMPASS (see Fig. 2.6) are published in Ref. [79].

²Details on COMPASS DY mass ranges will be given in Chapter 5

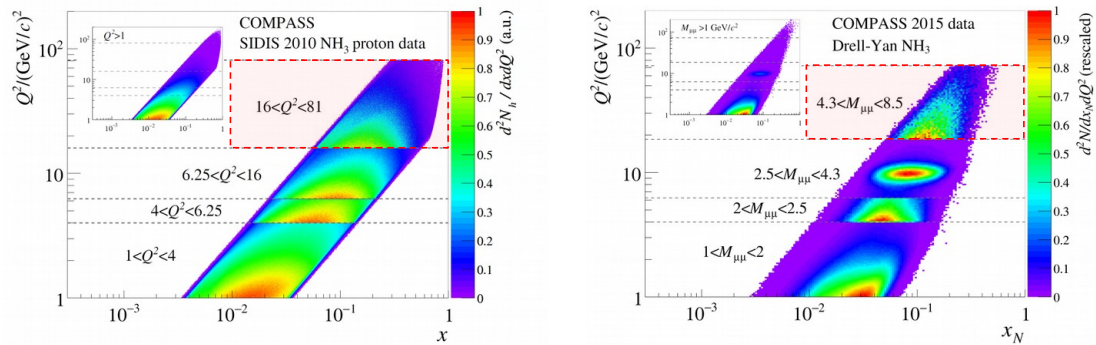


Figure 2.6: Left: charged hadron SIDIS 2010 two-dimensional phase space (Q^2, x) distribution for $z > 0.1$. Right: dimuon pairs DY 2015 two-dimensional phase space (Q^2, x_N). The SIDIS sub- Q^2 ranges correspond to four DY Q^2 ranges.

Chapter 3

The COMPASS experiment

COMPASS is a high-energy physics experiment located in the EHN2 experimental hall (bldg. 888) of the CERN North Area (NA). It is a fixed target experiment at the M2 beam line of the Super Proton Synchrotron (SPS) (Fig. 3.1).

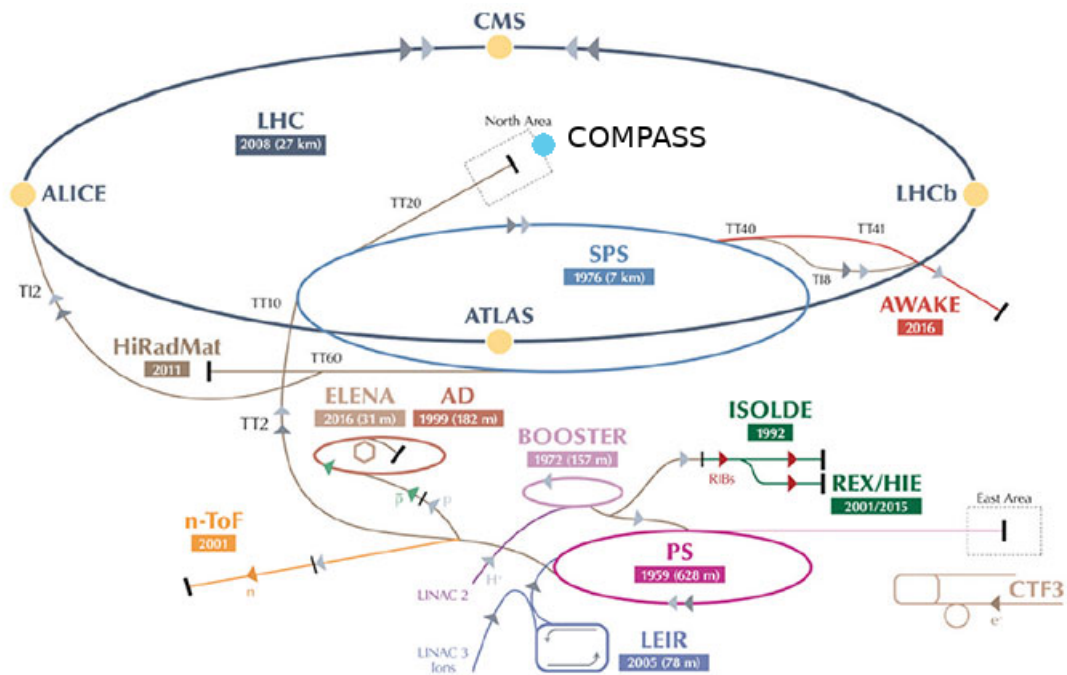


Figure 3.1: COMPASS location in CERN.

The COMPASS experiment takes its origin from February 1997, when the proposal [48] has been approved by the CERN committee. It was a result of the suggestion of the CERN committee for two different scientific teams to unite in one. These teams had various projects: one was going to study hadron spectroscopy with hadron beam followed by the CHEOPS

collaboration, another was interested in the research of nucleon spin structure using muon beam as a successor of the HMC experiment (Fig. 3.2). Since CERN's infrastructure had a facility to switch these kinds of beams inside one area, two projects joined their forces to create one, quite universal, experimental setup. Memorandum of Understanding was signed in September 1998 and then in October 1998 the experiment started to be built.

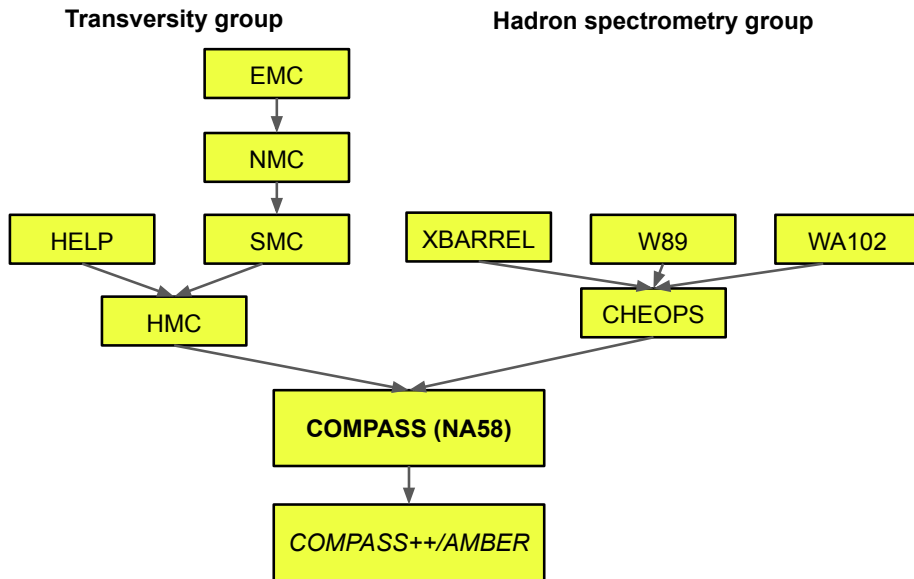


Figure 3.2: Scheme of previous collaborations on which COMPASS was founded.

In Tab. 3.1 the broad physics program exploited by the COMPASS experiment in all the years of data taking, starting from the first run in 2002, is shown. The COMPASS spectrometer is a multi-purpose two-stages spectrometer with two dipole magnets, SM1 and SM2. SM1 provides an integrated field of 1 Tm and identifies the so called Large Angle Spectrometer (LAS), mainly dedicated to the detection of small momentum particles scattered at large polar angles. SM2 has an integrated field of 4.4 Tm and is the core of the Small Angle Spectrometer (SAS), mostly dedicated to the detection of high momenta particles emitted with small polar angles. Both the stages are equipped with electromagnetic and hadronic calorimeters, as well as a system dedicated to detection of the muons (muon filter) and various tracking detectors. The two stages structure ensures a large polar ($18 \text{ mrad} < \theta < 180 \text{ mrad}$) and momentum acceptance. This chapter contains an overview of all the components contributing to the COMPASS data taking, namely the beam line, the polarized target, the various detectors stations and the trigger system, with a main focus on the experimental setup of the 2018 Drell-Yan run, since

this Thesis is devoted to the analysis of the Drell-Yan data. A sketch of this setup is shown in Fig. 3.3.

Year	Physics program	Target polarization	Beam
2002	deuteron SIDIS	20% trans., 80% long.	μ^-
2003	deuteron SIDIS	20% trans., 80% long.	μ^-
2004	deuteron SIDIS	20% trans., 80% long.	μ^-
2005	shutdown		
2006	deuteron SIDIS	longitudinal	μ^-
2007	proton SIDIS	50% trans., 50% long.	μ^-
2008	Hadron Spectroscopy		
2009			
2010	proton SIDIS	transverse	μ^-
2011	proton SIDIS	longitudinal	μ^-
2012	Primakoff/DVCS run		
2013	shutdown		
2014			
2015	Drell-Yan run	transverse	π^-
2016	DVCS run, proton SIDIS	unpolarised	μ^-
2017	DVCS run, proton SIDIS	unpolarised	μ^-
2018	Drell-Yan run	transverse	π^-
2019	shutdown		
2020			
2021	deuteron SIDIS	transverse	μ^-
2022	deuteron SIDIS	transverse	μ^-

Table 3.1: The COMPASS data taking by years.

3.1 Beam

Muon or hadron beam for COMPASS is originally provided by the SPS. The SPS has facilities to accelerate sulphur and oxygen nuclei, electrons, positrons, protons and antiprotons.

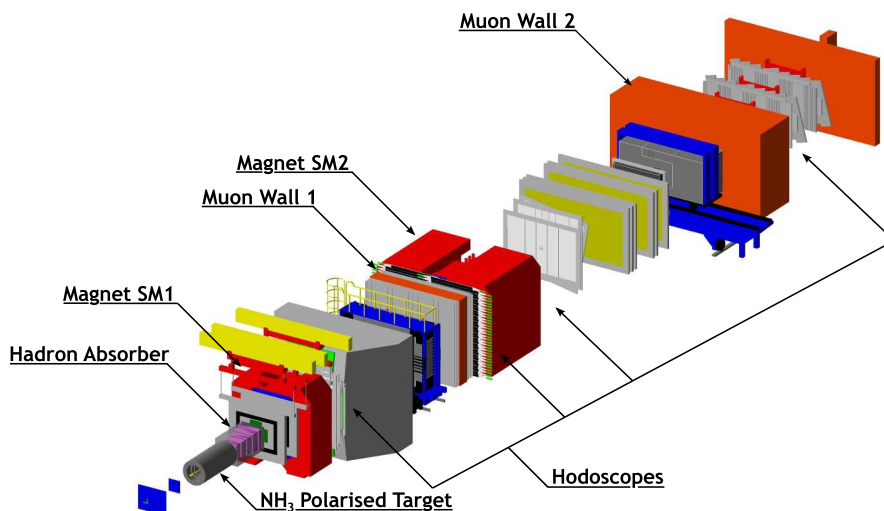


Figure 3.3: Scheme of the COMPASS setup.

At the circumference of the SPS there is an “appendix”, in which protons are injected between the LHC cycles. The appendix is a long straight section (LSS2) leading the proton beam (with momentum up to 400-450 GeV/c) to the North Experimental Area (NA). The extracted beam is transported by bending magnets and focusing elements over a few hundreds of meters and then it is branched into three beams by switching magnets and beam-splitting system. Each branched beam collides with targets: T2, T4 and T6 respectively. The targets produce the secondary particle beams with corresponding lines as shown in Fig. 3.4:

- H2 and H4 beam lines after T2 target;
- After T4 target there are 3l lines: H6 and H8 beam lines and P42/K12 beam line with additional T10 target (NA62);
- M2 beam line (NA58/COMPASS) after T6 target.

Each target has similar construction, which consists of a set of lead or beryllium blocks with different thickness. They are mounted on a common frame, which can be moved by the SPS control room to select or align the target and adjust some of the properties of the secondary beam. General properties of the SPS beam and North Area beams can be monitored from the SPS page 1, which is shown in Fig. 3.5 with the description of a spill diagram in Fig. 3.6.

The SPS page 1 shows the information about intensity (I/E11 column) — the number of protons sent towards the primary target in units of 10^{11} protons per spill; multiplicity (MUL

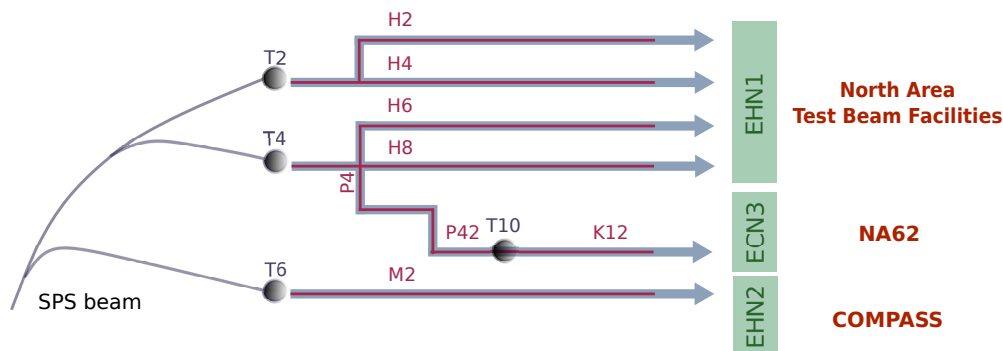


Figure 3.4: The scheme of the experimental Hall North 1 and 2 (EHN1, EHN2) and Experimental Cavern North 3 (ECN3).

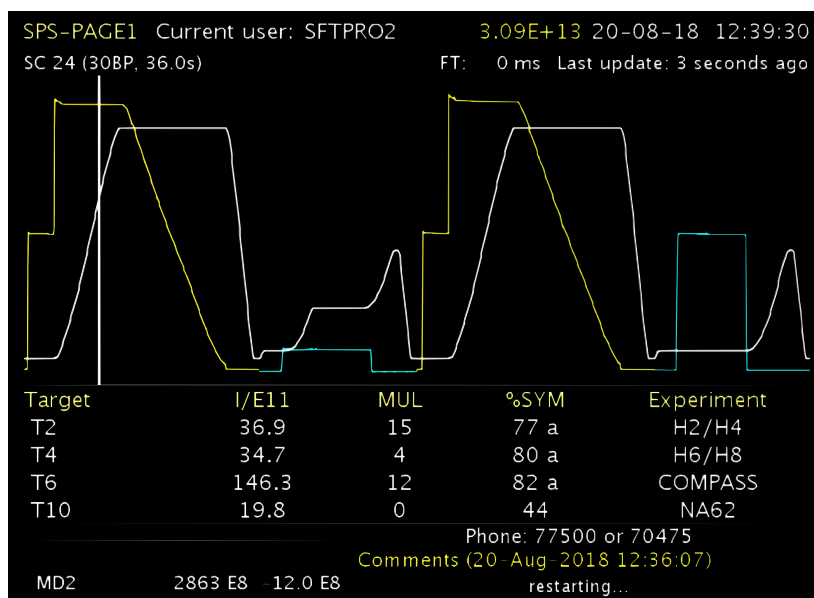


Figure 3.5: The SPS PAGE 1 monitoring.

column) — the ratio between the numbers of charged particles detected upstream of the target and by a detector downstream of the target; and symmetry (%SYM) — vertical and horizontal beam steering.

COMPASS uses the beam from the M2 line after the T6 target. Various thicknesses of the T6 target can be chosen to match the required intensity of the secondary beam. The maximum and typical length is 500 mm. This secondary beam is then selected by an array of quadrupoles and dipoles set to a chosen momentum range (Fig. 3.7). Interaction of the proton beam in this target produces a hadron secondary beam, made of π^\pm , K^\pm , p and \bar{p} . The fractions of these particles depend on charge of incoming particles and on the beam momentum. For example, in case of

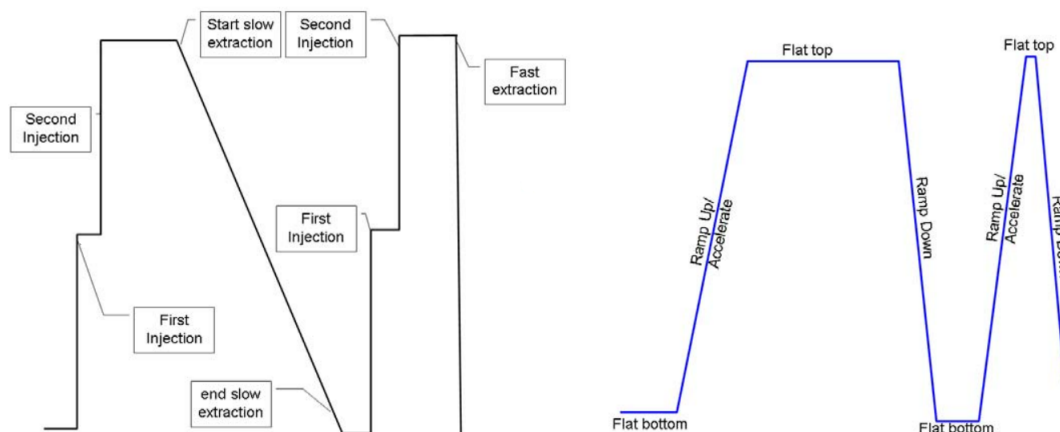


Figure 3.6: The SPS spill structure.

negative hadrons in the secondary beam at 190 GeV/c the fractions are about 0.95:0.045:0.05 for π^- , K^- and \bar{p} respectively. The secondary hadrons are sent to the experimental hall via 1 km long beamline. The momentum and angular distributions of the beam can be tuned by magnets and collimators. This sort of beam is used for the COMPASS hadron and DY runs.

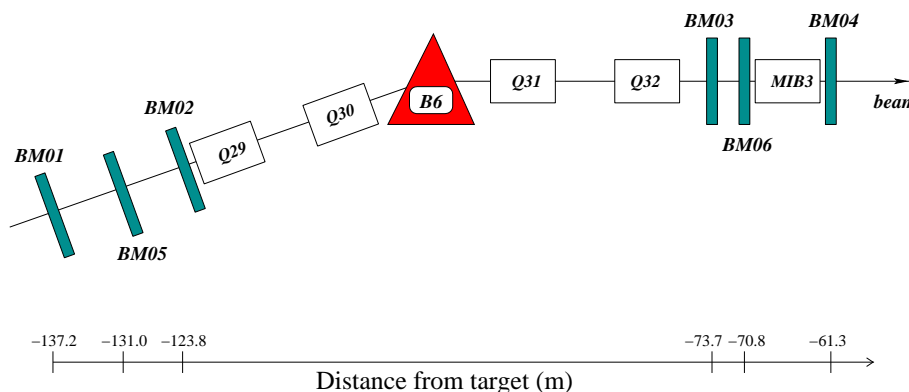


Figure 3.7: Beamline part.

As far as the COMPASS runs with muon beam are concerned (SIDIS or DVCS data taking), the tertiary muon beam results from second beam due to weak decays of π^+ and K^+ into $\mu^+\nu_\mu$. Since there is left-handed neutrino in the final state, muons are naturally longitudinally polarised. The remaining hadrons are removed by 9 thick absorbers, which are placed in the beamline. In case of the hadron beam mode the absorbers are not used and the products of the hadron decay as muons do not reach the main target of the experiment due to their lower momentum.

The hadron or muon beam turns up from the M2 beamline tunnel to the surface. Then the

beam is bent to the horizontal orientation by a set of three dipole magnets, B6 in Fig. 3.7. At this stage it is important to measure the beam momentum. This is done by magnets surrounded by six scintillator hodoscopes, together they are called the Beam Momentum Station (BMS). The BMS can measure the momentum of the beam muons with precision better than 1%.

In case of the hadron beam the Cherenkov-type detectors are used to monitor the beam contamination. They are called CEDAR stations and located 30 m upstream of the COMPASS target. CEDAR detectors are high pressure gas-Cherenkov counters making use of specially designed optics to select desired particle momenta for tagging. Two particles with the same momentum but with different masses radiate Cherenkov photons at different angles, resulting in rings with different radii. The rings of the required particle type are selected with a ring shaped diaphragm located in the focal plane perpendicular to the beam direction (Fig. 3.8). The CEDAR detectors, designed in the late 1970s to provide fast beam particle identification at high rates for particle momenta up to 300 GeV/c, have shown large inefficiency at the Drell-Yan beam intensity ($\sim 10^8$ particles/s) making the kaon and antiproton tagging very difficult. They were object of a major upgrade after the 2015 DY run but their commissioning was completed just at the end of the 2018 DY run.

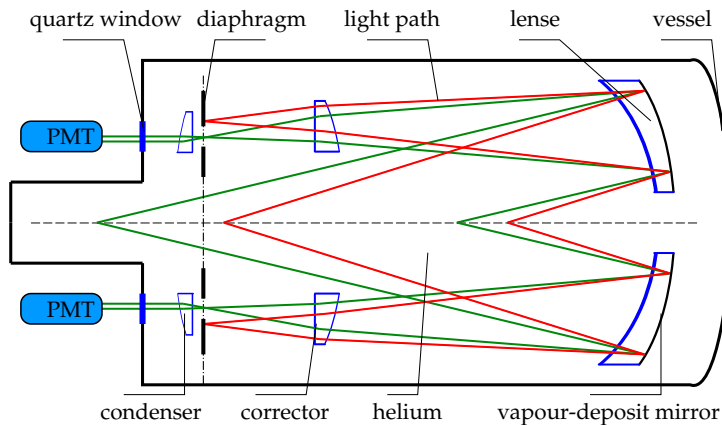


Figure 3.8: The principle of operation of CEDAR [68].

3.2 Polarized target

In the polarized DY measurements a significant role is played by the target with high-performance of nucleon polarization. COMPASS uses a target with ammonia (NH_3) where only

the hydrogen protons are polarizable. The target consists of two cells, one after another along the beam, with NH_3 . Each cell is 55 cm long and has a diameter of 4 cm. The distance between the cells is 20 cm. A scheme of the COMPASS polarized target is shown in Fig. 3.9.

The polarization of protons into those cells is performed by Dynamic Nucleon Polarization (DNP) method [191]. The method is based on the electron polarization transfer by microwave radiation (about 70.2-70.3 GHz) in a strong homogeneous magnetic field of 2.5 T directed along the beam. The magnetic field is produced by a superconducting solenoid magnet, about 1.4 m long, which is cooled by the ^3He - ^4He refrigerator system to temperature around 200 mK.

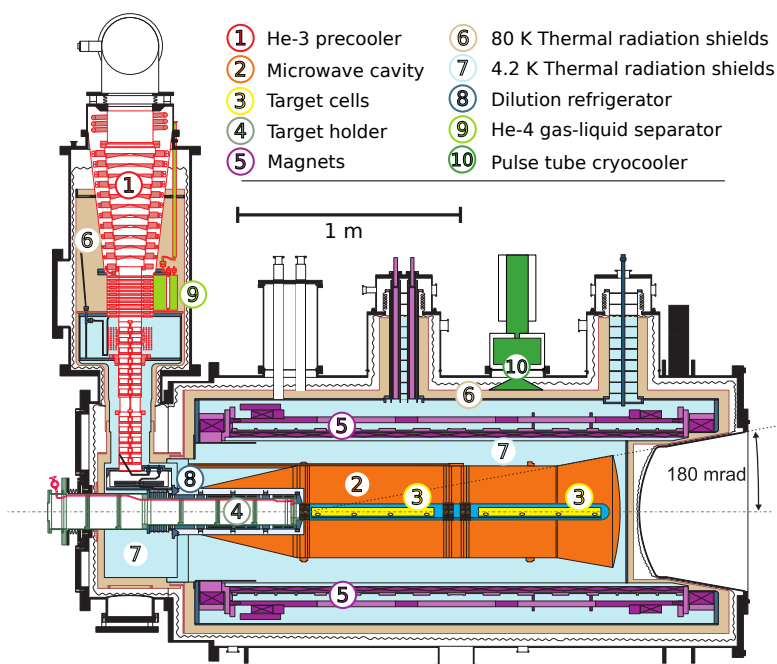


Figure 3.9: The COMPASS polarized target.

The presence of the high and homogeneous magnetic field would interfere to transverse polarization mode. Once the longitudinal polarisation is built up, a dipolefield 0.63 T strong is applied in order to pass to the transverse spin mode. The target material is cooled down to 90 mK. At this temperature the so-called “frozen spin” regime is maintained by a 0.42 T transverse dipole field. To reduce possible false asymmetries effects the cells are opposite polarized. The polarization of the cells is reversed by exchanging the microwave frequencies each time after 5 to 7 days of data taking. The polarisation is measured in the longitudinal 2.5 T field at the end of each transverse data taking period of about six days, using 10 NMR (Nuclear Magnetic Resonance) coils placed directly in the target cells; its value is saved in a database run by run.

Only a fraction of the target material is polarized, thus the dilution factor f is introduced, which is about 3:17 for NH_3 . However, the contamination of the material and radiative corrections to the dilution factor have to be taken into account. The dilution factor f is calculated for each event with the following formula

$$f = \frac{\sigma_p^{1\gamma}}{\sigma_p^{tot}} \frac{n_p \sigma_p^{tot}}{\sum_A n_A \sigma_A^{tot}} = \frac{n_p \sigma_p^{1\gamma}}{\sum_A n_A \sigma_A^{tot}}, \quad (3.1)$$

where

n_p — the number of polarizable protons,

n_A — the number of nucleons in a nucleus with mass A ,

σ_p^{tot} — the spin independent cross section per proton,

σ_A^{tot} — the spin independent cross section per nucleon,

$\sigma_p^{1\gamma}$ — the one photon exchange Born cross section, which is related to the total cross section as

$$\sigma_p^{tot} = \lambda \sigma_p^{1\gamma} + \sigma_{tail}^{inelastic} + \sigma_{tail}^{quasi\ elastic} + \sigma_{tail}^{elastic}, \quad (3.2)$$

where λ takes into account the higher order contributions. The inelastic tail $\sigma_{tail}^{inelastic}$ responds for the real photon radiation before or after the virtual photon emission. The quasielastic tail $\sigma_{tail}^{quasielastic}$ takes into account the interaction with proton and not with its content. The elastic tail $\sigma_{tail}^{elastic}$ accounts for the nucleus self-interaction.

3.3 Hadron absorber

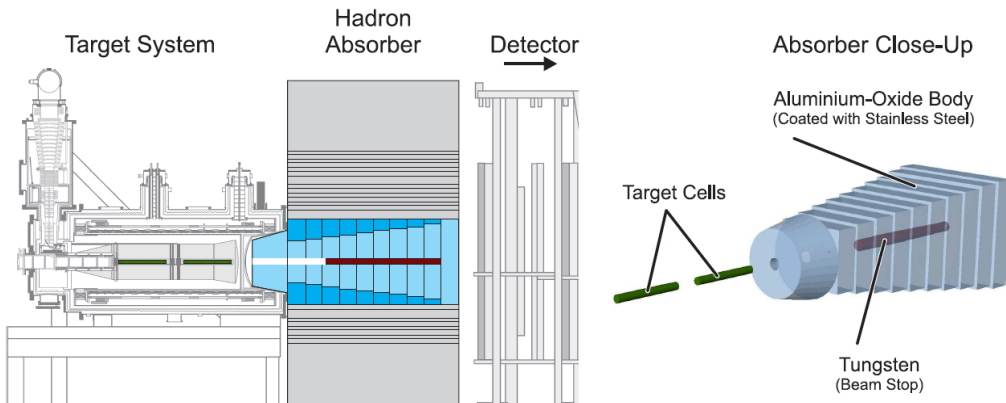


Figure 3.10: The COMPASS hadron absorber. Side view left. 3D view right.

Due to the low cross-section of the DY process, a high intensity beam (about 10^8 particles s^{-1}) has to be used. To stop the massive flux of secondary hadrons originated in the target and the non-interacting π^- beam an hadron absorber is used, in order to considerably reduce the detectors occupancy in the spectrometer [68]. It is placed right downstream the target and consists of three parts: a stainless steel block as outside layer, an aluminum oxide (Al_3O_3) block as main part, and tungsten beam plug (Fig. 3.10). The absorber is shielded with concrete to protect the target electronics and decrease the radiation level in the hall.

Herewith, the DY produced dimuon pairs easily penetrate through the absorber, but their multiply scatter inside it reduces the resolution of the spectrometer and degrades accuracy of the vertex reconstruction. The errors in the vertex reconstruction lead to the events migration from one target cell to another that badly influences the precision of asymmetries extraction. As a solution to this problem in [190] it was suggested to use an additional scintillating fiber detector as vertex detector, which was installed and tested before the COMPASS DY runs, but was found to have a very high number of correlated hits. For this reason, despite the efforts made in the data reconstruction, the expected improvement in the vertex resolution was not achieved.

3.4 Scintillating fibers

Ones of the tracking detectors are Scintillating fibers (SciFi) [192]. The SciFi detectors belong to the so-called Very Small Area Trackers (VSATs). The VSATs cover the area along the beamline up to a radial distance of 2.5-3 cm. In this region the particle rate is high and therefore a very good spatial and time resolution of the tracking detectors is required. The SciFi and Silicon detectors have appropriate resolutions but the latest were not used for the 2015 and 2018 DY runs with high intensity hadron beam due to their weak radiation tolerance. Fibers of the SciFi detectors are made of plastic from Japanese company Kuraray. The fiber arrays are connected by clear fiber light guides with position-sensitive photomultiplier tubes Hamamatsu H6568 (Fig. 3.11).

The characteristic time and space resolutions of the SciFi detectors are about 0.5 ns and 50 μm , respectively. Their pitch is between 0.41 and 0.70 mm.

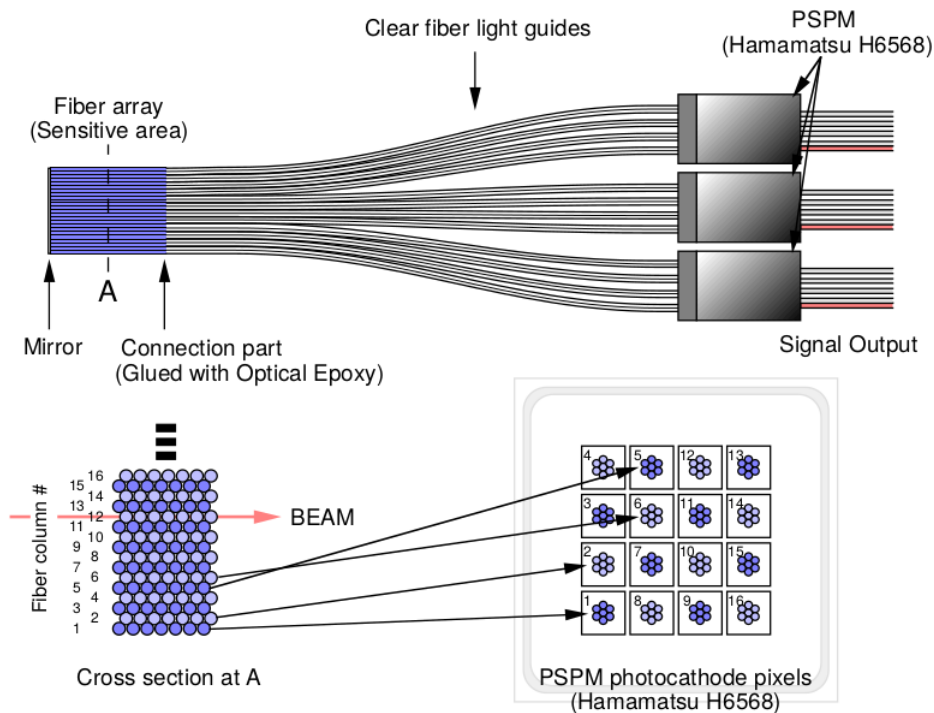


Figure 3.11: The principle of operation of the scintillating fibers.

3.5 Pixel Micromegas

Micromesh Gaseous Structure (Micromegas) detectors are used in COMPASS [193] for tracking measurements at small angle (radial distance of 2.5 cm to 30 - 40 cm from the beam line) and therefore they belong to the Small Angle Trackers (SAT). In total the COMPASS setup includes 3 stations of the pixel Micromegas detectors.

The Micromegas detectors are gaseous detectors with two regions: a conversion region and an amplification region (Fig. 3.12). The used gas mixture consists of Ne/C₂H₆/CF₄ taken in the proportion of 85:10:5.

The Micromegas detectors have been used in the COMPASS since the beginning of the experiments in 2002. In 2015 all the MicroMegas were upgraded to have a pixelized read-out in the central area [194].

The pixel parts are rectangular and parallel to the strips, with a size of 2.5x0.4 mm² in the center and 6.25x0.4 mm² at larger angles (Fig. 3.13). The remaining of the 40x40 cm² active area is covered by 20 cm long strips with 400 μm pitch in the center, and 40 cm long strips with 480 μm pitch on the edges. The active areas are combined into a triplet. The Micromegas

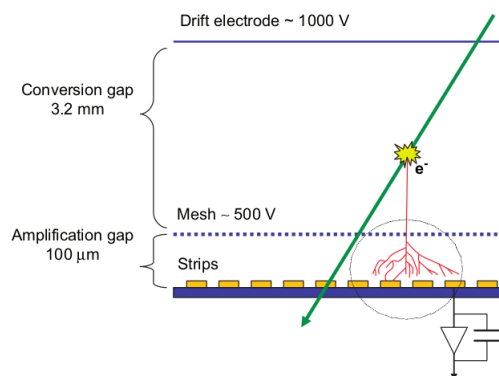


Figure 3.12: A principle of operation of the COMPASS Micromegas detector.

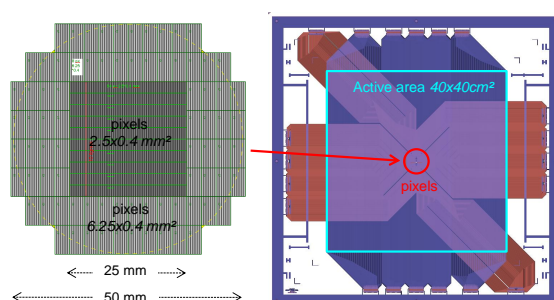


Figure 3.13: Sketch of pixelized Micromegas detector (right). Zoom of the pixel area (left).

have four triplets for each station, which form four coordinate planes: horizontal X, vertical Y, and planes U and V where the strips are tilted at $+45$ and -45 degrees respectively.

3.6 GEM

The next ones of the SAT detectors are Gas Electron Multipliers (GEMs). The GEMs are filled with gas mixture of argon and carbon dioxide (70:30) and divided into four gap regions by three thin foils ($50 \mu\text{m}$) made of polyamide with copper coating. Each foil has a large number of drifting holes (around 10^4 cm^2) with a diameter about of $70 \mu\text{m}$. The foils have a potential difference of several hundreds of volts and, consequently, the charged particles passing the gas induce a drift of electrons. The electrons are multiplied in holes of the foils that produce electron avalanches, which are detected on the readout strips (Fig. 3.14).

In order to minimise the material from detectors directly exposed to the hadron beam, some of the scintillating fibre detectors that were used with the muon beam were replaced by thinner detectors based on GEM foils [68]. Starting with the first hadron run in 2008, five

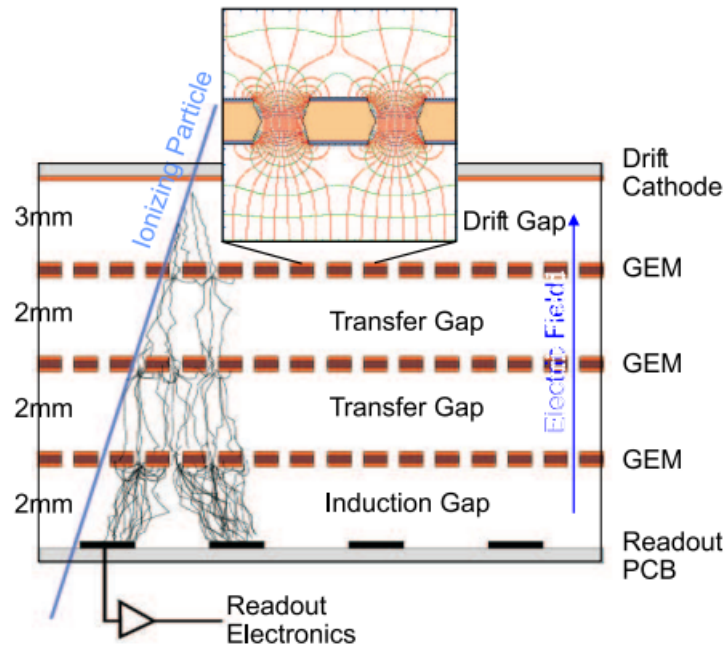


Figure 3.14: The COMPASS GEM detector.

PixelGEM detectors with a novel kind of readout and a thickness in the beam region of 0.26% of a radiation length and 0.1% of a nuclear interaction length each were installed, thereby reducing the material budget of the whole system by a factor of 5-10 compared to the scintillating fibre detectors.

The COMPASS setup includes 11 GEM stations, which are located in SAS and LAS areas of the spectrometer [195].

3.7 RICH Wall

Right downstream of RICH the so-called RICH Wall detector is located at the distance of about one meter from the target. It is a kind of drift-tube-detectors and the main purpose of its usage is improving the particle track reconstruction at large angles.

The detector's shape is a rectangle with sides $5.27 \times 3.91 \text{ m}^2$ having a rectangular $1.02 \times 0.51 \text{ m}^2$ dead zone in the center (Fig. 3.15). The angle acceptance of the RICH Wall is ranged from 150 to 300 mrad. The RICH Wall consists of eight planes of mini-drift-tubes — MDT modules, which are basic elements of the Rich Wall and the Muon Wall as well (Fig. 3.16). The planes are grouped in 4 sections and each section contains two planes with the same orientation of

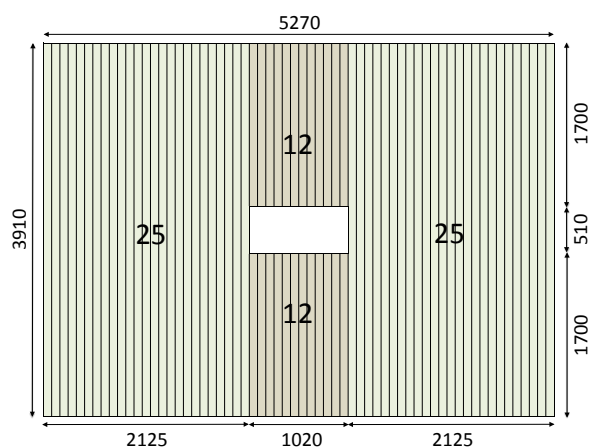


Figure 3.15: The COMPASS Rich Wall detector.

the tubes to resolve left-right ambiguity. The wire pitch is 10 mm and the space resolution is 400-500 μm . Readout electronics are capable to measure the drift time with resolution of 160 ps.

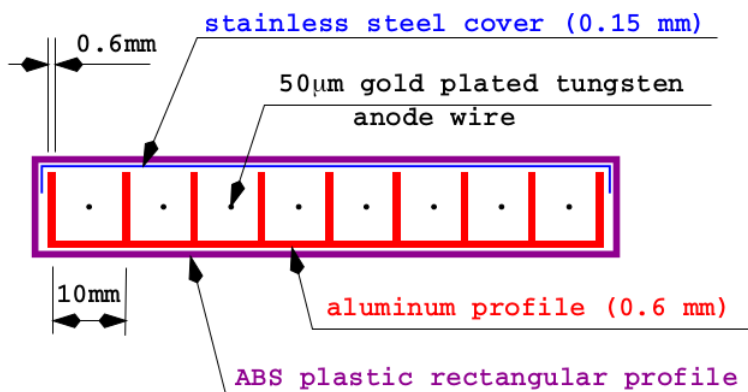


Figure 3.16: Module of the COMPASS Rich and Muon walls.

3.8 MWPC

Multi-wire proportional chambers (MWPCs) play a main role in Large Angle Tracking. Their peculiarity is multiple layers of wires mounted in a single volume filled with a gas mixture Ar/CO₂/CF₄ in the approximate ratio 74:6:20. A principle of operation of the detector is shown in Fig. 3.17.

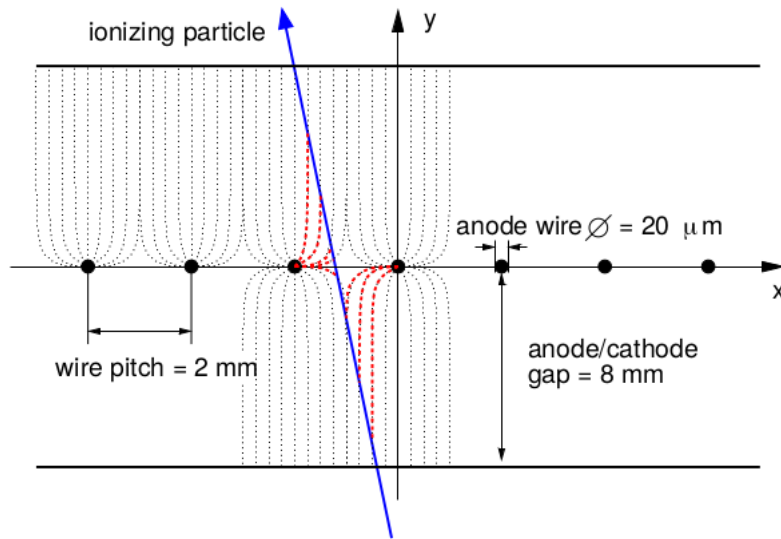


Figure 3.17: Principle of operation of the COMPASS MWPC detector.

There are 14 stations of MWPCs in COMPASS. They are grouped into three types of chambers: A-star (A*), A and B stations. The difference between them are the size of active area and the directions of the wires (projections). The A* and A stations have an active area of $178 \times 120 \text{ cm}^2$. The A* MWPCs have four projections: vertical and horizontal wires (X and Y projections), ± 10 degree rotated wires (U and V projections). The A and B stations have only three projections: X, U, and V. The B stations differ from A/A* ones by the size of active areas, which are $178 \times 120 \text{ cm}^2$ for the A/A* chambers and $178 \times 90 \text{ cm}^2$ for the B ones. The total number of planes for the tracking reconstruction is 34. Each plane has a round dead zone in the center with diameters of 16, 20 and 22 cm. The wire length is about 1 m and diameter is $20 \mu\text{m}$. The characteristic pitch of wires is 2 mm. The space resolution of these detectors is about 1.6 mm.

3.9 Drift Chambers

Around the SM1 magnet four Drift Chambers (DCs) are placed for the Large Angle Tracking. Two stations in front of the SM1 (together with the small angle trackers SciFis and MicroMegas) and two ones behind the magnet with one GEM station between them. Each station has 4 pairs of layers with two projection planes with a gas gap of 8 mm. The gas presents a mixture of Ar, $\text{C}_2 \text{H}_6$ and CF_4 with fractions of 45%, 45% and 10% respectively. The chamber

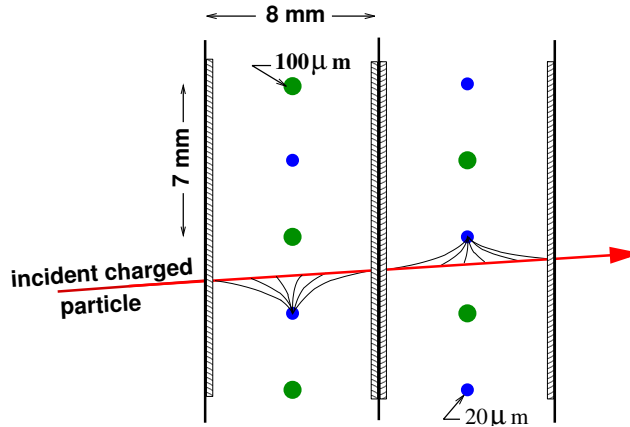


Figure 3.18: Principle of operation of the COMPASS Drift Chamber.

is enclosed by two Mylar foil of $25\ \mu\text{m}$ thickness as a cathode. Each two adjacent planes are shifted by $3.5\ \text{mm}$ and measure the same coordinate that allows to resolve left-right ambiguity (Fig. 3.18). The DCs have a central deactivated area with $30\ \text{cm}$ in diameter to avoid high occupancy rate near the beam direction. This region can be activated in low intensity beam mode *e.g.* during the alignment runs. The separate activation of the central parts is possible due to independent HV power supplies segmented in all cathode foils.

The first two DC stations upstream of SM1 have an active area of $180 \times 127\ \text{cm}^2$. The plane consists of 176 sensitive wires ($\varnothing\ 20\ \mu\text{m}$) and 177 potential wires ($\varnothing\ 100\ \mu\text{m}$). Their space resolution is about $190\ \mu\text{m}$

After SM1 the next two DC stations are positioned. Their purpose is to provide a good reconstruction of bent particles in the magnetic fringe. Therefore they have a larger active area size of $248 \times 208\ \text{cm}^2$ with 256 active wires made of gold plated with a tungsten and 257 ones made of beryllium. The space resolution of these larger DC stations is about $500\ \mu\text{m}$.

3.10 Straw

During the COMPASS Drell-Yan runs in 2015 and in 2018 one station of Straw detectors was used (the third station, ST03). The station was installed between the second and the third GEM stations downstream of the last Drift Chamber (DC5).

The Straw detector presents a wall with a large number of tubes layered one after another with a shift of half of the diameter and containing in their center tightened sensitive anode wires

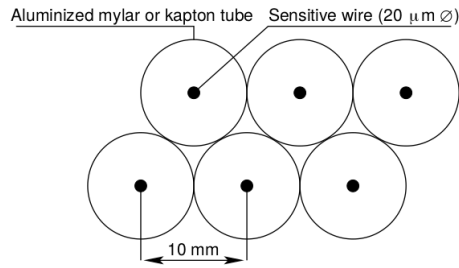


Figure 3.19: Scheme of the cross section of Straw tubes.

with 30 μm of diameter made of tungsten and plated with gold (Fig. 3.19). The tubes are filled with fast counting gas mixture of $\text{Ar}/\text{CO}_2/\text{CF}_4$ taken in the ratio of 74:6:20 as for the MWPC chambers. The tubes are made of two glued layers of the plastic films. The inner layer is 40 μm thickness graphite-coated kapton foil and the second layer is an aluminium-cladded foil of 12 μm thickness, which serves as a cathode. In COMPASS the Straw station has two planes per

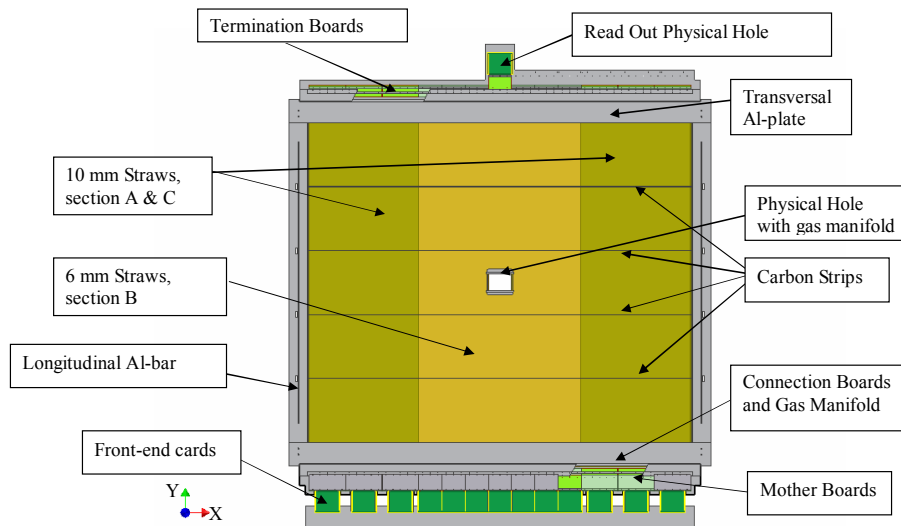


Figure 3.20: Sketch of the COMPASS Straw detector.

projection: one vertical plane with an active surface of $350 \times 243 \text{ cm}^2$ and one plane inclined at angle of 10 degrees with an active area of $323 \times 272 \text{ cm}^2$. Each plane is divided in three parts: the two outer parts with diameter of tubes of 9.6 mm, and one inner part (so-called B-part) containing the tubes with smaller diameter of 6.1 mm (Fig. 3.20). In the inner part there is a dead zone with approximate size of $20 \times 20 \text{ cm}^2$. The spatial resolution of the COMPASS Straw is around 400 μm .

3.11 Large area drift chambers (W45)

One more detectors among kinds of drift chambers in COMPASS are Large Area Drift Chambers, which are often called W45 (or sometimes DW) detector. This is a set of six drift chambers with large active area $5 \times 2.5 \text{ m}^2$ that makes them useful for the reconstruction in the large angle acceptance region.

Each station has two pairs of planes, one plane per projection. Two wire layers are used for one plane. As a usual drift-chamber-like detector, the W45 has sensitive anode wires, their diameter is $20 \text{ }\mu\text{m}$ and pitch is about 2 mm . Anode wires are separated with cathode wires with a diameter of $100 \text{ }\mu\text{m}$ and pitch of 4 mm . To improve the electric field homogeneity the cathode wires are inclined by 5 degrees with respect to vertical direction. The wire layers with the same orientation inside one chamber are shifted by half of their pitch. Since this sort of detectors cannot be stable at the high particle rate, the chambers have a circular inactive dead zone of 50 cm of diameter. These inactive areas are covered by neighboring stations of MWPCs.

All W45 chambers have two reconstruction planes. There are four types of planes in the W45, depending on their tilt in the global system coordinate of the spectrometer. They are X-plane, Y-plane, which coincide with global X and Y directions. The other two types are V and U planes, which are inclined by $+30$ and -30 degrees with respect to the X-plane respectively. The COMPASS W45 chamber stations are grouped by various combinations of the plane structure: XY, XV, XU, YV, and XU.

The chambers are filled with Ar/CF₄/CO₂ gas mixture taken in fraction 85%, 10%, and 5%. This fraction with voltage of 1925 V for anode and -800 V for cathode wires allows to obtain a maximum of the drift velocity and, consequently, to increase the efficiency of the track reconstruction.

3.12 Muon walls

The COMPASS setup in both LAS and SAS parts has a system for muon identification. As muons are weakly captured by material, the muon identification systems are located at the end of each spectrometer stage, right downstream the hadron calorimeters. The basic idea is to get rid of all charged particles apart from muons with the absorber and to measure their momenta by means of the medium resolution tracking detector stations.

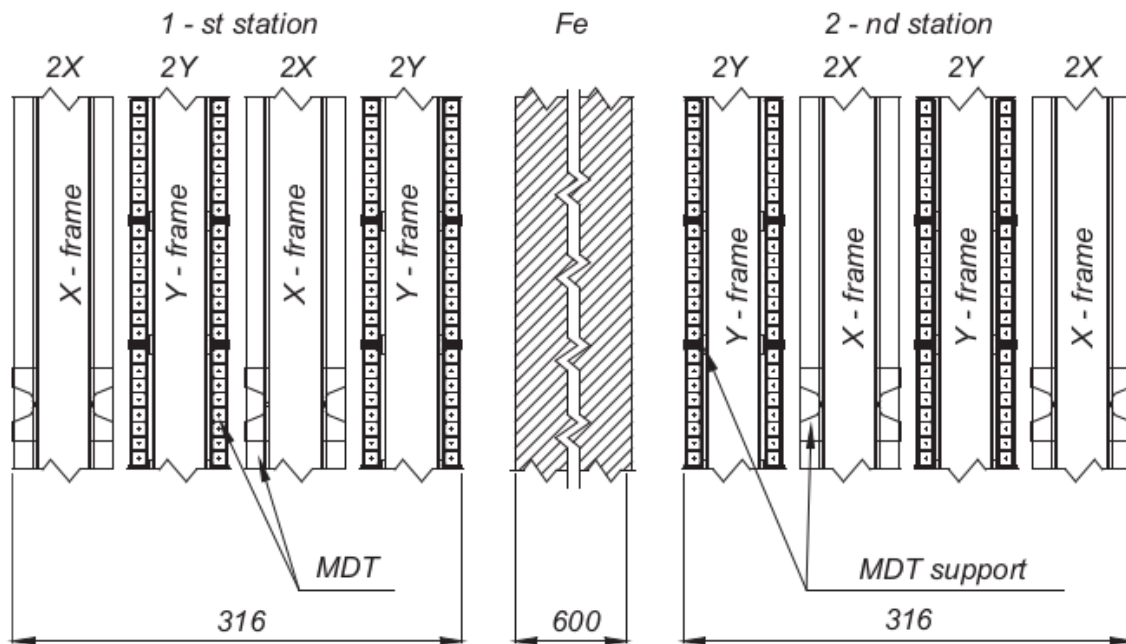


Figure 3.21: A sketch of cross-sectional side view of MW1.

The first muon system consists of two stations (MW1) with iron absorber (Muon Filter 1) between them (Fig. 3.21) with thickness of 60 cm. Each station has eight tracking planes with sensitive area of $480 \times 410 \text{ cm}^2$. The tracking planes are distinguished by inclination. In the MW1 stations there are vertical, horizontal and rotated by ± 10 degrees coordinate planes. The basic element of the MW1 is the MDT module as used for the Rich Wall (Fig. 3.16). The stations with the filter have a rectangular hole of central hole of $140 \times 80 \text{ cm}^2$ in the center as a dead zone, which is needed for beam passage. The gas used in the MW1 chambers is a mixture of Ar/CO₂ (70:30) that provides drift time below than 150 ns. The pitch of the wires is around 10 mm.

The second muon system is located downstream of the second hadron calorimeter in the SAS stage and consists of the concrete wall, 2.4 m long, as an absorber (Muon Filter 2) and two detector stations (MW2) behind the absorber among the MWPC stations from its B-type group. The active surfaces of the MW2 chambers are smaller than MW1 ones and have a size of $447 \times 202 \text{ cm}^2$. Both stations and filter have a central dead zone as a rectangular hole with size of $100 \times 80 \text{ cm}^2$, which is covered by the MWPC-B stations. The internal structure of the MW2 chambers presents stainless steel tubes with a diameter of 29 mm and a wall thickness of 0.5 mm filled by a gas mixture of Ar/CH₄ taken in fraction of 75:25. There are six layers

in each MW2 station, which are joined in double layers installed on a separate steel support. Three double layers provide three coordinate tracking planes: vertical X, horizontal Y, and one inclined at 15 degrees (w.r.t. the vertical) V plane. The space resolution is about 1.4 mm.

3.13 Hadronic calorimeters

Between the electromagnetic calorimeters and muon systems the hadronic calorimeters are placed. Also, as ECALs, the first one (HCAL1) is located in the LAS part and the second one (HCAL2) in the SAS path of the spectrometer [196]. They have lower spatial granularity.

The HCAL1 contains 480 modules and the HCAL2 consists of 220 modules. The HCAL1 module is a block with transverse size of $142 \times 146 \text{ mm}^2$ containing 40 alternating iron layers (20 mm thick) with scintillating plates (5 mm thick), Fig. 3.22. The HCAL2 has two types of

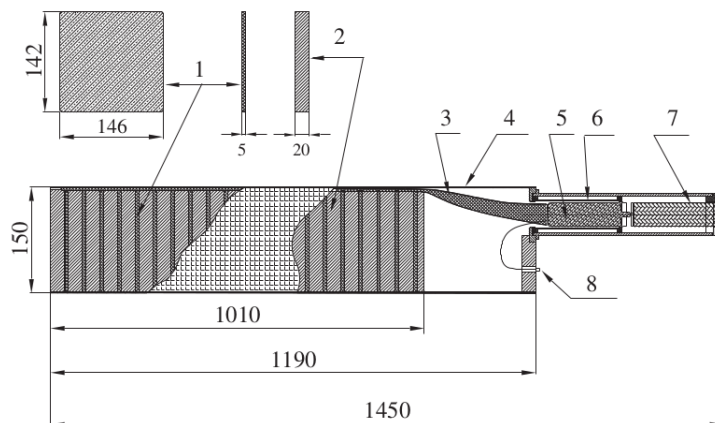


Figure 3.22: Structure of the HCAL1 module: 1, scintillators; 2, iron plates; 3, light guide; 4, container; 5, PMT; 6, PMT magnetic shielding; 7, Cockcroft–Walton divider; 8, optical connector for LED control. Dimensions are in mm.

modules. The central 8×6 cells of the detector are made of the first type of modules, which consist of 25 mm thick steel layers alternated with 5 mm thick scintillator plates. The rest of the calorimeter contains 36 modules of the second type, which are different from the first type by the larger transverse size.

Hadrons passing the iron (HCAL1) or steel (HCAL2) layers produce a shower of secondary particles, which illuminate in the scintillating with the intensity proportional to the deposited energy. They fully absorb hadrons with energies from 10 to 100 GeV and their efficiency is close

to 100%.

3.14 Trigger system

During data taking the detectors produce a lot of signals. It is almost impossible and actually not needed to save them all on a disk or tape. For a certain physics programme we are interested in specific events for which there is a sense to record them for a further reconstruction and analysis. Therefore some kind of online event selection has to be provided. To resolve this problem a trigger system is used, which is a set of very fast signal detectors and electronics with short dead time. The decision to store an event is provided by getting some coincidence information of certain types of the candidates from the trigger detectors.

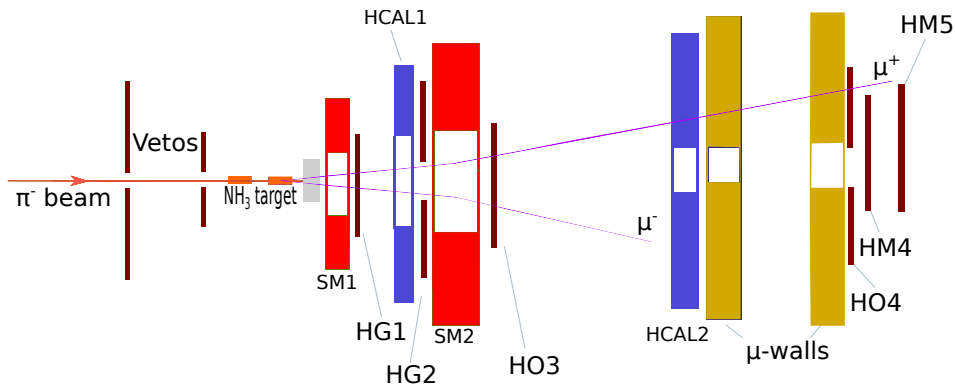


Figure 3.23: Schematic view (not in scale) of the location of the components relevant to the trigger system.

For the DY data taking in COMPASS the trigger system checks if the muon is produced in the target region. This check uses two facts:

- the spectrometer magnets bend trajectories of the charged particles only in horizontal direction, thus the candidates of muons more probably pass at some polar angle in the vertical direction; it is so-called **target pointing method**;
- the candidate muons have smaller momentum with comparison to the beam or halo particles that leads to their bigger deflection in a magnetic field, so the needed muons give a signal at some angle also in the horizontal direction; it is an **energy loss method**;

The COMPASS DY trigger system is based on scintillating hodoscopes and hadron calorimeters (Fig. 3.23). The hadron calorimeters are already briefly described in subsections 3.13. The

hodoscopes consist of scintillating slabs connected to photomultipliers, which have a time resolution of around 1 ns. The so-called Veto hodoscopes are positioned upstream of the target. Their function is to ignore a record of the events with halo tracks (Fig. 3.24).

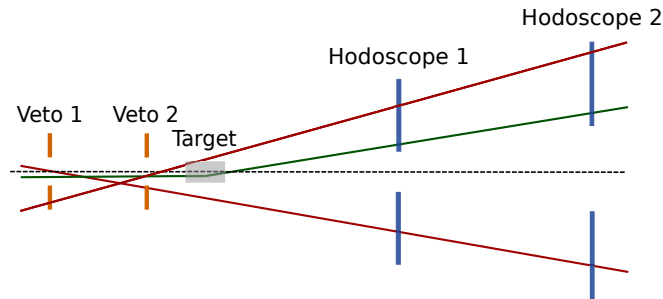


Figure 3.24: Principle of operation of the veto trigger. Muons passing the veto detector are removed (red) while other muons (which are probably produced in the target) are taken into account (green).

For the Drell-Yan measurements the physics trigger is a 2μ -trigger, for which the selection of candidates for dimuon tracks is implied. Physics trigger includes three hodoscope stations denoted as HO, HM and HG that correspond to the following trigger name conventions: Outer trigger (OT), Middle trigger and LAS area trigger (LAST) respectively.

Other auxiliary triggers used for the Drell-Yan data taking purpose can be found in Tab. 3.2.

3.15 Data acquisition system

The events selected by the trigger system by the trigger system are processed by the data acquisition system (DAQ), which collects and transmits data to the storage. Since 2015 the upgraded DAQ has been used in COMPASS [197]. One of the main difference between old and new DAQ is a replacement of layer of computers (which organized an event building network) with FPGA multiplexers and switch blocks – Data Handling Cards (DHC).

The pipeline of the COMPASS DAQ consists of the following steps (see also Fig. 3.25):

- Signals from the detectors come to the front-end electronics, which are readout cards usually surrounded by the detector and affixed to the support frames. Their main function is to convert the analog signals to the digital ones. The total amount of the channels in the COMPASS front-end cards is about 300 000.
- Digitized signals are transmitted by ≈ 1000 links to the trigger control system and the

Trigger Bit	Short-Name	Trigger	Method	Elements
0	MT+LAST	Dimuon Trigger	energy loss, target pointing	HM04Y1 (d/u), HM05Y1 (d/u); HG01Y1, HG02Y1, HG02Y2
1	MT	One muon Middle Trigger	energy loss, target pointing	HM04Y1 (d/u), HM05Y1 (d/u)
2	OT+LAST	Dimuon Trigger		
3	OT	One muon Outer Trigger	target pointing	HO03Y1, HO04Y1, HO04Y2
4	CT	Calorimeter Trigger		
5	VI	Inner Veto		
6	Halo	Halo Trigger (Veto Outer & HO4)		
7	BT	Beam Trigger		
8	LAST 2μ	Dimuon Trigger LAS	target pointing	HG01Y1, HG02Y1, HG02Y2
9	LAST 1μ	One muon Trigger LAS	target pointing	
10	TRand	True Random		
11	NRand	Noise Random		

Table 3.2: List of triggers used during DY runs.

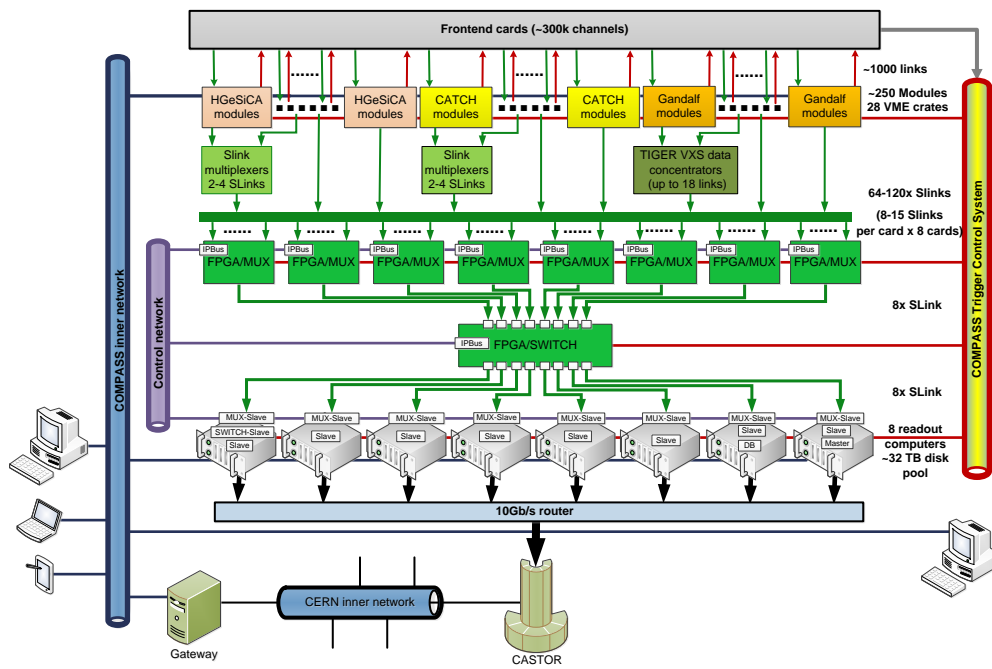


Figure 3.25: The COMPASS FPGA-based DAQ architecture.

concentrator modules: GeSiCA, CATCH, and GANDALF (total number of the all modules is around 250). The modules collect signals transferred by links and also receive the signals from the trigger and time system. If there is a trigger signal with signals from the detectors at the same time window, a sub-event is generated.

- The next step is the event builder system consisting of the cards based on FPGA. It provides online data consistency checks with a programmable error recovery algorithm.
- Then the full events are transmitted to 8 readout engine computers with needed firmware and software (labeled as pccXXXXX machines, see Fig. 3.26). Some of them are located in DAQ barrack (in bldg. 888) while other are in the Control room (in bldg. 892). At this stage the events are stored on the local disks with a total pool size of about 60 TB.
- Finally, the data are transferred to the CERN Advanced STORage (CASTOR) and there they are stored on tapes for further reconstruction and analysis.

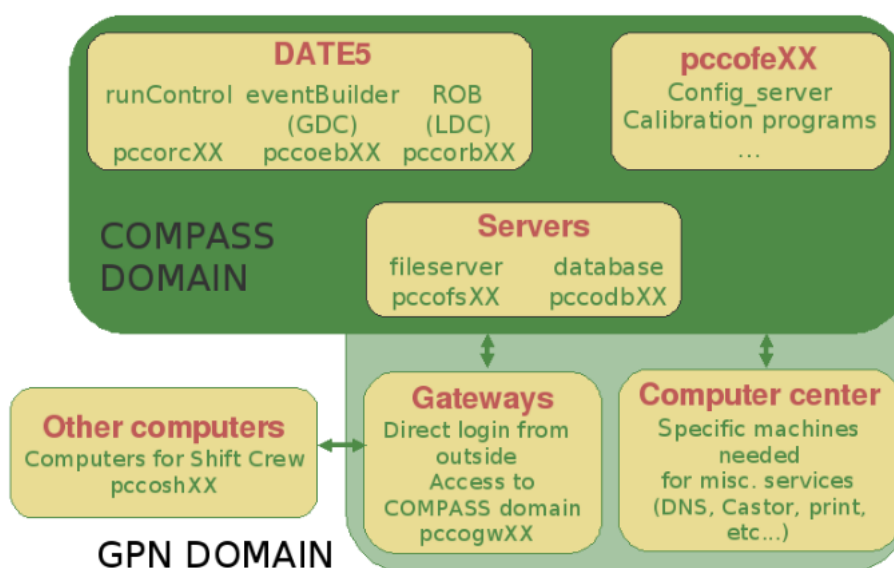


Figure 3.26: Scheme of the COMPASS network.

3.16 Future upgrade of the setup

In the future an upgrade of the experiment is planned. According to the plans new introducing changes will include:

- Further improvement of the PMT and front-end electronics for the CEDARs at high rates.
- New ten large-size PixelGEMs. They are foreseen to be built by 2022 as a replacement and spares for the present GEMs.
- New large-area micro-pattern gaseous detectors (MPGD) based on GEMs or Micromegas technology to replace aging MWPCs.
- New front-end electronics and trigger algorithms that are compatible with triggerless readout. It will be FPGA-based Time Digital Converters (TDCs) with a digital trigger that is capable of rates up to 100-200 kHz and time resolution down to 100 ps.

Note that only a general overview of the future upgrades is presented here. The details of the future upgrades and measurements can be found in [198].

Chapter 4

Data processing

Data collected by DAQ are stored on CASTOR (CERN advanced storage) as raw files. The data for each run are separated into chunk files with size of 1GB (*cdr{chunk_number}-{run_number}.raw*). A typical number of the chunk files for a full (200 spills) run is about 700. The raw files contain information about fired detectors channels digitized by the front-end electronics. These data have to be reconstructed for next analysis steps.

4.1 Reconstruction

Data reconstruction in COMPASS is performed by the CORAL (COmpass ReConstruction and ALignment) software package. It is an object-oriented package with a modular architecture written in C++, which takes raw files of either Real Data (RD) or Monte-Carlo (MC) data as one of its inputs in order to produce mDST files (mini Data Summary Trees).

Firstly, the CORAL does either decoding in case of RD or digitalization in case of MC data (Fig. 4.1). The decoding is performed by Daq Data Decoding Library (DDD) included in the CORAL package. Then the data are signed to clusters according to their associated detector positions in the setup. The clusters distinguish four zones of the spectrometer: the first one is between the target and the SM1, the next one is between SM1 and SM2, the third one is between SM2 and MF2, and the last one is downstream MF2. In these zones, parts of reconstructed tracks are expected to be approximately straight.

The track reconstruction is carried out by the TRAFFIC/TRAFDIC (Track Finding with Dictionary in COMPASS) library with three steps: pattern recognition, bridging and fit. At

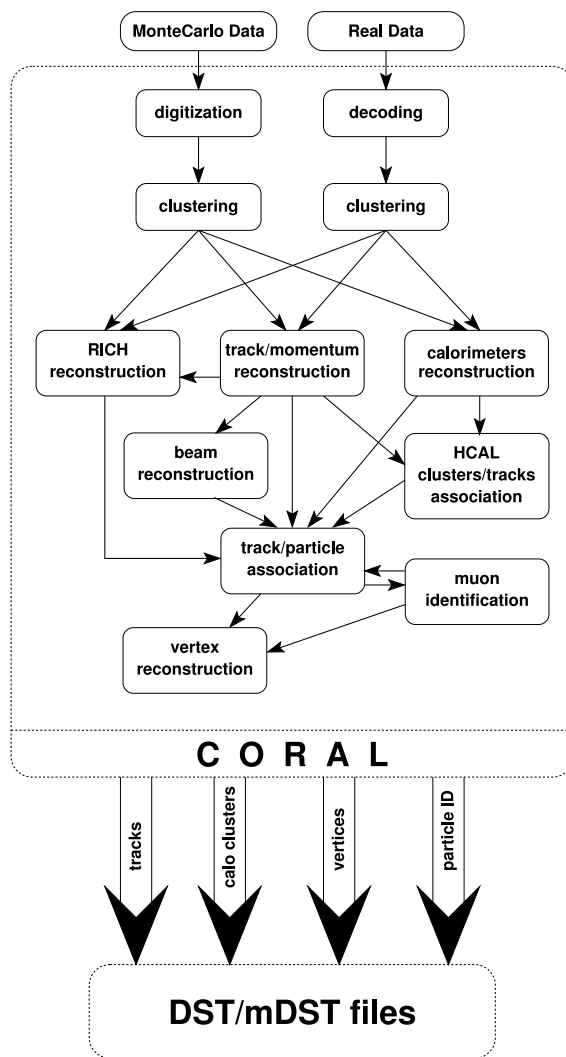


Figure 4.1: CORAL operations.

the first step, it searches for track segments in four separated zones described above. After that a bridging procedure tries to merge the obtained various segments to whole tracks. The last step is a fit, which evaluates track parameters for the found candidates. The fit procedure uses Kalman filter algorithm [199], [200].

At the end, CORAL performs a vertex reconstruction, which is based on two algorithms: Point Of Closest Approach (POCA) and inverse Kalman filter. In CORAL, there are two types of vertices: primary vertices and so-called V^0 vertices. The first ones contain a track associated with the beam. The second type is related to two-body decays of neutral particles. An event can have more than one beam track, therefore not only one primary vertex can be found. In such case the definition of the “best primary vertex” is introduced as the one with a maximum number of containing tracks and, if there are vertex candidates with the same number of tracks, the one with smaller vertex χ^2 is chosen.

Once CORAL is compiled, the reconstruction can be handled by option files (*trafdic.opt*), which contain a runtime configuration for the reconstruction procedures. Also one of the crucial inputs is the file with information about detectors and their positions, tilt angles of active areas, pitches etc. This file is called “*detectors.dat*”, in which, before the event reconstruction by CORAL, the detector position parameters have to be adjusted by dedicated subprograms in the CORAL package. For this purpose there is an alignment procedure in COMPASS, which includes: special alignment data taking runs with muon beam and lower intensity; specialized reconstruction; alignment process; and analysis. Some alignment study (constrained alignment) was done by the author of this Thesis, and this procedure will be described in the next section in details.

4.2 Alignment

4.2.1 Overview

Quality of the reconstruction strongly depends on accuracy of the description of the tracking detector positions in the “*detectors.dat*” file. Initially, the coordinates of the detector stations in the global reference frame are obtained by surveyors. The geodetic measurements are performed with a system of lasers and reflecting mirrors. The laser setup is firmly fixed on the ground, and a ray of laser is directed to the small mirrors, which are put in specially designed gaps on a

support frame in the detector station. The detection of the reflected ray allows us to calculate the coordinates of the gaps. Further the detector experts, knowing the sizes of the supported frame and detector areas, transform those values in the global coordinates. In such a way the nominal detector positions are input in the “*detectors.dat*” file. However, the accuracy of the

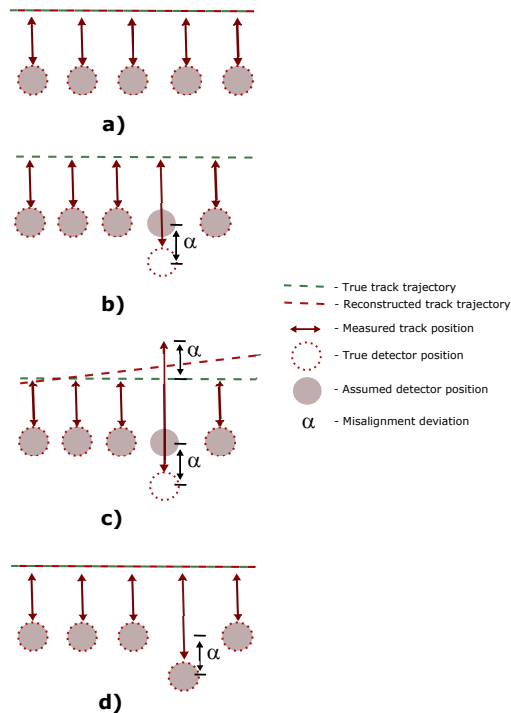


Figure 4.2: Misalignment impact on the track reconstruction: a) ideal case of absence of misalignment — the reconstructed track coincides to the real track; b) some position is shifted by α , which is larger than typical spatial resolution of the detector; c) the wrong reconstructed due to misalignment track is demonstrated; d) the reconstruction taking into account a misalignment correction.

survey measurements is about 0.5 mm, which is lower than detector spatial resolutions. The survey accuracy is not sufficient for the COMPASS physics program, which requires precision up to micron. Also, in addition to the geodetic uncertainties, there are lacks of the accuracy due to construction tolerances and assembly of detector elements w.r.t. their active volume, where particle interactions occur. The impact of the uncertainty of the detector position on the track reconstruction is shown in Fig. 4.2. In order to provide a reliable description with higher precision the so-called *track based alignment* is performed in COMPASS.

The idea of the track based alignment is to exploit information from a preliminary track reconstruction in order to obtain corrections to the geometrical detector description. This is mathematically achieved by consideration of a track model described with a matrix functional

$F_{ij}(u_{ij}, p_i, \alpha_j)$, which yields a difference between position of hits and coordinate expected from the track model, where p_i – track parameters in the model, α_i – alignment corrections, and where index i enumerates tracks, index j enumerates all planes of the tracking detectors involved in the alignment procedure; u_{ij} is a hit position of the track i detected by plane j . The corrections α are extracted from the condition of minimum for χ^2 -sum over all tracks n and detector planes m :

$$\chi^2 = \sum_{i=1}^n \sum_{j=1}^m \frac{[F_{ij}(u_{ij}, p_i, \alpha_j)]^2}{\sigma_j^2}, \quad (4.1)$$

where σ_j is a spatial resolution of the detector with plane j . The condition of the χ^2 -sum in (4.1) is determined by the vanishing of all partial derivatives over track and alignment parameters

$$\begin{aligned} \frac{\partial}{\partial p_i} \left(\sum_{r=1}^n \sum_{j=1}^m \frac{[F_{rj}(u_{rj}, p_r, \alpha_j)]^2}{\sigma_j^2} \right) &= 0, \\ \frac{\partial}{\partial \alpha_j} \left(\sum_{i=1}^n \sum_{s=1}^m \frac{[F_{is}(u_{is}, p_i, \alpha_s)]^2}{\sigma_j^2} \right) &= 0. \end{aligned} \quad (4.2)$$

As a rule, the functional F_{ij} is nonlinear, but with an assumption that its parameters are small, it can be expanded in Taylor series:

$$\begin{aligned} F_{ij} &= F_{ij}(u_{ij}, 0, 0) + \sum_r^n \frac{\partial F_{ij}(u_{ij}, p_i, \alpha_j)}{\partial \alpha_r} \Big|_{p_i=\alpha_j=0} \alpha_r \\ &+ \sum_s^m \frac{\partial F_{ij}(u_{ij}, p_i, \alpha_j)}{\partial p_s} \Big|_{p_i=\alpha_j=0} p_s + O(p_i, \alpha_j). \end{aligned} \quad (4.3)$$

For brevity denote

$$F_{ij}^0 \equiv F_{ij}(u_{ij}, 0, 0), \quad (4.4)$$

$$F_{ij,s}^0 \equiv \frac{\partial F_{ij}(u_{ij}, p_i, \alpha_j)}{\partial p_s} \Big|_{p_i=\alpha_j=0}, \quad (4.5)$$

$$F_{ij,r}^0 \equiv \frac{\partial F_{ij}(u_{ij}, p_i, \alpha_j)}{\partial \alpha_r} \Big|_{p_i=\alpha_j=0}. \quad (4.6)$$

Follow the Eq. (4.4) and remaining only the linear order one rewrites (4.3) in the form

$$F_{ij} = F_{ij}^0 + \sum_r^n F_{ij,r}^0 \alpha_r + \sum_s^m F_{ij,s}^0 p_s. \quad (4.7)$$

Substituting the leading order from (4.7) in (4.2) and calculating the derivatives by the chain

rule, one obtains

$$\sum_k^n \sum_j^m \frac{1}{\sigma_j^2} \left(F_{kj}^0 + \sum_r^n F_{kj,r}^0 \alpha_r + \sum_s^m F_{kj,s}^0 p_s \right) \quad (4.8)$$

$$\times \frac{\partial}{\partial p_i} \left(F_{kj}^0 + \sum_r^n F_{kj,r}^0 \alpha_r + \sum_s^m F_{kj,s}^0 p_s \right) = 0,$$

$$\sum_i^n \sum_l^m \frac{1}{\sigma_l^2} \left(F_{il}^0 + \sum_r^n F_{il,r}^0 \alpha_r + \sum_s^m F_{il,s}^0 p_s \right) \quad (4.9)$$

$$\times \frac{\partial}{\partial \alpha_j} \left(F_{il}^0 + \sum_r^n F_{il,r}^0 \alpha_r + \sum_s^m F_{il,s}^0 p_s \right) = 0.$$

Introducing the following compact notations for the sums emerged in (4.8)

$$C_i = \sum_{r=1}^n \sum_{s=1}^m \frac{1}{\sigma_s} F_{rs,i}^0 F_{rs,j}^0, \quad (4.10)$$

$$G_i = \sum_{r=1}^n \sum_{s=1}^m \frac{1}{\sigma_s} F_{rs,i}^0 F_{rs,j}^0, \quad (4.11)$$

$$\Gamma_i = \sum_{r=1}^n \sum_{s=1}^m \frac{1}{\sigma_s} F_{rs,i}^0 F_{rs,j}^0, \quad (4.12)$$

$$b_i = - \sum_{r=1}^n \sum_{s=1}^m \frac{1}{\sigma_s} F_{rs,i}^0 F_{rs}^0, \quad (4.13)$$

$$\beta_i = - \sum_{r=1}^n \sum_{s=1}^m \frac{1}{\sigma_s} F_{rs,j}^0 F_{rs}^0. \quad (4.14)$$

we can write down a system of equations on unknown vector of the track and alignment parameters $\{\alpha_j, p_i\}_{i=1..n, j=1..m}$ in the form

$$\begin{pmatrix} \sum_i C_i & \cdots & G_i & \cdots \\ \vdots & \ddots & 0 & 0 \\ \hline G_i^T & 0 & \Gamma_i & 0 \\ \vdots & 0 & 0 & \ddots \end{pmatrix} \begin{pmatrix} \alpha_a \\ \dots \\ p_i \\ \dots \end{pmatrix} = \begin{pmatrix} \sum_i b_i \\ \vdots \\ \beta_i \\ \vdots \end{pmatrix}. \quad (4.15)$$

The solution of the system of linear algebraic equations (4.15) gives corrections to the geometry values thus aligning the positions of the detectors w.r.t. each other.

4.2.2 Procedure

The alignment procedure takes its origin from dedicated alignment runs, which are runs with a muon beam (even for the hadron beam physics program) and lower intensity. Moreover,

these runs are separated into two: one without magnetic field and another with SM1 and SM2 magnets switched on. Subsequently, the dedicated runs allow to have simpler data (w.r.t. physics runs) in order to reconstruct muon tracks for alignment purposes only.

Alignment data with the magnets switched off are used for the first step — to get preliminary corrections to the geometry using the straight track model between the spectrometer zones (target–SM1, SM1–SM2, SM2–MF2 etc. described in the previous Chapter). As soon as the detector positions have been corrected with field off data, the obtained “*detectors.dat*” file is used as an initial geometry file for the next step — the alignment using data with a magnetic field. Finally, the alignment procedure on physics data is required to get reliable results for the further analysis on real data.

There are special subroutines for the alignment procedure in CORAL: a separate track reconstruction, adapted for the alignment data; a program performing the minimization (with MILLEPEDE [201]) for finding the corrections to the geometry parameters; a small utility, that updates “*detectors.dat*” file according to found corrections; quality check utilities, building residual histograms. The entire procedure is iterative (Fig. 4.3) and can include many cycles of investigations.

One distinguishes two coordinate reference frames in the COMPASS spectrometer for the position description: local and global ones (Fig. 4.4). The local coordinates represent points measured w.r.t. the coordinate plane in the station itself. The origin is in the center of the active area and one direction, V -coordinate, is chosen along the wires (strips) and another, U -coordinate, is perpendicular to it. As far as the global reference frame is concerned, their axis are chosen along the beam direction (Z -coordinate), perpendicular to the ground from bottom to top (Y -direction), and perpendicular to the Z and Y axis in the direction from the Jura¹ side to Salève side of the setup – X -axis. Thus, the frame is right-handed. The origin of the global frame is assigned to the center of the target and it does not depend on the target type in various COMPASS physics programs.

4.2.3 Quality criteria

In order to estimate sufficiency of the alignment treatment, there is a set of methods:

¹Jura and Salève are two mountains around the CERN area. Their names are often used to indicate a direction according to the location of the mountains.

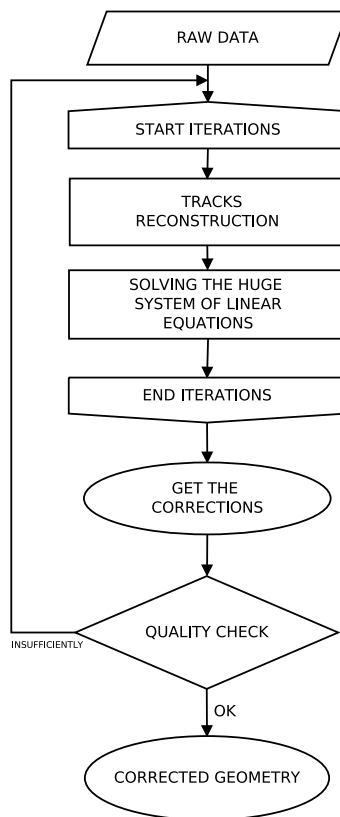


Figure 4.3: Alignment procedure flowchart.

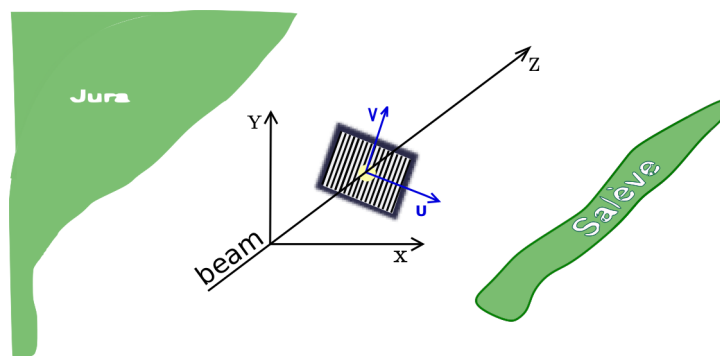


Figure 4.4: Scheme of the CORAL coordinate reference frames: global in black and local associated with a certain detector plane in blue.

1. basic quality criteria that uses residual distributions;
2. stability checks² of the detector description files;
3. pseudo performance study of the detectors.

The first method is implemented in the CORAL alignment utilities (namely “*CheckTracks*”), and, as a rule, it is applied during the procedure by default for each iteration. It allows to get minimal, but important and useful, information about the current picture at a certain iteration. At the end of the procedure, checks of the stability of values in the output “*detectors.dat*” files can be performed — the values should not be vary in comparison to other reliable “*detectors.dat*” files in the absence of a valid reason (*e.g.* moving the detector station). Finally, the most informative method for the alignment quality estimation is the detector pseudo-performance study (DPS). It is realized as a separate tool based on Phast User Event, which requires a piece of an mDST production. Therefore it is used after the alignment procedure is finished and when already there is a preliminary “*detectors.dat*” file for the quality analysis. Below we will focus on each quality method in more details with examples.

Residual distributions. Main criterion used for the quality evaluation of the procedure is the shape and statistical characteristics of residual distributions. The residual is defined as

$$\Delta u = u_{det} - u_{track}, \quad (4.16)$$

where u_{det} is the position of hit in the detector plane, measured in the direction perpendicular to wires (or strips) and u_{track} is the hit position associated with a track. The following residual distributions are used:

1. Δu distribution;
2. Δu versus v ;
3. Δu versus u .

The residual distribution itself (counts of Δu measurements) is assumed to conform to standard normal statistics. Thereby the shape of the distribution is gaussian, the mean value

²should not be confused with the stability checks of data taking

must be close to zero, and the root mean square has to represent the resolution of the detector. Also for the bound active areas (*e.g.* X/Y and U/V for the most of the detectors) the counts should not significantly distinguish between coordinate planes. Any discrepancy with these assumptions tells about misalignment of the center detector position.

In Fig. 4.5 the residual distribution with a misalignment is shown, that is characterized by a shift of the mean value from zero, a bit lower counts for X -plane w.r.t. Y -plane, and an asymmetry of the Gaussian shape. The Fig. 4.6 demonstrates results of 5 iterations of the alignment procedure for the misalignment shown in Fig. 4.5.

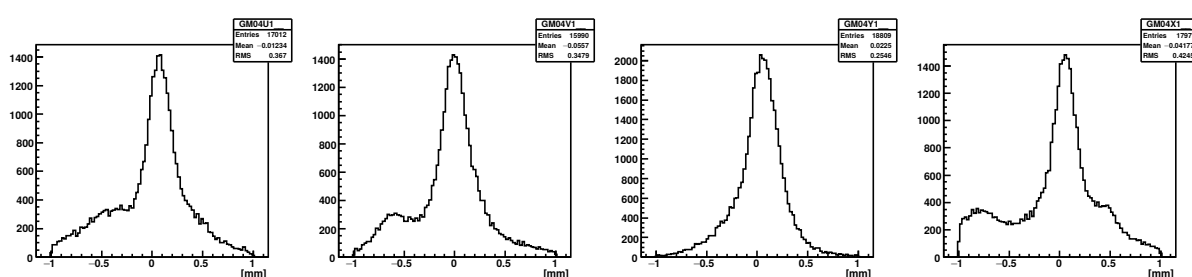


Figure 4.5: Δu distributions for the 4th GEM station before the alignment procedure performed. The misalignment is clearly seen as asymmetric shapes of the distributions.

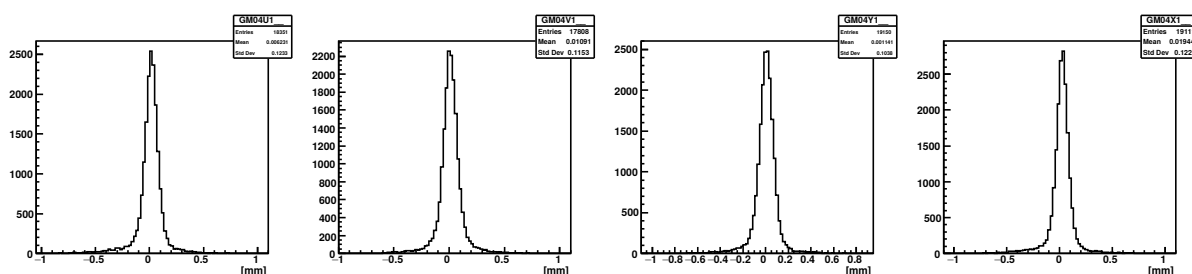


Figure 4.6: Δu distributions for the 4th GEM station after performing 5 iterations of the alignment procedure.

Distributions for Δu versus v are assumed to be uniform. The observation of a slope on the plots points to the angle misalignment in the plane that is perpendicular to the beam direction.

Δu versus u distribution should also be uniform. Slope of the distribution is correlated with pitch and Z -coordinate misalignment.

Stability checks of the detector files

In addition to quality checks of the treatment of the proper alignment procedure some stability checks can be useful. The concept of the method is to compare crucial values for alignment (such as X and Y coordinate of center, angle, Z -coordinate, pitch, dead zone positions) in the obtained “*detectors.dat*” file with corresponding values from another “*detectors.dat*” files (which are already investigated and reliable enough). The difference between the values should not be large if there is no known reason. This check can be useful either in case of inability to converge during the minimization with current options (then not valid values are written in the output) or in case of other damage of the “*detectors.dat*” file in the chain of the alignment procedure.

A tool for such kind of stability checks was developed by the Thesis author. The tool was used for comparison of the “*detectors.dat*” files between data taking periods and between alignment iterations for 2012, 2016 and 2017 runs. Examples of the checks are presented in Figs. 4.7, 4.8.

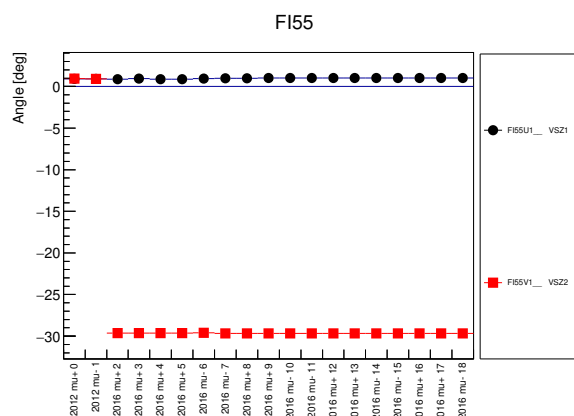


Figure 4.7: Run-by-run comparison of the angle value. It is seen that V1 of FI55 was rotated between 2012 and 2016 runs.

Detector pseudo performance study

Since alignment impacts on the coordinate reconstruction in each of the tracking planes, the detailed study of the detector efficiencies gives useful picture regarding the alignment quality or reveals problems that can not be resolved by the usual standard procedure (*e.g.* miscalibrations, local inefficiencies, hardware problems, etc.).

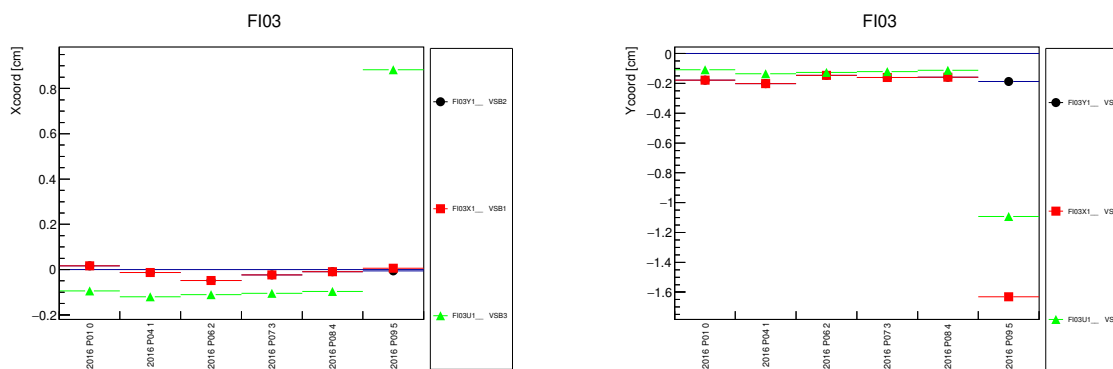


Figure 4.8: Run-by-run comparison of the center coordinates. One can see a displacement correction in P09 for FI03.

In COMPASS the calculated efficiency of detectors is widely used by analysts and detector experts. We define efficiency as the number of tracks crossed the detector divided by the number of hits in it. One distinguishes two types of efficiency: true- and pseudo-efficiency. In the first one the considering detector does not participate in the reconstruction whereas the pseudo-efficiency means taking hits of the detector into account. The true efficiency gives unbiased evaluation, but it requires significant CPU resources. Due to its computational expense it is not convenient to use true efficiency in the alignment analysis, since the alignment can be modified a lot before it has been got the final stable version. Therefore pseudo efficiency is more often used for the alignment analysis. In addition with residual and time resolution distributions it is called *Detector Pseudo-performance Study (DPS)*.

4.2.4 Alignment with constraints

Many of the detector planes are depend on a part of one detector station. Such planes are constrained by construction of their stations (*e.g.* joint framework etc.). However the alignment procedure considers the planes as independent parts by default.

The author of the Thesis investigated the impact of constraints in the alignment procedure. The constraints in this context mean taking into account various constant geometrical structures of the detector stations and the spectrometer, such as: the distance between two planes, the constant right angle between some U and V axis etc.

Constraint is described by the following linear combination:

$$\alpha_1 P + \alpha_2 P + \dots + \alpha_N P = \beta, \quad (4.17)$$

where the alpha letters are the coefficients derived from derivatives with respect to aligning parameter P (*i.e.* residual U , angle T etc.) and β is a free parameter (that can be *e.g.* distance or angle between planes).

In the minimization of χ^2 (which is equivalent to searching the solution of the system of equations as shown above) the constraint accounting corresponds to the solution of the system of linear equations (4.15) with an additional linear condition (4.17) via Lagrange multiplier method.

Technically, a constraint has to be initially fixed in the geometry description. In other words, the values from the “*detectors.dat*” file must satisfy all taking into account constraints. Then the alignment procedure with an additional option in the “*align.opt*” file preserves the fixed differences for the result output “*detectors.dat*” files so that the aligned geometry values will also satisfy the necessary constraints. Therefore a good alignment for the initial “*detectors.dat*” file is required in order to safely modify the input geometry values so that they have the constraints by default. The implemented option of constraints in the MILLEPEDE program just guarantees a conservation of the constrained difference during the alignment procedure.

As a test of subject the constraints between planes of the GEM detectors were considered. The GEM detector has the joint active planes for X and Y (U and V) directions. Due to their design the angle between two adjacent planes is rigidly fixed and equal to 90° . The corresponding constraint reads as

$$|GM(X/U)_{angle} - GM(Y/V)_{angle}| = 90^\circ, \quad (4.18)$$

which has to be hold in the geometry file. In terms of the alignment output it means to produce the same corrections for $X(U)$ and $Y(V)$ -planes.

The results of the tests are presented in Fig. 4.9, 4.10, 4.12 and Tab. 4.1, 4.2. The Tab. 4.1 shows the output corrections for the geometry description for the constrained and non-constrained procedure. It is seen that the values of angle and its increment are simultaneously changing on the same quantity for joint planes. The final geometry values in the “*detectors.dat*” file is shown in Tab. 4.2.

Despite the logicality of the simultaneous change in the values for the joint parts of the

detectors the impact of the constrained alignment is small and ambiguous. This is demonstrated in Figs. 4.9, 4.10, 4.12. Similar tests were also performed for angle constraints in the micromega, pixel GEM and drift chamber detectors, during which small and ambiguous impact was also observed. Mainly due to dependence on the initial constrained values, which can be misaligned by default. For an example, the initial 90° difference was obtained as an average during the test of the angle constraints for the GEM detectors: $90^\circ + 1/2 \times (\text{sum of the tilt values})$. Taking of the simple average is an assumption that the both planes are equivalently misaligned, which is true in the reality for the rigorous bound parts by construction, but it is not hold after a few iterations of standard alignment, at which one of the plane will be better aligned than another, and as a consequence, the average has to be calculated with weights (which seem impossible to determine).

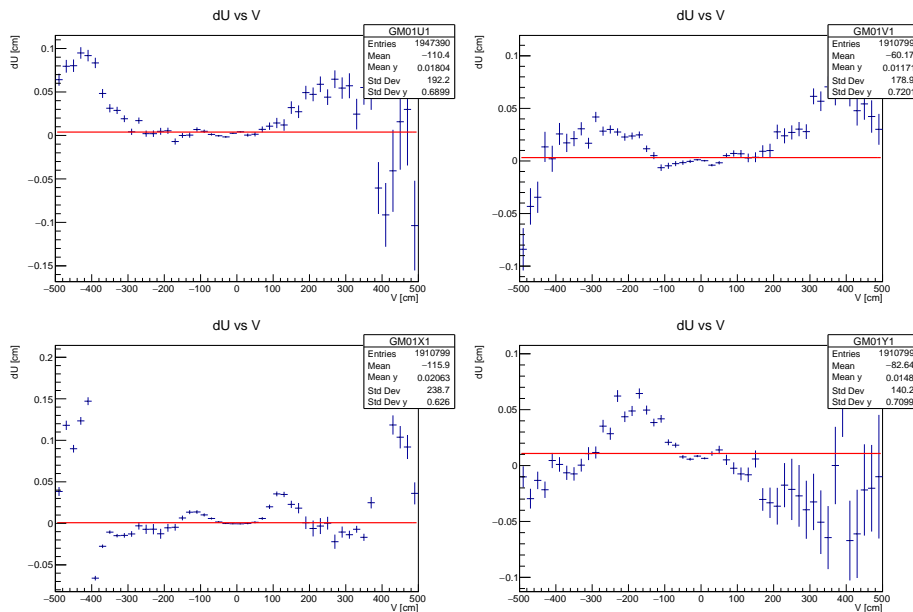


Figure 4.9: Δu versus v distribution before alignment procedure (GM01 station, alignment run 278902 with magnetic field, $\mu+$ beam).

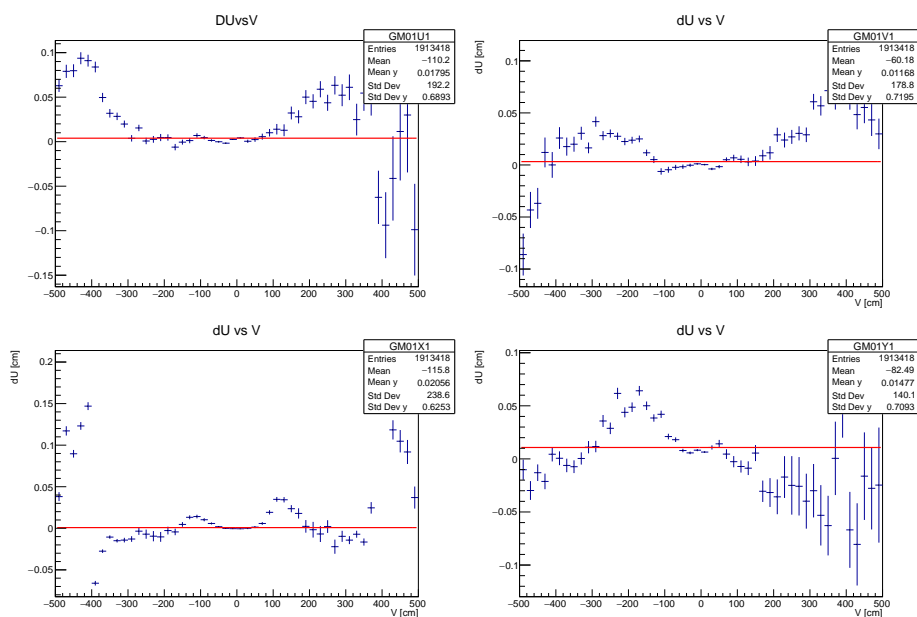


Figure 4.10: Δu versus v distribution after 5 iterations without angle constraint for GEMs (GM01 station, alignment run 278902 with magnetic field, $\mu+$ beam).

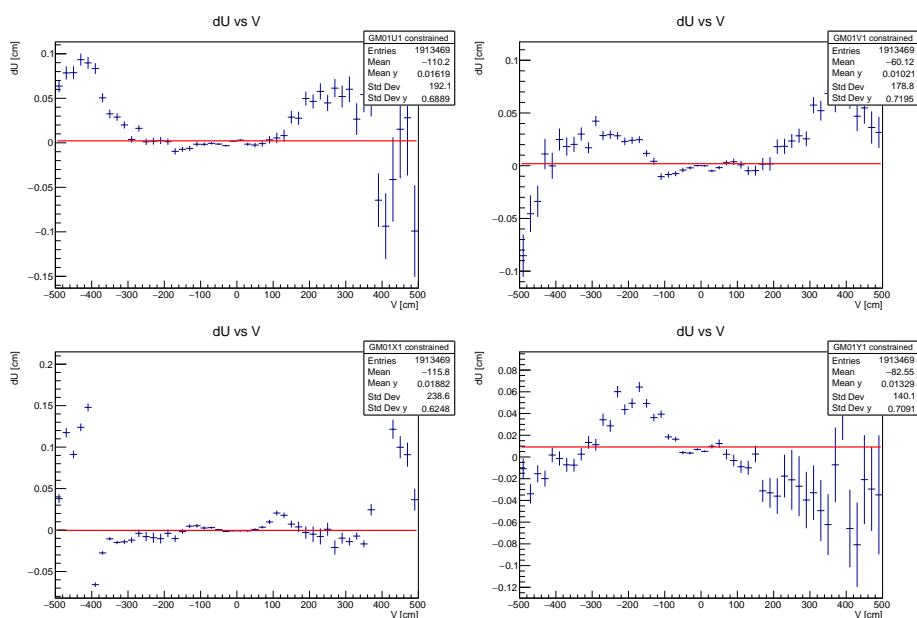


Figure 4.11: Δu versus v distribution after 5 iterations with angle constraint for GEMs (GM01 station, alignment run 278902 with magnetic field, $\mu+$ beam).

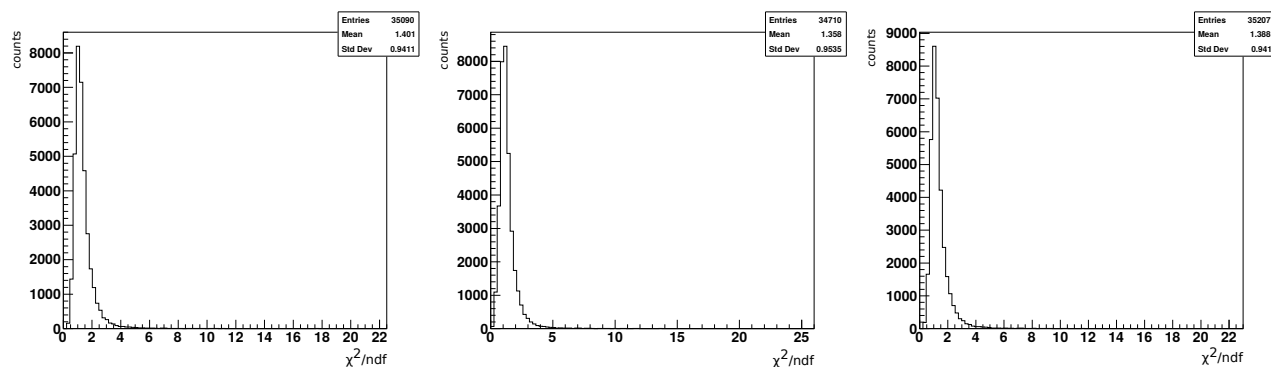


Figure 4.12: χ^2 -distributions of the track reconstruction: left – before alignment; middle – after 5 iterations of standard alignment; right – after 5 iterations of constrained alignment.

plane	output of the procedure with constraints					output of the procedure without constraints				
	U [mm]	dU [mm]	T [deg]	dT [deg]	Ntracks	U [mm]	dU [mm]	T [deg]	dT [deg]	Ntracks
GM01U1	+0.21822	+0.0011623	-0.014895	+0.00081208	15524	+0.21587	+0.0011756	-0.0089161	+0.0011618	15525
GM01V1	+0.062495	+0.0011437	-0.014895	+0.00081208	16294	+0.064337	+0.0011594	-0.022520	+0.0011079	16291
GM01Y1	+0.10612	+0.0011232	-0.010839	+0.00078947	16272	+0.10650	+0.0011231	-0.012190	+0.0015922	16275
GM01X1	+0.090259	+0.0011461	-0.010839	+0.00078947	16245	+0.090088	+0.0011516	-0.011246	+0.00089734	16249
GM02U1	-0.024107	+0.0011039	-0.0053541	+0.00075098	17340	-0.024301	+0.0011115	+0.0062688	+0.0010529	17334
GM02V1	-0.031197	+0.0011012	-0.0053541	+0.00075098	17612	-0.031069	+0.0011137	-0.021048	+0.0010433	17609
GM02Y1	-0.0065567	+0.0011144	-0.014831	+0.00076056	16540	-0.0058573	+0.0011127	-0.011640	+0.0015634	16548
GM02X1	-0.11239	+0.0011160	-0.014831	+0.00076056	17299	-0.11196	+0.0011204	-0.016385	+0.00085780	17315

Table 4.1: Output of the alignment procedure (“*align.out*”) after 5 iterations with and without angle constraints for the GEM detectors (alignment run 278902 with magnetic field, $\mu+$ beam).

TBName	“ <i>detectors.dat</i> ” values from constrained alignment			“ <i>detectors.dat</i> ” values from standard alignment		
	X center [cm]	Y center [cm]	Angle [deg]	X center [cm]	Y center [cm]	Angle [deg]
GM01U1	-0.07580	-0.64007	-0.029	-0.07586	-0.64029	-0.020
GM01V1	-0.07580	-0.64007	-90.029	-0.07586	-0.64029	-90.041
GM01Y1	-0.19947	-0.65332	90.022	-0.19950	-0.65327	90.023
GM01X1	-0.19947	-0.65332	0.022	-0.19950	-0.65327	0.020
GM02U1	-0.03002	-0.18005	-0.049	-0.03003	-0.18003	-0.051
GM02V1	-0.03002	-0.18005	-90.049	-0.03003	-0.18003	-90.052
GM02Y1	-0.05710	-0.18191	89.920	-0.05706	-0.18184	89.926
GM02X1	-0.05710	-0.18191	-0.080	-0.05706	-0.18184	-0.084

Table 4.2: Result values in the “*detectors.dat*” file after 5 iterations with and without angle constraints for the GEM detectors (alignment run 278902 with magnetic field, $\mu+$ beam).

Chapter 5

Analysis

In Chapter 1 the pion-nucleon Drell-Yan cross-section and associated spin (in)dependent asymmetries were introduced. The relations between the asymmetries and respective pion and proton PDFs were given. Measurements of Drell-Yan asymmetries in an experiment provide a unique access to the spin-structure of the hadrons. In this section we will describe several methods employed COMPASS for extraction of Drell-Yan asymmetries from the data. The results obtained from COMPASS 2015 and 2018 data will be presented.

From the polarized proton (NH_3) target data collected by COMPASS one can extract both the Transverse Spin and Unpolarized Asymmetries (TSAs and UAs, respectively). In COMPASS the TSA and UA analyses are done separately, since the latter study requires acceptance-corrections and thus a detailed simulation of the spectrometer. In the TSA analysis the data from both target cells and opposite polarization configurations (collected in two sub-periods of a given period) are combined in a way that the acceptance of the apparatus cancels out. The polarized analysis thus requires only corrections related to the dilution factor and target polarization. In present work the following extraction methods were applied: Histogram Binned Likelihood (HBL) for UAs, one-dimensional double ratio (1DDR) and Extended Weighted Unbinned Maximum Likelihood (EWUML) for TSAs.

Note that COMPASS in addition performs extractions of dimuon transverse momentum weighted asymmetries [202, 203] which serve as an alternative way to access the TMD PDFs (not discussed in this Thesis).

5.1 Data sample

In 2015 and 2018 COMPASS recorded Drell-Yan data with 190 GeV/c π^- beam impinging on a set of cylindrical targets aligned along the beam axis; two transversely polarized NH_3 target cells, followed by two nuclear targets (aluminum (Al) and tungsten (W) beam plug) for unpolarized Drell-Yan studies.

2015 sample: The data collected in 2015 between July 8 and November 12 (approximately 18 weeks) were taken in relatively stable conditions and are considered to be good for physics analyses. The data from these 18 weeks were combined into 9 periods: “coupled weeks” with opposite target polarization. These neighboring weeks that are separated by a polarization reversal, are called sub-periods (SPs). Data taking intervals, the corresponding polarization states and start/end run numbers for each sub-period are summarized in Tab. 5.1 and in Fig. 5.1.

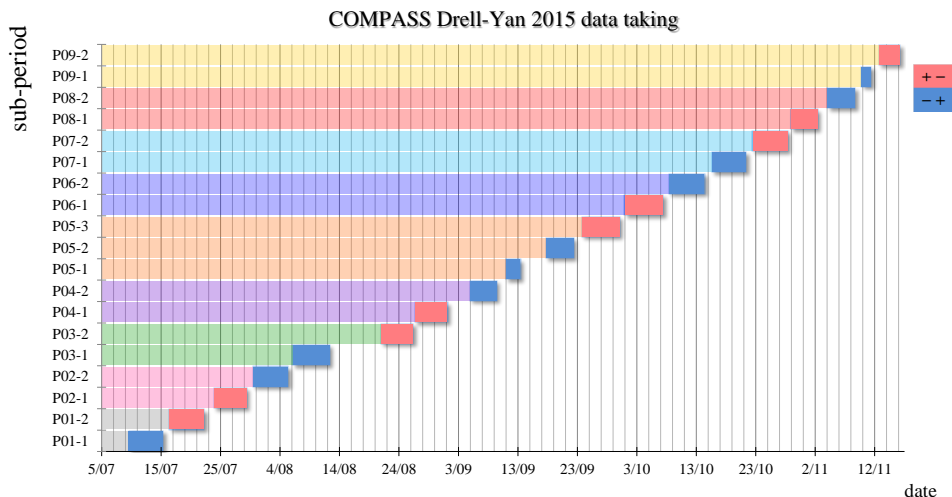


Figure 5.1: Performed physics data collection schedule for 2015 run. The $+-$ and $-+$ polarization configurations are indicated by red and blue boxes, correspondingly.

2018 sample: The data collected in 2018 between May 16 and November 12 (approximately 25 weeks) were considered for physics analyses. The data from these 25 weeks were combined into 9 periods. In 2018, four out of nine periods took longer than the usual two weeks (P00 and P04 ≈ 3 weeks, P02 and P07 ≈ 4 weeks). Those long periods eventually required special treatment. In particular, the very first period (P00) is affected by evident differences between the sub-periods (trigger problems between SP-1 and SP-2 and change of the beam-file between

Period	Sub-period	Polarization up/down cell	First-last runs	Begin date	End date
W07 (P1)	SP-1	$\downarrow\uparrow (+-)$	259363 - 259677	09 Jul	15 Jul
	SP-2	$\uparrow\downarrow (-+)$	259744 - 260016	16 Jul	22 Jul
W08 (P2)	SP-1	$\uparrow\downarrow (-+)$	260074 - 260264	23 Jul	29 Jul
	SP-2	$\downarrow\uparrow (+-)$	260317 - 260565	29 Jul	05 Aug
W09 (P3)	SP-1	$\downarrow\uparrow (+-)$	260627 - 260852	05 Aug	12 Aug
	SP-2	$\uparrow\downarrow (-+)$	260895 - 261496	12 Aug	26 Aug
W10 (P4)	SP-1	$\uparrow\downarrow (-+)$	261515 - 261761	26 Aug	01 Sep
	SP-2	$\downarrow\uparrow (+-)$	261970 - 262221	04 Sep	09 Sep
W11 (P5)	SP-1	$\downarrow\uparrow (+-)$	262370 - 262772	11 Sep	22 Sep
	SP-2	$\uparrow\downarrow (-+)$	262831 - 263090	23 Sep	30 Sep
W12 (P6)	SP-1	$\uparrow\downarrow (-+)$	263143 - 263347	30 Sep	07 Oct
	SP-2	$\downarrow\uparrow (+-)$	263386 - 263603	08 Oct	14 Oct
W13 (P7)	SP-1	$\downarrow\uparrow (+-)$	263655 - 263853	15 Oct	21 Oct
	SP-2	$\uparrow\downarrow (-+)$	263926 - 264134	22 Oct	28 Oct
W14 (P8)	SP-1	$\uparrow\downarrow (-+)$	264170 - 264330	28 Oct	02 Nov
	SP-2	$\downarrow\uparrow (+-)$	264429 - 264562	04 Nov	08 Nov
W15 (P9)	SP-1	$\downarrow\uparrow (+-)$	264619 - 264672	09 Nov	11 Nov
	SP-2	$\uparrow\downarrow (-+)$	264736 - 264857	12 Nov	16 Nov

Table 5.1: 2015 data taking periods.

SP-2 and SP-3). For this reason the P00 is excluded from the TSA analyses.

Performed data-collection schedule is illustrated in Fig. 5.2. Data taking intervals and corresponding polarization states and start/end run-numbers for each sub-period are summarized in Tab. 5.2.

5.2 Analysis of transverse spin asymmetries

In this section we discuss the extraction of transverse spin asymmetries, which are present in the single polarized DY leading-order cross-section (2.39). There are seven azimuthal asymmetries in (2.39): two of them ($A_U^{\cos\varphi_{CS}}$ and $A_U^{\cos\varphi_{CS}}$) are spin independent¹, while the other five ($A_{UT}^{\sin(\varphi_{CS}+\varphi_S)}$, $A_{UT}^{\sin(\varphi_{CS}-\varphi_S)}$, $A_{UT}^{\sin(\varphi_S)}$, $A_{UT}^{\sin(2\varphi_{CS}+\varphi_S)}$ and $A_{UT}^{\sin(2\varphi_{CS}-\varphi_S)}$) depend on the transverse

¹The eq. (2.39) also indirectly contains one more spin independent asymmetry A_U^1 in the denominator of the unpolarized part of the cross-section σ_U . In LO approximation A_U^1 is assumed to be equal to unity.

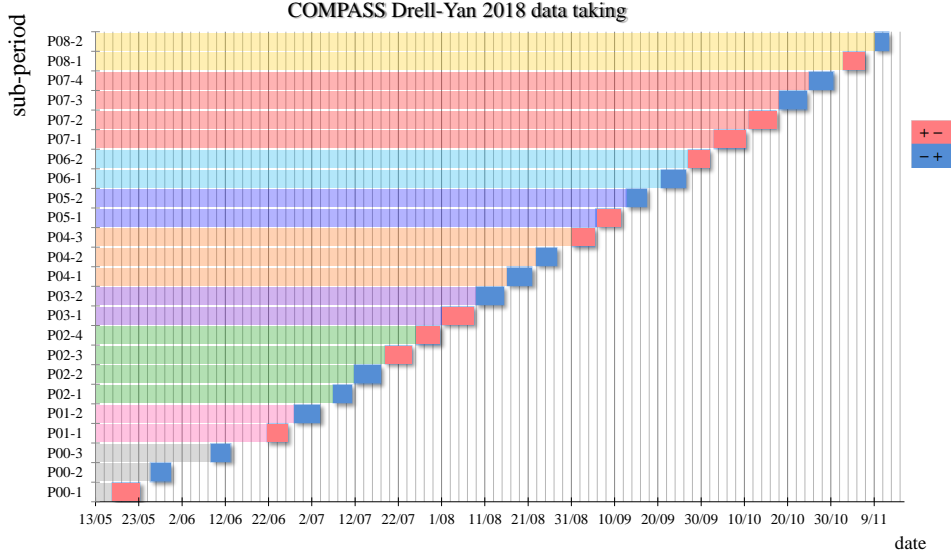


Figure 5.2: Performed physics data collection schedule for 2018 run. The $+-$ and $-+$ polarization configurations are indicated by red and blue boxes correspondingly.

component of the spin of the nucleon. The $A_{UT}^{\sin(\varphi_S)}$, $A_{UT}^{\sin(2\varphi_{CS}+\varphi_S)}$ and $A_{UT}^{\sin(2\varphi_{CS}-\varphi_S)}$ asymmetries are related to the Sivers, pretzelosity and transversity TMD PDFs, respectively. The other two TSAs ($A_{UT}^{\sin(\varphi_{CS}+\varphi_S)}$ and $A_{UT}^{\sin(\varphi_{CS}-\varphi_S)}$) are purely higher-twist effects. In order to extract the TSAs one needs first to run the event-selection procedure on the reconstructed data (DST files produced by CORAL). A sample of good-quality Drell-Yan events passing various selection criteria is then ready to be passed to the TSA analysis.

5.2.1 Event selection

COMPASS PHAST (PHysics Analysis Software Tools) is a C++ and CERN-ROOT based software package used to process the DST files and select the events of interest, as well as define and store kinematic and angular variables in the output (ROOT trees, and histograms). Most of the selection criteria (tracks, vertices, certain kinematic cuts, etc.) are implemented at the level of PHAST “user functions” the so-called “UserEvent”s. The bulk of mini- or micro-DST files is then processed in the batch mode *e.g.* at CERN-lxplus.

The selection of Drell-Yan pairs starts from a loop over the primary vertices keeping only those with two opposite charge outgoing tracks. In each PHAST event (PaEvent object) there is an index associated with the so-called “best primary vertex” of the event that is defined by

Period	Sub-period	Polarization up/down cell	First-last runs	Begin date	End date
P00	SP-1	$\uparrow\downarrow(-+)$	283117 - 283285	16 May	23 May
	SP-2	$\downarrow\uparrow(+ -)$	283338 - 283464	25 May	30 May
	SP-3	$\downarrow\uparrow(+ -)$	283588 - 283705	08 Jun	13 Jun
P01	SP-1	$\uparrow\downarrow(-+)$	283849 - 284003	21 Jun	26 Jun
	SP-2	$\downarrow\uparrow(+ -)$	284022 - 284233	27 Jun	03 Jul
P02	SP-1	$\downarrow\uparrow(+ -)$	284348 - 284469	06 Jul	11 Jul
	SP-2	$\downarrow\uparrow(+ -)$	284471 - 284623	11 Jul	17 Jul
	SP-3	$\uparrow\downarrow(-+)$	284642 - 284802	18 Jul	25 Jul
	SP-4	$\uparrow\downarrow(-+)$	284815 - 284935	26 Jul	31 Jul
P03	SP-1	$\uparrow\downarrow(-+)$	284941 - 285141	01 Aug	08 Aug
	SP-2	$\downarrow\uparrow(+ -)$	285149 - 285333	09 Aug	15 Aug
P04	SP-1	$\downarrow\uparrow(+ -)$	285359 - 285512	16 Aug	21 Aug
	SP-2	$\downarrow\uparrow(+ -)$	285517 - 285646	22 Aug	27 Aug
	SP-3	$\uparrow\downarrow(-+)$	285707 - 285844	31 Aug	05 Sep
P05	SP-1	$\uparrow\downarrow(-+)$	285865 - 285994	05 Sep	11 Sep
	SP-2	$\downarrow\uparrow(+ -)$	286019 - 286103	12 Sep	17 Sep
P06	SP-1	$\downarrow\uparrow(+ -)$	286170 - 286324	20 Sep	26 Sep
	SP-2	$\uparrow\downarrow(-+)$	286330 - 286462	26 Sep	01 Oct
P07	SP-1	$\uparrow\downarrow(-+)$	286481 - 286742	03 Oct	10 Oct
	SP-2	$\uparrow\downarrow(-+)$	286749 - 286929	11 Oct	17 Oct
	SP-3	$\downarrow\uparrow(+ -)$	286941 - 287096	17 Oct	24 Oct
	SP-4	$\downarrow\uparrow(+ -)$	287107 - 287256	25 Oct	30 Oct
P08	SP-1	$\uparrow\downarrow(-+)$	287296 - 287404	01 Nov	06 Nov
	SP-2	$\downarrow\uparrow(+ -)$	287458 - 287537	09 Nov	12 Nov

Table 5.2: 2018 data taking periods.

the reconstruction software. If there is more than one primary vertex (PV) in the event, the so-called “best primary vertex” is selected. It can happen that, in a given event, none of the primary vertices with a dimuon pair of tracks associated, is identified as the “best primary vertex”. In this case the primary vertex with the smallest vertex χ^2 is selected. When the vertices are selected, the following criteria are applied to the event samples for the purpose of the TSAs extraction²:

²The described PHAST methods used in presented analysis are conditional and can partially be replaced by another ones.

1. The requirement that between the first and the last measured points the muon/anti-muon candidate has crossed more than 30 radiation lengths along the spectrometer, $x/X_0 > 30$. The x/X_0 value is obtained by the *PaTrack::XX0()* method. This criterion is used for separation of muons from hadrons at COMPASS.
2. The requirement to have only events with LAST-LAST and/or LAST-Outer dimuon trigger fired. Events with LAST-Middle dimuon trigger fired are rejected since they are strongly contaminated by the muons from decay of the beam pions (Beam Decay Muons (BDMs)). The rest of the BDMs is removed by the “hodoscope-pointing”-cut presented below.
3. The selection of tracks for which the first measured Z -coordinate is smaller than 300 cm and the last value of Z is greater than 1500 cm. This cut selects the tracks which have the first measured point before SM1 and the last measured point downstream of the MF1 (the latter means that the particle was not absorbed in MF1).
4. Check that the time of the track (w.r.t. the trigger time) is defined. In terms of PHAST it is a check that the *PaTrack::SigmaTime()* method does not return zero.
5. A time coincidence for the positive and negative muon tracks of each pair is ensured by the criterion $|\delta t_{\mu\pm}| < 5$ ns (Fig. 5.3). The criterion removes uncorrelated pairs *e.g.* pairs including a muon from the beam pion decay. In the PHAST UserEvent it is performed by comparing results returned by the *PaTrack::MeanTime()* method for the tracks in the pair.
6. Quality criteria for the tracks $\chi^2 < 3.2$. The reduced χ^2 value is obtained by taking the ratio of the values returned by *PaTrack::Chi2tot()* and *PaTrack::Ndf()* methods. The standard selection $\chi^2 < 10$ used in previous releases has been modified for this analysis. Stricter cut has proven to improve the stability of the TSA in 2018 case and to reduce the systematic uncertainties. It has no significant impact on 2015 TSA. However, it was chosen to apply the same cut in both cases.
7. Hodoscope pointing. A check that dimuon tracks extrapolated to the Z -position of the hodoscopes of the fired LAST-LAST and/or LAST-Outer trigger indeed fall into the

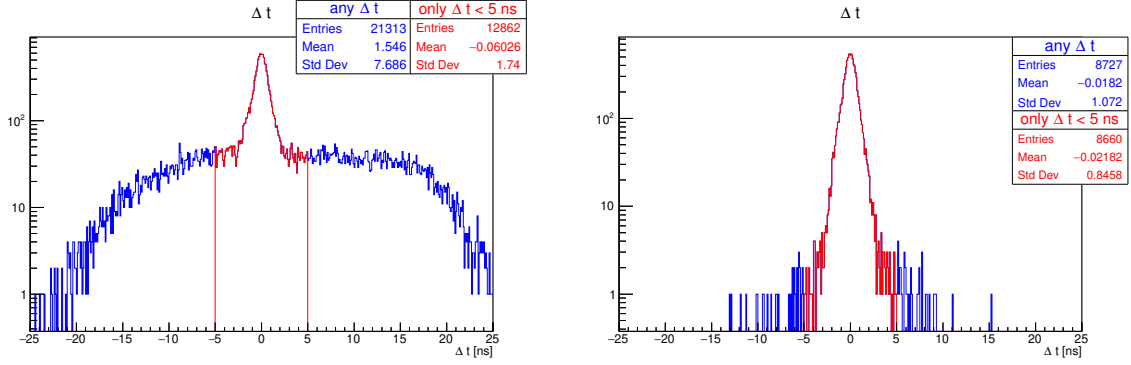


Figure 5.3: Impact of trigger time difference cut (based on P02 period of 2015 t8-production data). Events without trigger validation cut (left), events passed by trigger validation (right). Red color represents the applied time window.

geometrical acceptance of those hodoscope-planes. In PHAST it can be done by the means of *PaTrack::Extrapolate()* method that has to return *true* value and extrapolated track parameters. In combination with exclusion of the LAST-Middle trigger this cut rejects the BDM muons. be skipped.

8. Check for x_π , x_N and x_F variables to be in their ranges of definition: x_π and x_N must be in range of $[0; 1]$ and $x_F \in [-1; 1]$.
9. Cut for transverse momenta of virtual photon in the target rest frame $0.4 < q_T < 5.0$ GeV/c. The lower limit requirement was obtained by DY MC studies and ensures a good resolution of the azimuthal angles (in average below 0.2 rad, see Sec. 5.2.5). The upper limit has a negligible impact, it removes the tail of high q_T events (high q_T range is in tension with TMD factorization domain).
10. Check of the Z -coordinate of the primary vertex — ensuring that the dimuon pair was produced inside the NH_3 target cells. Target cell positions slightly differ between two years of DY data taking, their Z -positions are presented in Tab. 5.3. The values are provided by the COMPASS target group. A distribution along the Z -coordinate is illustrated in Fig. 5.4 for the HM (left) and the J/ψ mass (right) ranges.
11. Check of X and Y coordinates of the primary vertex to ensure that the dimuon pair was produced inside the NH_3 target cells. Cut requires that extrapolated beam tracks associated to selected primary vertices cross both upstream and downstream edges of

	Upstream cell		Downstream cell	
2015 setup	-294.5	-239.3	-219.5	-164.3
2018 setup	-294.5	-239.4	-219.1	-163.9

Table 5.3: Target cells positions in cm along Z -axis in the DY data-taking runs.

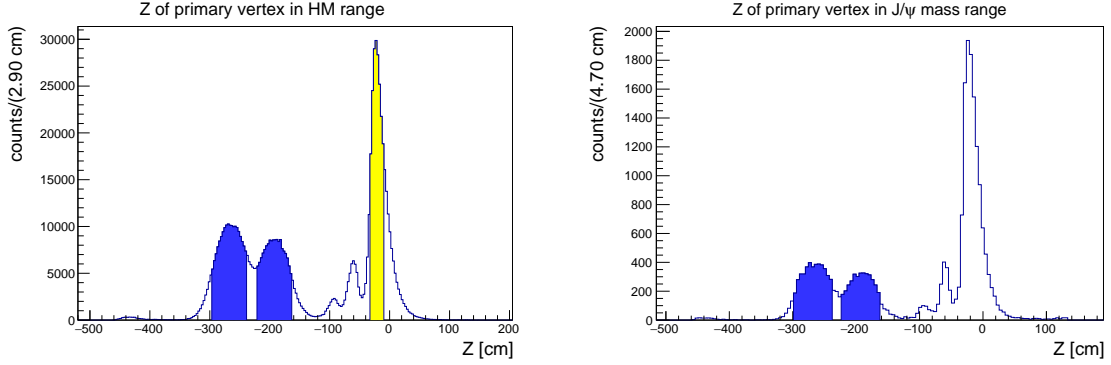


Figure 5.4: Impact of Z -coordinate cut for the NH_3 target cells (in blue) target and a part of the W target used for unpolarized analysis (in yellow). Left HM range, right J/ψ mass range.

the target volume. The aim of the cut is to equalize flux and beam conditions in both cells. The cells have a cylindrical form with a radius of 2 cm and a radial cut is applied, minimizing the migration of events from the surrounding volume. The limit value for the radial cut is based on target tomography study for each year: $r_{PV} < 1.8$ cm for 2015 and $r_{PV} < 1.9$ cm for 2018. The impact of the cut is illustrated in Fig. 5.5.

12. Momentum cut for muon tracks: $P_{\mu^\pm} > 7$ (GeV/c). This cut is based on MC studies and is meant to reject certain fake tracks present in real data in the high mass range. Note, this cut is not applied for the TSA analysis in the J/ψ region.
13. Cut for the sum of muon track momenta: $P_{\mu^+} + P_{\mu^-} < 180$ (GeV/c). The cut is similar to the previous one, but it is also applied in the J/ψ mass range.
14. Applying bad spill/run lists — rejection of events associated with a run/spill rejected in the data stability analysis (see the next Sec. 5.2.3).

The criteria listed above are applied to pick up good dimuon candidates. The impact of

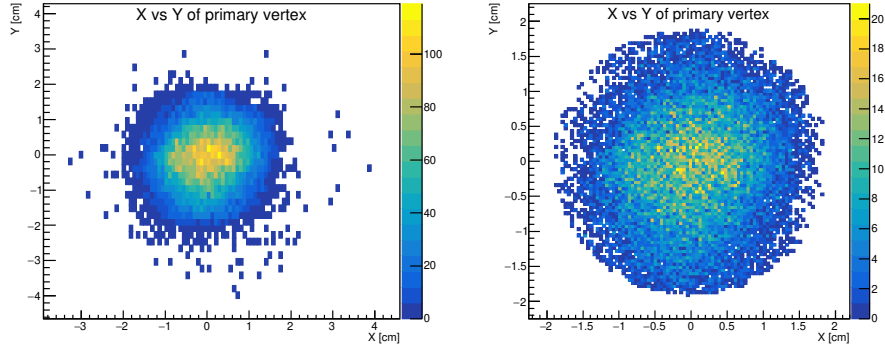


Figure 5.5: Impact of radial cut for NH_3 target (based on P06 slot1 2015 data). Left before the cut, right the result of the cut.

each criterion on the invariant mass distribution is shown in Fig. 5.6, where one can observe that with each cut the J/ψ -peak becomes more prominent.

The dimuon mass $M_{\mu\mu}$ spectrum accessed by COMPASS can be sub-divided into four ranges:

1. $M_{\mu\mu} \in (1.0; 2.0) \text{ GeV}/c^2$ – “low mass” range, DY cross-section is large, but the sample is dominated by background processes: combinatorial background, semi-leptonic decays;
2. $M_{\mu\mu} \in (2.0; 2.5) \text{ GeV}/c^2$ – “intermediate mass” range. From the background contamination point of view it is similar to the first range;
3. $M_{\mu\mu} \in (2.5; 4.3) \text{ GeV}/c^2$ – “ J/ψ (or charmonium)” mass range, is totally dominated by the J/ψ and ψ' contributions, and is thus interesting for charmonium studies.
4. $M_{\mu\mu} \in (4.3; 8.5) \text{ GeV}/c^2$ – “high mass” (HM) range, dominated by Drell-Yan, integrated contribution of all other channels is at the level of 4%;

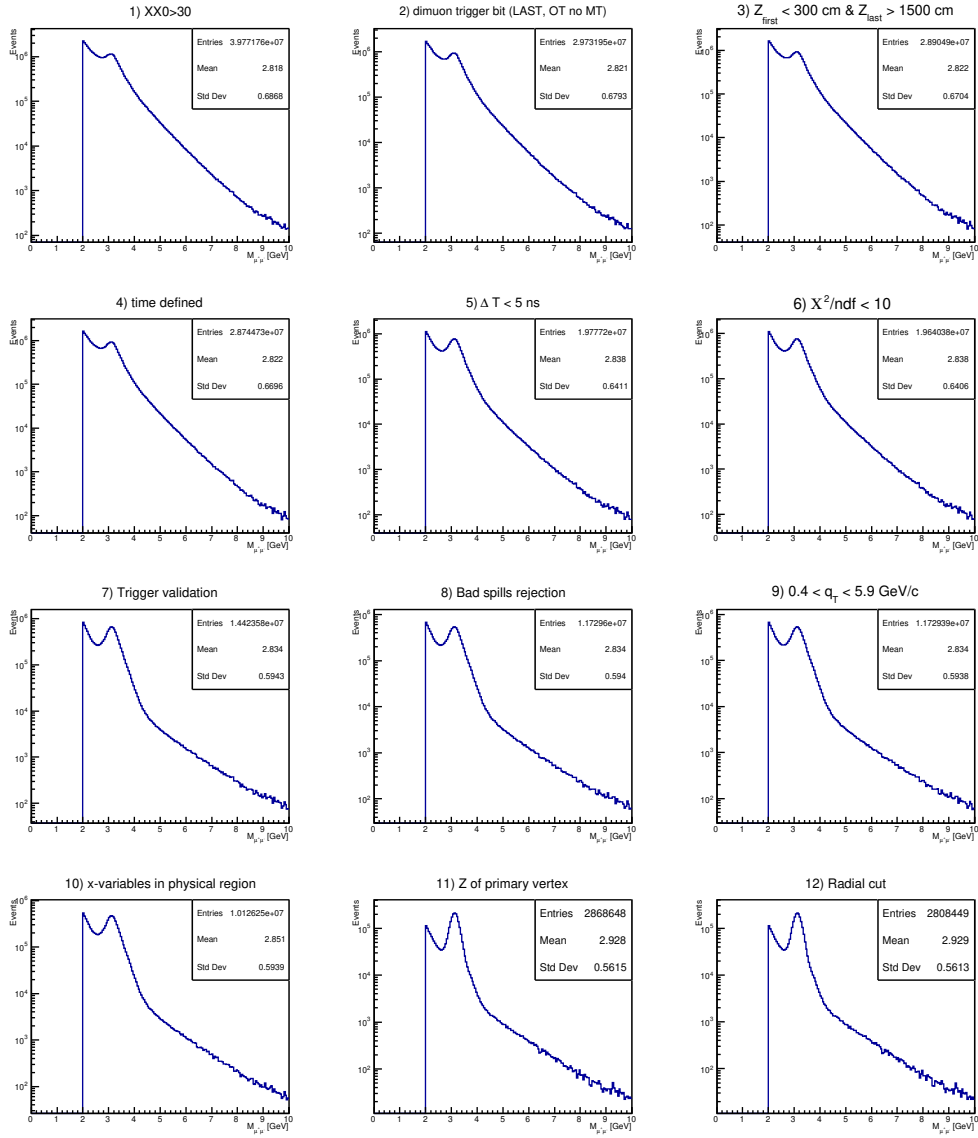


Figure 5.6: Dimuon invariant mass distribution cut-by-cut, events with $M_{\mu\mu} > 2.0$ GeV (based on all periods of slot1 2015 data).

5.2.2 Kinematic binning

The asymmetries are evaluated in kinematic sub-ranges (bins) of x_N , x_π , x_F , q_T , and $M_{\mu\mu}$, while always integrating over all the other variables. For this purpose the event-samples are being split into nearly equally populated kinematic sub-ranges over those observables. The corresponding bin limits are presented in Tab. 5.4-5.17.

Various kinematic distributions are shown in Fig. 5.7 and in Fig. 5.8 for the HM and for the J/ψ mass ranges, respectively.

x_N	0.0	0.13	0.19	1.0
x_π	0.0	0.4	0.56	1.0
x_F	-1.0	0.21	0.41	1.0
q_T	0.4	0.9	1.4	5.0
$M_{\mu\mu}$	4.3	4.75	5.5	8.5

Table 5.4: Kinematic bins for TSAs analysis in the HM range.

x_N	0.0	0.06	0.08	0.11	1.0
x_π	0.0	0.21	0.28	0.38	1.0
x_F	-1.0	0.1	0.2	0.31	1.0
q_T	0.0	0.72	1.04	1.48	10.0
$M_{\mu\mu}$	2.85	3.02	3.12	3.22	3.4

Table 5.5: Kinematic bins for TSAs analysis in the J/ψ mass range.

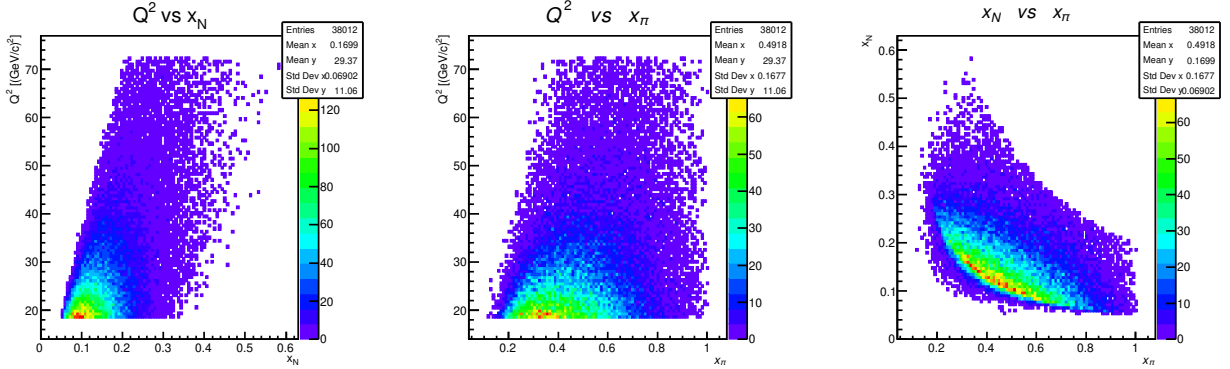


Figure 5.7: Distributions of x -variables and Q^2 in the HM range (based on all periods of slot1 2015 data).

The so-called “kinematic maps” showing the correlations between different variables in the bins selected for the analysis are shown in Fig. 5.7 (HM range) and in Fig. 5.8 (J/ψ mass range). The points correspond to average values of different kinematic observables evaluated in bins of other variables. Different colors indicate three examined samples defined by target selections: upstream cell, downstream cell and both cells together. The trends remain the same

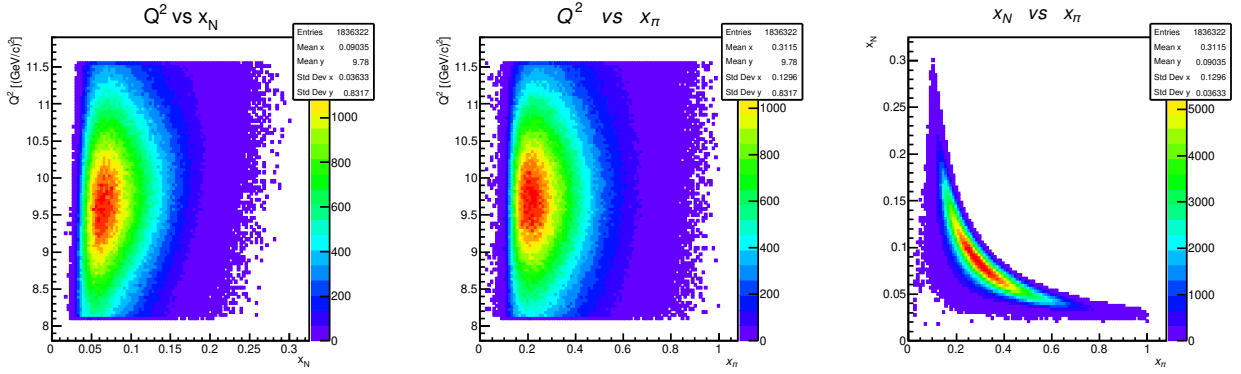


Figure 5.8: Distributions of x -variables and Q^2 in the J/ψ mass range (based on all periods of slot1 2015 data).

between different target samples, while average values are slightly different. The latter effect is conditioned by slightly different acceptance and thus also kinematic phase space, accessible by events originating from upstream and downstream cells.

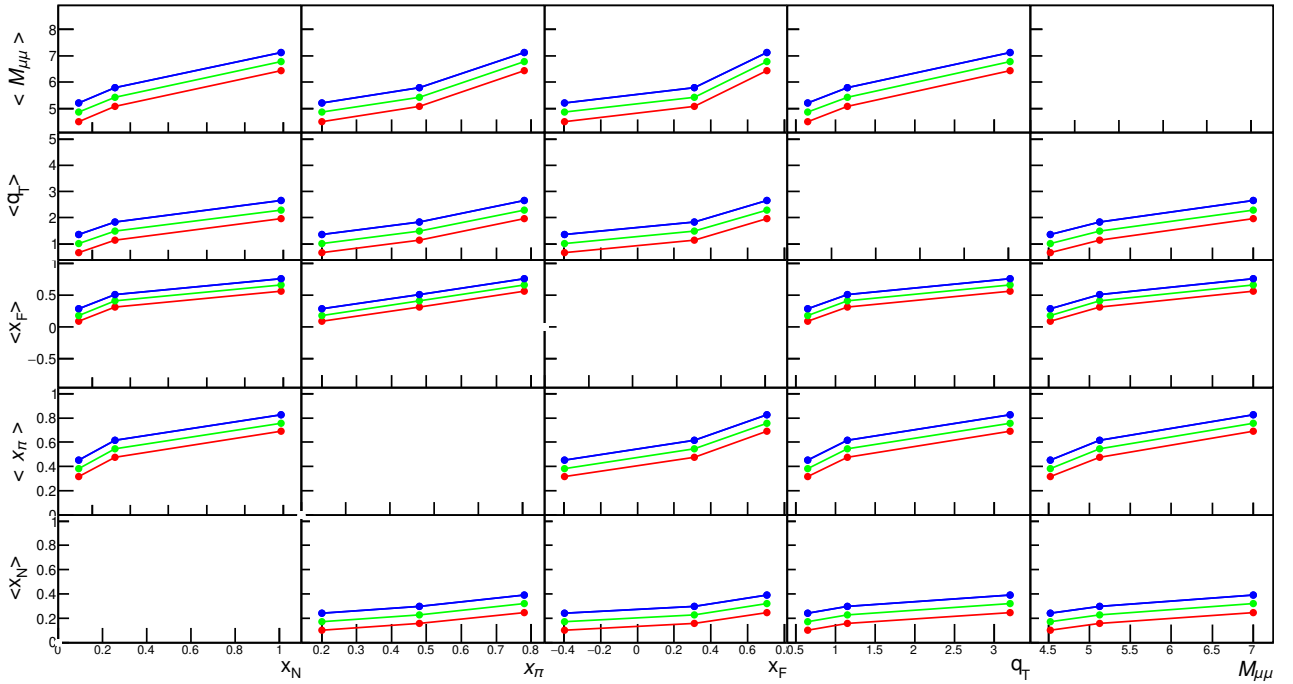


Figure 5.9: Kinematic maps for the HM range (2015 slot1 data). The values are shifted horizontally for a better visibility. U-cell in red, D-cell in green, both cells of the NH₃ target in blue.

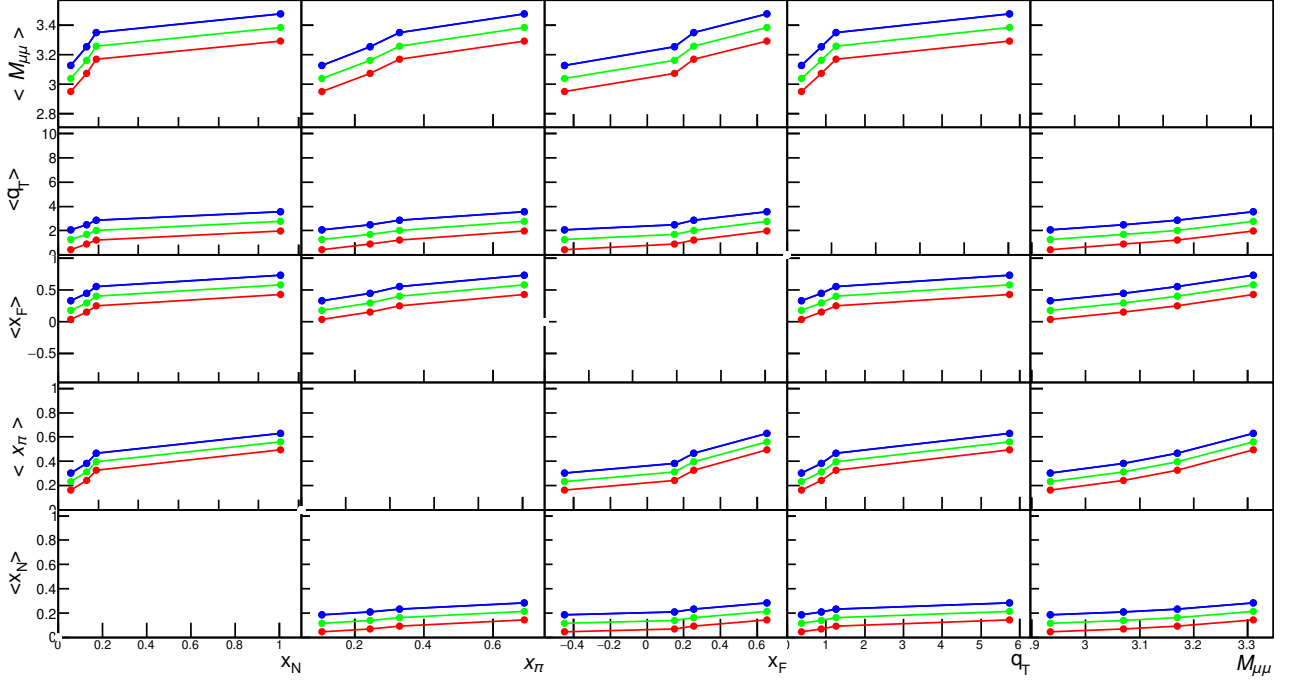


Figure 5.10: Kinematic maps for the J/ψ range (2015 slot1 data). The values are shifted horizontally for a better visibility. U-cell in red, D-cell in green, both cells of the NH_3 target in blue.

5.2.3 Data stability checks

One of the important selection criteria is the exclusion of “bad” spills and runs from the analysis. Two program frameworks are used for this purpose. One of them is checking for instabilities among spills, while the other one analyses the stability of the runs.

Bad spill identification

To select reliable spills the following per-spill quantities are monitored for each data taking period:

- Number of beam particles divided by number of events,
- Number of beam particles divided by number of primary vertices,
- Number of beam particles hits divided by number of beam particles,
- Number of primary vertices divided by number of events,
- Number of outgoing tracks divided by number of events,

- Number of outgoing particles divided by number of events,
- Number of outgoing particles from primary vertex divided by number of primary vertices,
- Number of outgoing particles from primary vertex divided by number of events,
- Number of hits in outgoing particles divided by number of outgoing particles,
- Number of μ^- (μ^+) divided by number of events,
- Number of μ^- (μ^+) from primary vertex divided by number of events,
- Sum of χ^2 of outgoing particles divided by number of outgoing particles,
- Sum of χ^2 of all vertices divided by number of all vertices,
- Trigger rates of dimuon triggers: MT-LAST, OT-LAST, LAST-LAST.

Under an assumption of stable data taking conditions during a given period, these quantities should be constant in time, with a spill being chosen as a time unit. Each single spill is compared with a range of neighboring spills (2500 spills before, and 2500 after the current one). If the value in the spill passes into a specific compatibility interval (“sigma box”) more than a certain number of times (“minimum number of neighbours”), spill is marked as good otherwise bad and to be rejected. The “sigma box” and the “minimum number of neighbours” are optimized for each variable and period of data taking. An example of the spill monitoring for a number of primary vertices divided by number of events is shown in Fig. 5.11.

Bad run identification

Bad run identification is based on the monitoring analysis of the shapes and means values of various distributions, performed on a run-by-run basis. About 40 variables are monitored: the main kinematic variables x_N , x_π , q_T , $M_{\mu\mu}$ (or Q^2); various laboratory observables, such as muon track momenta P_{μ^+} , P_{μ^-} , polar angles ϕ_{μ^+} , ϕ_{μ^-} , and azimuthal angles θ_{μ^+} , θ_{μ^-} , virtual photon momentum P_γ ; physical angles θ_{CS} , φ_{CS} , φ_S , etc. First, the run-by-run mean values have been monitored on period-by-period basis comparing the sub-periods with opposite spin configurations. If the mean value of a given observable in a certain run is more than 5σ away from the overall mean per period, the run is marked as “bad”. The comparison of shapes of

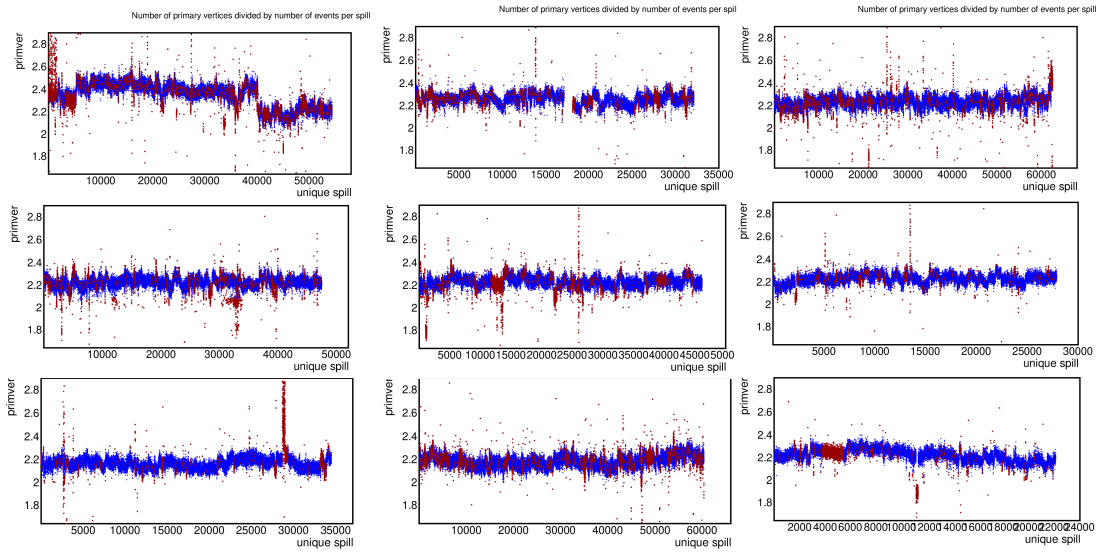


Figure 5.11: An example of instabilities indication among spills.

run-by-run distributions is done for each variable using the unbinned-Kolmogorov (UK) method [204]. The UK test fails if a shape of a certain run is incompatible with most of the runs in a given period. The runs which failed the UK test are also marked as “bad”. Examples of UK test and mean comparison are shown in Fig. 5.12.

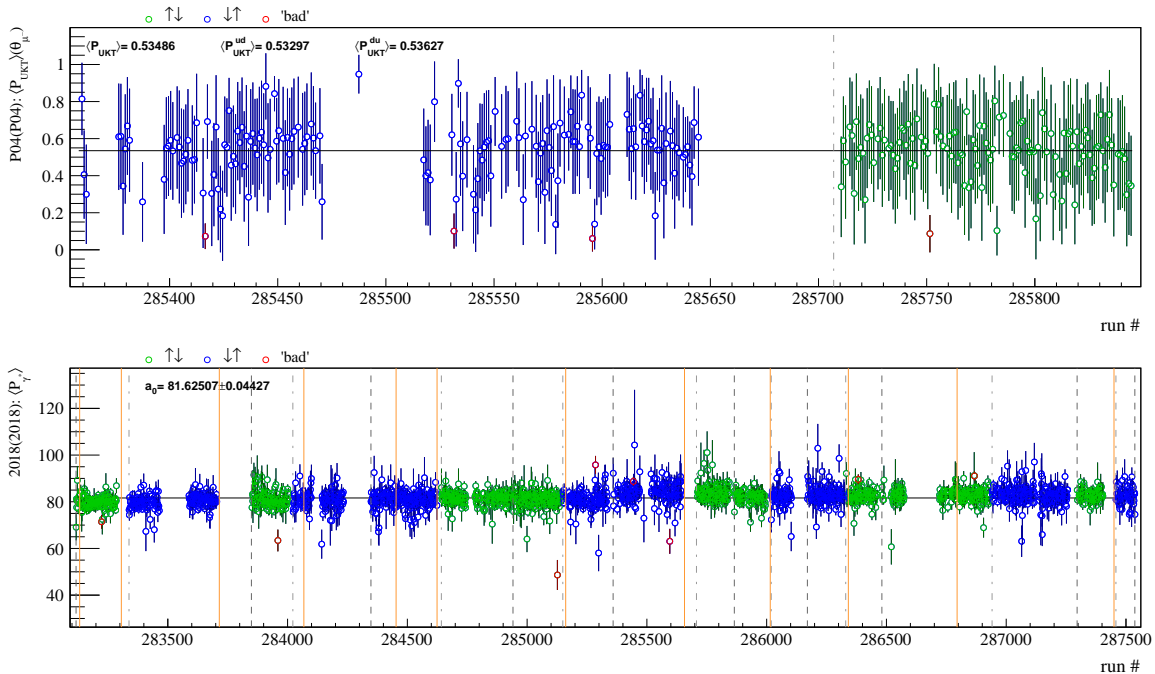


Figure 5.12: Examples of instabilities indication among runs.

5.2.4 Data productions

Massive data production campaigns at COMPASS presume full processing of raw data collected during given year using the data reconstruction software (CORAL). Normally, several such campaigns take place each including new set of corrections identified during the analysis of previous production data (such as improved detector calibrations, corrected alignment “*detectors.dat*” files, updated reconstruction settings etc.). The productions are labeled as “t#” or “s#” (slot#). The data productions used for this Thesis are summarized in Tab. 5.6, where the total number of the selected events for the TSA extraction is presented for two analysed mass ranges. The detailed tables listing cut-by-cut statistics can be found in the Appendix 5.9.

	J/ψ mass range	High mass range
2015 slot2	1 574 994	34 729
2018 t8	1 683 920	36 869

Table 5.6: Total statistics after the event selection from the data productions used for the TSAs extraction in the Thesis.

The reconstructed data from the 2015-t3 production were used in the published analysis of DY TSAs [84]. Preliminary results for Drell-Yan TSAs from the 2018 t2 production data (50% of the sample) were released in early 2019 note [205]. Later these data samples were analysed by the Author of this Thesis to reproduce released results and to prepare and cross-check the analysis tools, which were then used to obtain the results presented in this work. The most recent 2018 t8-production was a subject of several improvements and corrections, among them:

- updated position for the reference planes used for vertexing;
- corrected positions for the trigger hodoscopes and updated timing calibrations;
- updated calibrations for the drift chamber detectors (DC05, DC04);
- updated calibrations for the MWPC detectors;
- corrected material description and position for aluminum and tungsten targets;
- improvements in the CORAL package: optimization of the tracking in SM1-SM2 range, improved hit association for the Muon Wall A detectors, etc.

A detailed comparison between t2 and t8 production of 2018 data was done. The impact of the changes between two production are illustrated in Figs. 5.13-5.24. The updates in the reconstruction lead to a gain in statistics of about 9% in the J/ψ mass range and of about 4% in the high mass range. One of the noticeable changes was an improvement of the mass resolution, which is manifested *e.g.* in the reduced width of the J/ψ -peak, as demonstrated in Fig. 5.13. The changes have affected also the HM range, in particular, the distribution of the dimuon invariant mass difference calculated for the events that are in common between two productions³ is broader for higher mass ranges, see Fig. 5.14.

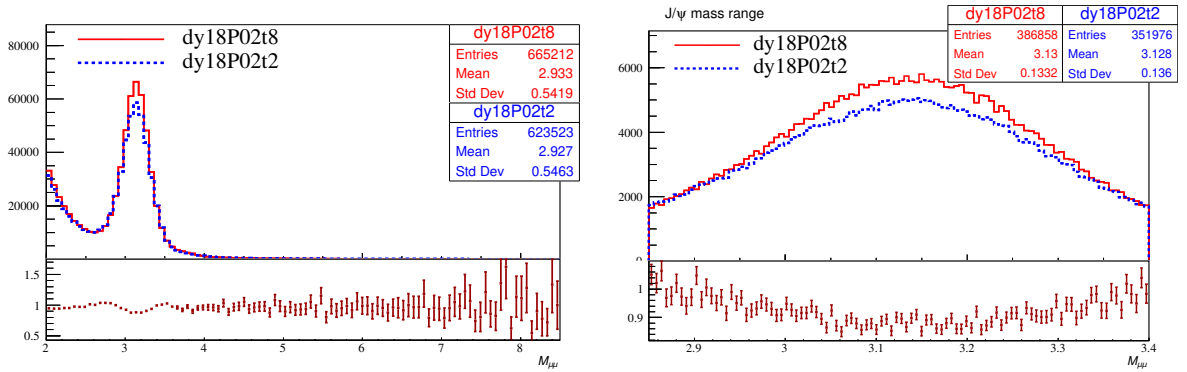


Figure 5.13: Dimuon invariant mass distribution between two data productions.

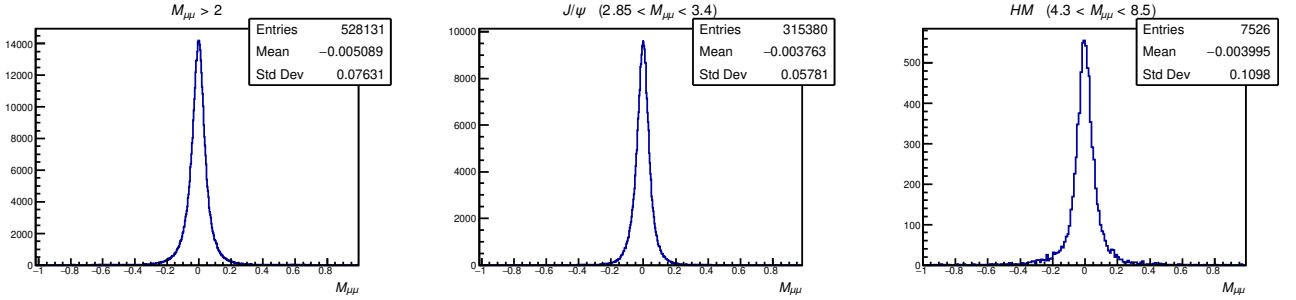


Figure 5.14: Distributions of invariant dimuon mass differences for events that are in common between the two data productions are shown for three mass ranges.

The characteristics of primary vertices have been also affected by the reconstruction changes (Figs. 5.15, 5.16). As it is shown in Fig. 5.17, going from one production to the other, the Z -coordinate of the primary vertex for same events can change by more than 10 cm.

³Events with the same time-stamp encoded in the so-called unique event numbers defined in the PHAST program.

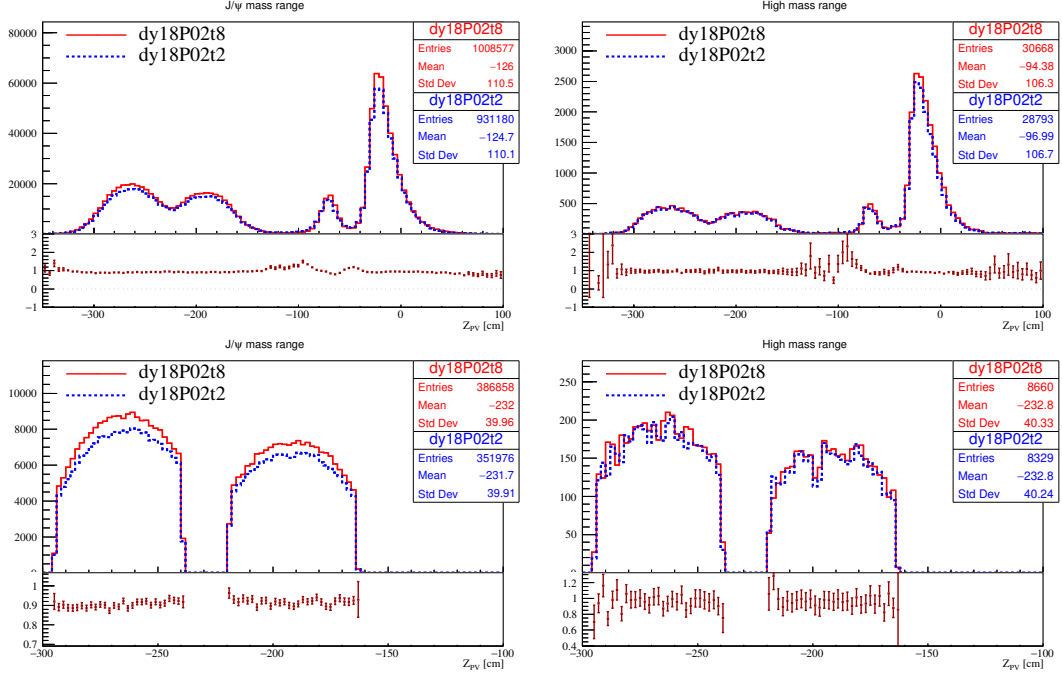


Figure 5.15: Primary vertex Z -coordinate distributions and their ratio for the two productions in one period (P02): J/ψ mass range is on the left, HM range is on the right. Same distributions for the NH_3 cells data are shown in the bottom panels.

The main kinematic variables x_π , x_N , x_F , q_T , the characteristics of reconstructed muon tracks in the laboratory rest frame (*e.g.* the momentum and laboratory polar and azimuthal angles), as well as physics angles⁴ φ_S , φ_{CS} , θ_{CS} have been also compared between the two productions (some examples are shown in Figs. 5.18-5.23).

Additionally the distributions of the events that were not in common (the so-called “extra” reconstructed events in one or the other production) between the final samples obtained with two productions were also studied. As an example the dimuon invariant mass $M_{\mu\mu}$ distributions for common and uncommon events are shown in Figs. 5.24. The aforementioned data reconstruction changes and improvements in the t8-production of 2018 have triggered a new re-production campaign for 2015 data, which has been labeled as “slot2” (s2). The same reconstruction updates and options as for t8 have been applied to get a consistency in the processing of the data from both years. One of the monitoring tools to watch the production changes is the position and the resolution of the J/ψ -peak in different periods. The J/ψ characteristics

⁴The *physics angles* are those which enter in the definitions of angular modulations in the differential cross section (2.39)

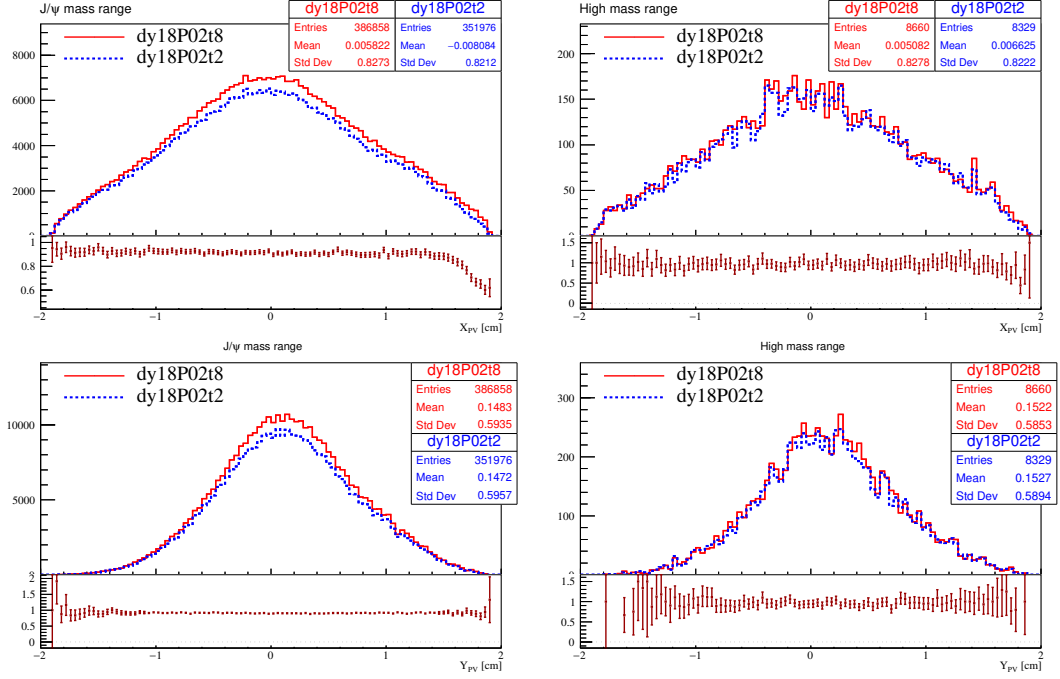


Figure 5.16: Distributions for X and Y coordinates of the primary vertex and their ratio for two productions in one period (P02). Results for J/ψ mass range are on the left, HM range is on the right. Same distributions for the NH₃ cells data are shown in the bottom panels

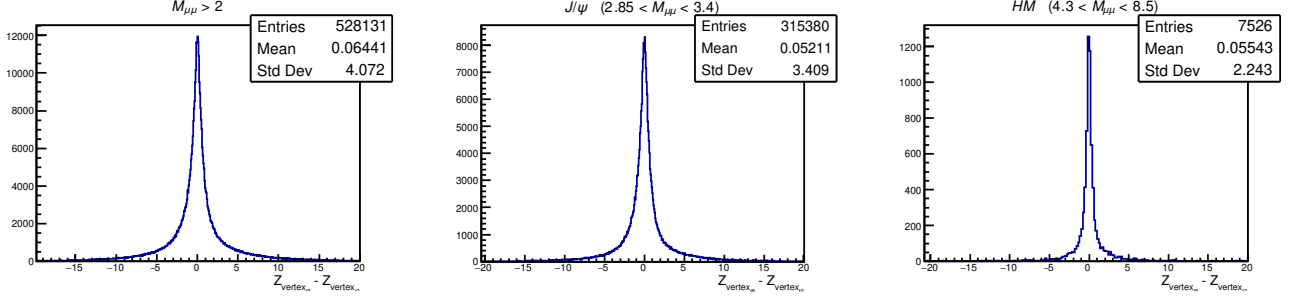


Figure 5.17: Distributions of the difference of the primary vertex Z-coordinate for events that are in common between the two data productions.

must remain constant and potential variations would reflect certain changes in the data-taking conditions during the run, or some mistakes introduced in the reconstruction stage (misalignment, incorrect calibrations, erroneous magnetic field maps, etc.). The results of this check are shown in Fig. 5.25. The values presented in Fig. 5.25 are an output of a fit to the data using the following function:

$$f(x|p_0, p_1, p_2, p_3, p_4) = p_0 \exp\left(-\frac{1}{2} \frac{(x - p_1)^2}{p_2^2}\right) + p_3 x^{p_4}, \quad (5.1)$$

where the mean (p_1) and width (p_2) of the Gaussian give the position and the resolution of the

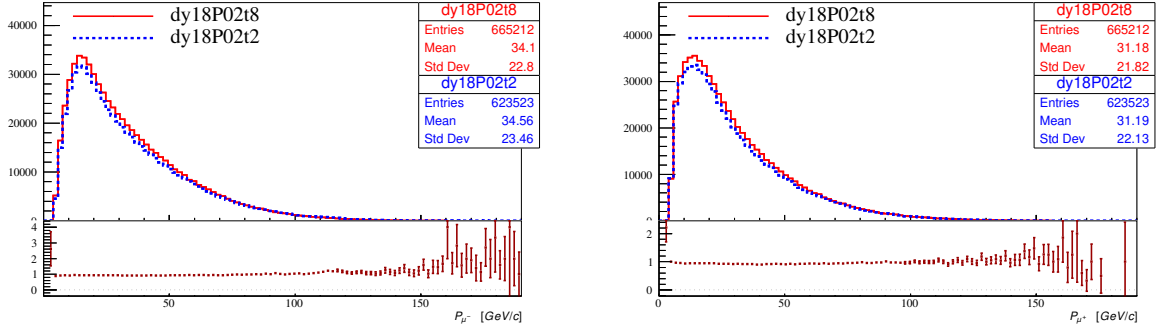


Figure 5.18: Muon momenta distributions in the laboratory frame and their ratio two productions in one period (P02). Muons on the left, anti-muon on the right.

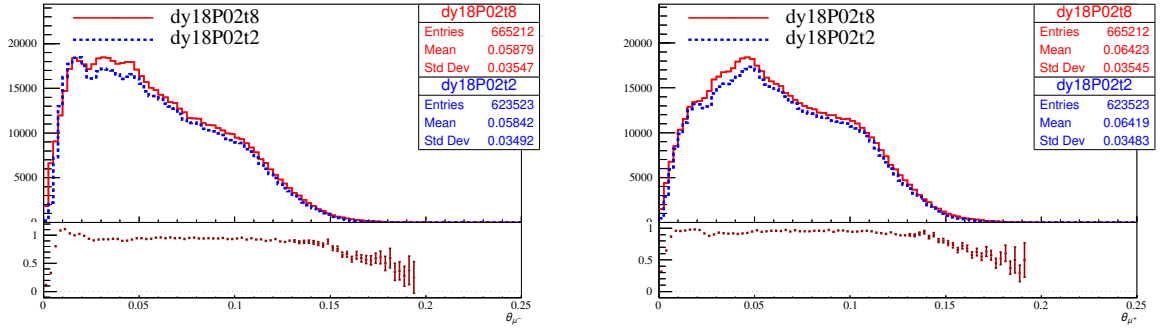


Figure 5.19: Muon polar angle distributions in the laboratory frame and their ratio for two productions in one period (P02). Muons on the left, anti-muons on the right.

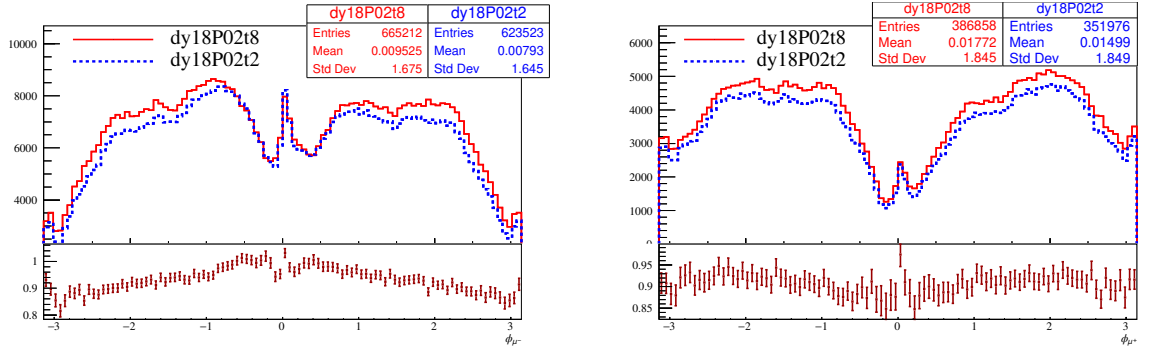


Figure 5.20: Muon azimuthal angle distributions in the laboratory frame for two productions in one period (P02). Muons on the left, anti-muons on the right.

J/ψ peak, respectively. It has to be noted, that it is a simplified approach and an appropriate fit function would also take into account the contribution of ψ' meson (*e.g.* as a second Gaussian). However, here the fit is used for monitoring purposes only, since the main interest is to check the relative changes between different periods, and adopted simple functional form (5.2.4) converges

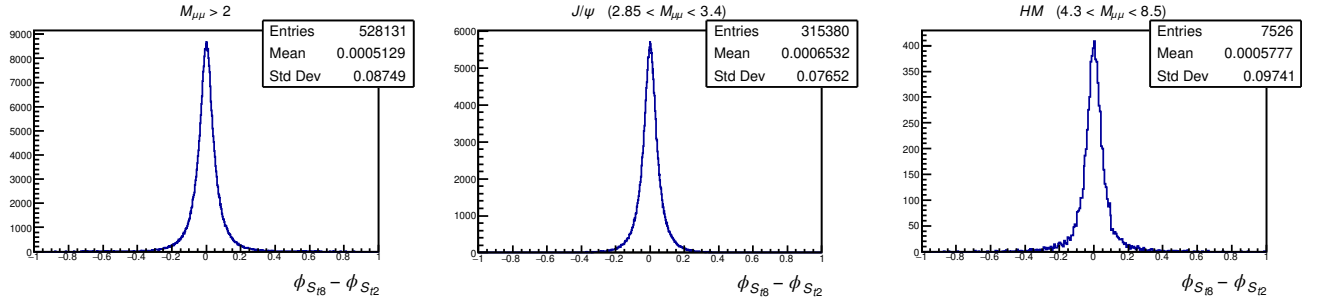


Figure 5.21: Distributions of ϕ_S differences for events that are in common between the two data productions are shown for three mass ranges.

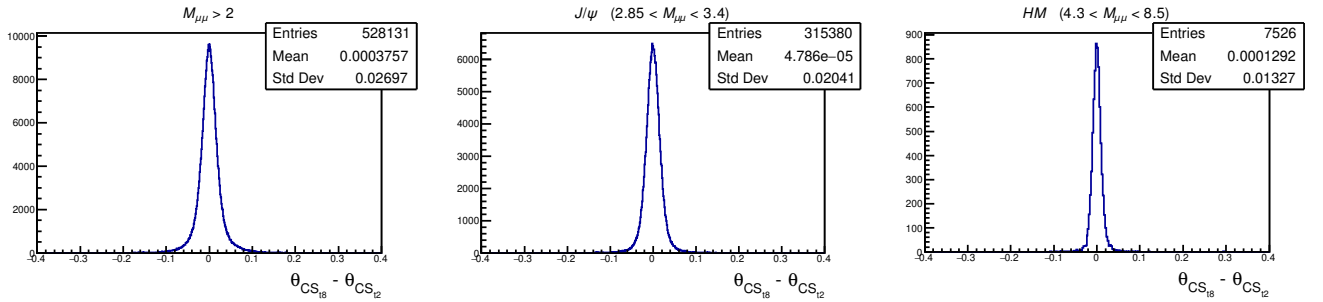


Figure 5.22: Distributions of θ_{CS} differences for events that are in common between the two data productions are shown for three mass ranges.

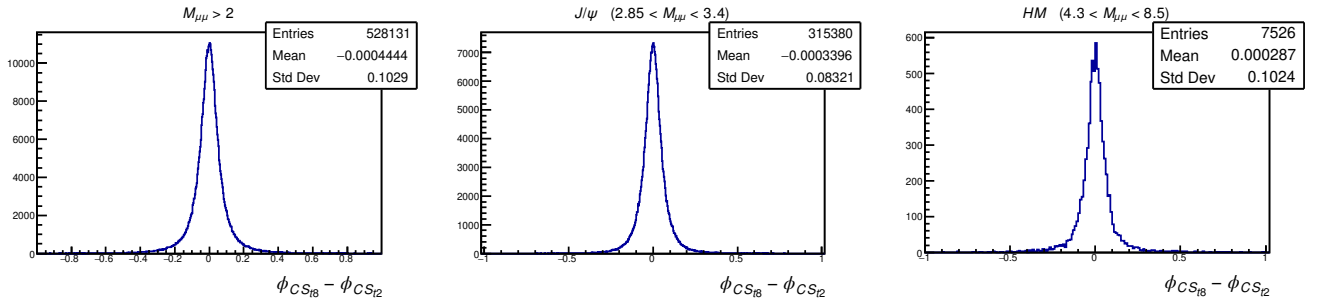


Figure 5.23: Distributions of ϕ_{CS} differences for events that are in common between the two data productions are shown for three mass ranges.

well using the same initial settings when fitting different samples. The fits have been done for periods (*e.g.* Fig. 5.27), sub-periods (Fig. 5.25) and runs (*e.g.* Fig. 5.26) for both years and different productions.

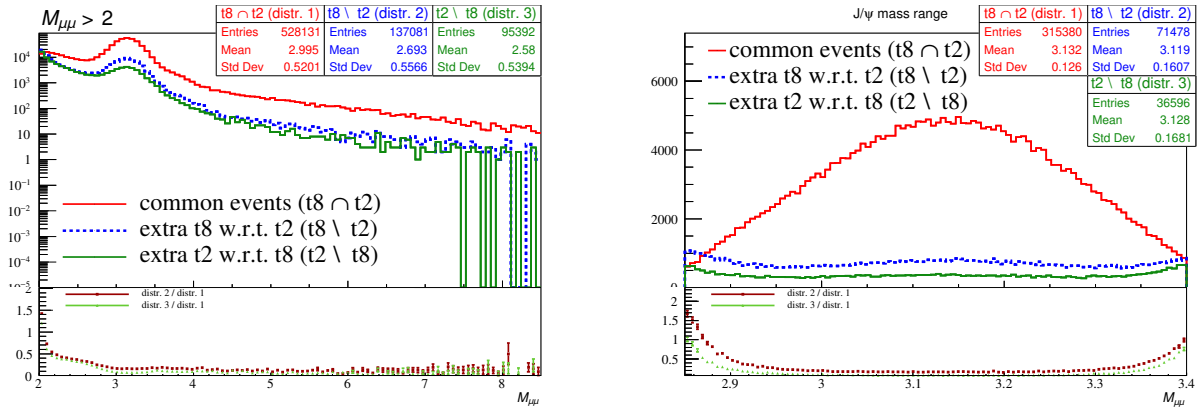


Figure 5.24: Dimuon invariant mass distributions for common and uncommon events from two productions in one period (P02).

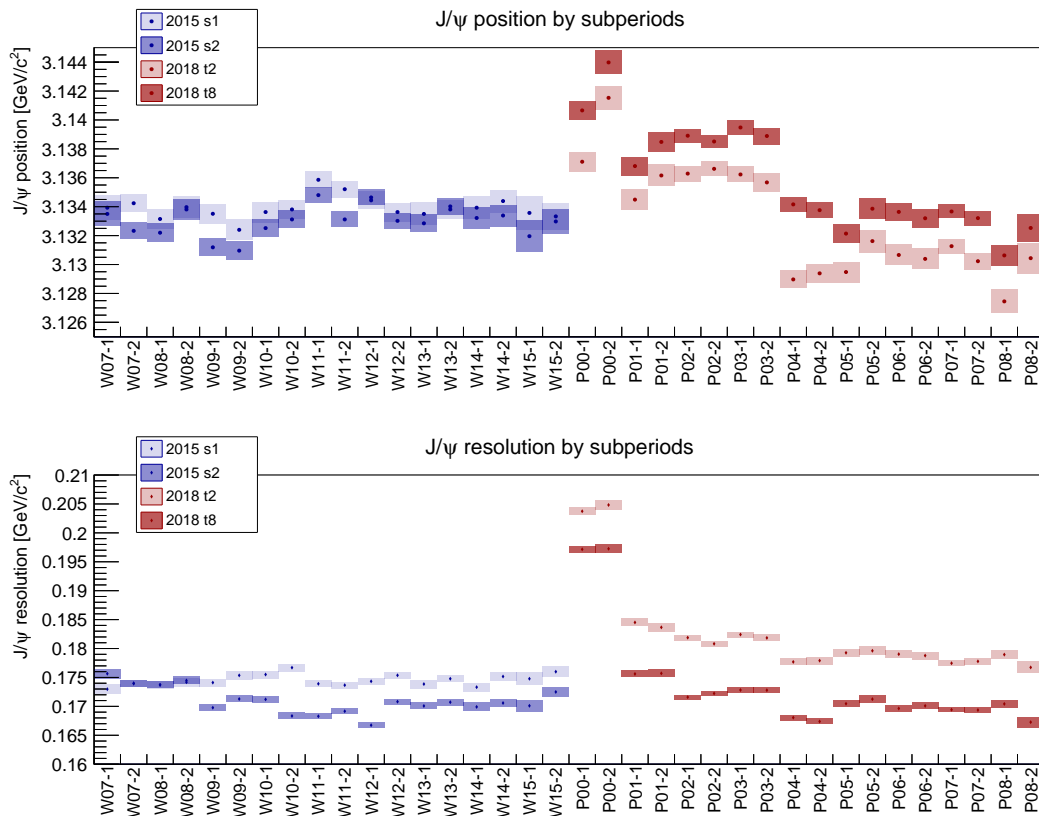


Figure 5.25: Position (top plot) and resolution (bottom plot) of the J/ψ by sub-periods.

5.2. ANALYSIS OF TRANSVERSE SPIN ASYMMETRIES

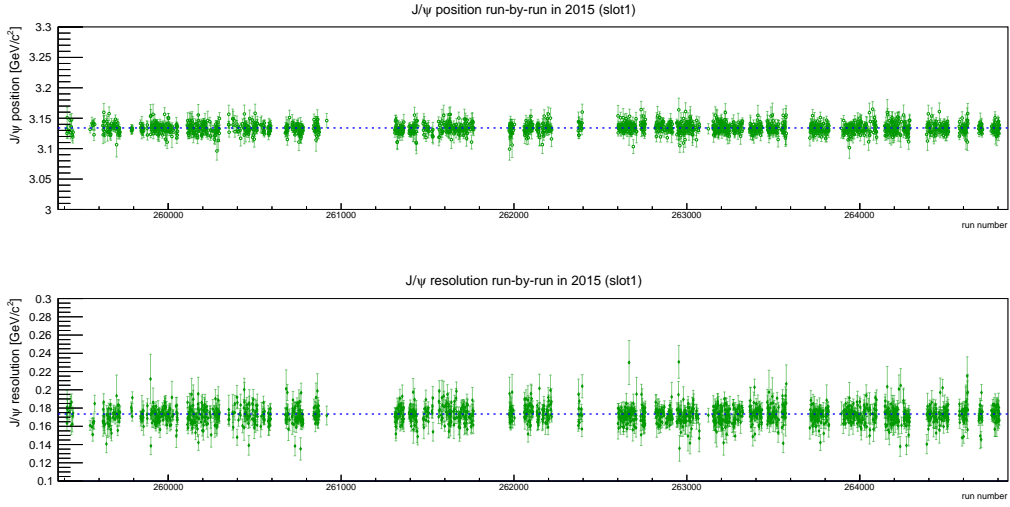


Figure 5.26: Position (top plot) and resolution (bottom plot) of the J/ψ by runs in 2015 from slot1 production.

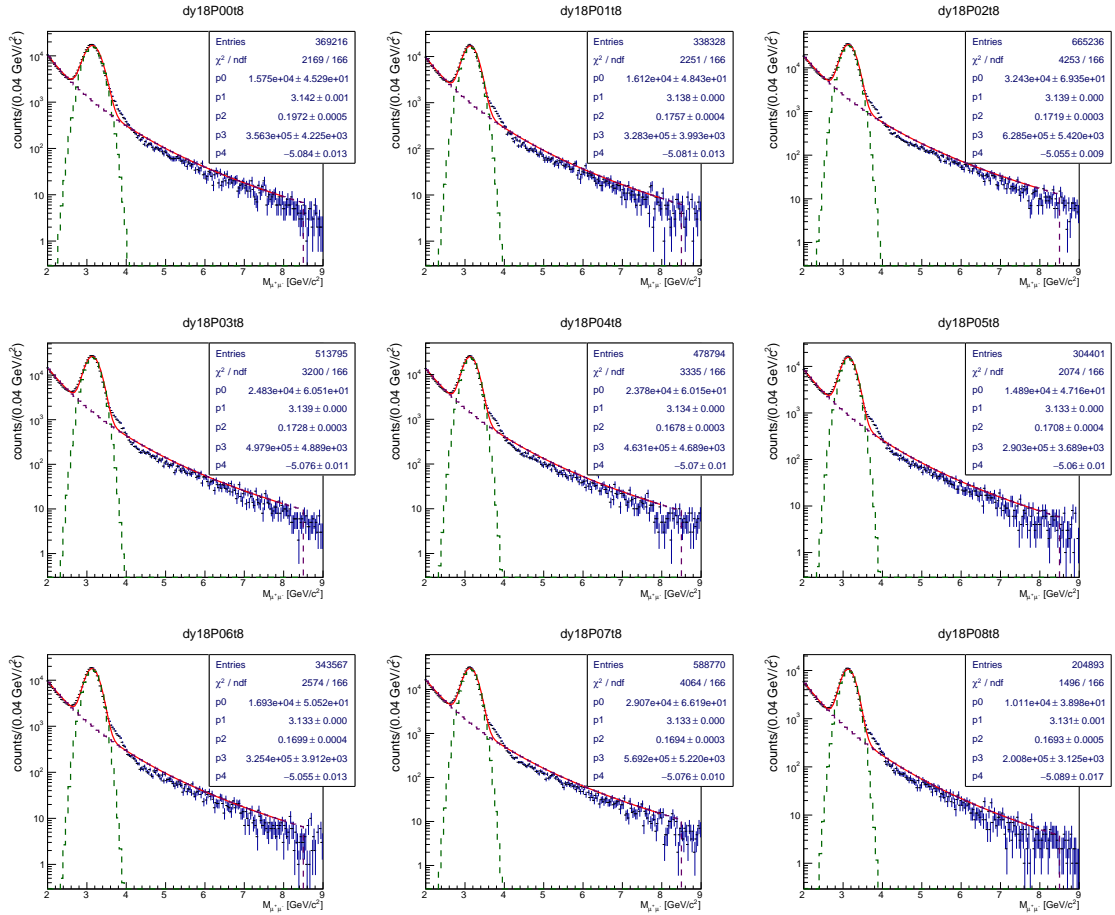


Figure 5.27: An example of J/ψ -peak fit by periods (2018 t8-production data).

5.2.5 Monte-Carlo studies: resolutions, target event mixing

Experimental resolutions of different kinematic and angular variables were estimated based on the results of dedicated MC simulations. The summary on resolutions is given in Tab. 5.7. Two columns represent results obtained with two different estimators. First is the RMS of the residuals⁵ while the second is obtained from the two-Gaussian fit (leading signal + tails) and corresponds to the σ of the leading Gaussian distribution. The latter estimate doesn't take into account the tails of the residual-distribution and thus gives an optimistic estimate, while the former one is sensitive to the selected range of the residual-distribution. In Fig. 5.28, the q_T dependences of φ_{CS} and φ_S angular resolutions, evaluated using the RMS estimator, are presented.

Variable	RMS	leading gaussian σ
Xv (cm)	0.04039	0.0279
Yv (cm)	0.03823	0.02396
Zv (cm)	10.97	8.22
$M_{\mu\mu}$ (GeV/c ²)	0.19068	0.18146
x_N	0.01863	0.01104
x_π	0.01314	0.00896
x_F	0.01951	0.0139163
q_T (GeV/c)	0.1487	0.1070
φ_S (rad)	0.19333	0.09005
φ_{CS} (rad)	0.19756	0.09461
θ_{CS} (rad)	0.0263969	0.01719

Table 5.7: Resolutions for main kinematic and angular variables.

The contribution of Drell–Yan and other channels into the dimuon mass range of interest was estimated in a dedicated study. Apart from the dimuons produced in Drell–Yan process, one has to consider the following contributions: the combinatorial background (CB) produced by uncorrelated pion and kaon decays; the open charm background (OC) originated from D meson decays; Charmonia (J/ψ' and ψ') decays. Contribution of different channels is illustrated in Fig. 5.29.

⁵the difference between the generated value and the reconstructed one evaluated event-by-event

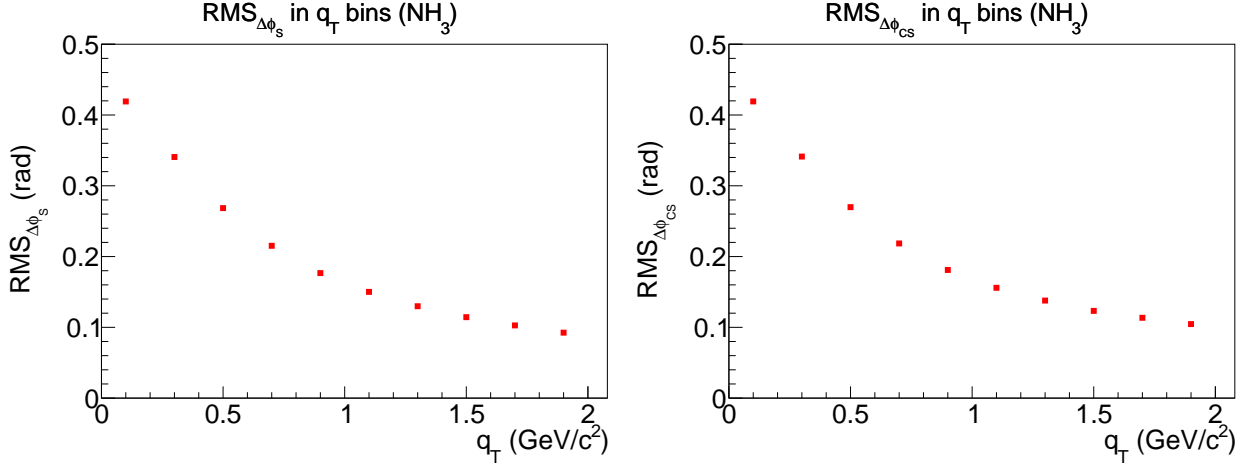


Figure 5.28: q_T dependence of the ϕ_S (left) and ϕ_{CS} (right) angular resolutions.

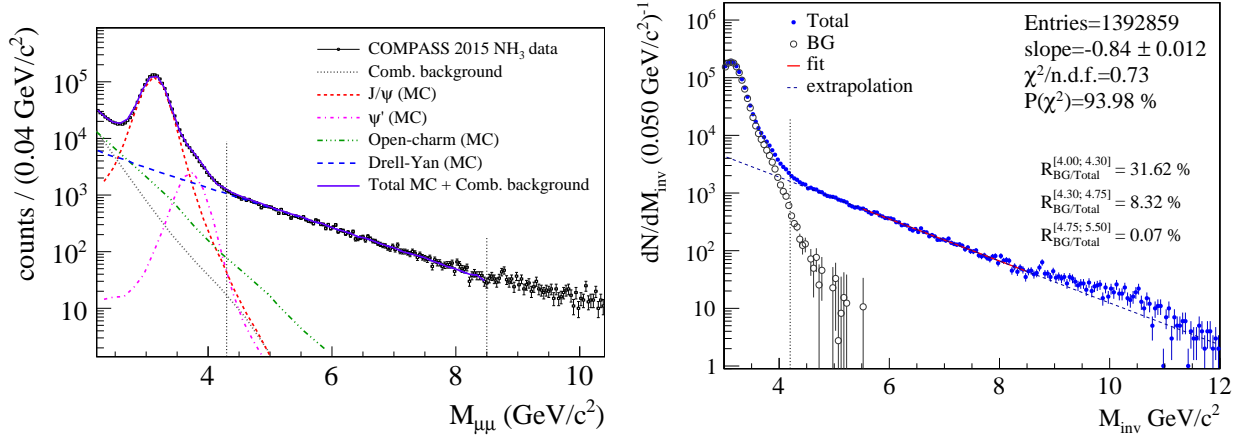


Figure 5.29: Left panel: decomposition of the dimuon mass spectrum using CB estimated from real data like-sign pairs, and physics contributions evaluated by MC. Right panel: independent estimation of the background fraction in the HM range.

The combinatorial background contribution is estimated using the collected events with like-sign pairs as:

$$N_{\mu+\mu-} = 2\sqrt{N_{\mu-\mu-}N_{\mu+\mu+}}. \quad (5.2)$$

This approach is only valid if the spectrometer is charge-symmetric, which is ensured by applying the so-called “image cut”. Each muon pair is accepted if both muons would still be in the acceptance of trigger hodoscopes if their charge-signs were flipped to opposite. Apart from the CB-contribution estimated from the real data, the overall description of the opposite sign dimuon mass distribution in Fig. 5.29 includes also MC components corresponding to DY, J/ψ , ψ' and OC channels. Events corresponding to these four different processes are generated in-

independently using PYTHIA simulation program and then passed to TGEANT to simulate the spectrometer response. Obtained output is passed then to the reconstruction software CORAL and analyzed in PHAST following the same approach as for the real data. Dimuon pairs from each of the channels are filled into separate histograms and a simultaneous fit is performed using all five components; CB is fixed, DY component is fixed based on a pre-fit to the data in the higher mass region, the normalizations of the other three components are determined by the set of free parameters of the fit. The data is reasonably described by the estimated CB and five MC samples. The DY process dominates for high masses. For the TSA analysis the mass region from 4.3 to 8.5 GeV/ c^2 was selected, in order to have a background contamination level below 5%. The background is mainly concentrated in the lower masses, from 4.3 to 5.0 GeV/ c^2 as it can be seen from the plot shown in the right panel in Fig. 5.29. This is an independent exercise, based exclusively on data and assuming that the region from 5.5 to 8.5 GeV/ c^2 contains only DY events. This region is fitted with an exponential, which is then extrapolated to lower masses. Black histogram illustrates the overall background distribution obtained after subtraction of the DY exponent from the dimuon mass distribution, which is then used to define the background fraction in the range of interest. A global level of the background is below 5% in the selected mass region. In the first mass bin of TSA analysis (4.3-4.75 GeV/ c^2) it is $\sim 32\%$, while already in the second bin (4.75-5.50 GeV/ c^2) it is negligible, $\sim 0.1\%$.

An MC-study was carried out to estimate the event migration from one NH₃ cell to the other and from the surrounding unpolarized material to each of the cells. This migration and mixing of events was taken into account as an additional dilution effect (see Sec. 5.2.7) in TSA analysis. The estimated composition of the events reconstructed in the NH₃ cells is presented in Tab. 5.8 and illustrated in Fig. 5.30. In Fig. 5.30 the target event mixing in different kinematic bins is shown for HM and J/ψ peak ranges. One can see that due to different acceptance conditions and *e.g.* Z -vertex resolution, the mixing slightly changes from one kinematic bin to another.

5.2.6 Target polarization

During 2015 and 2018 Drell-Yan data taking solid ammonia bids were used as a polarized proton target material. The material was enclosed in two 55 cm long target cells with 4 cm diameter. The cells separated by 20 cm gap were installed along the beamline inside COMPASS dilution refrigerator and were polarized with opposite orientations, perpendicular to the beam

Events generated in	%	Events generated in	%
1 st cell	94.94	2 nd cell	92.92
LHe gap	1.57	LHe gap	3.88
LHe upstream the cell	2.37	LHe downstream the cell	0.60
2 nd cell	0.15	1 st cell	1.49
Other materials (R < 2)	0.29	Other materials (R < 2)	0.26
Other materials (R > 2)	0.69	Other materials (R > 2)	0.85

Table 5.8: Composition of the events reconstructed in the polarized target cells.

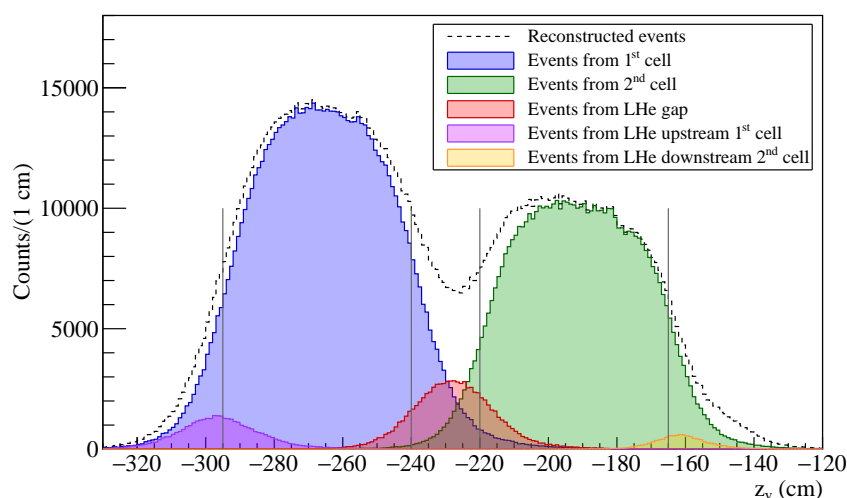
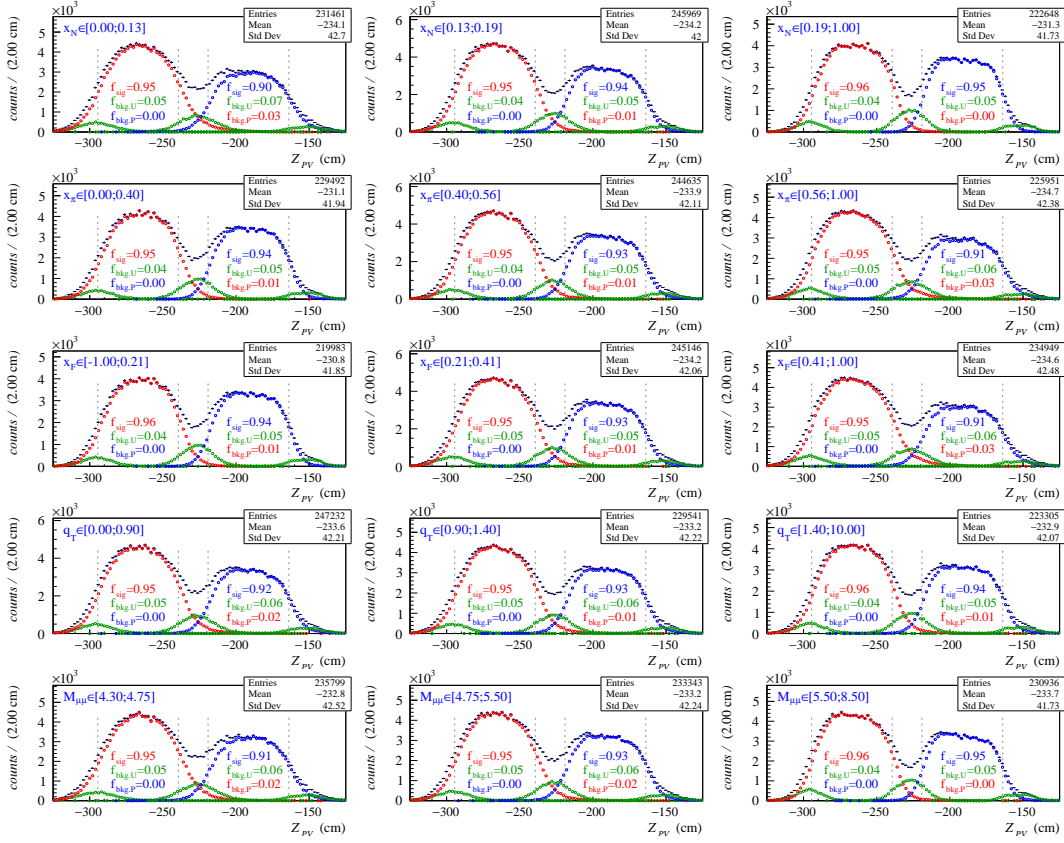


Figure 5.30: Z-vertex distribution of the events originating from different materials in the NH₃ target region.

direction. Five Nuclear Magnetic Resonance (NMR) coils made of stainless steel were installed in each cell: 3 outer coils were fixed on the outside surface of the cell, while 2 inner ones were placed on the beam spot, inside the cell. The NMR coils measured the proton polarization of the target material around them.

The polarization was measured to be non-uniform and changing along the length of both cells. This can be explained by several factors such as: a heat generated by the beam and secondary particles crossing the material, a change of optimum microwave frequency for DNP (Dynamic Nuclear Polarization), the non-uniformity of the ³He supply, the tuning of the trim coils, etc. The difference in polarization values measured by different coils of the same target cell in previous COMPASS runs was less than few percent, while for the DY run it was ranging

4.3 < $M_{\mu\mu}/(\text{GeV}/c^2)$ < 8.5: (2018-t2 MC)



3.0 < $M_{\mu\mu}/(\text{GeV}/c^2)$ < 3.25: (2018-t8 MC)

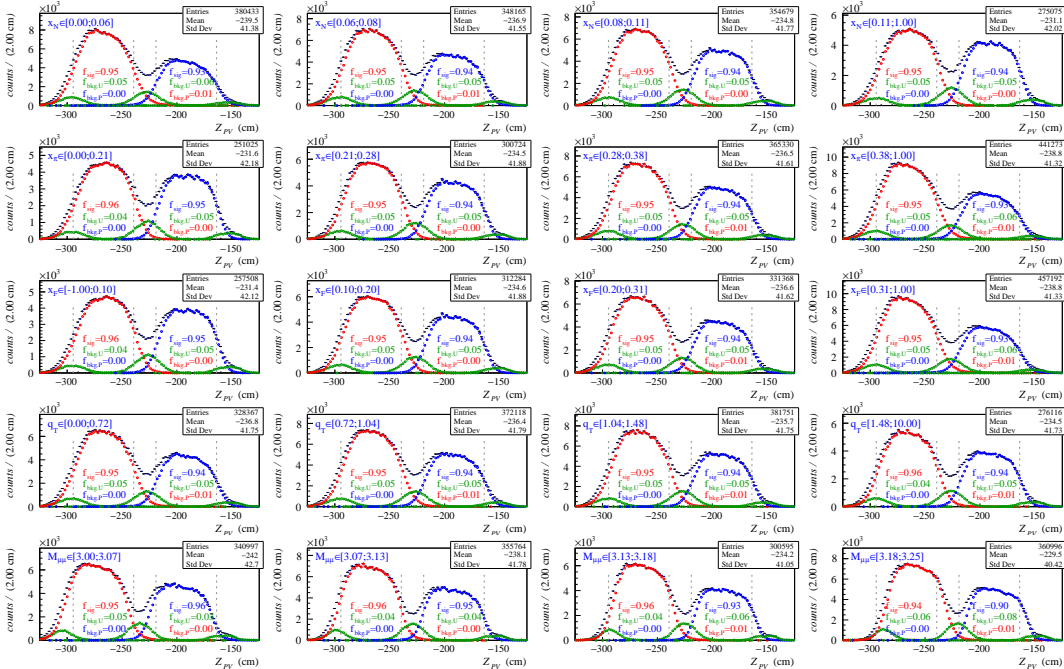


Figure 5.31: NH_3 Z-vertex distribution of the events originating from upstream and downstream cells and unpolarized medium in different kinematic bins in high mass (top panel) and J/ψ (bottom panel) regions. The plots are based on MC simulations done with 2018(t2) configuration.

between 4 to 13%. In order to minimize aforementioned effects, the polarization was evaluated as a function of Z -coordinate.

Note that the polarization could not be measured during the physics data-taking with dipole magnetic field on, but only when the target was being polarized in a longitudinal magnetic field with a PT magnet in a solenoid mode. This is because the PT system was optimized for a precise longitudinal polarization measurement in a very homogeneous solenoid magnetic field at 2.5 T. The polarization values during each period were interpolated with an exponential decrease formula: $P(t) = P_0 \exp(-t/\tau) + P_{TE}$, where τ (the relaxation time) characterises the rate of polarization loss and P_{TE} is the polarization at thermal equilibrium. The polarization measured before and after each period was used for the interpolation. The relaxation time as well as the polarization varied from coil to coil because of inhomogeneity of the dipole magnetic field and all aforementioned reasons.

In Fig. 5.32 the polarization values across the 2018 run are shown. In 2018 the average upstream cell polarization was around 75.5% or -69.8%, while the average downstream cell polarization was around -68.4% and 72.4%, which is slightly below the average values of 2015, as can be seen in Fig. 5.33. The normalization uncertainties associated to the the target polarization systematics are estimated to be of 5%.

5.2.7 Dilution factor

The dilution factor accounts for the fraction of polarizable material inside the target volume. It depends on the composition of the target and on the physics process:

$$f = \frac{n_H \sigma_{\pi-H}^{DY}}{n_H \sigma_{\pi-H}^{DY} + \sum_A n_A \sigma_{\pi-A}^{DY}}. \quad (5.3)$$

where n_H , n_A represent the amount of polarizable protons and nuclei in the target⁶ and σ^{DY} is the pion-induced Drell-Yan cross-section. The latter has been determined from a parton-level Monte-Carlo program, MCFM [206], performing calculations up to NNLO. Nuclear effects are taken into account via PDF correcting factors extracted by EKS group [207].

The evaluation of the dilution factor for J/ψ production is more elaborate. On the partonic level, J/ψ is produced via the gluon-gluon fusion, quark-antiquark annihilation, and to

⁶the polarizable material is only the hydrogen (H_3), while non-polarizable material is represented by helium-4 and nitrogen-14. Minor presence of helium-3, deuteron and nitrogen-15 is neglected

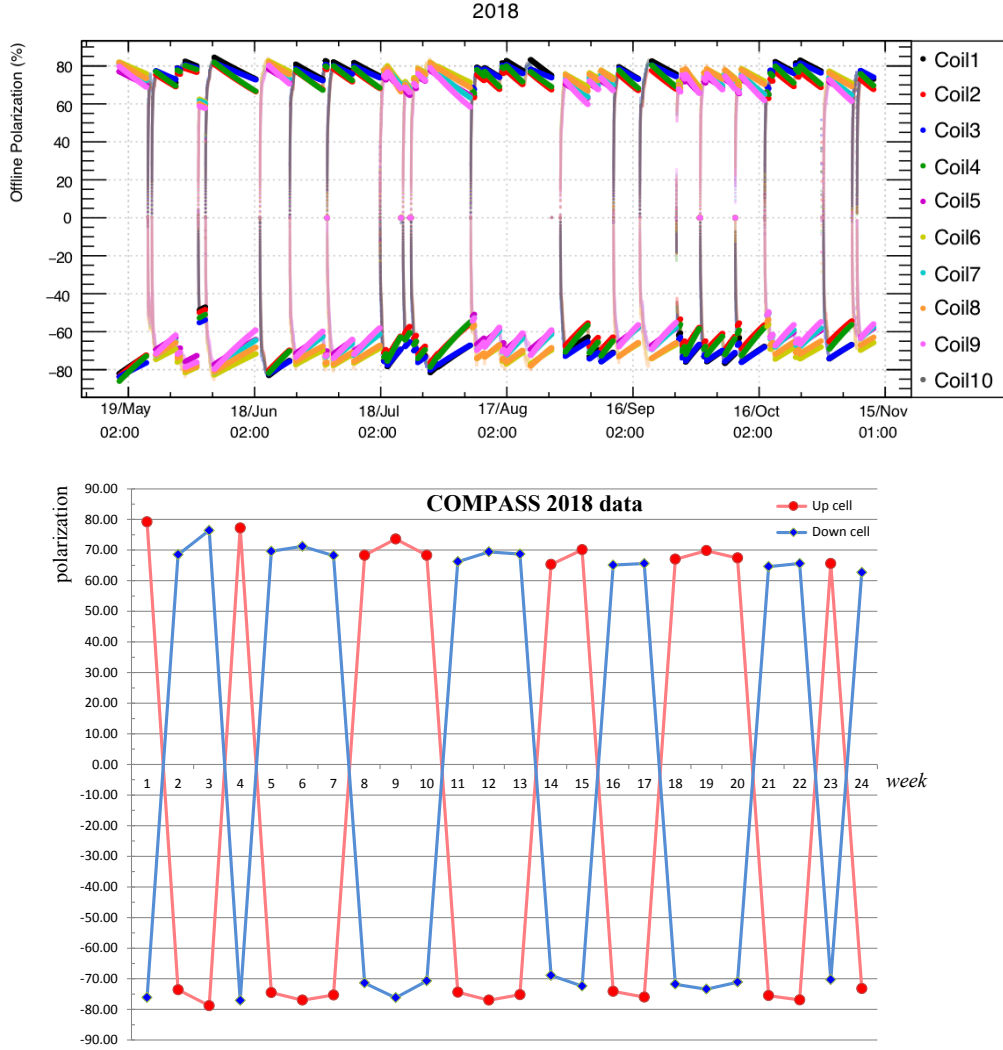


Figure 5.32: Average polarization values along the time (top - coil by coil, bottom -integrated).

a minor extent via quark-gluon processes. Thus, taking into account nuclear PDFs, results in nontrivial dependencies of the dilution factor for differential cross-sections. The next ingredient to determine the dilution factor is the J/ψ production mechanism, which currently remains poorly understood. The estimate of the dilution factor used in this analysis is based on the cross sections obtained in the framework of the non-relativistic QCD model (NRQCD) [165]. The PDF sets used are the GRVPI1 for pion and nCTEQ15 [208] for proton and nitrogen (the ammonia+He target mix is approximated to just nitrogen in this calculation).

The cell-to-cell and material-to-cell event migrations discussed in Sec. 5.2.5 are accounted as additional suppression factors, which were defined for each kinematic bin (summarized in Tab. 5.9). Fig. 5.34 shows the dilution factor as a function of kinematic variables. The normal-

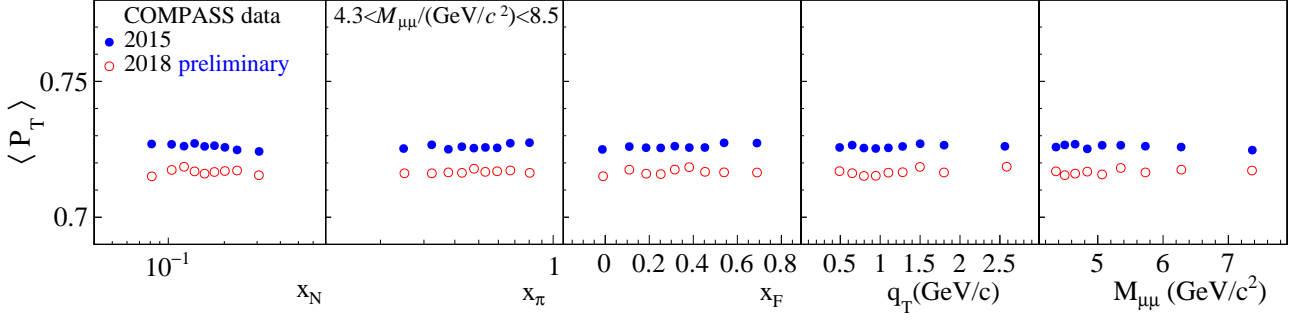


Figure 5.33: Target polarization in 2015 and 2018 as a function of kinematic variables.

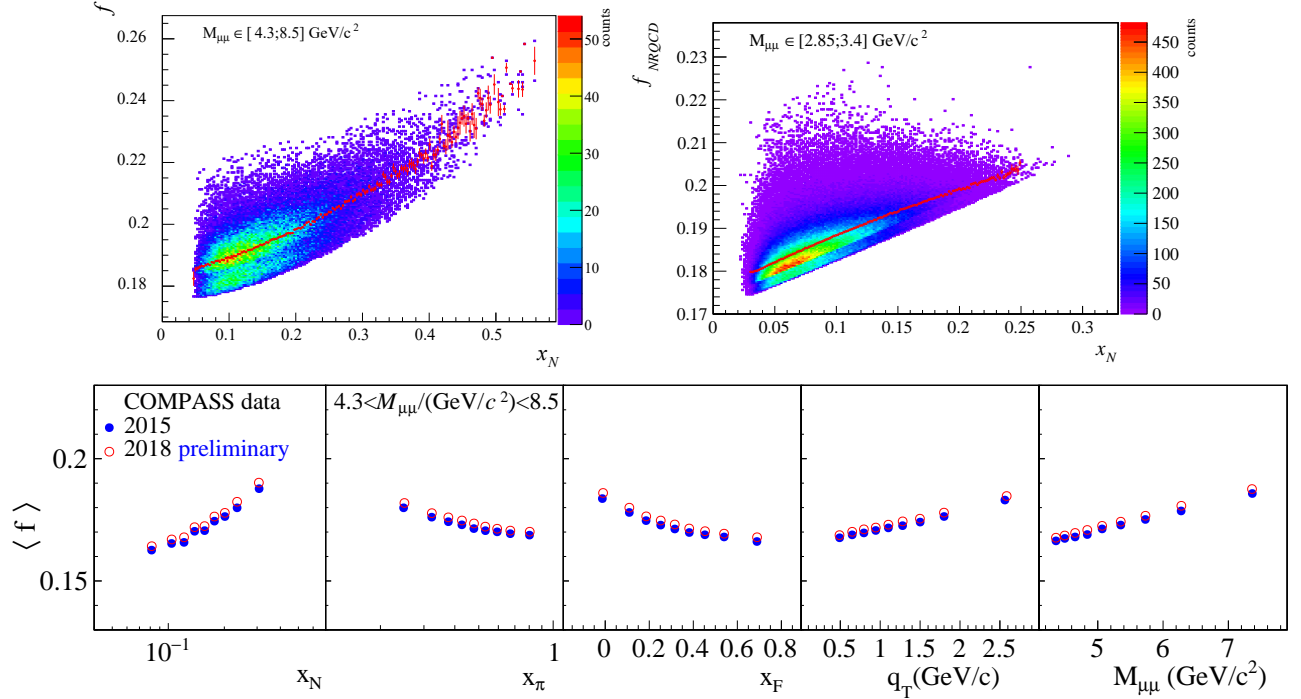


Figure 5.34: Dilution factor calculated for COMPASS dimuon pairs. Top plots: DY dilution factor in HM range x_N (left) and dilution factor for J/ψ production versus x_N (right). Two different subsamples corresponding to the target cells are visible. Bottom plot: Average Drell-Yan dilution factor in 2015 and 2018 as a function of kinematic variables. Target compositions in 2015 and 2018 were slightly different, which causes small differences at the level of the dilution factor.

ization uncertainties originating from the uncertainties on dilution factor are estimated to be of 5%.

variable	bin range	additional mixing factors	
		upstream cell	downstream cell
x_N	0.00, 0.13	0.95	0.89
	0.13, 0.19	0.95	0.94
	0.19, 1.00	0.96	0.96
x_π	0.00, 0.40	0.95	0.94
	0.40, 0.56	0.95	0.93
	0.56, 1.00	0.96	0.91
x_F	-1.0, 0.21	0.95	0.95
	0.21, 0.41	0.96	0.94
	0.41, 1.00	0.95	0.90
q_T	0.50, 0.90	0.95	0.92
	0.90, 1.40	0.96	0.93
	1.40, 5.00	0.95	0.94
$M_{\mu\mu}$	4.30, 4.75	0.95	0.91
	4.75, 5.50	0.96	0.93
	5.50, 8.50	0.95	0.95

Table 5.9: Additional dilution factors due to cell-to-cell event migration in each kinematic bin.

5.2.8 Depolarization factors

In Fig 5.35 the depolarization factors introduced in Chapter 2 are shown as extracted from the data. The impact of different “ λ -value” hypotheses ($\lambda = 1.0, 0.8, 0.5$) is shown for HM case. Maximal deviation is at the level of 10%, while in the bins selected for the analysis it is about 5%.

For J/ψ production the situation is more complicated, since λ is not necessarily close to 1 in that case. Due to this reason, a dedicated preliminary extraction of λ was done and the value has been estimated to be about 0.2, which was put in the J/ψ TSA analysis.

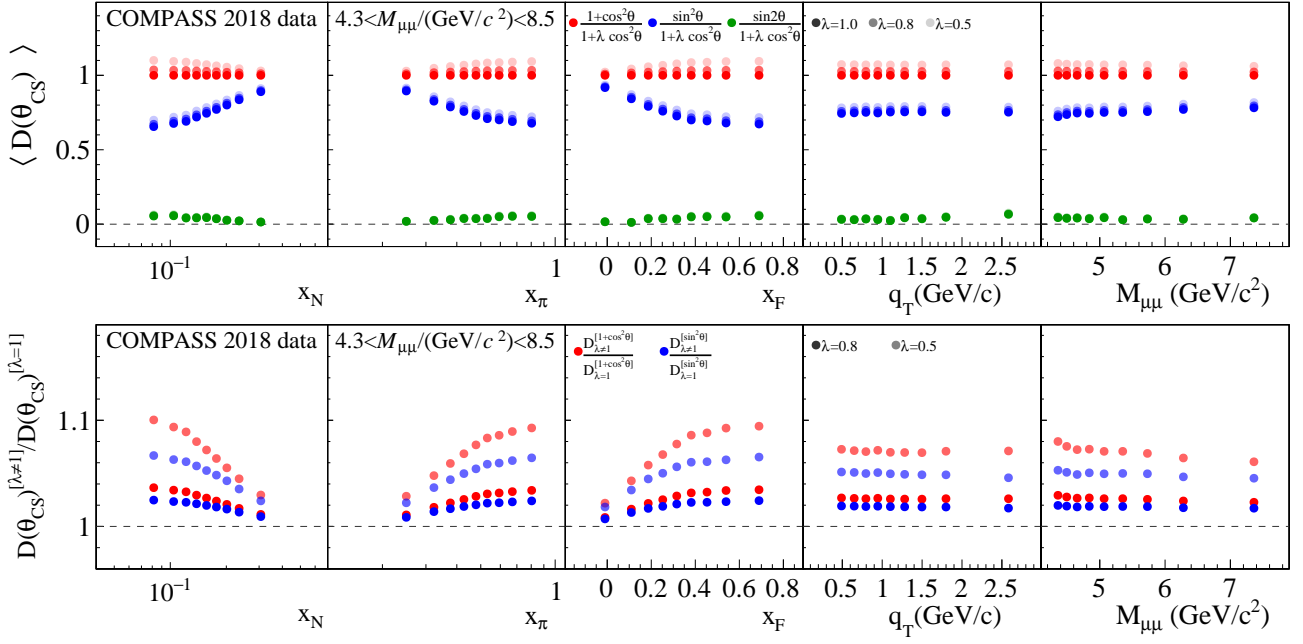


Figure 5.35: Depolarization factors shown as function of kinematic variables. Top plot: impact of different “ λ -value” hypotheses ($\lambda = 1.0, 0.8, 0.5$) is shown. Bottom plot: relative impact of different “ λ -value” hypotheses w.r.t. to the case $\lambda = 1.0$.

5.3 One-dimensional double ratio

First transverse asymmetry extraction approach to be discussed, is the so-called Double Ratio method, which was one of the first estimators used in the deuteron SIDIS TSA analyses at COMPASS [71, 72]. During transverse-deuteron data taking in 2002-2004 COMPASS used a similar double-cell configuration of the target as for the Drell-Yan case. In this configuration the two target cells are being polarized in opposite directions and the polarization of both cells is being reversed approximately once per week. Within such an approach, the experiment collects data with both polarization states simultaneously. The data taking is sub-divided into periods. Each of the periods consists of two balanced (usually a week long) subsequent sub-periods separated by a target field reversal, so that the data in the first and second halves of a period are collected with opposite target-cell-polarization configurations. Within such an approach, the experiment collects data with both polarization states simultaneously and spectrometer acceptance variations within a given sub-period affect the events originating from both cells (and thus polarization states) nearly equally. It is then reasonable to assume that, in each angular bin the acceptance ratios for the target cells after polarization reversal (second sub-

period) are equal to those before (first sub-period) [71, 72], which can be expressed via the equality:

$$\frac{a_u^\uparrow(\varphi_i)}{a_d^\downarrow(\varphi_i)} = \frac{a_u^\downarrow(\varphi_i)}{a_d^\uparrow(\varphi_i)} \quad (5.4)$$

where $\uparrow\downarrow$ indicates up(down) target polarization, the u(d) subscript indicates the upstream (downstream) target cell, $a_{u/d}^{\uparrow\downarrow}(\varphi_i)$ is the φ_i dependent acceptance for the corresponding cell and polarization state, with φ_i being the physics angle of interest⁷. Same kind of relation holds also for the beam fluxes in two cells.

For a given cell, polarization state and kinematic range, the number of events as a function of the azimuthal angle of interest φ_i can be described as follows:

$$N_{u/d}^{\uparrow\downarrow}(\varphi_i) = F_{u/d}^{\uparrow\downarrow} n_{u/d} a_{u/d}^{\uparrow\downarrow}(\varphi_i) \sigma (1 \pm A_i \sin(\varphi_i)). \quad (5.5)$$

Here σ stands for the unpolarized cross-section, $F_{u/d}^{\uparrow\downarrow}$ is the flux, $n_{u/d}$ is the target density for the given cell (u/d) and A_i is the amplitude of the physics modulation $\sin(\varphi_i)$. In Fig. 5.36 the distribution of φ_S angle in the first x_N bin is shown as extracted for u/d cells and $\uparrow\downarrow$ polarization states from one of the periods of 2015.

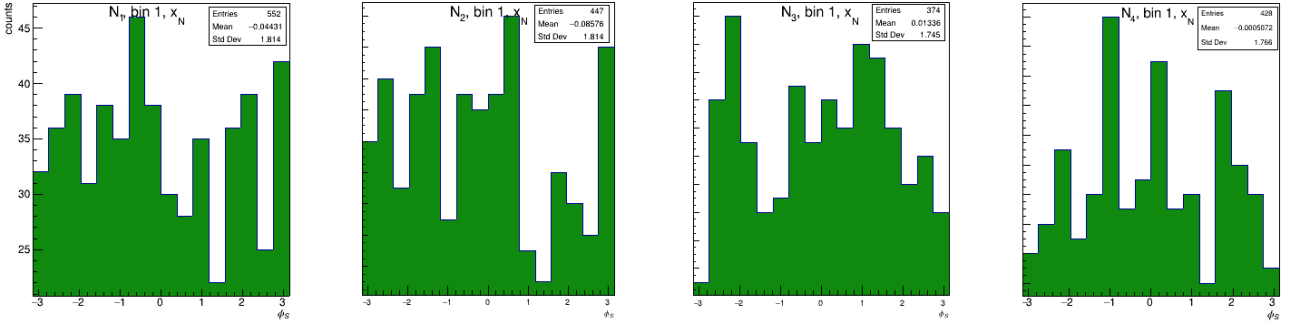


Figure 5.36: The φ_S distribution in the first x_N bin is shown as extracted for u/d cells and $\uparrow\downarrow$ polarization states (2015-P06 data, slot1 production).

The following Double Ratio (DR) can be formed for each period of the data taking and a given kinematic bin:

$$R(\varphi_i) = \frac{N_u^\uparrow(\varphi_i) N_d^\uparrow(\varphi_i)}{N_u^\downarrow(\varphi_i) N_d^\downarrow(\varphi_i)}. \quad (5.6)$$

The expectation value of the DR estimator is 1. This can be used to extract specific modulation amplitudes by applying Taylor expansion of $R(\varphi_i)$. Assuming that A_i is small and keeping

⁷ where φ_i is one of the physics angles: $\varphi_1 = \varphi_S - \text{Sivers angle}$, $\varphi_2 = 2\varphi_{CS} + \varphi_S - \text{pretzelosity angle}$, and $\varphi_3 = 2\varphi_{CS} - \varphi_S - \text{transversity angle}$

only leading terms, using Eqs. 5.4 and 5.5 one obtains:

$$R(\varphi_i) \approx \frac{F_u^\uparrow F_d^\uparrow}{F_u^\downarrow F_d^\downarrow} \cdot \frac{a_u^\uparrow(\varphi_i) a_d^\uparrow(\varphi_i)}{a_u^\downarrow(\varphi_i) a_d^\downarrow(\varphi_i)} \cdot (1 + 4A_i \sin(\varphi_i)) = C \cdot (1 + 4A_i \sin(\varphi_i)). \quad (5.7)$$

This expression can then be used as a fit-function to be applied to the binned in φ_i distribution of DR estimators $R(\varphi_i)$ (usually 16 bins are used), as shown in Fig. 5.37. Here the necessary assumption is that the ratio of fluxes and acceptances does not depend on φ_i , which is equivalent to an extension of the reasonable assumption from Eq. 5.4 to all φ_i bins. The respective uncertainty associated to the $R(\varphi_i)$ estimators is defined as follows:

$$\sigma_R(\varphi_i) = \sqrt{\frac{1}{N_u^\uparrow(\varphi_i)} + \frac{1}{N_d^\uparrow(\varphi_i)} + \frac{1}{N_u^\downarrow(\varphi_i)} + \frac{1}{N_d^\downarrow(\varphi_i)}}. \quad (5.8)$$

Extracted from the fit A_i parameters are the so-called *raw* asymmetries. In order to obtain physics asymmetries: $A_{UT}^{\sin(\varphi_S)}$, $A_{UT}^{\sin(2\varphi_{CS}+\varphi_S)}$, $A_{UT}^{\sin(2\varphi_{CS}-\varphi_S)}$ the corresponding raw asymmetry needs to be corrected for the target polarization, for the dilution factor and the depolarization factor.

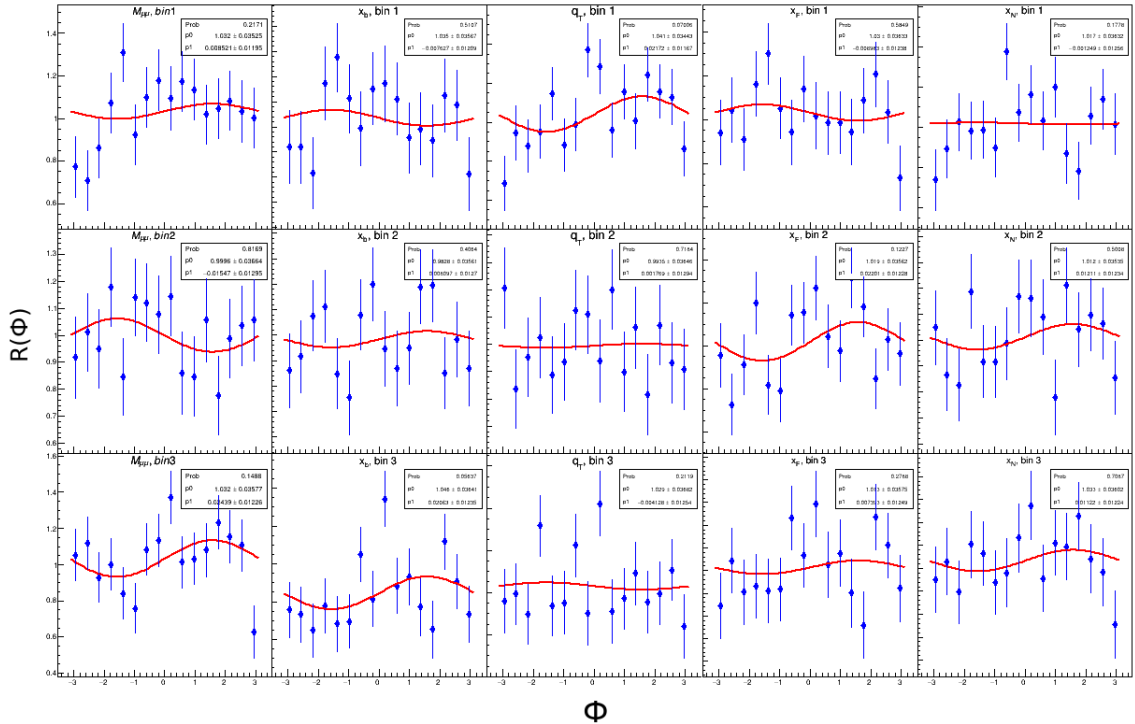


Figure 5.37: Results of 1DDR fit for Siverts asymmetry (based on HM 2015 data from all periods of slot1).

Since we only deal with single azimuthal angle dependence in (5.6), this double ratio is called one-dimensional (1D). In general, it is also possible to have more dimensions⁸, but in the DY case due to lack of statistics 2D methods are not feasible.

5.4 Extended Weighted Unbinned Maximum Likelihood

In the previous subsection the 1DDR method has been discussed. Another method used in this work is the Extended Weighted Unbinned Maximum Likelihood (EWUML), which is based on a classical Maximum Likelihood (ML) approach commonly used in particle physics. This method has been adopted for recent COMPASS SIDIS and Drell-Yan analyses [79, 84].

The starting point is the Probability Distribution Function (*PDF*)⁹ $p(\vec{x}, \vec{a})$, which describes the frequency of occurrence of a data point \vec{x} , via a vector of parameters \vec{a} . The normalization of the *PDF* is done by normalizing the integrated over the entire range probability density to a unity:

$$\int d^n p(\vec{x}, \vec{a}) = 1, \quad \forall \vec{a}. \quad (5.9)$$

The Extended Maximum Likelihood (EML) approach [210] differs from the standard ML method, through a revision of normalization condition, changing it from unity to \mathcal{N} , where the latter is the total number of events expected in the whole range of observation. The *PDF* is exchanged by the “extended probability distribution”:

$$P(\vec{x}, \vec{A}) = \mathcal{N}p(\vec{x}, \vec{a}), \quad (5.10)$$

where $\vec{A} = \{\mathcal{N}, \vec{a}\}$ is a new parameter set, which includes \mathcal{N} – total number of events. The normalization condition (5.9) then takes the form:

$$\int d^n x P(\vec{x}, \vec{A}) = \int d^n x \mathcal{N}p(\vec{x}, \vec{a}) = \mathcal{N} \int d^n x p(\vec{x}, \vec{a}) = \mathcal{N}. \quad (5.11)$$

Note that the usage of \mathcal{N} as a fit parameter has an advantage in two cases. Firstly, in the case where the actual number of events is not known. Secondly, such an approach also allows one to avoid performing the exact normalization of $p(x, a)$, which is helpful in case of DY-TSA extraction where the normalization depends on the acceptance study.

⁸E.g., 2D double ratio in SIDIS where angles ϕ_h, ϕ_S are taken into consideration [209].

⁹we use italic fonts in order to avoid confusion with Parton Distribution Functions (PDFs).

Adopting the “extended probability distribution” (5.10), the construction of the likelihood function has to be revised with respect to the “classical” case. The introduced parameter \mathcal{N} can be described by Bernoulli process (as a total number of trials), for this in the data set each event can be either “true” (observed event) or “false”. In order to satisfy this condition data can be subdivided into small enough bins, so that each bin contains maximum one observed event, *i.e.* the probability to have more than one event in a given bin is negligible [211]. This consideration leads to Poisson statistics with:

$$\begin{aligned} \text{Probability of Zero Events in bin} &= e^{-\Delta^n x P(\vec{x}, \vec{A})}, \\ \text{Probability of One Event in bin} &= \Delta^n x P(\vec{x}, \vec{A}) e^{-\Delta^n x P(\vec{x}, \vec{A})}. \end{aligned} \quad (5.12)$$

Thus, the extended likelihood is the combined probability for a complete data set:

$$\mathcal{L} = \prod_i^n \Delta x_i P(x_i, \vec{A}) \prod_j^{\mathcal{N}=\text{all bins}} e^{-\Delta x_j P(x_j, \vec{A})}, \quad (5.13)$$

where n – number of bins containing one measured event.

Further modification that can be done in the EML method is to move to the unbinned treatment of the likelihood function, which is more resistant to statistical fluctuations. Following [212], one should replace each bin Δx by its infinitesimal increment dx . Hence, the probabilities (5.12) take the following forms:

$$\begin{aligned} \text{Probability of Zero Events in bin} &= e^{-d^n x P(\vec{x}, \vec{A})}, \\ \text{Probability of One Event in bin} &= d^n x P(\vec{x}, \vec{A}) e^{-d^n x P(\vec{x}, \vec{A})}, \end{aligned} \quad (5.14)$$

and, consequently, the likelihood function (5.13) reads:

$$\mathcal{L} = \prod_i^n dx P(x, \vec{A}) \prod_j^{\mathcal{N}=\text{all bins}} e^{-dx P(x, \vec{A})}. \quad (5.15)$$

Taking a logarithm of the obtained likelihood expression (5.15), one moves from products to a sum and thereby the second product in (5.15), according to the definition of Riemann integral $\sum dx P(x, \vec{A}) \approx \int dx P(x, \vec{A}) = \mathcal{N}$, can be approximated to \mathcal{N} . As far as, the first product is concerned, it is supposed to neglect the factor $d^n x$ in the maximization procedure since it is independent of the parameters \vec{A} . Finally, for the log-likelihood one obtains:

$$\ln \mathcal{L} = \sum_i^N \ln P(x, \vec{A}) - \mathcal{N}. \quad (5.16)$$

In the particular case of the DY asymmetries analysis $\vec{x} = (\varphi^k, \varphi_S^k)$, $k = 1..N_c^\pm$, where events are sampled based on the target cell (upstream or downstream) of origin (denoted as c) and the polarization orientation (denoted as \pm):

$$P^\pm(\varphi, \varphi_S; a_c^\pm, \vec{A}) = a_c^\pm(\varphi, \varphi_S) \cdot \sigma^\pm(\varphi, \varphi_S; \vec{A}), \quad (5.17)$$

where $a_c^\pm(\varphi, \varphi_S)$ is a parameter, which accounts for the acceptance, and $\sigma^\pm(\varphi, \varphi_S; \vec{A})$ is the corresponding cross-section defined as:

$$\sigma^\pm(\varphi, \varphi_S; \vec{A}) = 1 + A_U^{\cos\varphi} + A_U^{\cos 2\varphi} \pm \sum_{i=1}^5 \langle P_T \rangle fD(\theta_{CS})^{w_i(\varphi, \varphi_S)} A_T^{w_i(\varphi, \varphi_S)}. \quad (5.18)$$

The correction factors $fD(\theta_{CS})^{w_i(\varphi, \varphi_S)}$ are applied to the TSAs in the likelihood function on an event-by-event basis, which is the reason why the method is referred to as EWUML *i.e.* *weighted* EUML. Note that the correction for the polarization is not done on an event-by-event basis, the average value per period and kinematic bin $\langle P_T \rangle$ is used instead.

Deriving the likelihood with Eqs. (5.17), (5.18), one obtains:

$$\mathcal{L} = \prod_{c=1}^2 \left(e^{-I_c^+} \prod_{i=1}^{N_c^+} P^+ \left(\varphi_i, \varphi_{S_i}, a_c^+, \vec{A} \right) \right)^{\frac{\bar{N}}{N_c^+}} \left(e^{-I_c^-} \prod_{j=1}^{N_c^-} P^- \left(\varphi_j, \varphi_{S_j}, a_c^-, \vec{A} \right) \right)^{\frac{\bar{N}}{N_c^-}}, \quad (5.19)$$

where \bar{N} – the total number of dimuon pairs, N_c^\pm – number of the dimuon pairs in a certain target cell “c“ and a polarization configuration “ \pm “, $I_c^\pm = \int \int d\varphi d\varphi_S P^\pm(\varphi, \varphi_S, a_c^\pm, \vec{A})$ – the normalisation coefficient. The function (5.19) is written in a convenient form for the analysis, in which the events from the different target cells and direction of the polarization are explicitly separated. Taking the negative logarithm, one obtains:

$$-\ln \mathcal{L} = - \sum_{c=1}^2 \frac{\bar{N}}{N_c^+} \left(-I_c^+ + \sum_{n=1}^{N_c^+} \ln \left(A'(\varphi, \varphi_S) \sigma^+ \left(\vec{A}, \varphi, \varphi_S \right) \right) \right) - \sum_{c=1}^2 \frac{\bar{N}}{N_c^-} \left(-I_c^- + \sum_{n=1}^{N_c^-} \ln \left(A'(\varphi, \varphi_S) \sigma^- \left(\vec{A}, \varphi, \varphi_S \right) \right) \right). \quad (5.20)$$

It was proven previously in COMPASS SIDIS analyses that assuming functional form for acceptance parameters, or taking an averaged value, does not affect the final result. In the presented analysis acceptance parameters are taken as φ_S and φ_{CS} -averaged cell and polarization dependent scalars. This simplifies the normalization integral $I_c^\pm = 4\pi^2 \bar{N}$. The extraction of the

asymmetries is performed by minimization of the negative log-likelihood (5.19). For the minimization a MINUIT-based software tool was required to be developed and implemented in the ROOT framework. The following settings for MINUIT were used in the minimization procedure:

- the initial parameters are zero for the asymmetries and equal to one for the acceptance parameters;
- MIGRAD and IMPROVE algorithms are called;
- 0.5 for *SetErrorDef* parameter;
- 0.1 for step;
- 0.01 as tolerance level.

5.5 Systematic studies

Extensive studies and a number of tests were performed in order to assess the systematic uncertainty of the measured transverse spin asymmetries. Several tests were inherited from SIDIS TSA analyses, while some were new. For brevity, only results from the following main studies will be presented: the check of compatibility of asymmetries extracted from different periods; the so-called RLTB (Right-Left-Top-Bottom) test, checking the compatibility of asymmetries extracted from different acceptance-segments; the study of the false asymmetries due to residual acceptance variations within pairs of data taking sub-periods. Among other performed studies that have not been included in this Thesis there were: the rejection of the runs collected in the beginning and in the end of the periods, too enforce more similar data-taking conditions in two sub-periods; testing of different target cuts (*e.g.* splitting the target cells into two halves, or shrinking the size of the cells); studying the sensitivity of the results to mass-cut variations; checking beam-dependence by applying same flux conditions to both cells or imposing various radial and elliptic cuts to select the events originating from the beam spot; investigating trigger dependence of the results; comparison of results obtained from SAS and LAS parts of the spectrometer and many others. None of those did not reveal any significant systematic biases.

In the next subsections selected systematic tests are described and the corresponding results are presented.

5.5.1 Compatibility of asymmetries from different periods

The physics results obtained from different data-taking periods (see Fig. 5.38) are supposed to be statistically compatible. Possible systematic biases might then point to *e.g.* spectrometer instabilities during the periods. The purpose of the “periods compatibility” test is to verify that the fit-results from different periods are in agreement and if not, to identify problematic periods or kinematic bins and estimate related systematic uncertainties. The test is performed separately for each TSA, by evaluating the weighted average over kinematic bins for each period. Obtained values are to be compared with the weighted average over all periods, as shown in Figs. 5.39,5.40. Alternatively, the “pulls” distributions are built filling into a histogram the following quantities:

$$pull \equiv \Delta A_i = \frac{A_i - \langle A \rangle}{\sqrt{\sigma_{A,i}^2 - \sigma_{\langle A \rangle}^2}}, \quad (5.21)$$

where i runs over the number of bins, kinematic variables and periods. If the deviations from period to period have purely statistical origin, obtained histograms are expected to be represented by standard normal distributions centered at zero and with an RMS that tends to 1. Obtained pull histograms are shown Figs. 5.41, where red curves represent Gaussian fits. In general the pull distributions turn out to be in a good agreement with the standard normal distributions and there are no significant indications of systematic biases. Observed in some cases mild deviations from the nominal picture are taken into account in the evaluation of systematic uncertainties.

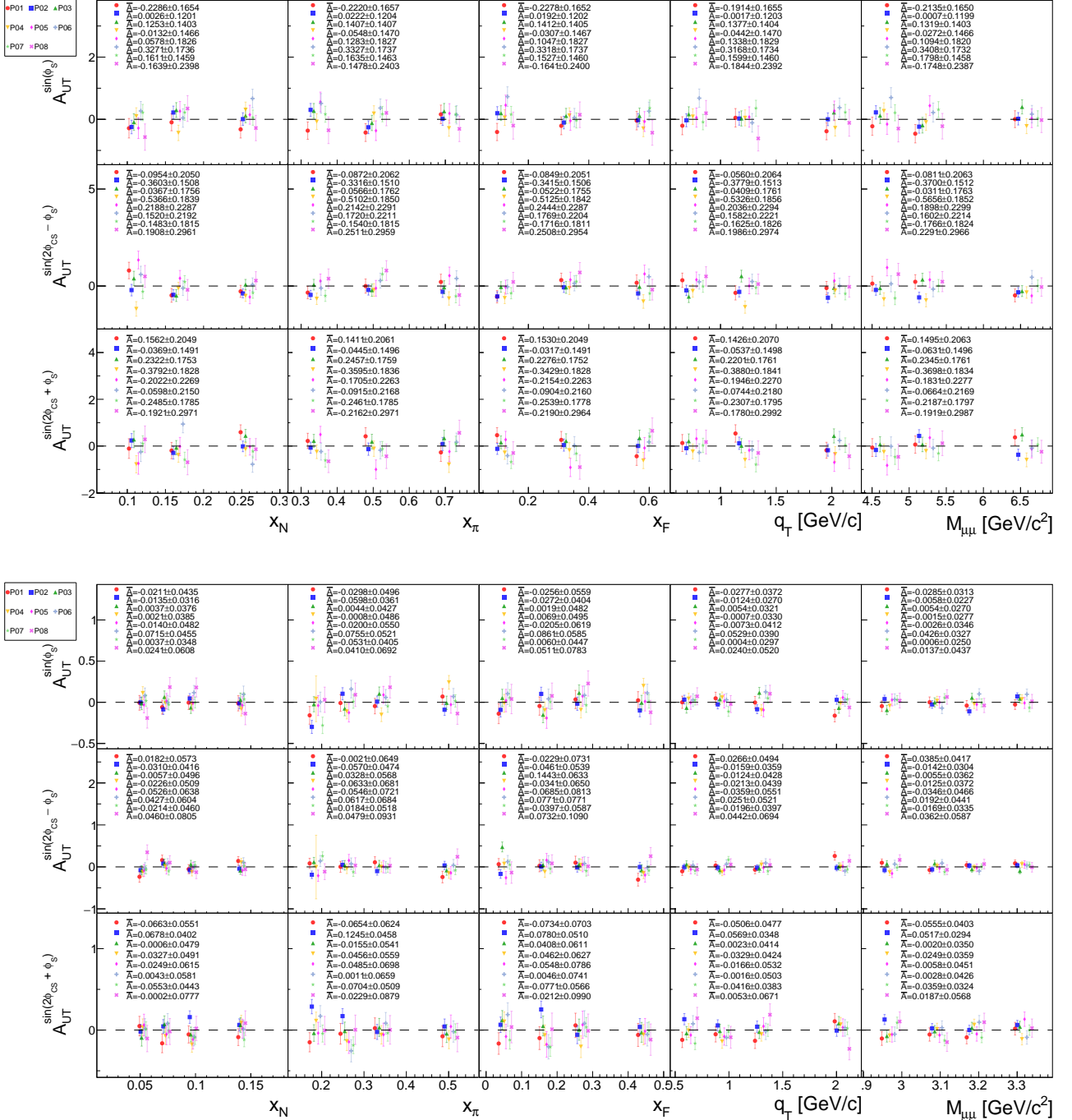


Figure 5.38: Period-wise LO asymmetries in the HM (top) and J/ψ mass (bottom) ranges (2018 data, $t8$ production).

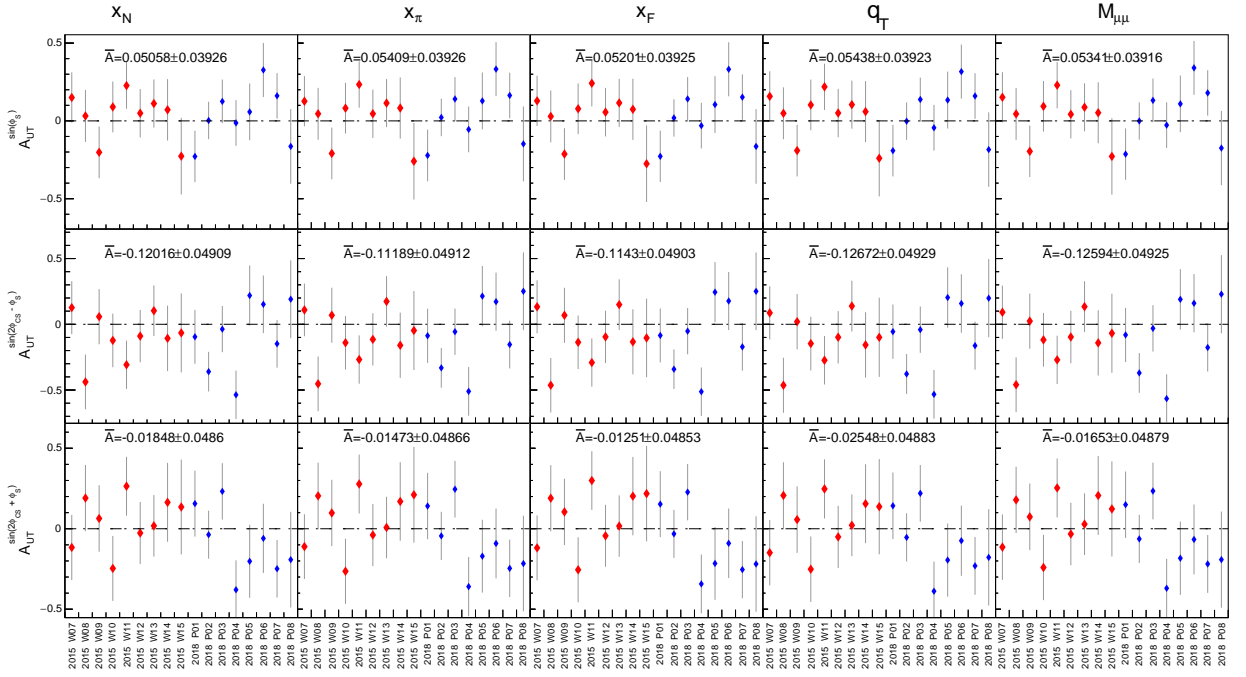


Figure 5.39: TSAs in the HM range by periods from two years averaged over kinematic bins. Red points represent asymmetries from 2015 (s2) while blue ones correspond to 2018 (t8).

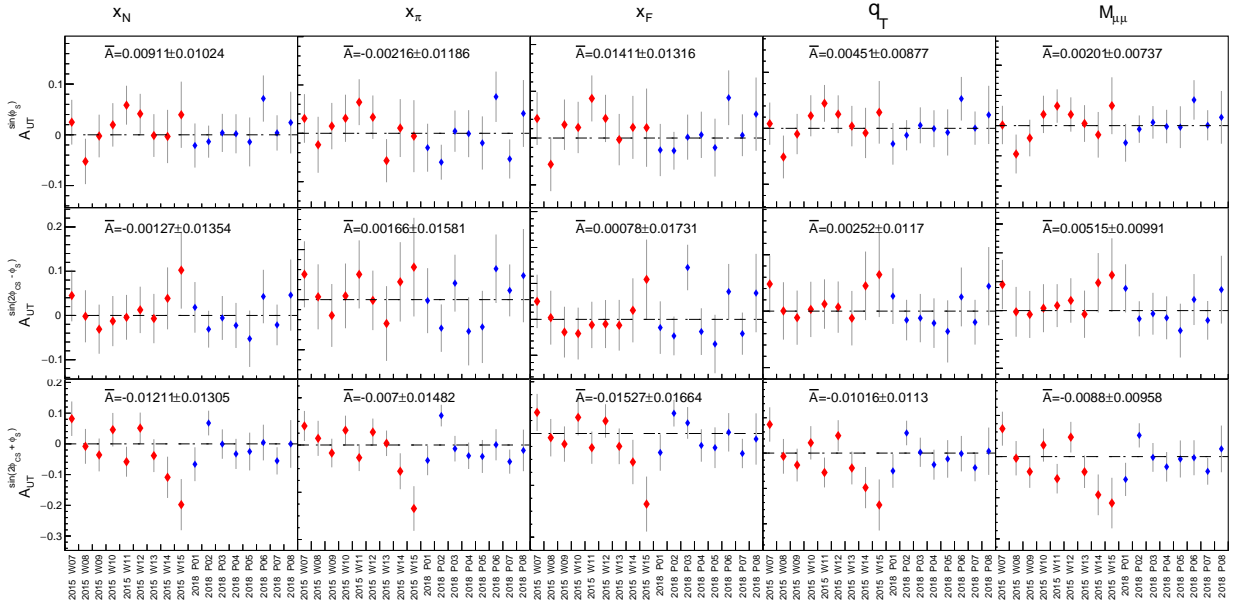
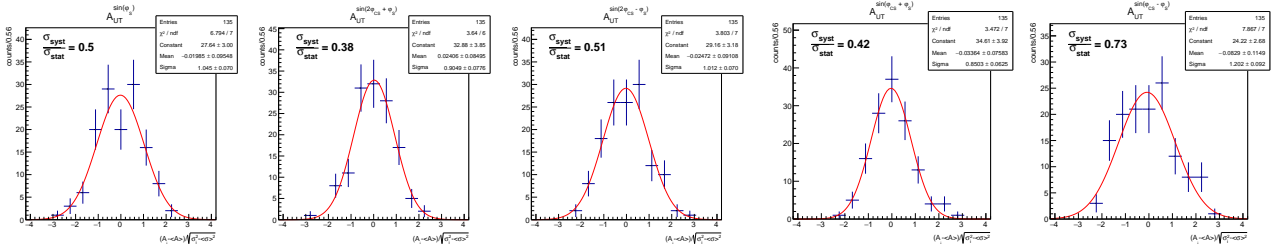
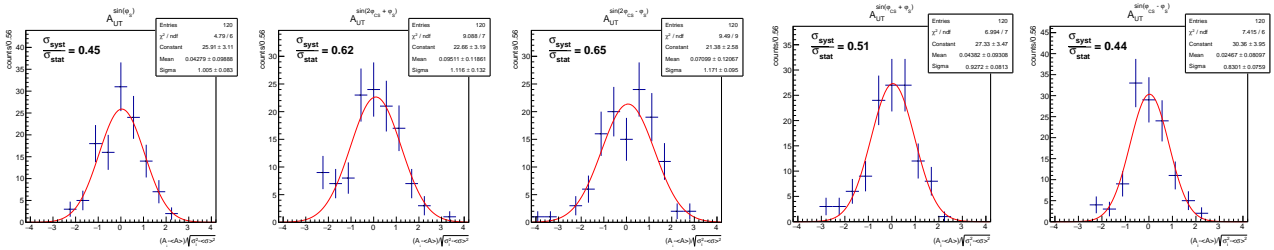


Figure 5.40: TSAs in the J/ψ mass range by periods from two years averaged over kinematic bins. Red points represent asymmetries from 2015 (s2) while blue ones correspond to 2018 (t8).



(a) 2015 data (s2), HM range



(b) 2018 data (t8), HM range

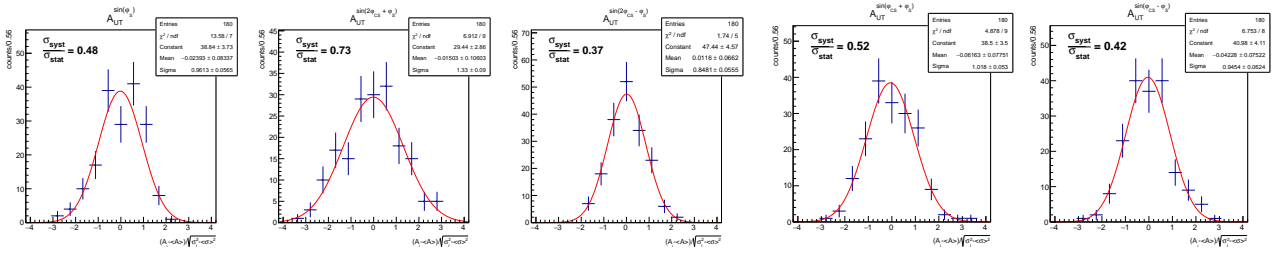
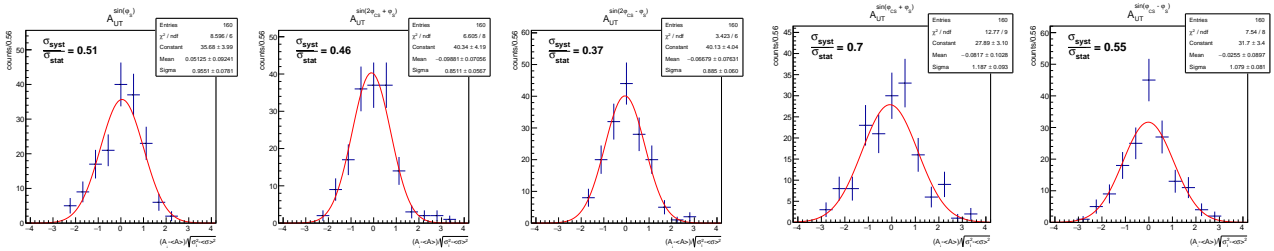
(c) 2015 data (s2), J/ψ mass range(d) 2018 data (s2), J/ψ mass range

Figure 5.41: Pull-histograms for period compatibility check.

5.5.2 Right-Left-Top-Bottom (RLTB) test

The RLTB (or Right-Left-Top-Bottom) test aims to check the consistency between the asymmetries obtained with events that are related to different hemispheres of azimuthal acceptance of the spectrometer. The test has different variations *e.g.* one can study possible sensitivity to laboratory azimuthal acceptance of dimuons, single-muons or beam pions, or involve polar and physics angles. In the following the case of the azimuthal angle of μ^+ (ϕ_{μ^+}) in the laboratory frame will be discussed (here μ^+ is the antimuon component of the muon-pair). The angle ϕ_{μ^-} can also be used, but it is sufficient to choose only one of the angles due to strong correlation between ϕ_{μ^+} and ϕ_{μ^-} . The test is performed as follows: the spectrometer phase space over ϕ_{μ^+} is divided into paired segments (top and bottom, or left and right) as shown in Fig. 5.42 and asymmetries are extracted separately from the corresponding four data-samples. Even if there were observed some non-trivial correlations between different angles and kinematic variables the TSAs are not expected to change from one segment to another.

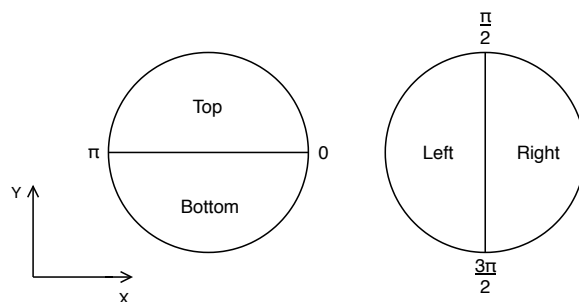


Figure 5.42: Acceptance sub-division scheme over ϕ_{μ^+} used for RLTB-test.

Hence, the difference between Right- and Left (Top- and Bottom-) asymmetries is expected to be compatible with zero. Extracted RLTB-asymmetries are presented in Figs. 5.43,5.44 (in the HM range for 2015 and 2018 data, respectively). As one case see, in general, the TSAs from different ϕ_{μ^+} hemispheres appear to be in agreement and differences are compatible with zero. To have an estimation of associated systematic uncertainties, the absolute values of the normalized (to their statistical uncertainties) differences $A_{LR} = |A_{Left} - A_{Right}| / \sqrt{\sigma_{Left}^2 + \sigma_{Right}^2}$ and $A_{TB} = |A_{Top} - A_{Bottom}| / \sqrt{\sigma_{Top}^2 + \sigma_{Bottom}^2}$, have been computed and used to determine the $\alpha = \sqrt{A_{LR\text{ or }TB}^2 - 0.68^2}$ systematic error estimators, separately for left-right and top-bottom configurations for each period and kinematic bin¹⁰. Here ~ 0.68 is the expectation value for

¹⁰In case the expression under the square root is negative ($A_{LR\text{ or }TB}^2 - 0.68^2 < 0$), the α is assigned to zero.

A_{LR} and A_{TB} distributions¹¹. The systematic uncertainty has been calculated separately for each of the TSAs and both tests (LR, TB) as a statistically weighted mean of α quantities over the periods and kinematic bins. Since the final asymmetries are built on overall sample and not the segmented one (each segment contributes in overall asymmetry with reduced statistical strength), as estimate for the overall 'RLTB' systematic error the average between 'R-L' and 'T-B' is taken. An example of the estimation of the systematic uncertainties from this test is shown in Fig. 5.45.

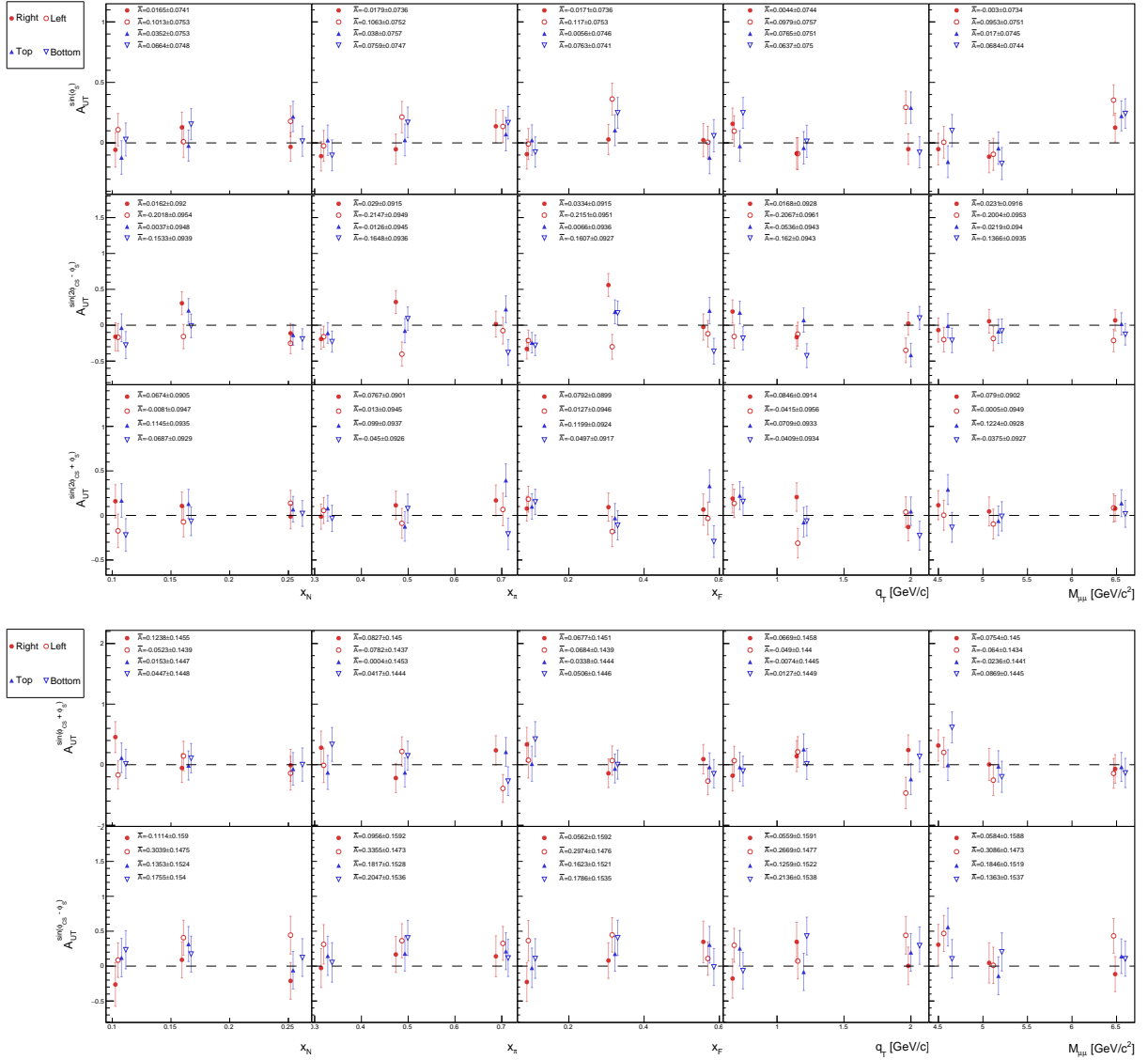


Figure 5.43: Asymmetries extracted from the Right-, Left- (red points) and Top-, Bottom- (blue points) segments of the target cells in the HM range (2015 data, s2 production).

¹¹The median value of the standard half-normal distribution $\sqrt{2} \operatorname{erf}^{-1} \left(\frac{1}{2} \right) \approx 0.67449$.

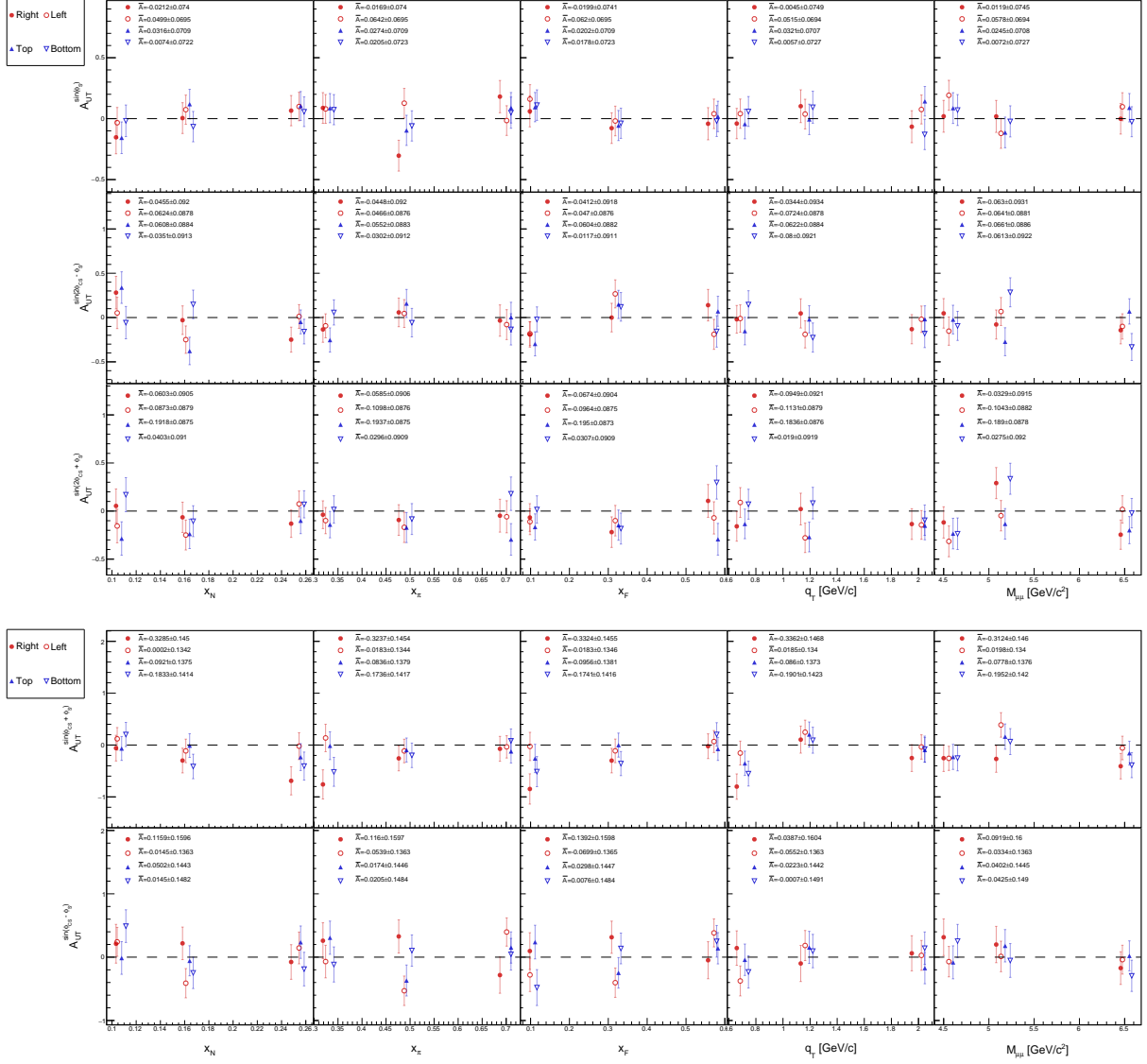


Figure 5.44: Asymmetries extracted from the Right-, Left- (red points) and Top-, Bottom- (blue points) segments of the target cells in the HM range from 2018 data (t8 production).

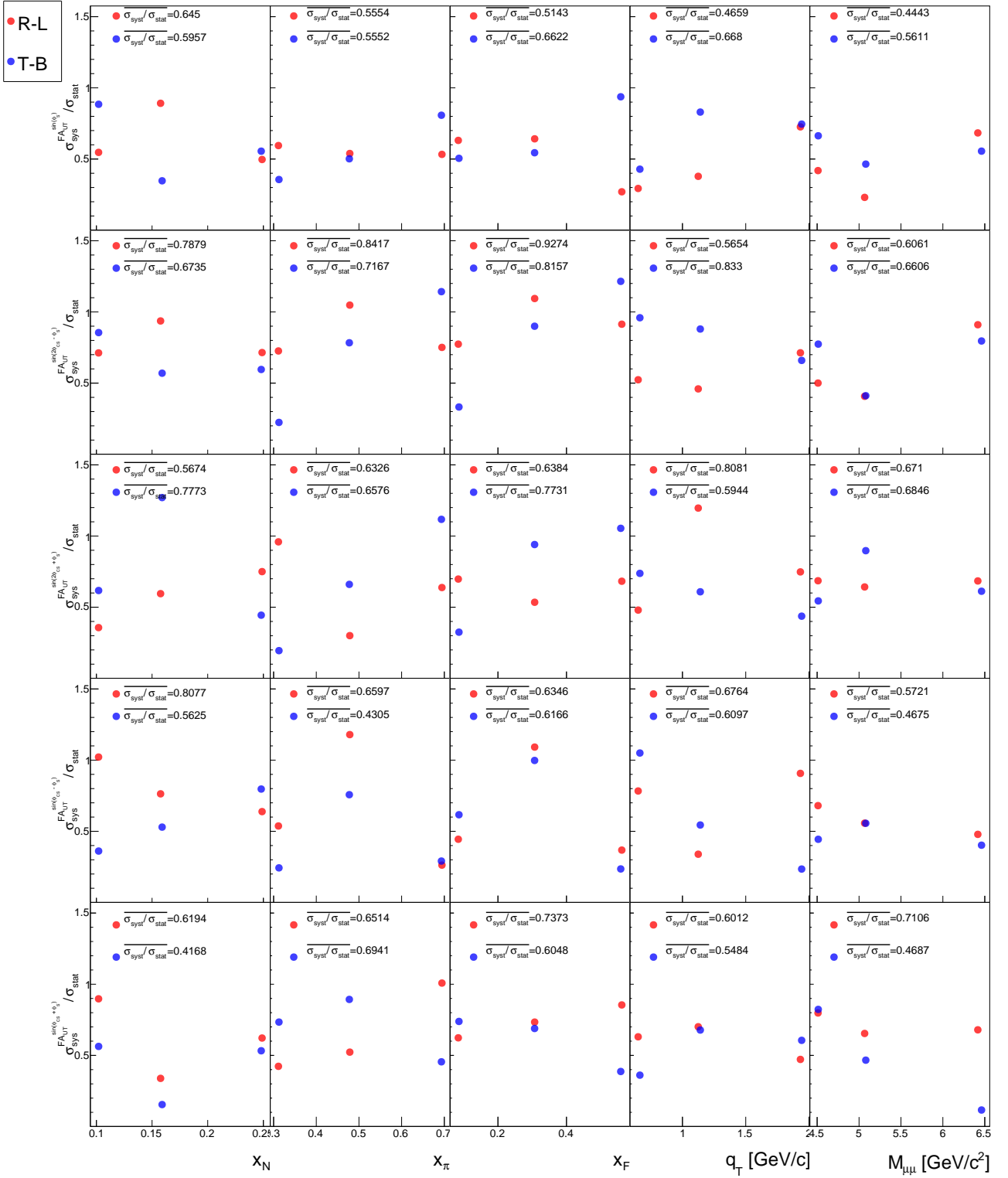


Figure 5.45: An example of the point-by-point estimation of the systematic uncertainties in terms of statistical ones from RLTB-test (HM range, 2015 data, s2 production).

5.5.3 False-asymmetries

The study of so-called “false” asymmetries (FA) aims to quantify residual spectrometer acceptance variations in data-taking periods and to estimate corresponding systematic uncertainties associated to TSA measurements. One general technique, commonly used in SIDIS analysis, is to build a TSA-like estimator¹², which combines the data in a way that both spectrometer acceptance and physics amplitudes are expected to cancel out. Extracting non-zero amplitudes with such an estimator would point then to residual variations in spectrometer conditions during given data-period violating acceptance cancellation assumption.

For the FA extraction same “EWUML” method is used as for the TSA analysis (see Sec. 5.4). The following main types of false asymmetries have been considered:

- a) The Log-Likelihood estimator is re-defined in a way that physical amplitudes from the two sub-periods cancel out. This is done deliberately flipping the sign of polarization for one of the cells in both sub-periods. In obtained configuration acceptance assumptions defined in Sec. 5.4 still hold, thus non-zero false asymmetries would point to residual acceptance variations violating acceptance-cancellation conditions.
- b) Definition of both target cells is reconfigured, forming two pairs of “fake” sub-cells as demonstrated in Fig. 5.46. The sign of polarization is then flipped for one of the sub-cells in each pair and two fake sub-periods with polarization reversal are formed. The TSAs for each of the cell are then extracted using these fake-sub-period configurations. Since physics component would certainly vanish in this configuration, non-zero false asymmetries would again point to acceptance-cancellation failure.
- c) Data of each given period has been reshuffled into two “fake” sub-periods in a way that runs with even numbers are moved to one sub-period and the runs with odd numbers are put in another sub-period. False asymmetries are then extracted from formed two fake sub-periods.

Typical examples for these three types of the false-asymmetries are shown in Fig. 5.47 for HM LO TSAs. Here “a”, “b”, and “c” symbols are assigned to distinguish the false-asymmetry types in accordance with the list above. Several other similar tests have been performed, but

¹²Usually same fitting method, fit-settings and set of modulations are used as for TSAs extractions

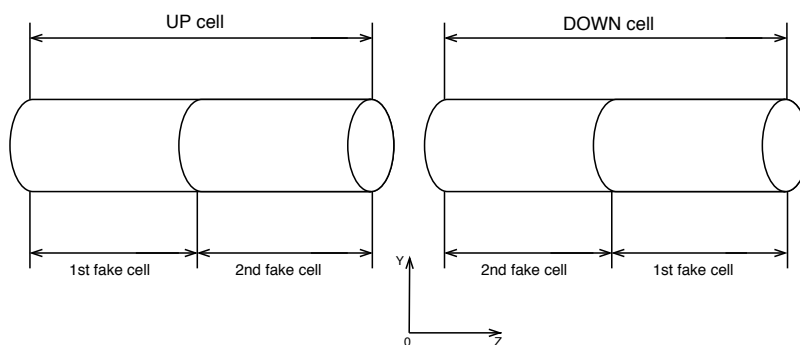


Figure 5.46: “Fake-cells” configuration with respect to real ones.

the outcome was found to be strongly correlated with the aforementioned studies and is thus omitted. In addition, false asymmetries and physics asymmetries have been extracted as functions of laboratory variables such as: the z -position of the vertex, target radius R , azimuthal angles of beam and muons, etc.

To large extent, no significant false amplitudes were identified in these tests. Measured deviations of FAs from zero are then used to estimate the systematic uncertainties using the same technique as for RLTB test.

5.5.4 The total systematic uncertainty

It was found that the upper limits for systematics uncertainties estimated from ‘RLTB’-test and from study of false asymmetries can be correlated and treating them equally will lead to a double-counting, thus the largest of the two is kept. All uncorrelated systematic uncertainties, that were estimated in the above systematic studies, are taken into account for the evaluation of the final systematic uncertainty of a certain azimuthal asymmetry. This includes the additive systematic errors from joined RLTB and FA tests plus estimation from periods compatibility and $0.4 \times \sigma_{stat}$ from other tests, all summed up in quadrature. Total systematic uncertainties for each asymmetry are presented in Tabs. 5.10, 5.11 for the analysis in the HM range and in Tabs. 5.12, 5.13 for the J/ψ case.

The dilution factor f and the depolarization factor D entering the definition of TSAs are calculated on an event-by-event basis and used to weight the asymmetries. For the magnitude of the target polarization P_T , an average value is used for each data taking period in order to avoid possible systematic bias. In the evaluation of the depolarization factors, the approximation $\lambda =$

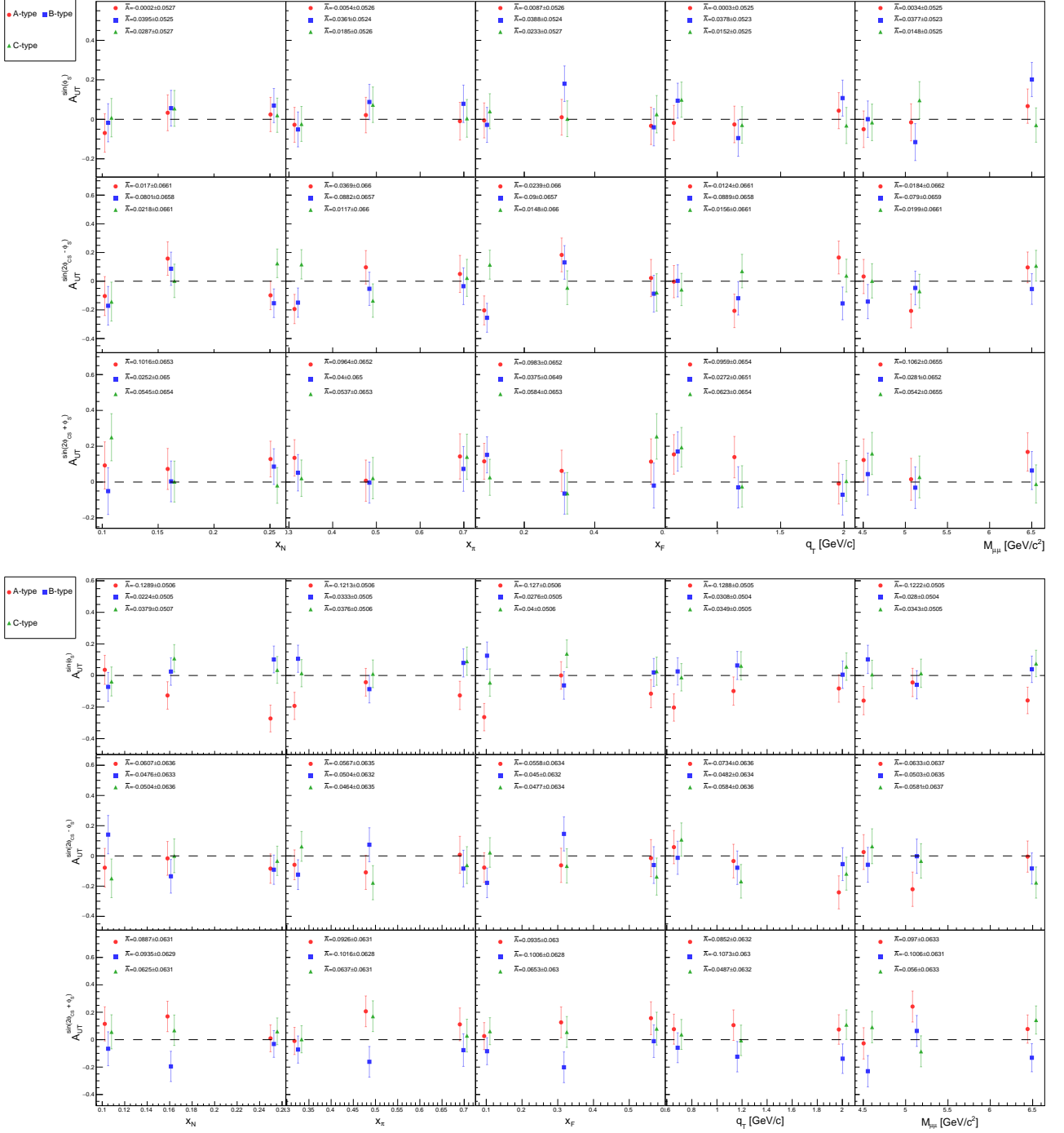


Figure 5.47: Three types of false-asymmetries extracted for LO modulations in the HM range from 2015 (top) and 2018 (bottom) data.

1 is used. Known deviations from this assumption with λ ranging between 0.5 and 1 [128, 213] decrease the normalization factor by at most 5% for HM-case and up to 20% for J/ψ -case. The normalization uncertainties originating from the uncertainties on target polarization (5%) and

dilution factor (8%) are not included in the quoted systematic uncertainties.

Method \ Asymmetry	$A_T^{\sin \varphi_S}$	$A_T^{\sin(\varphi_S+\varphi_{CS})}$	$A_T^{\sin(\varphi_S-\varphi_{CS})}$	$A_T^{\sin(2\varphi_S+\varphi_{CS})}$	$A_T^{\sin(2\varphi_S-\varphi_{CS})}$
R-L	0.53	0.66	0.67	0.66	0.75
T-B	0.61	0.55	0.54	0.70	0.74
RLTB	0.57	0.61	0.61	0.68	0.74
$F_a A$	0.40	0.53	0.45	0.58	0.55
$F_b A$	0.45	0.69	0.49	0.44	0.47
$F_c A$	0.48	0.50	0.30	0.62	0.46
Other tests	0.44	0.44	0.40	0.50	0.45
Total	0.7	0.8	0.8	0.8	0.8

Table 5.10: Estimations of the systematic uncertainties in the HM range for analysis of 2015 data in units of $\sigma_{sys}/\sigma_{stat}$.

Method \ Asymmetry	$A_T^{\sin \varphi_S}$	$A_T^{\sin(\varphi_S+\varphi_{CS})}$	$A_T^{\sin(\varphi_S-\varphi_{CS})}$	$A_T^{\sin(2\varphi_S+\varphi_{CS})}$	$A_T^{\sin(2\varphi_S-\varphi_{CS})}$
R-L	0.57	0.52	0.59	0.51	0.50
T-B	0.53	0.43	0.48	0.59	0.51
RLTB	0.55	0.48	0.56	0.55	0.51
$F_a A$	0.57	0.46	0.69	0.61	0.62
$F_b A$	0.45	0.48	0.40	0.63	0.71
$F_c A$	0.57	0.56	0.60	0.65	0.53
Other tests	0.75	0.80	0.80	0.90	1.00
Total	1.0	1.0	1.1	1.1	1.2

Table 5.11: Estimations of the systematic uncertainties in the HM range for analysis of 2018 data in units of $\sigma_{sys}/\sigma_{stat}$.

Method \ Asymmetry	$A_T^{\sin \varphi_S}$	$A_T^{\sin(\varphi_S+\varphi_{CS})}$	$A_T^{\sin(\varphi_S-\varphi_{CS})}$	$A_T^{\sin(2\varphi_S+\varphi_{CS})}$	$A_T^{\sin(2\varphi_S-\varphi_{CS})}$
R-L	0.37	0.48	0.55	0.48	0.55
T-B	0.50	0.45	0.43	0.63	0.63
RLTB	0.44	0.47	0.49	0.56	0.59
$F_a A$	0.60	0.61	0.74	0.57	0.68
$F_b A$	0.50	0.45	0.58	0.67	0.35
$F_c A$	0.53	0.46	0.37	0.53	0.56
Other tests	0.48	0.52	0.42	0.73	0.37
Total	0.84	0.87	0.97	0.96	0.99

Table 5.12: Estimations of the systematic uncertainties in the J/ψ mass range for analysis of 2015 data in units of $\sigma_{sys}/\sigma_{stat}$.

Method \ Asymmetry	$A_T^{\sin \varphi_S}$	$A_T^{\sin(\varphi_S+\varphi_{CS})}$	$A_T^{\sin(\varphi_S-\varphi_{CS})}$	$A_T^{\sin(2\varphi_S+\varphi_{CS})}$	$A_T^{\sin(2\varphi_S-\varphi_{CS})}$
R-L	0.85	0.54	0.61	0.40	0.55
T-B	0.60	0.73	0.65	0.66	0.70
RLTB	0.73	0.64	0.63	0.53	0.63
$F_a A$	0.47	0.67	0.55	0.44	0.51
$F_b A$	0.46	0.48	0.65	0.44	0.41
$F_c A$	0.46	0.42	0.58	0.61	0.48
Other tests	0.51	0.70	0.55	0.46	0.37
Total	0.95	1.01	0.99	0.90	0.90

Table 5.13: Estimations of the systematic uncertainties in the J/ψ mass range for analysis of 2018 data in units of $\sigma_{sys}/\sigma_{stat}$.

5.6 Results

Kinematic dependences of transverse spin asymmetries were extracted from each data-taking period of 2015 and 2018. The weighted average over periods was evaluated for each kinematic bin, separately for each year. The final results were obtained by evaluating in each kinematic bin the weighted average of 2015 and 2018 asymmetries, taking into account both statistical and point-to-point systematic uncertainties [78, 214]. The final combined results are presented in Figs. 5.48, 5.49 for the high mass and J/ψ mass ranges, respectively.

In general, the results from 2015 and 2018 data were found to be statistically compatible. Maximum differences are not exceeding $1.5 \sigma_{stat}$, which is similar to the results of period-by-period comparisons within a given year (See *e.g.* Fig. 5.38). The results obtained in this Thesis have been also compared to the COMPASS published ones [84], which were based on t3-production of 2015. The comparison between published COMPASS results (2015-t3), the results obtained from newly re-processed 2015 data (2015-s2) and final results obtained in this Thesis (based on 2015-s2 and 2018-t8 productions) is shown in Fig. 5.50. The corrections and changes introduced in the recent reproductions of 2015 and 2018 data (the reconstruction software settings and various technical inputs, such as detector calibrations and alignment) have been discussed in Sec. 5.2.4 along with the impact of those modifications at the level of various observables. After applying all selection criteria the final event-samples used for TSA extractions from different reproductions of same data are not identical. Even the kinematics and angular characteristics of events that are in common between given reproductions may change, which obviously affects also the TSAs. It was however verified that main deviations at the level of TSAs from different productions were caused by the events that were not in common between the samples.

Compared to the published COMPASS Drell-Yan TSA data, final results from combined 2015 and 2018 data presented in this Thesis have significantly lower statistical uncertainties. In general, final Sivers, Transversity and pretzelocity TSA amplitudes in HM are found to be smaller in absolute values compared to the published ones. In Fig. 5.48 obtained results are compared with available predictions from Ref. [136]. One can see that measured TSAs are in good agreement with theoretical model-calculations.

The transverse spin asymmetries for the J/ψ mass range (right plot in Fig. 5.51) are pre-

sented in this Thesis for the first time. Similarly to the HM case, the asymmetries have been extracted separately for 2015 and 2018 and then combined. The 2015 and 2018 results statistically agree with each other.

In Fig. 5.51 integrated over the full kinematic range results for HM and J/ψ mass ranges are shown for 2015, 2018 and for the summed sample.

In the HM range, the Drell-Yan Sivers effect was found to be relatively small and positive, but comparable with zero within statistical uncertainties. The amplitude related to the pretzelosity PDF was found to be slightly negative and also compatible with zero. The DY transversity asymmetry shows an indication of a possible negative signal with a significance of about one standard deviation of the total uncertainty. The asymmetries in the J/ψ mass range are small and compatible with zero. This can indicate possible dominance of gluon-gluon fusion mechanism for J/ψ production at COMPASS kinematics and very weak gluon TMD effects in that region. It should be noted that all results presented in this Section were successfully cross-checked with the COMPASS-Illinois group.

Detailed physics interpretation of the results will be presented in the concluding Chapter of this Thesis.

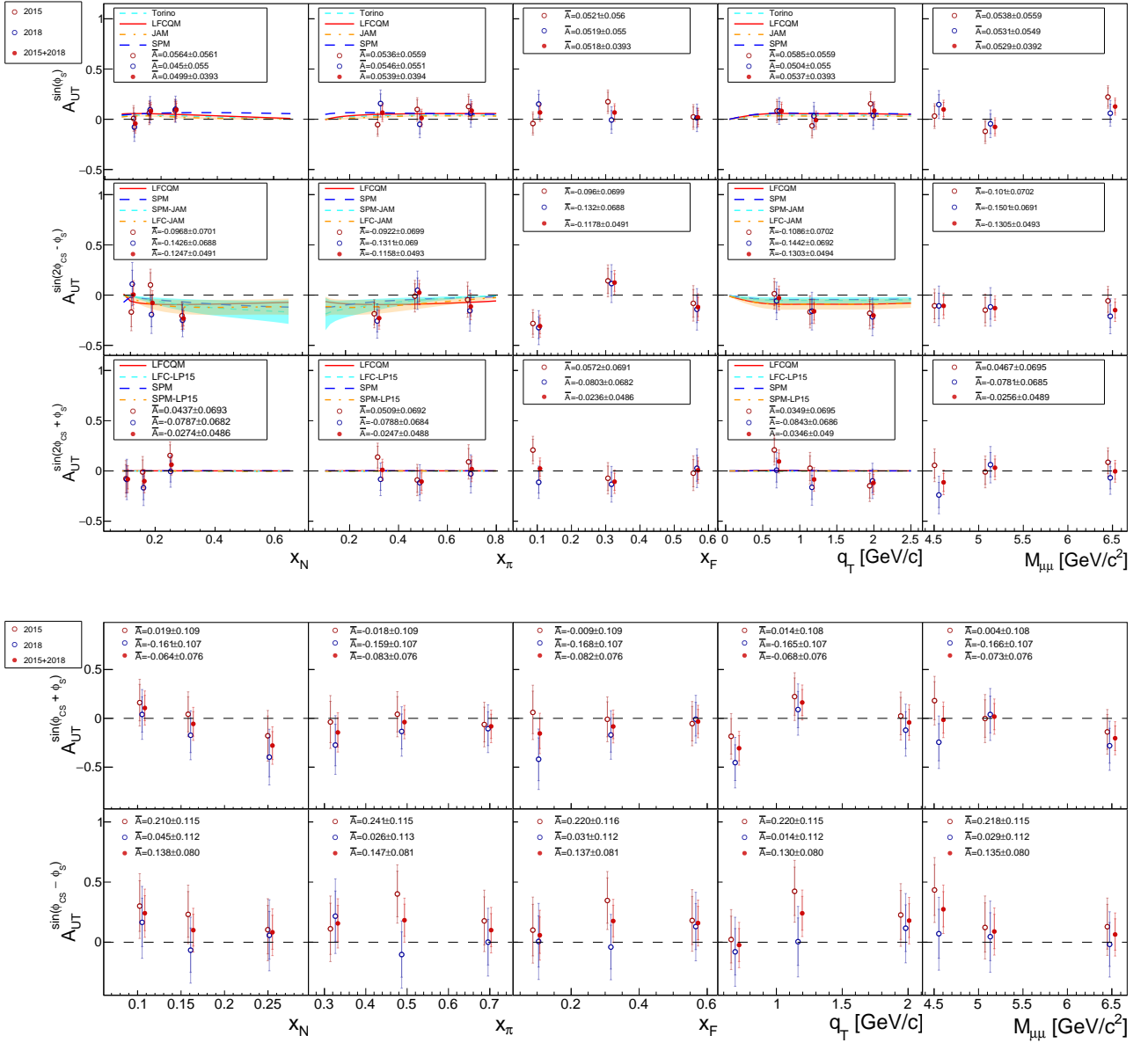


Figure 5.48: TSAs in the HM range as functions of kinematic variables. Available model predictions for twist-2 TSAs from Ref. [136] are shown as functions of x_N , x_π , q_T (top plot).

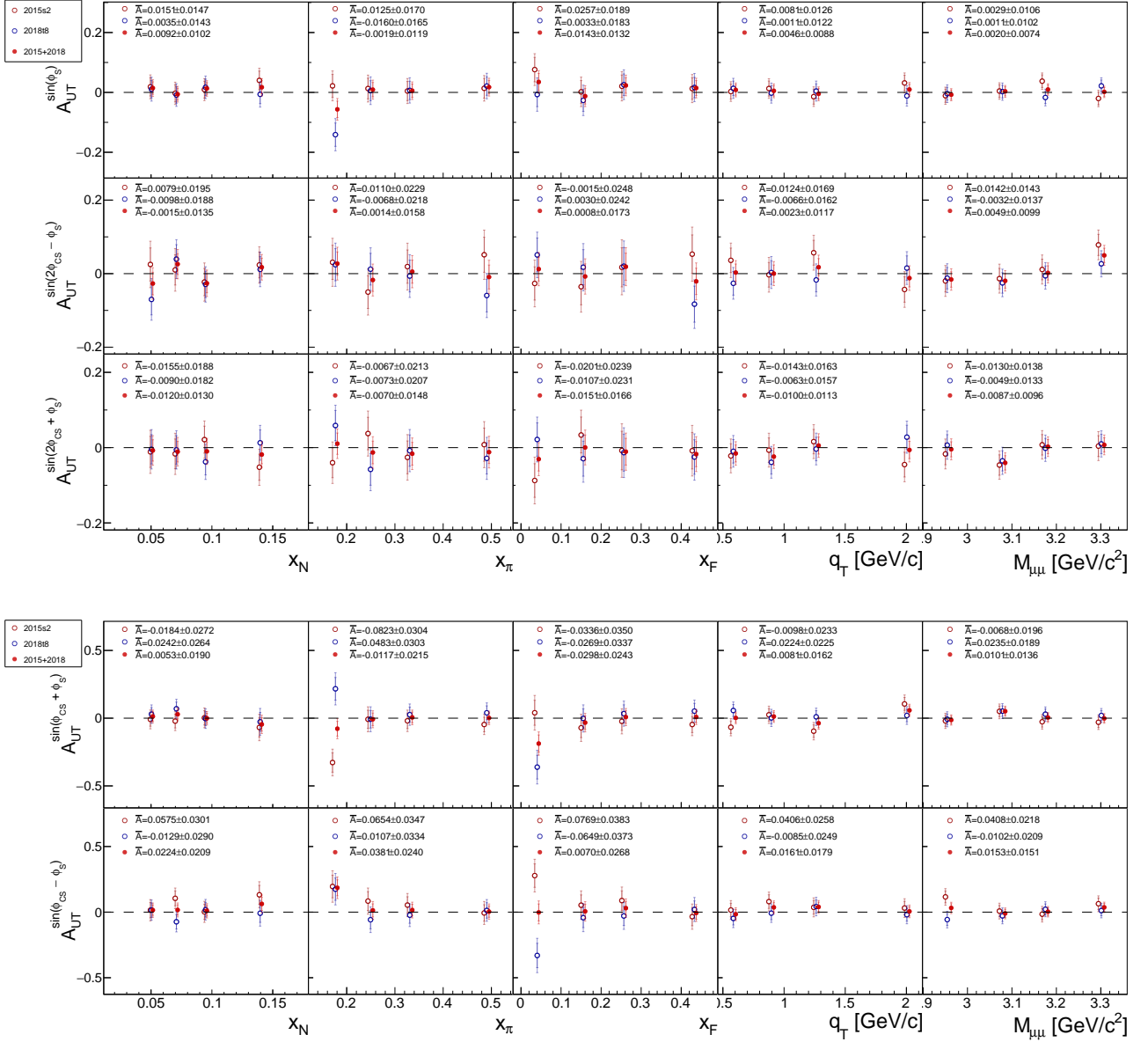


Figure 5.49: TSAs in the J/ψ mass range as functions of kinematic variables.

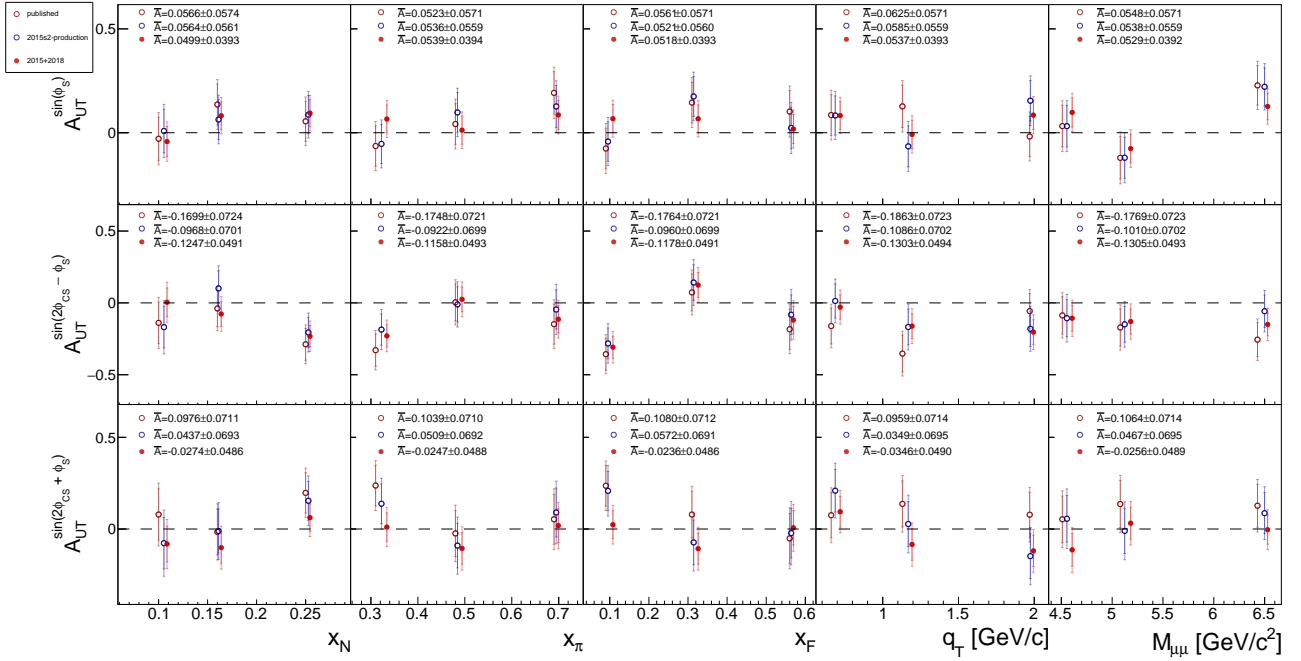


Figure 5.50: COMPASS published TSAs from 2015-t3 data [84] compared to the 2015-s2 and joint 2015-s2+2018-t8 results.

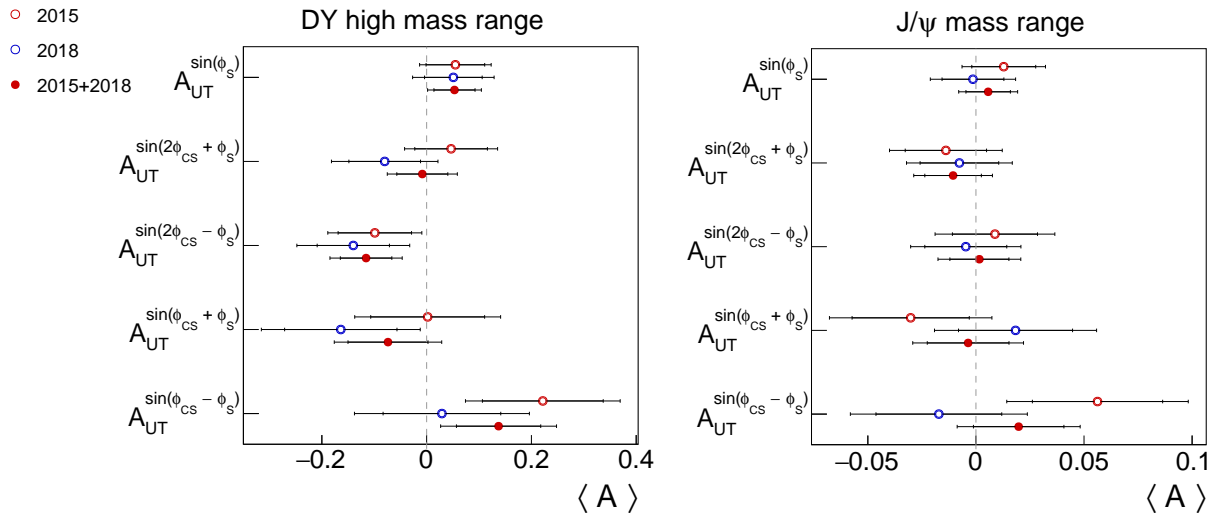


Figure 5.51: 5 TSAs extracted from 2015 (red points) and 2018 data (blue points) with the joint results (green points).

5.7 Analysis of spin-independent azimuthal asymmetries

In addition to the TSA analysis, the study of Unpolarized Asymmetries (UAs), incorporated in the DY cross-section (2.39), is another important aspect of the COMPASS Drell-Yan programme. The UA analysis is carried out for dimuons produced both in NH_3 target and in the upstream part (20 cm) of the tungsten beam plug, which is treated as a nucleon target. The unpolarized part of the DY cross-section $\hat{\sigma}_U$ contains azimuth-independent structure functions F_U^1 and F_U^2 and two azimuth-dependent ones $F_U^{\cos\varphi_{CS}}$ and $F_U^{\cos 2\varphi_{CS}}$. In terms of the structure functions the unpolarized part of the cross-section can be written as follows:

$$\begin{aligned} \frac{d\sigma}{dq d\Omega} = \frac{\alpha^2}{6\pi Q^2 s^2} & (F_U^1(1 + \cos^2 \theta_{CS}) + F_U^2(1 - \cos^2 \theta_{CS}) \\ & + F_U^{\cos\varphi_{CS}} \sin 2\theta_{CS} \cos \varphi_{CS} + F_U^{\cos 2\varphi_{CS}} \sin^2 \theta_{CS} \cos 2\varphi_{CS}), \end{aligned} \quad (5.22)$$

From this equation one can derive the expression for the normalized angular distribution of Drell-Yan events:

$$\begin{aligned} \frac{dN}{d\Omega} = \frac{3}{8\pi} & \left(\frac{F_U^1(1 + \cos^2 \theta_{CS}) + F_U^2(1 - \cos^2 \theta_{CS})}{2F_U^1 + F_U^2} \right. \\ & \left. + \frac{F_U^{\cos\varphi_{CS}} \sin 2\theta_{CS} \cos \varphi_{CS} + F_U^{\cos 2\varphi_{CS}} \sin^2 \theta_{CS} \cos 2\varphi_{CS}}{2F_U^1 + F_U^2} \right). \end{aligned} \quad (5.23)$$

Using the notations (2.20), the expression (5.23) takes a compact and convenient form:

$$\frac{dN}{d\Omega} = \frac{3}{4\pi} \frac{1}{\lambda + 3} \left[1 + \lambda \cos^2 \theta_{CS} + \mu \sin 2\theta_{CS} \cos \varphi_{CS} + \frac{\nu}{2} \sin^2 \theta_{CS} \cos 2\varphi_{CS} \right], \quad (5.24)$$

where λ , μ , ν are the spin-independent asymmetries. The analysis has been carried out for three reference frames: Collins-Soper, Gottfried-Jackson and Helicity. In this Chapter the extraction procedure and obtained results for DY UAs are presented.

5.7.1 Monte-Carlo production

Kinematic and azimuthal distributions obtained from collected experimental data are a result of a convolution of the outcome of physics processes (Drell-Yan, J/ψ production, etc.) and various constrains imposed by the measurement (geometry and constructional features of the spectrometer, the state of different elements of the experimental setup during the data-taking, kinematic selections, etc.). COMPASS setup is a classic forward-spectrometer and it's geometry

imposes natural limitations on the phase-space accessible for the measurement. Due to various constructional features of different detector-systems (such as dead-zones, finite dimensions, supporting structures and incorporation of heavy materials, etc.) particles that were emitted at certain polar or azimuthal angle segments, may not be detected. It may also happen that due to hardware problems, detector or trigger inefficiencies, the information (hits in different detector planes) left by particles crossing affected zones of the spectrometer, will not be enough to fully reconstruct corresponding tracks. Aforementioned aspects will affect the kinematic and angular acceptance of the measurement and can thus have an impact on different laboratory and physics observables *e.g.* distorting the shapes of kinematic distributions and inducing additional modulations in azimuthal angular distributions. Monte-Carlo simulations are used to reproduce experimental data taking conditions, *e.g.* the profile of the beam, realistic detector efficiencies, the efficiency of the trigger system, the geometrical acceptance of the experiment, etc. This information can then be used to correct the experimental data for aforementioned acceptance distortions, undoing their impact, and thus accessing the pure physics component of the measurement. In case of unpolarized angular asymmetry analysis, one needs to determine the relevant angular acceptance in different kinematic bins in order to apply the corrections to the experimentally measured distributions. However, this is not the only implication of MC simulations. Monte-Carlo data can be used for various systematic studies *e.g.* to understand the origin of observed false asymmetries, to estimate background contaminations, to estimate the role of certain detector systems and to optimise detector positions and configurations for future measurements, etc. Details on evaluation of the MC acceptance corrections for Drell-Yan unpolarized asymmetries analysis are presented in Sec. 5.7.4.

For DY analyses in COMPASS a dedicated MC software chain is used, which includes: physics generator Pythia 8 [215]; COMPASS setup simulation software framework, TGEANT (based on Geant4 [216]); COMPASS data reconstruction software, CORAL.

Firstly, Drell-Yan events ($q + \bar{q} \rightarrow \gamma^* \rightarrow \mu^+ \mu^-$) are produced at the level of the physics generator. In recent simulations we used Pythia 8 with LHAPDF sets: NNPDF30_nlo_as_0119 for nucleon [217] and GRVPI1 for pion [92]. The proton-neutron (p - n) mixture is evaluated based on the given target composition (following relation was used to constrain n cross-section $\sigma_p/\sigma_n = 1.96$). Main options used to tune the generator are listed in Tab. 5.14. Generated particles are then transported through the spectrometer model described in TGEANT to simulate

detector hits, trigger response, etc.

General settings	
Pion PDF	GRVPI1
Nucleon PDF	NNPDF30_nlo_as_0119
PartonLevel:ISR - Initial State Radiation Switch	on
PartonLevel:FSR - Final State Radiation Switch	on
PartonLevel:MPI - Multiparton Interactions	on
23:mMin - Lower Invariant Mass Limit	3.5 GeV/c ²
23:mMax - Upper Invariant Mass Limit	11.0 GeV/c ²
BeamRemnants:primordialKT - selection of primordial k_T	on

Table 5.14: Main part of the Pythia 8 settings used in the MC for the DY process.

By default, TGEANT produces the MC hits in all detector planes (sensitive areas), assuming 100% efficiency for the planes. The simulation of inefficiencies is done at the reconstruction stage in CORAL, where simulated hits are discarded based on the efficiency information for the given plane and sector. The 2D efficiency maps are extracted from real data for each detector plane. The efficiency maps are prepared in a form of 2D histograms binned in X and Y directions of a certain sensitive plane. The efficiency value in each bin is evaluated according to the following ratio:

$$\varepsilon(x_b, y_b) = \frac{N_{hits}(x_b, y_b)}{N_{hits}(x_b, y_b) + \bar{N}_{hits}(x_b, y_b)}, \quad (5.25)$$

where x_b and y_b are the coordinates of the bin b , $N_{hits}(x_b, y_b)$ is the number of hits correlated in space and time to a track that hits the detector plane in the bin b and $\bar{N}_{hits}(x_b, y_b)$ accounts for the cases when no hits are found, or when they are found to be uncorrelated with the track examined.

Apart from the simulation of the detector responses, it is mandatory to describe the efficiency of the trigger system, which should account both for the hardware (hodoscope slab efficiencies) and trigger coincidence matrix performances. Having well described the hodoscope and trigger matrix geometrical acceptances and efficiencies is crucial for angular analysis since the acceptance of muon pairs is to a large extent defined by the trigger system. As it was mentioned, the overall trigger performance is described by two components: the efficiency of

the trigger hodoscopes and the state of the trigger coincidence matrices. The procedure to extract hodoscope efficiencies is in general similar to the one used for the detector planes. However, it requires a dedicated data-sample of unbiased single muon trigger events collected with Calorimeter Trigger (CT). Firstly, good muon track candidates are selected from the Calorimeter Trigger events and extrapolated to each hodoscope. Then the number of the extrapolated tracks N_{tracks} is counted and the hodoscope efficiency is defined for each slab number $\#$ as follows:

$$\epsilon_{\text{hodoscope}} = \frac{N_{\text{tracks}} \otimes (f_{(\text{slab } \#)} \text{ OR } f_{(\text{slab } \#+1)} \text{ OR } f_{(\text{slab } \#-1)})}{N_{\text{tracks}}}, \quad (5.26)$$

here $f_{(\text{slab}\#)}$ is a boolean function returning *true* if there was a hit in a given slab.

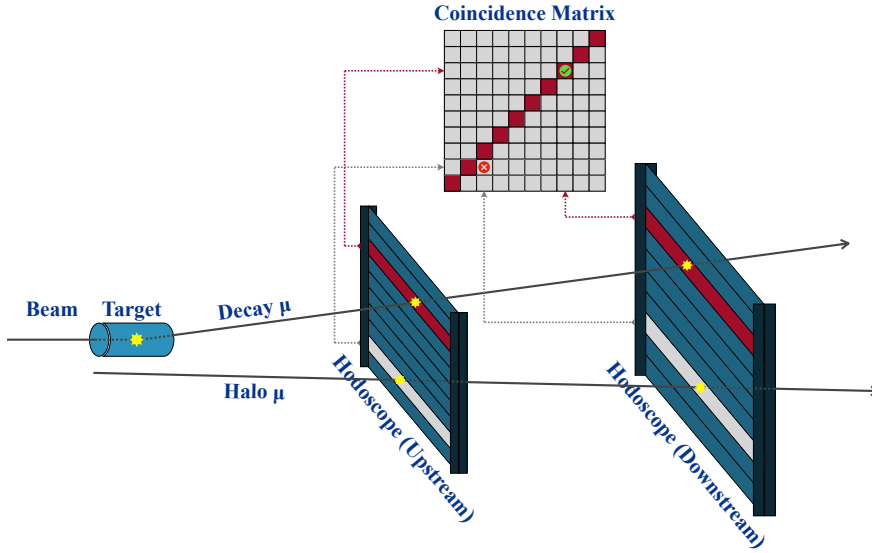


Figure 5.52: The principle of determination of coincidence matrix.

The second input, the efficiency of coincidence matrices, is based on the information from paired upstream and downstream hodoscope hits, which satisfy two conditions (illustrated in Fig. 5.52): 1) registered hits are in the time window of corresponding trigger; 2) coincidence matrix pattern compatibility, which is shown in Fig. 5.53. If more than one pair passes the criteria, the candidates are rejected from the consideration in order to avoid ambiguity. Finally, the coincidence matrix efficiency elements are defined using the following ratio:

$$\epsilon_{\text{matrix}} = \frac{(\# \text{ of selected hit pairs}) \otimes (\text{muon trigger bit})}{(\# \text{ of selected hit pairs})}. \quad (5.27)$$

The coincidence matrices and hodoscope efficiencies applied in the MC production for the present analysis are shown in Fig. 5.54 and Fig. 5.55, respectively.

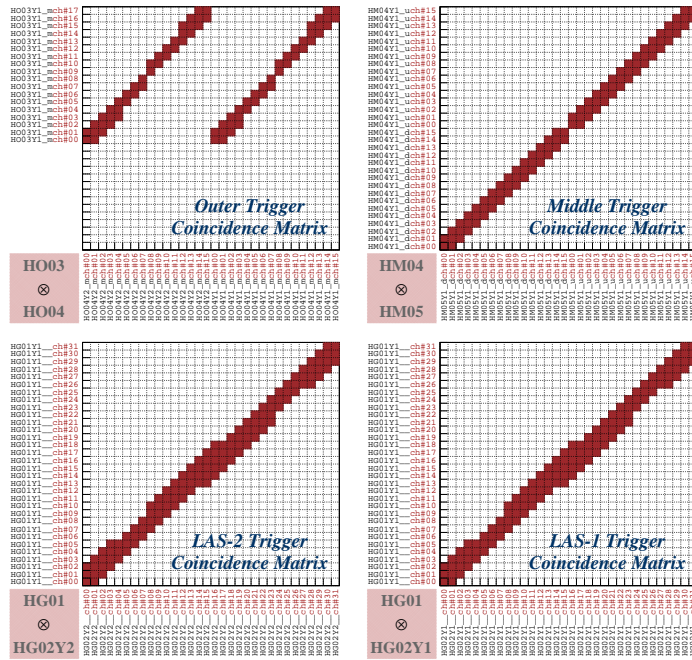


Figure 5.53: The digit pattern of coincidence matrices. For each matrix, the x axis corresponds to the slab number of downstream hodoscope of each hodoscope pair, and the y axis corresponds to the slab number of upstream hodoscope. Each pixel corresponds to a combination of paired signal from two slabs.

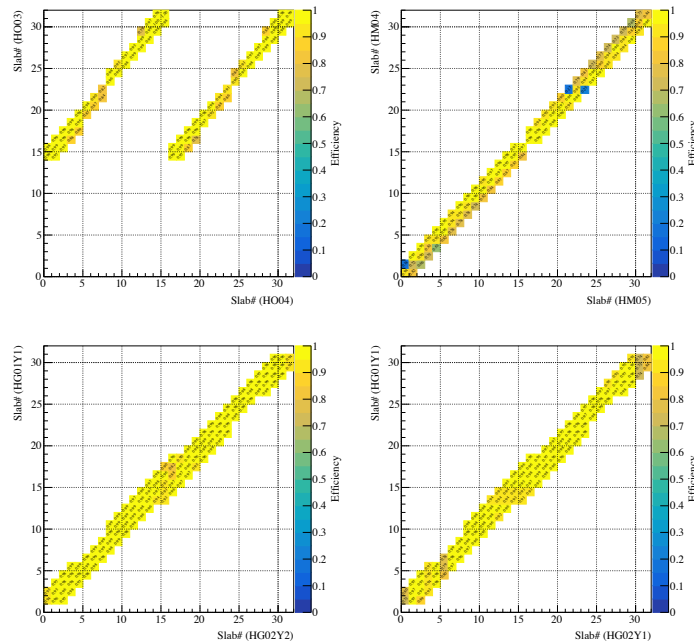


Figure 5.54: The efficiencies of coincidence matrices.

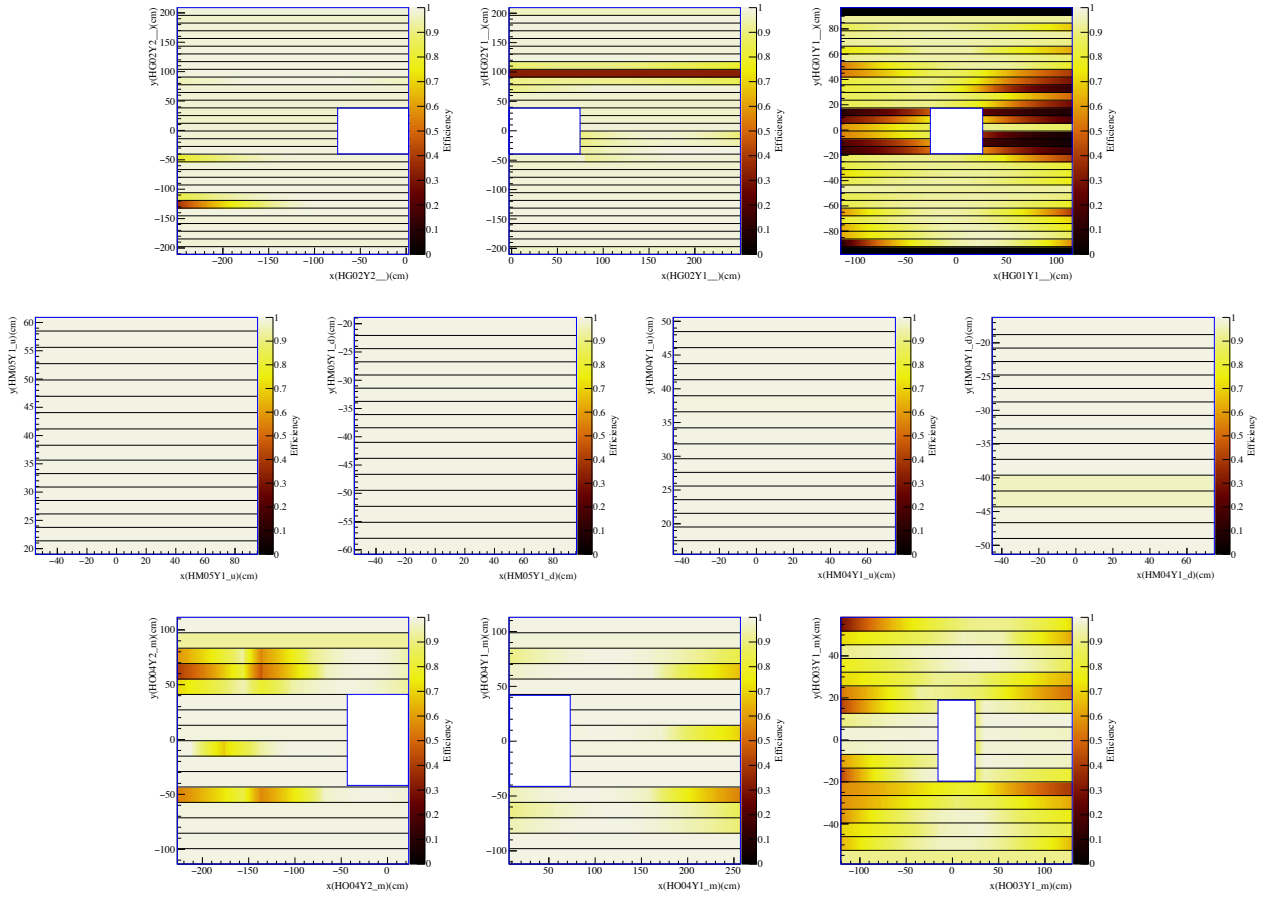


Figure 5.55: The 2D hodoscope efficiencies for period P03 of 2018. For each hodoscope plane, the X axis corresponds to the x position in laboratory frame, and the Y axis corresponds to the y position in laboratory frame.

The geometry of the spectrometer, the parameters of the beam and various other data-taking conditions may differ from period to period. Therefore a dedicated period-by-period MC production campaign had to be performed. Achieved level of agreement between Monte-Carlo and real data is illustrated in Fig. 5.56 where MC and RD x_F distributions are compared on a period by period basis both for NH_3 and tungsten targets. One can also observe a good agreement between MC and RD average kinematic values in multi-D kinematic bins (the so-called kinematics maps) shown in Figs. 5.57, 5.58.

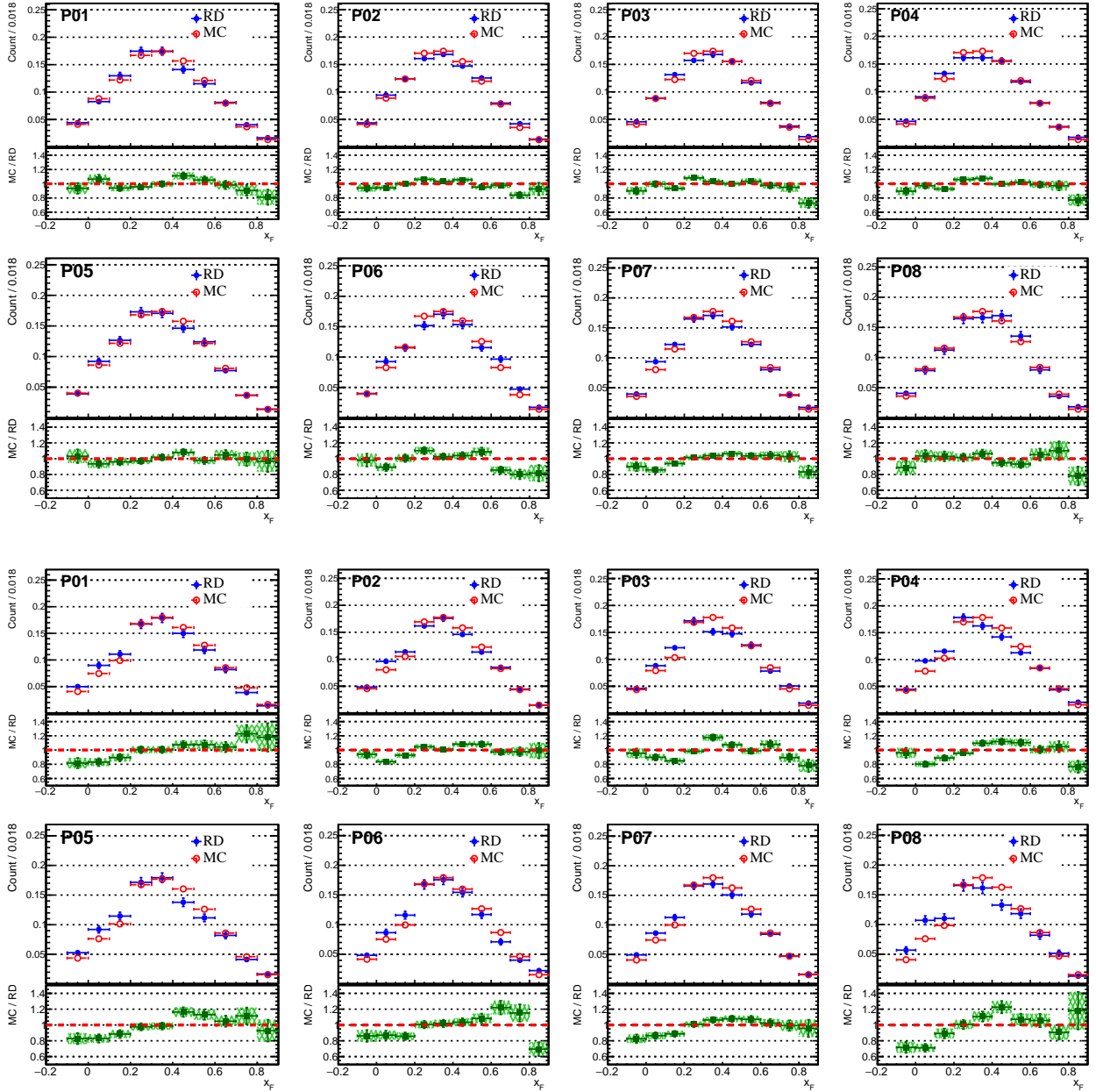


Figure 5.56: Illustration of agreement between RD and MC data as a function of x_F , for the NH_3 target on the top and for the W target on the bottom.

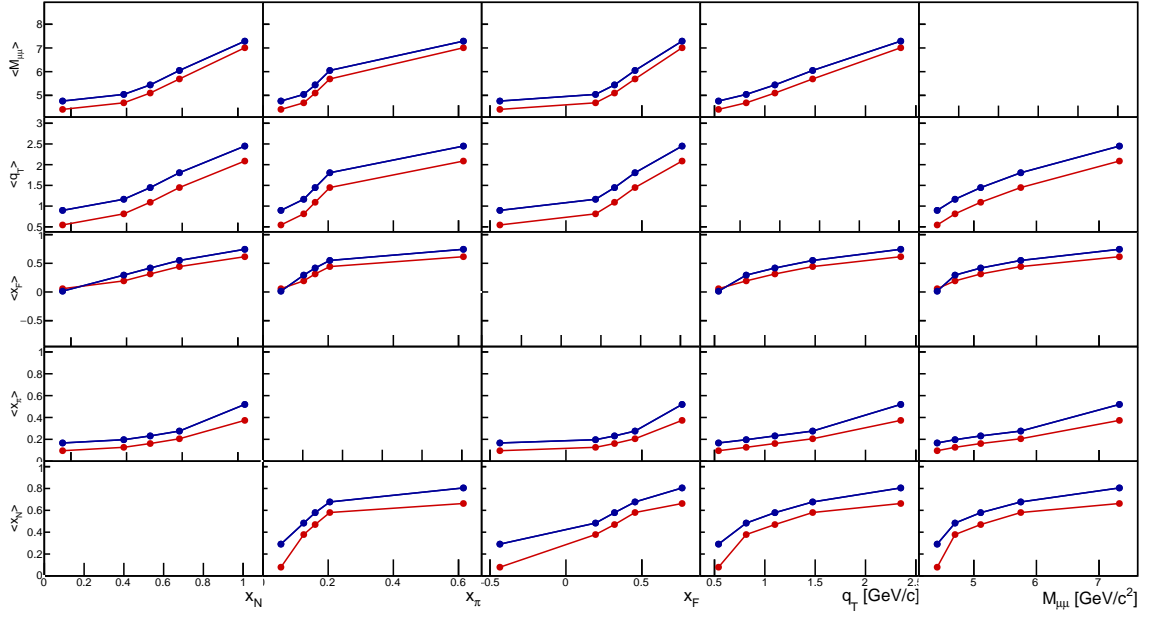


Figure 5.57: Kinematic maps for the NH_3 target. RD in blue, MC data in green. The values are shifted horizontally for a better visibility.

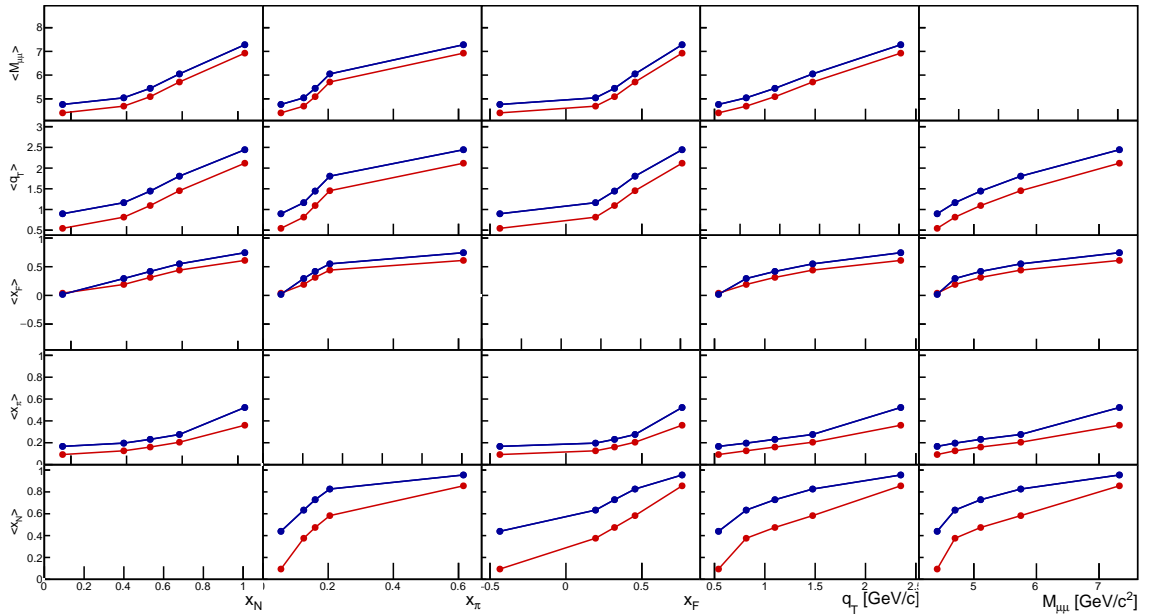


Figure 5.58: Kinematic maps for the W target. RD in blue, MC data in green. The values are shifted horizontally for a better visibility.

5.7.2 Event selection

Selection of the dimuon events for the UAs extraction is similar to the procedure used for the TSAs analysis 5.2.1. Several additional selection criteria are introduced in order to ensure good enough acceptance determination and better MC/RD agreement (not necessary for the TSAs). Different best primary vertex tagging function $PaEvent::iBestCoralPrimaryVertex()$ has been used instead of $PaEvent::iBestPrimaryVertex()$ used in the TSA cut-flow. Referring to the numbering used in the TSA event selection 5.2.1, cuts number 1, 3,..5,7,8,12,...,14 remain unchanged.

Cut #2: LAS-Middle events are not vetoed, which means that events with both LAS-Middle and LAS-Outer triggers fired are included in the analysis.

Cut #6: Quality criteria for the muon tracks. For this analysis, the standard selection $\chi^2 < 10$ was applied, which was tuned based on MC simulations.

Cut #9: The upper q_T -cut has been enforced, while the lower limit stays the same: $0.4 < q_T / (\text{GeV}/c) < 3.0$. The upper limit removes the tail of high- q_T events for which the agreement between RD and MC data is not good enough.

Cut #10: Vertex Z -position limits have been introduced for tungsten case: $-30.0 < Z_{PV}/(\text{cm}) < -10.0$, while NH_3 Z -range is the same as in the TSA analysis (Tab. 5.3). Applied restriction for tungsten target allows one to limit the contamination of Drell-Yan and background events caused by re-interactions of secondary hadrons.

Cut #11: The radial cut used in TSA analysis is replaced by an “elliptical” cut applied on X and Y positions of the primary vertex:

$$\frac{(X_{PV}/(\text{cm}))^2}{1.9^2} + \frac{(Y_{PV}/(\text{cm}) - 0.15)^2}{1.3^2} < 1. \quad (5.28)$$

Five more additional to TSA-case selection criteria have been introduced:

13. Mass cut for the tungsten target: $4.7 < M_{\mu\mu}/(\text{GeV}/c^2) < 8.5$. This cut is introduced to cope with worse dimuon mass resolution in the W target due to multi-scattering and larger background contamination in the high mass range region.
14. Enlarged dead zone cut for the LAST and OT hodoscopes. Slabs around the hodoscope dead zones have non-regular positioning and efficiency variations, which are too difficult to be properly described in the MC. This cut is similar to the criteria #7 (trigger validation),

but with additional rejection of events passing through a narrow (2.5 cm) region around the dead zones of LAS and OT hodoscopes.

15. “Theta-cut” – a cut on μ^- polar angle in the laboratory frame: $\theta_{\mu^-} < 0.02$ (rad). The cut is introduced for the NH_3 case only, since the inconsistency between MC and RD data was observed in the region of small polar angles for μ^- tracks originating from the target cells.
16. Lower x_F cut: $x_F > 0.1$. In the negative x_F region the acceptance is very low and its determination is unreliable.

The selection was applied on the 2018 data (t8-production). The corresponding detailed cut-by-cut statistics is presented in Tab. 5.15.

5.7.3 Kinematic binning

The unpolarized asymmetries λ , μ , ν are evaluated in bins of five kinematic variables x_N , x_π , x_F , q_T , $M_{\mu\mu}$. The bin limits applied for each kinematic dependence are presented in Tab. 5.16 for the NH_3 target and in Tab. 5.17 for the W target. They are chosen in a way that all bins contain nearly the same amount of events.

5.7.4 Evaluation of the Angular Acceptance

As it was discussed in the introductory sections of this Chapter, the main purpose of MC simulations is the precise evaluation of the angular acceptance in different kinematic bins. This information is then used to correct the real data distributions for the acceptance and extract the physics amplitudes. The amplitudes of unpolarized Drell-Yan modulations depend on θ_{CS} and φ_{CS} angles (5.23). Hence, in order to access physics amplitudes in different kinematic bins, the corresponding two-dimensional angular distributions need to be corrected for acceptance. This generalized *acceptance* context invokes all spectrometer-related effects (geometrical acceptance, efficiencies, etc.) and *e.g.* also the reconstruction efficiency impact on angular distributions. In order to evaluate the acceptance, two Monte-Carlo data samples are required. One is the so-called *generated* MC, that is based on “MC-truth” information *i.e.* the original events as they

5.7. ANALYSIS OF SPIN-INDEPENDENT AZIMUTHAL ASYMMETRIES

	P01	P02	P03	P04	P05	P06	P07	P08
1.	158978	288558	221313	210520	124529	135931	244166	88529
2.	114406	204144	156558	147640	86827	94571	170248	61544
3.	113050	201177	154346	145484	85468	93140	167603	60371
4.	112191	199668	153187	144396	84775	92425	166275	59850
5.	60938	110725	86170	80625	46683	52474	92756	33716
6.	60412	109719	85441	79902	46222	52042	91952	33399
7.	21390	42223	31865	30490	17961	21216	36709	13458
8.	19058	37579	29122	26879	17065	19723	33550	11658
9.	19038	37536	29092	26847	17048	19702	33504	11642
10.	16817	33149	25723	23665	14972	17380	29656	10268
NH ₃ target cuts								
11.	4653	9204	7183	6636	4213	4687	8074	2781
12.	4129	8199	6374	5922	3727	4195	7170	2472
13.	4129	8199	6374	5922	3727	4195	7170	2472
14.	3931	7827	6096	5660	3562	4015	6854	2350
15.	3892	7759	6031	5601	3540	3975	6795	2322
16.	3616	7240	5645	5233	3315	3713	6393	2176
17.	3579	7166	5585	5202	3279	3671	6335	2149
W target cuts								
11.	5509	11081	8576	7909	4947	5853	10133	3501
12.	4865	9779	7598	7030	4409	5206	8992	3100
13.	3039	6052	4752	4418	2765	3238	5650	1923
14.	2729	5475	4322	4015	2501	2886	5129	1731
15.	2697	5381	4249	3933	2451	2828	5041	1703
16.	2697	5381	4249	3933	2451	2828	5041	1703
17.	2631	5250	4158	3853	2403	2756	4935	1668

Table 5.15: Cut-by-cut event flow by periods in t8 production of 2018 for UAs analysis.

x_N	0.00	0.11	0.14	0.18	0.23	1.00
x_π	0.00	0.34	0.44	0.53	0.65	1.00
x_F	-0.10	0.13	0.26	0.38	0.53	1.00
q_T	0.40	0.68	0.95	1.25	1.70	3.00
$M_{\mu\mu}$	4.30	4.53	4.87	5.35	6.15	8.50

Table 5.16: Kinematic bin limits for UAs analysis in the HM range for data from the NH₃ target.

x_N	0.00	0.13	0.17	0.21	0.27	1.00
x_π	0.00	0.34	0.43	0.53	0.65	1.00
x_F	-0.10	0.10	0.23	0.35	0.50	1.00
q_T	0.40	0.74	1.02	1.34	1.77	3.00
$M_{\mu\mu}$	4.70	4.95	5.29	5.75	6.55	8.50

Table 5.17: Kinematic bin limits for UAs analysis in the HM range for data from the W target.

were generated and propagated through the simulated spectrometer. Only events passing kinematic selections applied in real data are considered. The other sample is the *reconstructed* MC. It consists of MC-events that are processed (reconstructed) using simulated detector responses. The MC data in this case undergo same reconstruction process as the real data. Simulations and acceptance extractions are done on a period-by-period basis (beam simulation, trigger and detector efficiencies, detector positions, etc.). The acceptance distribution is obtained as the ratio of MC generated (N_{MC}^{gen}) and reconstructed (N_{MC}^{rec}) counts in 2D angular bins:

$$A(\cos\theta, \varphi) = \frac{N_{MC}^{rec}(\cos\theta, \varphi)}{N_{MC}^{gen}(\cos\theta, \varphi)}. \quad (5.29)$$

In Figs. 5.59-5.61 different angular generated, reconstructed and acceptance distributions are shown.

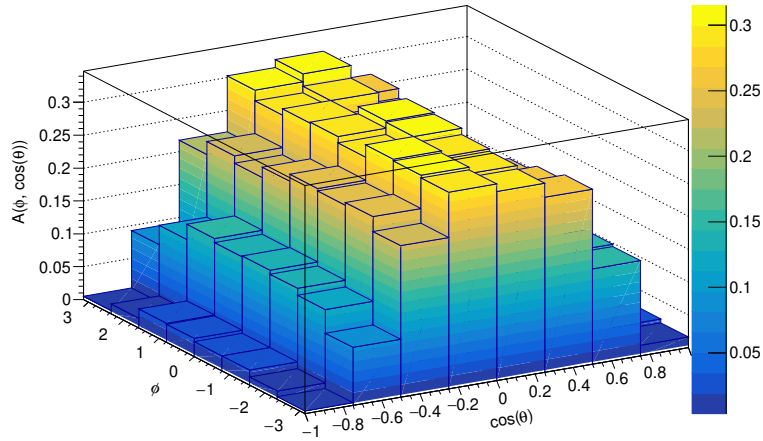


Figure 5.59: An example of a two-dimensional $\cos(\theta) \times \varphi$ histogram built for reconstructed MC data.

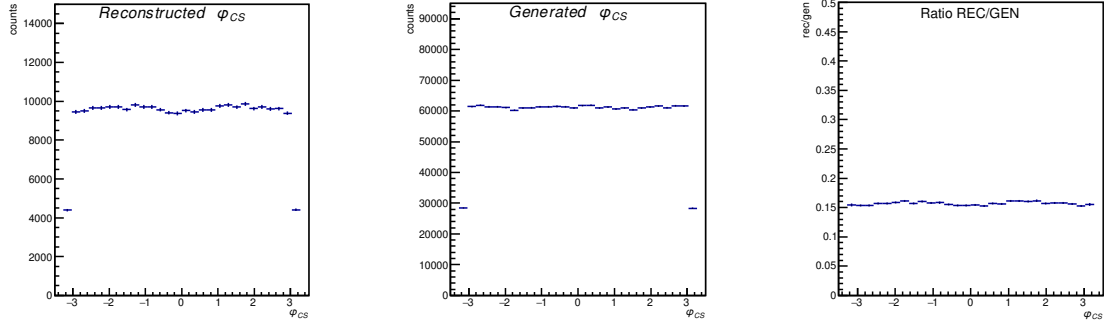


Figure 5.60: From left to right: reconstructed, generated distributions and reconstructed to generated ratio for φ_{CS} angle.

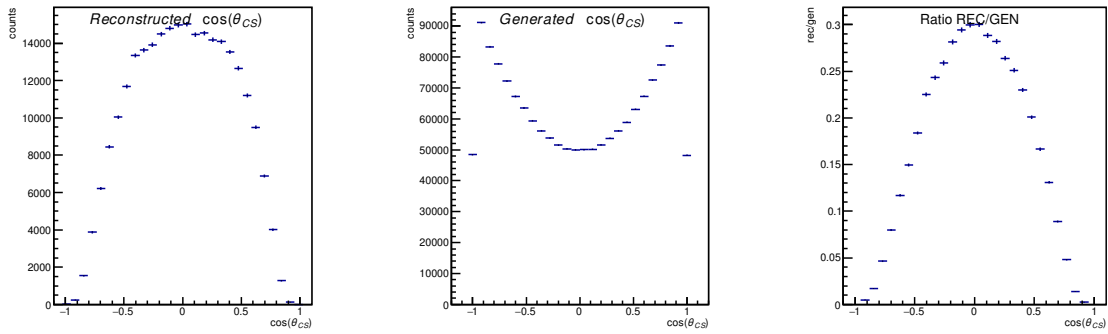


Figure 5.61: From left to right: reconstructed, generated distributions and reconstructed to generated ratio for $\cos(\theta_{CS})$.

5.7.5 Extraction of Drell-Yan Unpolarized Asymmetries

In this section the method used for the extraction of the spin-independent azimuthal asymmetries is presented. Three unpolarized asymmetries λ , μ and ν are evaluated in kinematic bins using the so-called Histogram Binned Likelihood (HBL) method. It is a reconsideration of the SIDIS 1D-Ratio (1DR) approach used in COMPASS SIDIS unpolarized asymmetry analyses [123]. In order to extract physics amplitudes, in 1DR method the cross-section function comprising the azimuthal asymmetries was being fit to an acceptance-corrected ratio histogram¹³. At first, the same approach has been used also for DY UA extractions extending the ratio to a 2D-case (2DR method) of Drell-Yan (8×8 binned 2D $(\cos\theta, \varphi)$ histograms). However, in case of limited DY statistics, in low-acceptance kinematic and angular region in the corners of the phase-space, the method was yielding biased results. This has been overcome in the HBL approach discussed in the next sections, which was further extended to fit simultaneously

¹³ratio-histogram was obtained by a division of one-dimensional real data and MC-acceptance histograms

LAST-LAST and LAST-OT histograms.

Histogram Binned Likelihood

For each kinematic bin, Histogram Binned Likelihood fit method is applied to two-dimensional $(\cos \theta, \varphi)$ data-histograms (eight by eight equidistant bins over $[-1,1]$ for $\cos \theta$ and $[-\pi, \pi]$ for φ), with Poissonian errors assigned to the bin content. The acceptance is defined on the same 8×8 angular grid. The MC sample is chosen to be large enough and the acceptance (A) enters as a scale-factor with the uncertainties (σ_A) assigned by binomial formula [218]:

$$\sigma_A = \frac{\sqrt{N_{MC}^{Gen} \cdot A \cdot (1 - A)}}{N_{MC}^{Gen}}. \quad (5.30)$$

The corresponding fit function is then defined as follows:

$$f(\cos \theta, \varphi) = A(\cos \theta, \varphi) \cdot N \cdot \left(1 + \lambda \cos^2 \theta + \mu \sin 2\theta \cos \varphi + \frac{\nu}{2} \sin^2 \theta \cos 2\varphi \right), \quad (5.31)$$

where N, λ, μ, ν are parameters to be fitted.

The fit is performed using CERN-ROOT framework and the `TH2D::FindFit()` method (“`RILEMQN0`” option is used). Initial values are set to zero for three asymmetries and to one for the normalization factor N . Thus, three unpolarized asymmetries are extracted simultaneously.

Histogram Binned Likelihood – Three-dimensional simultaneous fit

The standard HBL approach is used to extract the asymmetries separately for LAST-LAST and LAST-OT trigger events. Extraction of asymmetries without differentiating the data from different triggers is not straightforward *i.e.* one cannot just add the data from both triggers into a single histogram in MC and RD and perform acceptance-corrected fit. The reason for this is that MC lacks the veto-life-time description for the triggers, while both the veto-life-time and the acceptance coverage for LAST-LAST and LAST-OT are different. Hence, the mix of LAST-LAST and LAST-OT events would by default not have the same proportions in MC and RD. In addition, the dimuon triggers have different coverage of kinematics, therefore it is difficult to combine the results from two triggers after the UAs extraction. A way to overcome this is to extend the method to perform a simultaneous fit of disentangled LAST-LAST and LAST-OT data. In order to do this, the abscissa ($\cos \theta$) of the two-dimensional angular histogram is extended from eight bins over $[-1,1]$ to sixteen bins over $[-1,3]$, where the original range $[-1,1]$ is

filled by inclusive LAST-LAST trigger events, while the extended range [1,3] contains OT-LAST trigger events (no LAST-LAST trigger fired). The same modification of the angular histogram is done also for the MC acceptance extraction. Obtained data-histograms for one of the periods are presented in Fig. 5.62. The HBL fitting function $f(\cos\theta, \phi)$ is modified then as follows:

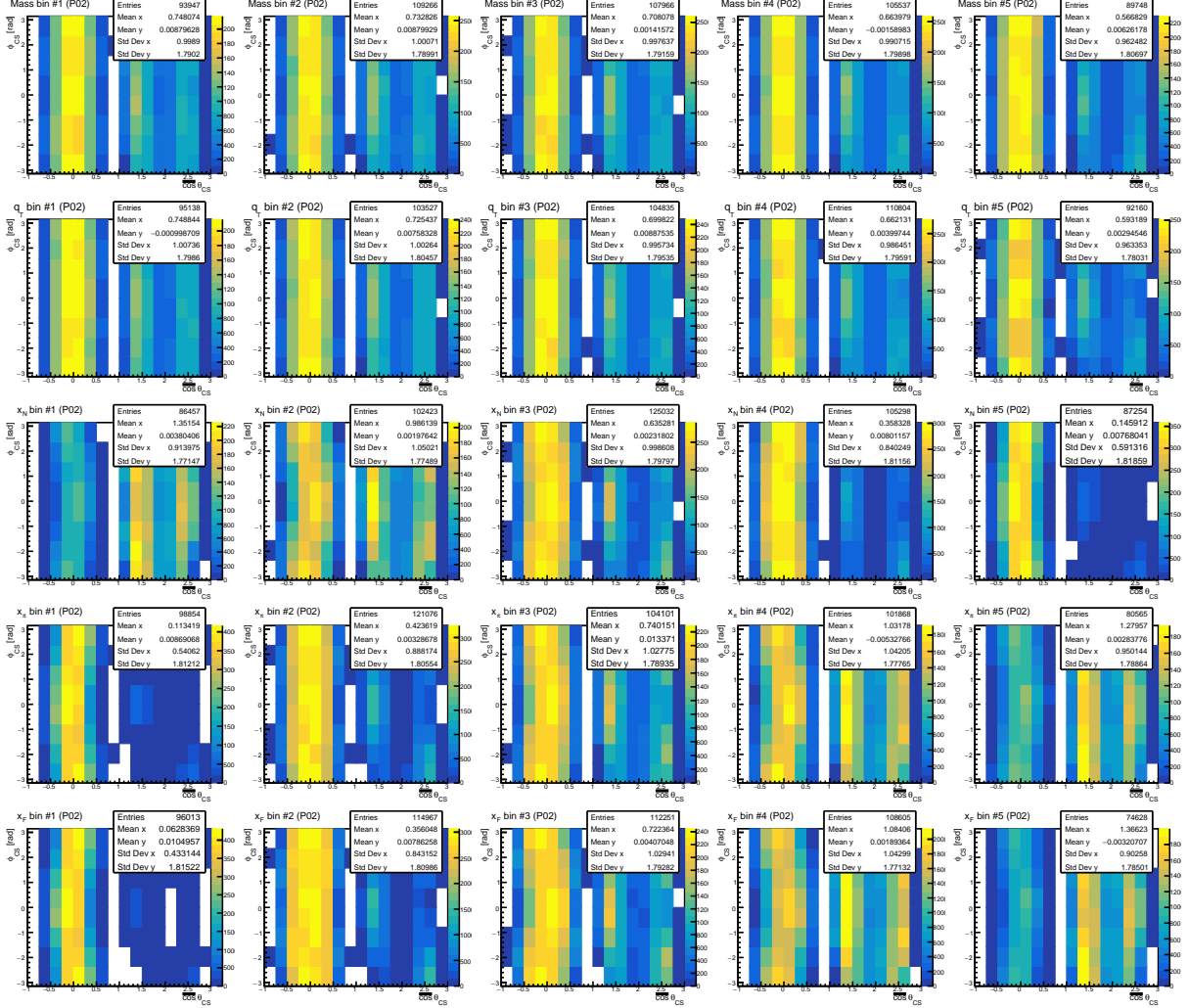


Figure 5.62: An example of the extended 16x8 histograms used in the acceptance estimation in case of HBL Three-dimensional simultaneous fit (P02, reconstructed MC).

$$f(\cos\theta, \varphi) = \begin{cases} A(\cos\theta, \varphi)N_0(1 + \lambda \cos^2\theta + \mu \sin 2\theta \cos\varphi + \frac{\nu}{2} \sin^2\theta \cos 2\varphi), & \text{if } -1 < \cos\theta \leq 1 \\ A(\cos\theta, \varphi)N_1(1 + \lambda \cos^2\theta' + \mu \sin 2\theta' \cos\varphi + \frac{\nu}{2} \sin^2\theta' \cos 2\varphi), & \text{if } 1 < \cos\theta \leq 3 \end{cases}, \quad (5.32)$$

where $\cos\theta' = \cos\theta - 2$, and N_0 and N_1 are normalization parameters, which are not supposed to be the same due to the inconsistency of veto-life-time of two triggers. Thus, five parameters

N_0 , N_1 , λ , μ , ν are extracted from the fit.

5.7.6 Systematic studies

Various aspects of the UA analysis were checked for possible systematic effects. The list of performed tests is very extensive. Only results from selected studies are commented in the next sections for brevity, among them: the compatibility of the results in the periods, compatibility of the results in the target cells, check of rotational invariants for different reference frames, possible biases due to different selection criteria and dependence on the bin size.

Compatibility of results from different periods

Compatibility of spin-independent azimuthal asymmetries from different periods was checked using the same method as for TSAs analysis (see Sec. 5.5.1). In case of UAs the method was separately applied for each set of the results of λ , μ , ν for three reference frames (Collins–Soper, Gottfried-Jackson and Helicity frame). The maximum of the $\sigma_{syst}/\sigma_{stat}$ value among these sets is taken as a systematic uncertainty associated with this test. The corresponding pull-histograms fitted to a normal distribution and evaluated $\sigma_{syst}/\sigma_{stat}$ values are shown in Fig. 5.63 for the NH_3 target and in Fig. 5.64 for the W target. In general, no strong incompatibilities between different periods were found.

Compatibility of results from different target halves

Results extracted from upstream and downstream halves of the targets¹⁴ are supposed to be the same. This assumption holds if the acceptance is properly determined from the MC simulations. Thus, possible inconsistencies in the acceptance corrections could lead to biases when comparing the results from the upstream and downstream target halves. To estimate this systematic uncertainty the pull method can be also applied using a formula:

$$pull = \frac{A_u - A_d}{\sqrt{\sigma_{A,u}^2 + \sigma_{A,d}^2}}, \quad (5.33)$$

¹⁴In case of NH_3 this refers to the cells, while for tungsten target the upstream half is defined as first 10 cm ($-10 < Z_{PV}/(\text{cm}) < -20$), and the downstream corresponds to the second 10 cm ($-20 < Z_{pv}/(\text{cm}) < -30$).

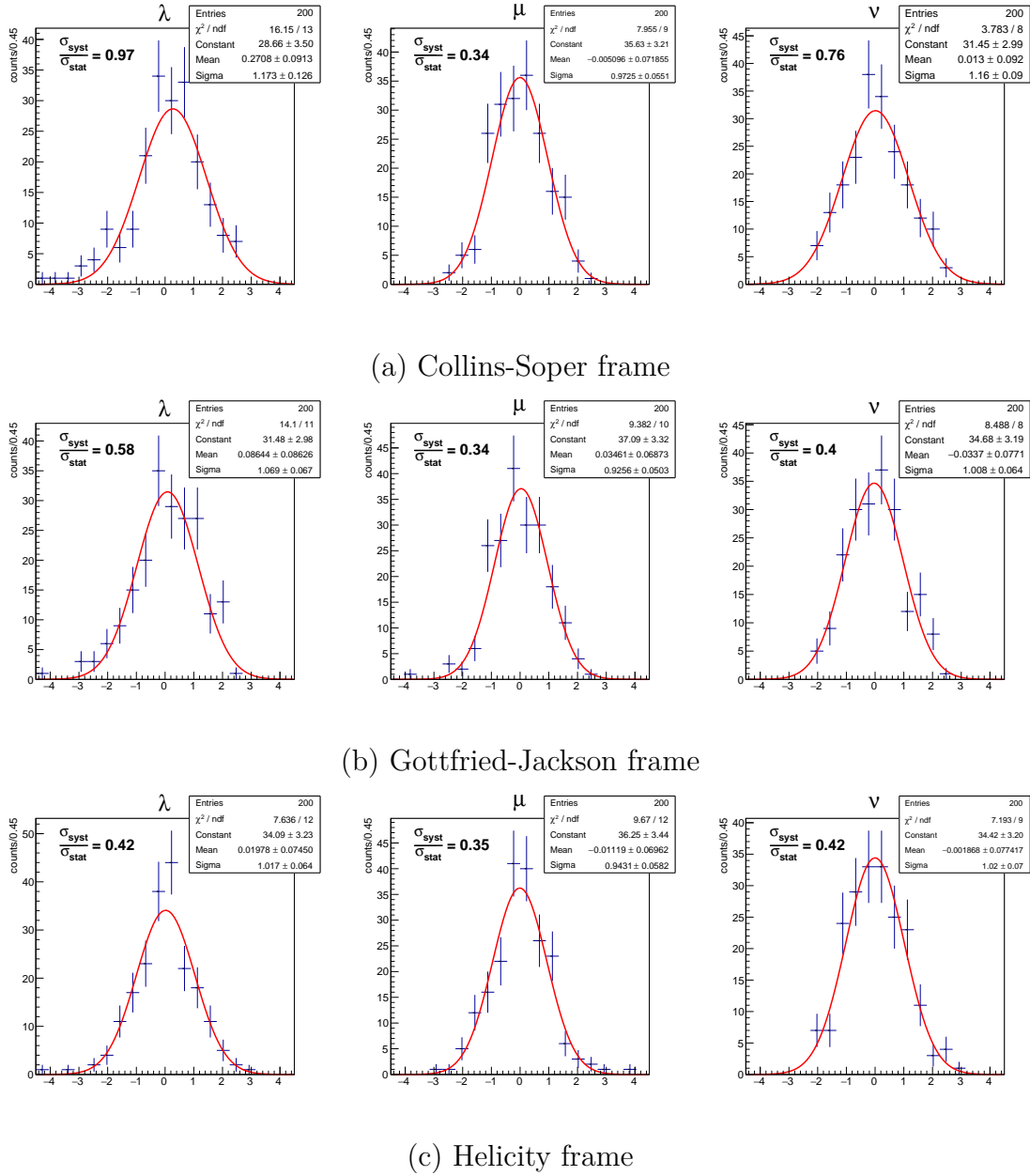


Figure 5.63: Pull-histograms and their fit from different periods for the NH_3 target.

where u and d indices correspond to the values obtained from the upstream and the downstream halves, respectively. The pull-histograms fitted with Gaussian functions and estimated $\sigma_{\text{syst}}/\sigma_{\text{stat}}$ values are shown in Fig. 5.65 for the NH_3 target and in Fig. 5.66 for the W target.

Check of rotational invariance

The asymmetries λ , μ , ν may differ depending on the dilepton rest frame used (in case of COMPASS: Collins–Soper, Gottfried–Jackson and Helicity frames). However, the following

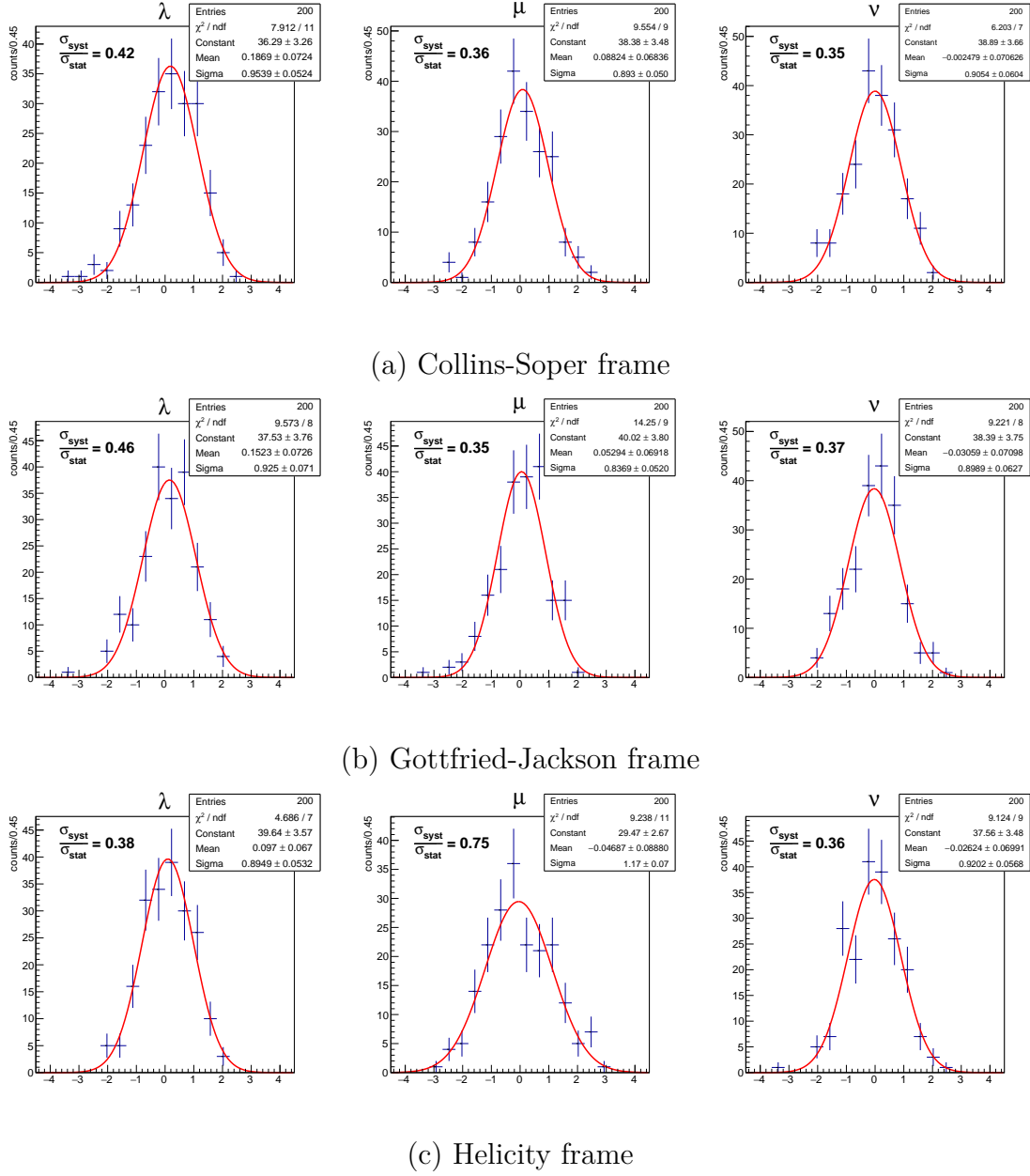
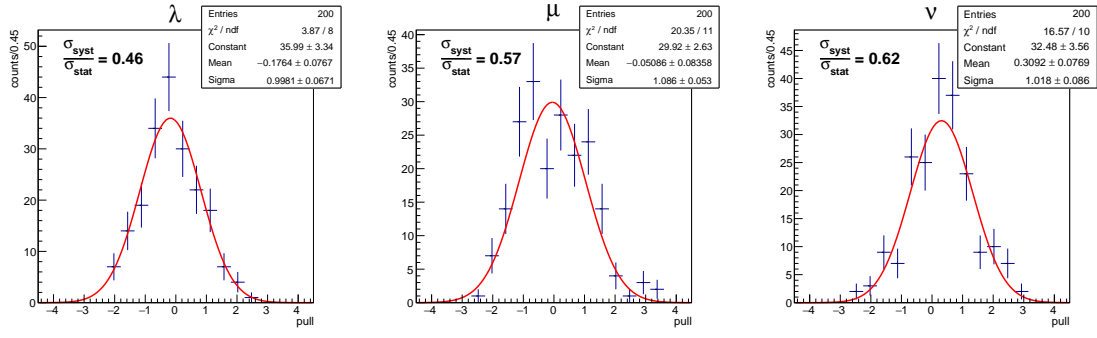


Figure 5.64: Pull-histograms and their fit from different periods for the W target.

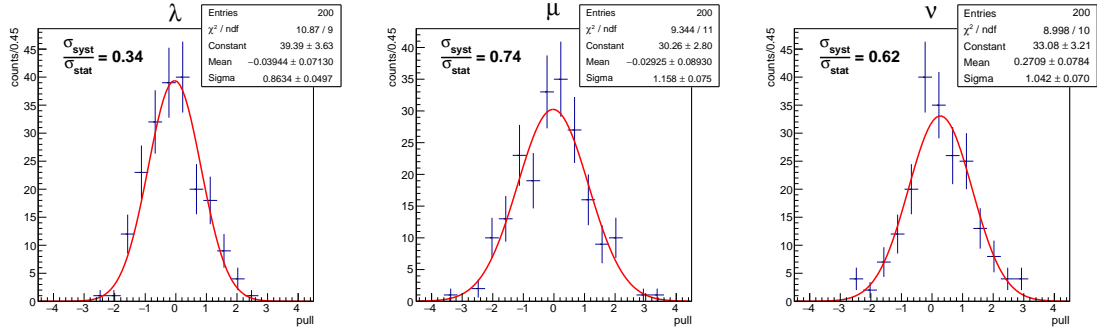
rotational invariant quantities are supposed to be frame-independent [168, 219, 220]:

$$\tilde{\lambda} = \frac{2\lambda + 3\nu}{2 - \nu}, \quad F = \frac{1 + \lambda + \nu}{3 + \lambda}. \quad (5.34)$$

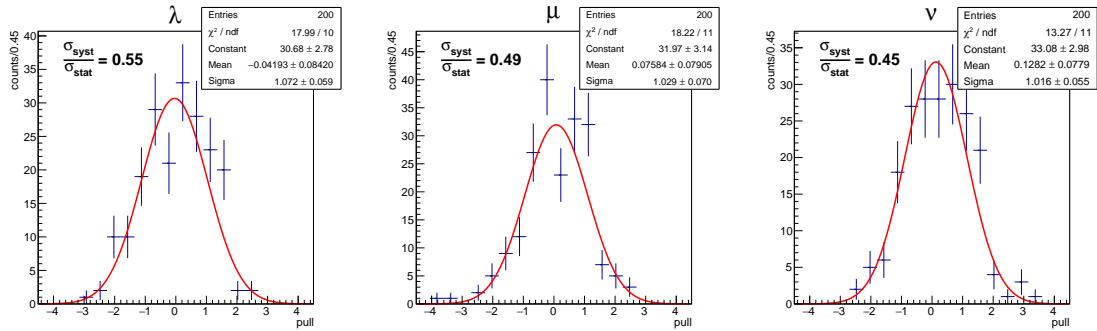
The evaluation of these invariant observables has been performed for each of the three dilepton rest frames selected for the analysis and results have been compared. In case of inconsistencies it would point to possible systematic effects in the analysis. The $\tilde{\lambda}$ and F values compared in various frames are shown in Figs. 5.67 and 5.68. The results are in agreement within one



(a) Collins-Soper frame



(b) Gottfried-Jackson frame



(c) Helicity frame

Figure 5.65: Pull-histograms and their fit from two target cells of the NH_3 target.

standard deviation (apart from a value from the 4th bin in x_N in the Helicity frame, which is slightly off the trend).

Summary on systematic uncertainties

As it was mentioned in the beginning of this section, the results of several performed tests are not quoted here for brevity reasons. In particular, the following studies were performed: the relaxation of q_T cuts, different options for hodoscope dead-zone cuts, changing the number of

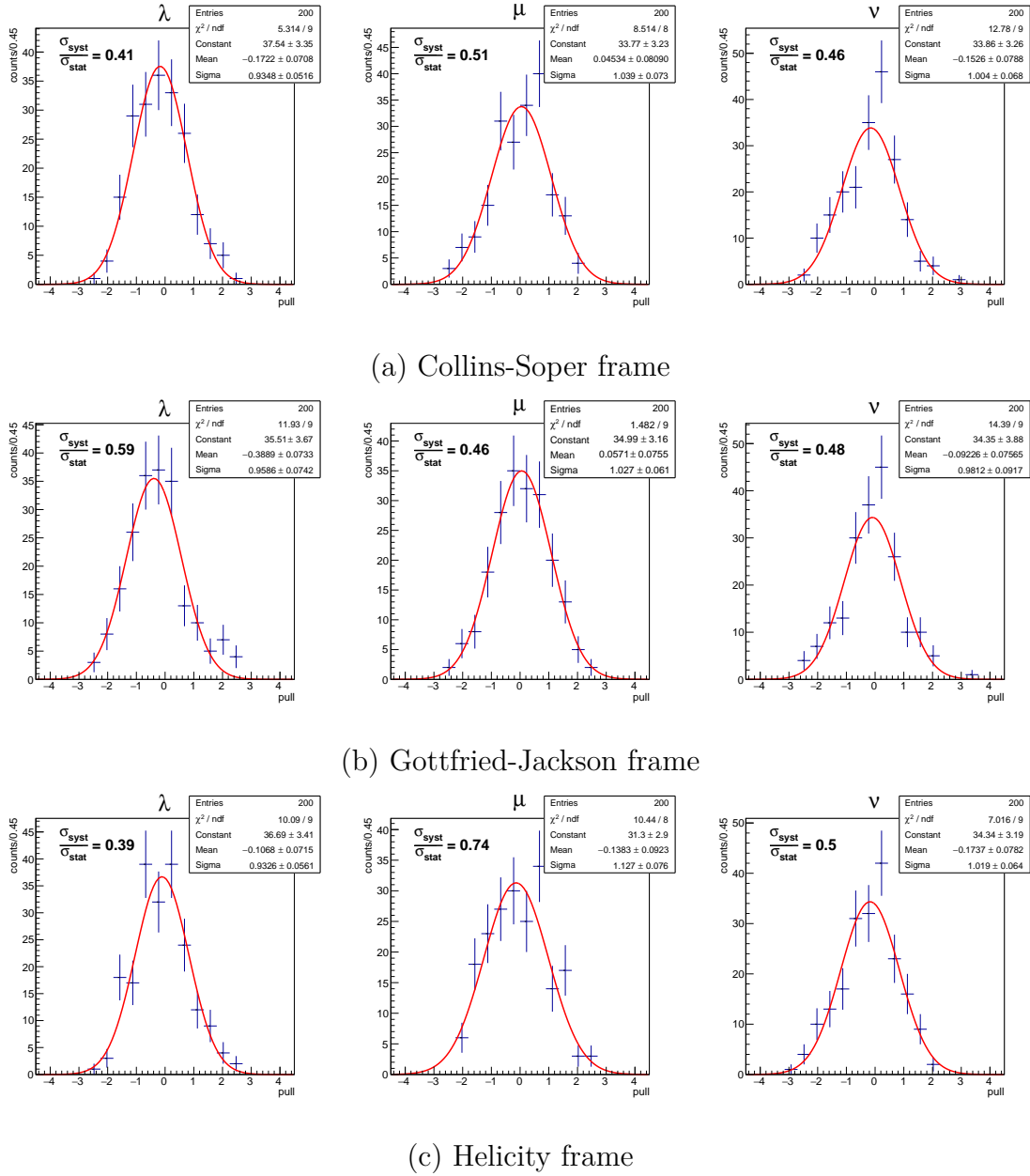


Figure 5.66: Pull-histograms and their fit from two target halves of the W target.

the bins in RD and acceptance 2D histograms, various options for θ_{μ^-} -cut, detector alignment changes, etc. None of these tests did not reveal significant systematic distortions. Several additional studies are ongoing or planned to be performed, among them: variation of hodoscope geometries (pitch, position) and efficiencies, different generator settings and inputs (*e.g.* different pion, proton PDFs), reweighing of the MC events to better fit the RD distributions, etc. These tests require dedicated MC productions that will be done in the near future. For the moment conservative estimations of systematic uncertainties suggest that they are about the

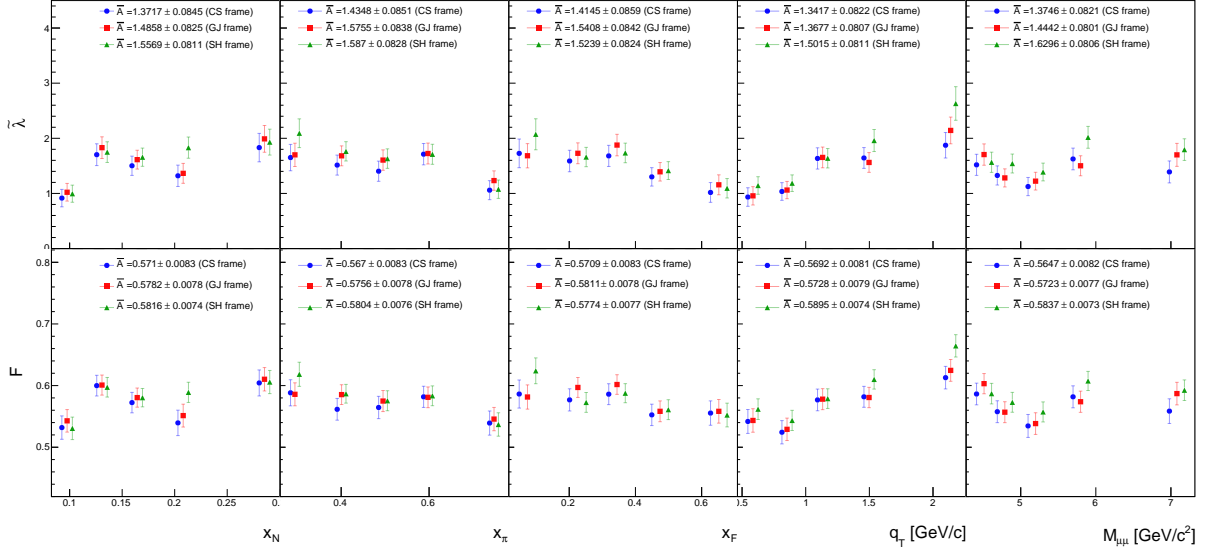


Figure 5.67: Invariant $\tilde{\lambda}$ and F extracted from three dilepton rest frames for the NH_3 target (2018 data, t8 production).

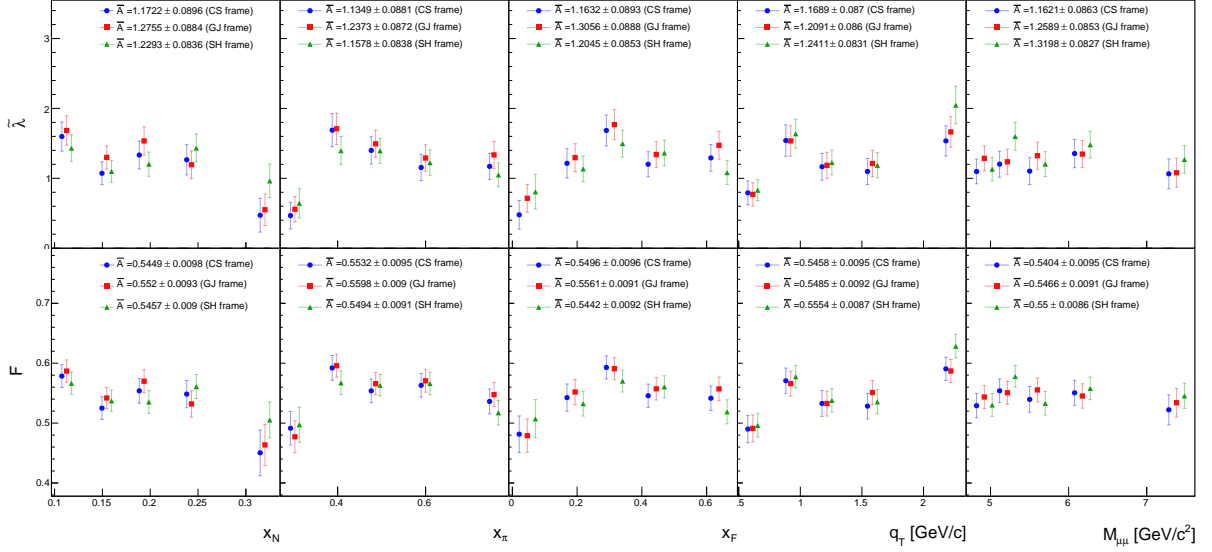


Figure 5.68: Invariant $\tilde{\lambda}$ and F extracted from three dilepton rest frames for the W target (2018 data, t8 production).

statistical ones $\sigma_{\text{sys}} \approx \sigma_{\text{stat}}$.

5.7.7 Extraction of J/ψ Unpolarized Asymmetries

The framework for the extraction of unpolarized asymmetries is also applicable for the J/ψ mass range. The main fit formula (5.31) and its modification for the 3D simultaneous fit (5.32)

remain valid in J/ψ production, so, the same fitting procedure can be adopted for the J/ψ UA analysis. Main differences in the procedure are the corresponding MC and RD inputs. While the RD samples are identical to the TSA analysis, the MC data have to be additionally produced and studied, that goes out of the scope of this Thesis. However, within the J/ψ TSA analysis an estimation of the λ value was needed. Therefore, a part of available J/ψ MC samples has been used to preliminary estimate the spin-independent azimuthal asymmetries in the J/ψ region.

The extraction was done in the mass range from 3.0 to 3.3 GeV/c^2 using the P03 data of 2018, since there was the most appropriate available MC sample for this period, which was reconstructed with corresponding 2D detector and trigger efficiencies. The asymmetries were obtained as functions of four kinematic variables: x-variables (x_N, x_π, x_F) and q_T . The binning used is the same as in the J/ψ TSA analysis for the same variables (Tab. 5.5). The obtained results are presented in the next Section.

5.7.8 Results

The extractions of Drell-Yan UAs were performed for three dilepton rest frames: Collins–Soper, Gottfried–Jackson and Helicity frame. The results are presented in Figs. 5.70, 5.71 for both NH_3 and W targets. Similar to the TSAs, at the first step the asymmetries are obtained for each data taking period separately (period-wise results for the CS frame are presented in Fig. 5.69). Afterwards, the fit results are merged as weighted averages; corresponding results for NH_3 and tungsten are presented in Figs. 5.70, 5.71. Note that the positions of NH_3 and W points in Figs. 5.70, 5.71 along the abscissa do not match due to slightly different mass ranges and kinematic binning (see Tabs. 5.16, 5.17). Presented results are obtained from the P01-P08 periods of the 2018 t8-production and the acceptance corrections were performed using MC sample that was 100 times larger compared to the real data statistics.

All results, obtained in the HM range, were successfully cross-checked with COMPASS-Taipei group (Academia Sinica of Taiwan): maximum difference between the results is below 0.006 in units of statistical uncertainty.

As it was mentioned earlier, the evaluated systematic uncertainties are estimated to be about the statistical ones $\sigma_{syst} \approx \sigma_{stat}$.

Preliminary results on UAs in $J\psi$ production are shown in Figs. 5.72–5.73 for three dilepton rest frames comparing two targets. The extraction was done only from the P03 period of

2018 due to the use of an appropriate MC sample available at that moment. There is also no conclusion on the final systematic uncertainty for the same reason. Nevertheless, preliminary estimations were obtained using only one period. The λ asymmetry was found as value of 0.2 and was used for the TSA analysis in the J/ψ mass range. In Fig. 5.74, the results are also presented in terms of invariant $\tilde{\lambda}$ and F in order to avoid possible ambiguities in the interpretation of the results due to the definition of a reference frame [168].

It is interesting to compare the results obtained with NH_3 and tungsten targets *e.g.* in the view of possible nuclear effects. For a direct comparison one needs to employ same binning and kinematic cuts, which means that the dimuon mass selection used for tungsten case ($4.7 < M_{\mu\mu}/(\text{GeV}/c^2) < 8.5$, see Sec. 5.7.2) has to be applied also to the NH_3 data. The comparison is presented in Fig. 5.75 (top panel). One can see that while λ and μ are compatible, ν asymmetries differ. The deviations are evident in correlated low x_π and x_F regions, but also at large q_T . However, it appears that the difference is mainly driven by low $x_\pi(x_F)$ region. In Fig. 5.75 (bottom panel) same comparison is shown after additional $x_\pi > 0.34$ cut. The agreement further improves if one implies a cut on x_F ($x_F > 0.23$). Similar test has been also performed for the J/ψ mass range ($3.0 < M_{\mu\mu}/(\text{GeV}/c^2) < 3.3$). In case of UAs in $J\psi$ production, the cut of the first x_π bin ($x_\pi > 0.25$) improves the agreement between the targets for the μ asymmetry (Fig. 5.76). These observations might point to *e.g.* a potential problem with acceptance description in the region of low $x_\pi(x_F)$, or a signature of DY events produced from the secondary hadron interactions, or nuclear effects. A deeper investigation is required to clarify these hypotheses, which goes beyond the scope of this Thesis.

The comparison with other experimental DY results from the past and with DY NNLO calculations and available model predictions are presented in concluding Chapter of this Thesis 5.7.8.

5.7. ANALYSIS OF SPIN-INDEPENDENT AZIMUTHAL ASYMMETRIES

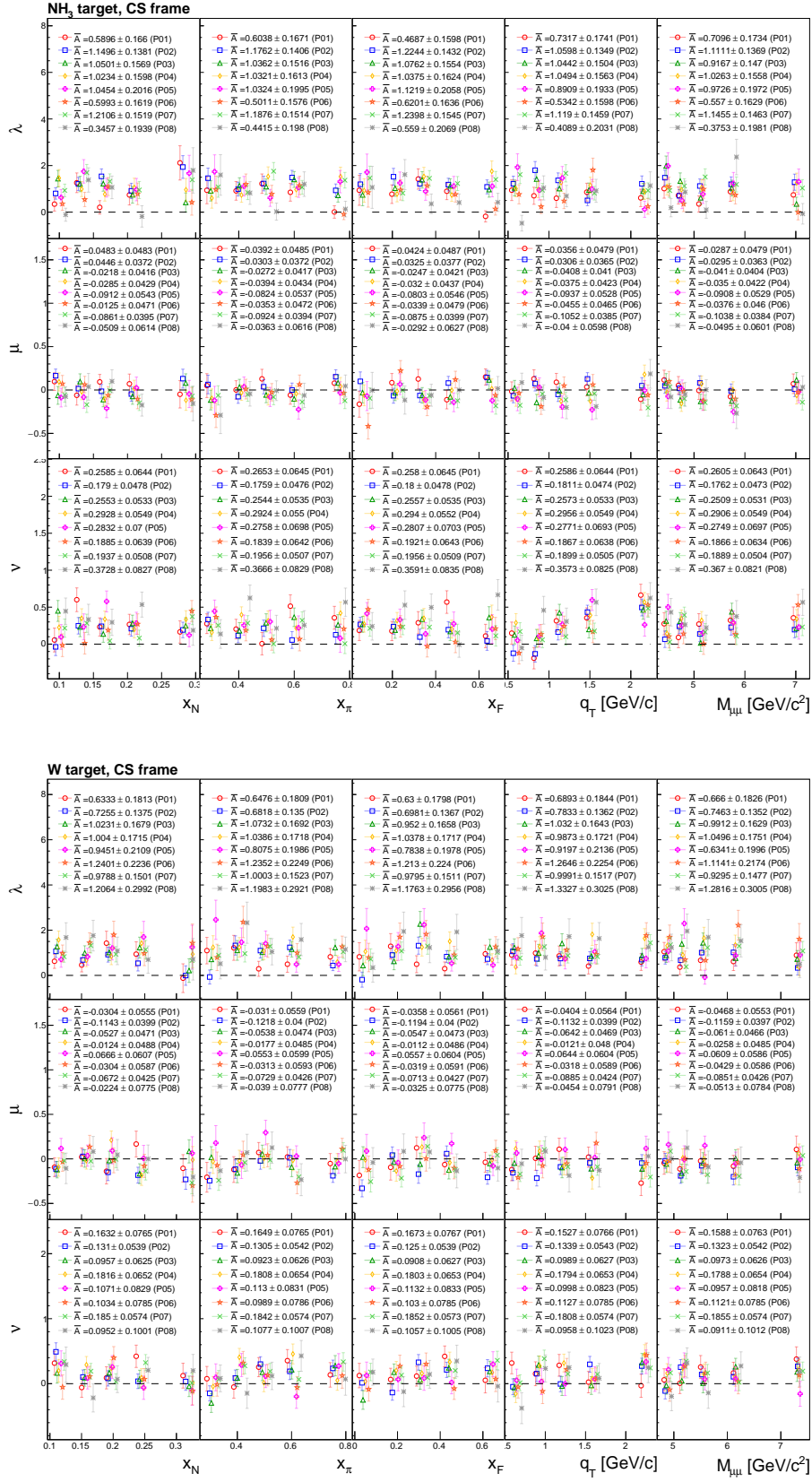


Figure 5.69: UAs by periods for the NH₃ (top panels) and W (bottom panels) targets in the Collins-Soper frame (2018 data, t8 production).

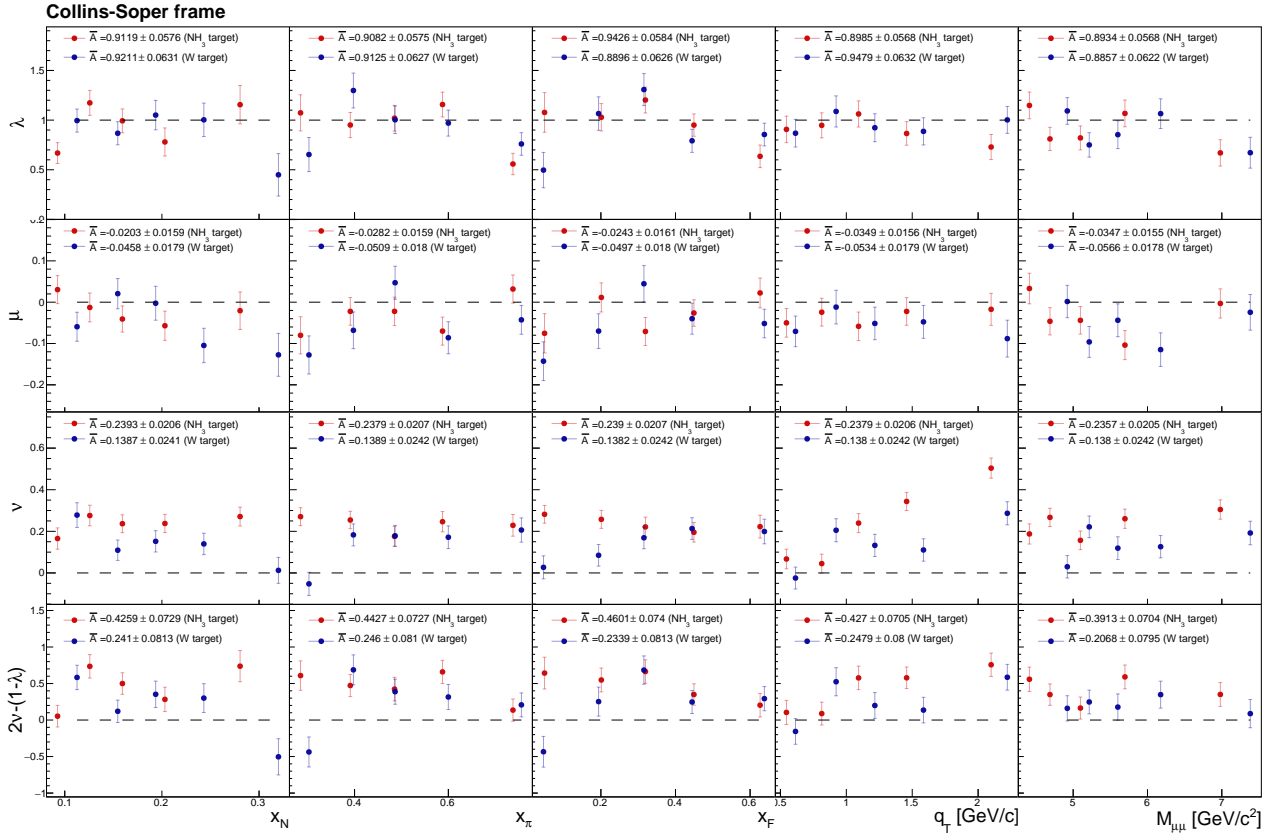


Figure 5.70: NH_3 (red points) and W (blue points) UAs and Lam-Tung relation in the HM range in the Collins-Soper frame (2018 data, t8 production).

5.7. ANALYSIS OF SPIN-INDEPENDENT AZIMUTHAL ASYMMETRIES

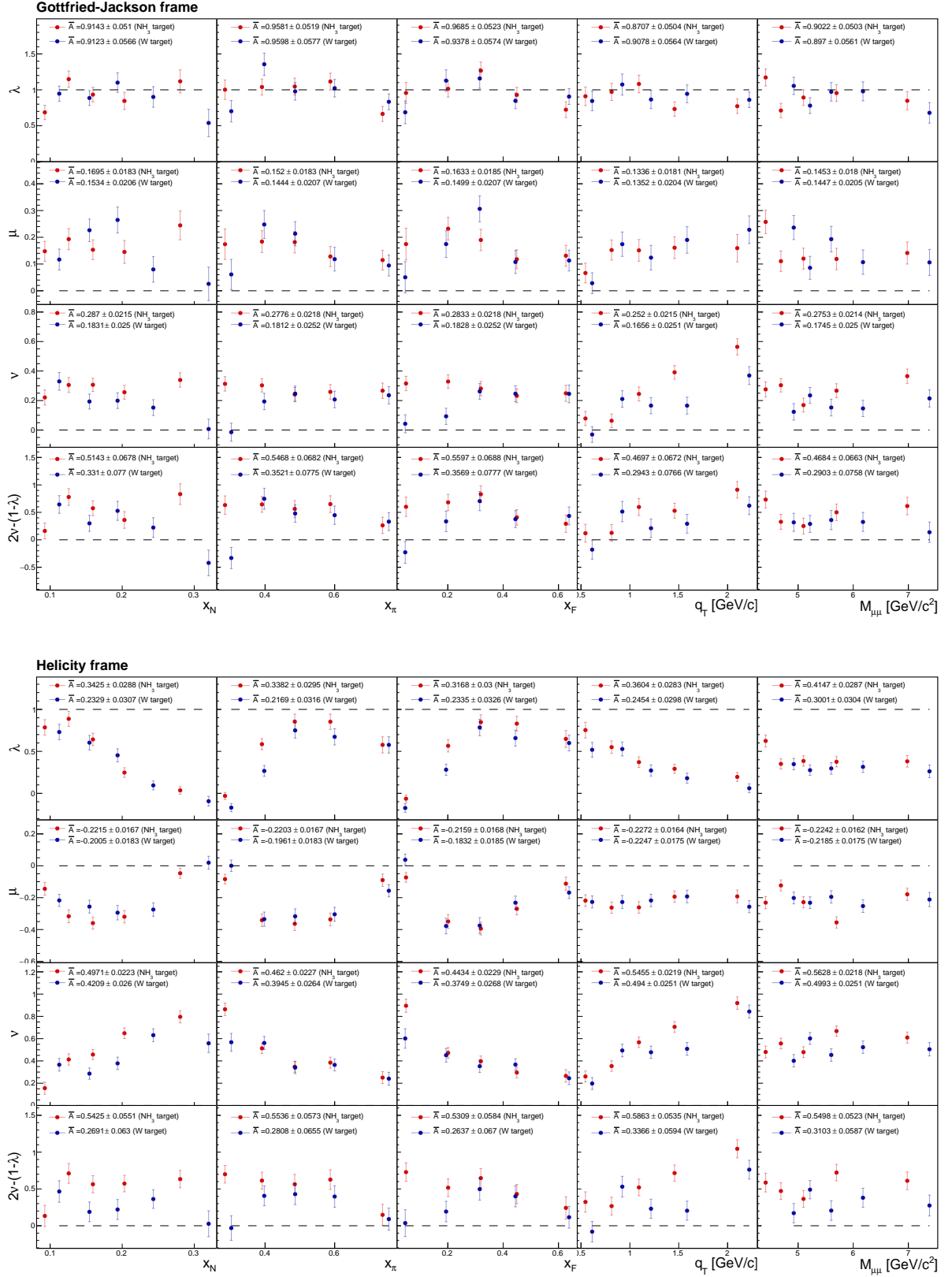


Figure 5.71: NH_3 (red points) and W (blue points) UAs and Lam-Tung relation in the HM range (2018 data, t8 production). Top panel: Gottfried-Jackson frame, Bottom panel: Helicity frame.

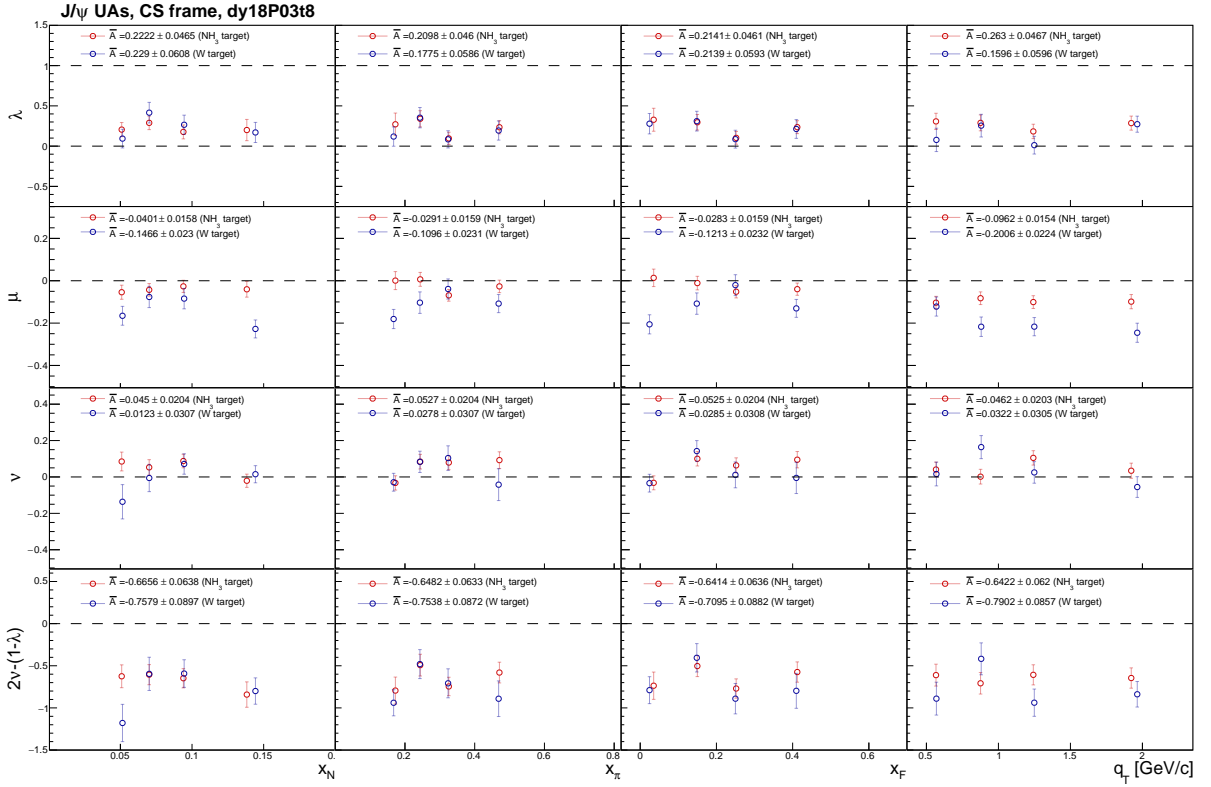


Figure 5.72: NH_3 (red points) and W (blue points) UAs and Lam-Tung relation in the Collins-Soper frame from J/ψ production (2018 data, only P03 period).

5.7. ANALYSIS OF SPIN-INDEPENDENT AZIMUTHAL ASYMMETRIES

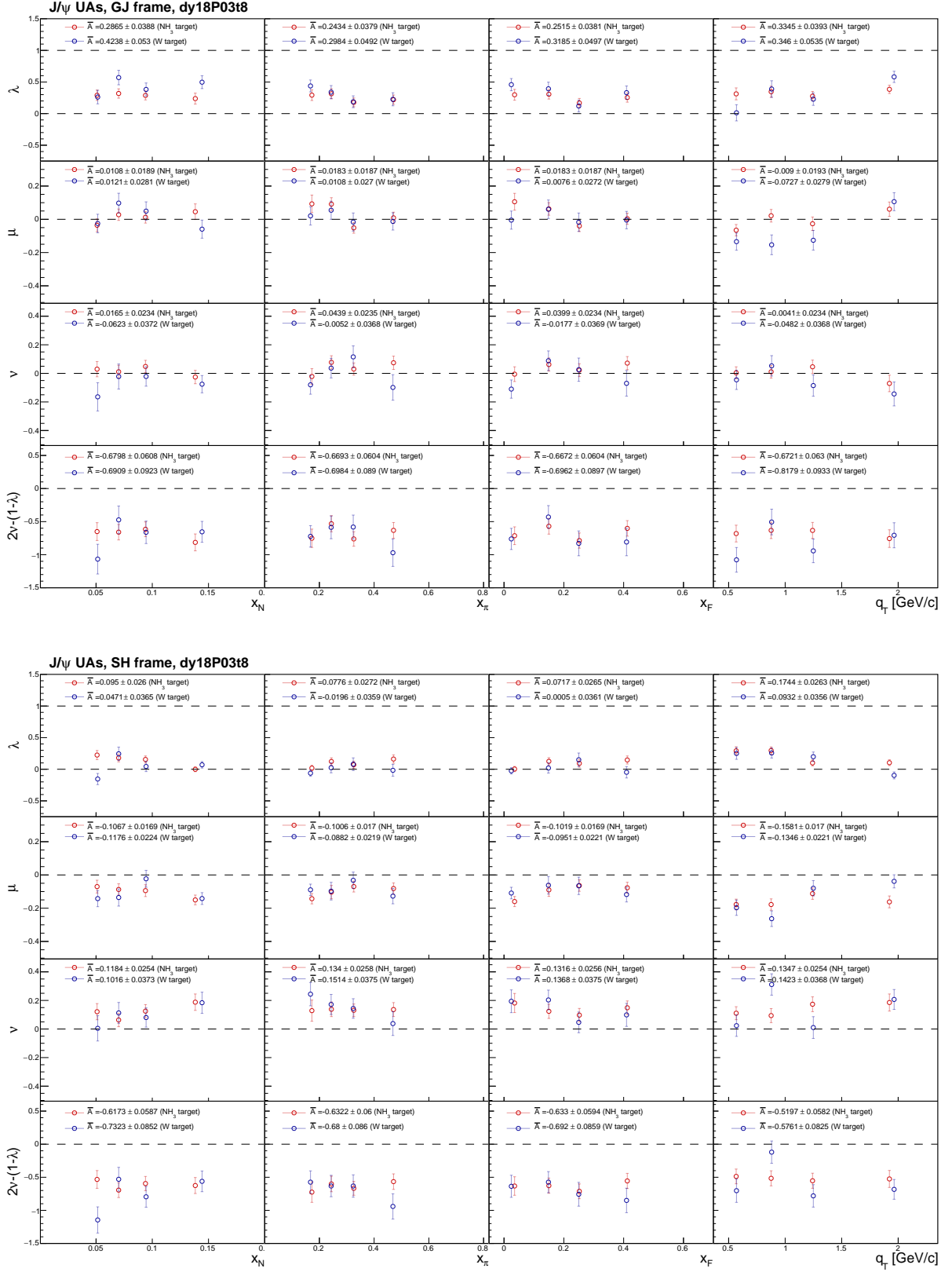


Figure 5.73: NH₃ (red points) and W (blue points) UAs and Lam-Tung relation from J/ψ production (2018 data, only P03 period). Top panel: Gottfried-Jackson frame, Bottom panel: Helicity frame.

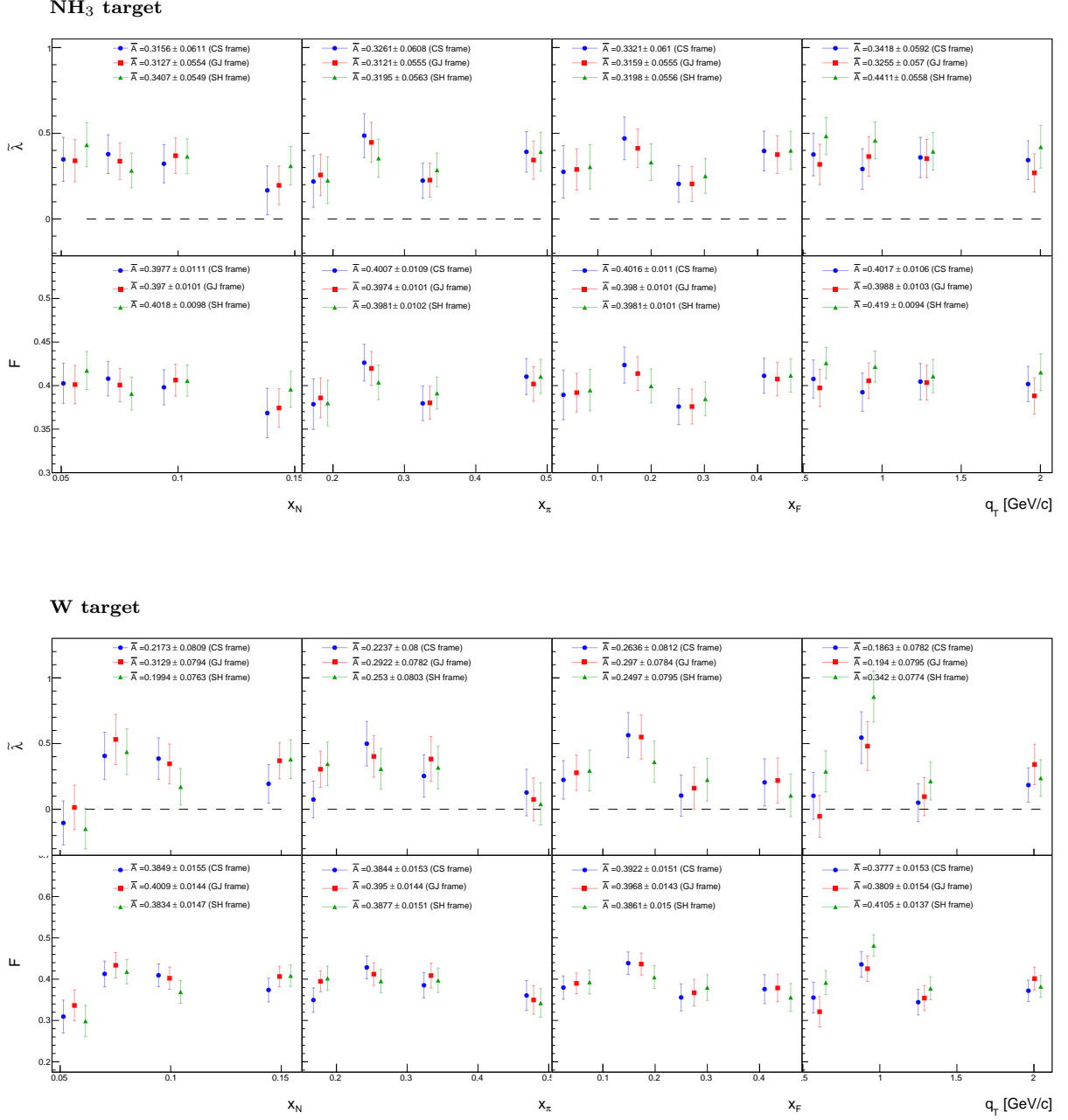


Figure 5.74: Invariant $\tilde{\lambda}$ and F extracted from three dilepton rest frames for the NH₃ target from J/ψ production ($3.0 < M_{\mu\mu}/(\text{GeV}/c^2) < 3.3$). Top panel: NH₃ target, Bottom panel: tungsten target.

5.7. ANALYSIS OF SPIN-INDEPENDENT AZIMUTHAL ASYMMETRIES

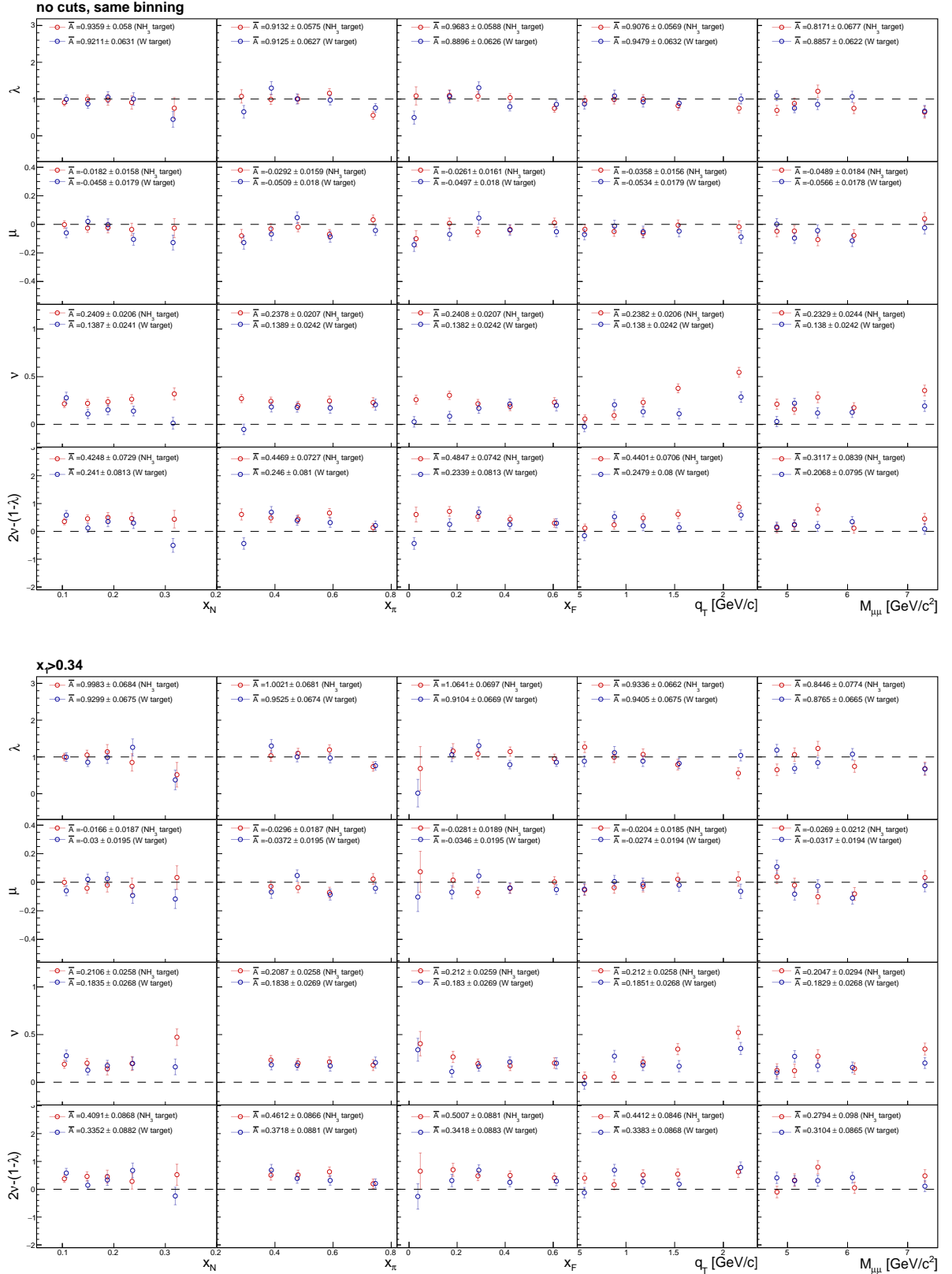


Figure 5.75: Comparison of NH_3 and tungsten results in the same high mass range. Top panel: standard cuts. Bottom panel: idem but with an additional cut $x_\pi > 0.34$.

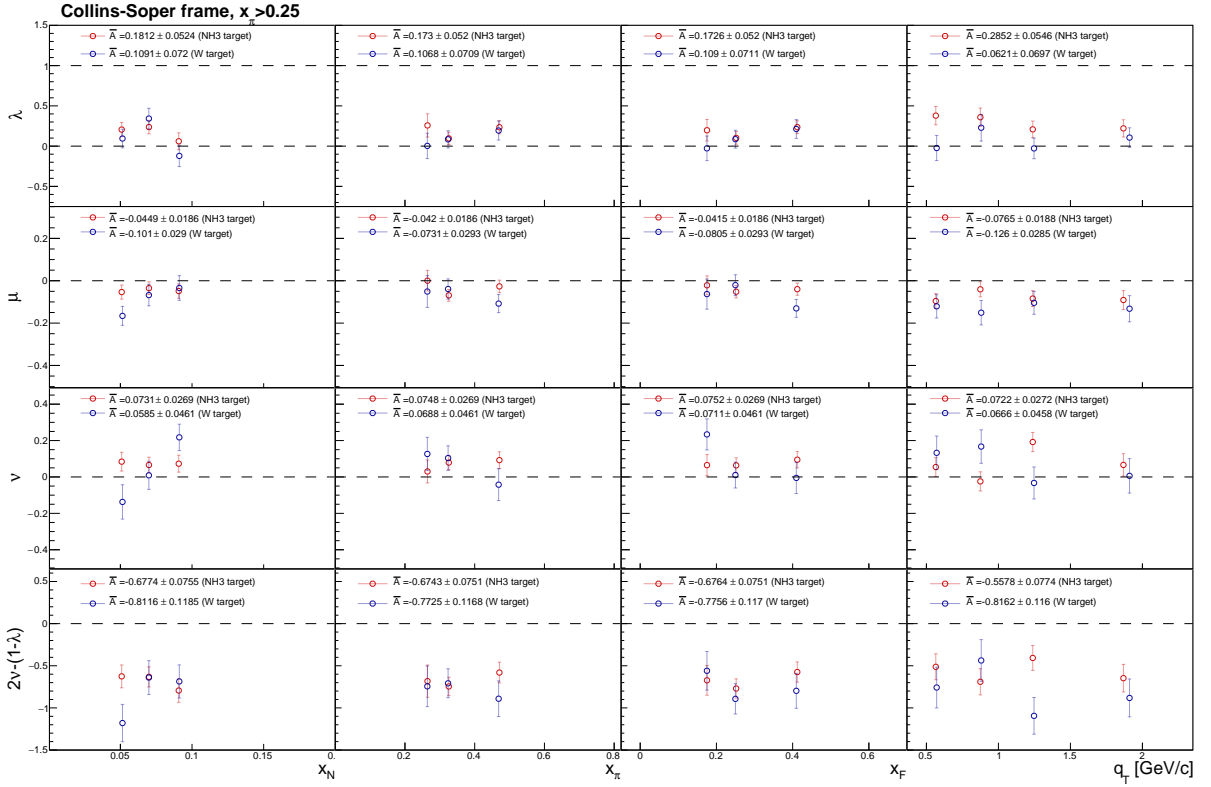


Figure 5.76: Comparison of NH₃ and tungsten results in the same J/ψ mass range ($3.0 < M_{\mu\mu}/(\text{GeV}/c^2) < 3.3$) with an additional cut $x_\pi > 0.25$.

Conclusions and discussion

The present work is dedicated to the study of partonic spin structure of hadrons and related analysis of Drell-Yan dimuon production and J/ψ production data collected by the COMPASS experiment by scattering a high energy pion beam off a transversely polarized proton (both Drell-Yan and J/ψ channels) and unpolarized tungsten targets (only Drell-Yan channel). The general expression of differential cross-section of the single-polarized Drell-Yan process in the Collins-Soper dilepton rest frame can be written in terms of specific target spin (in)dependent angular asymmetries¹⁵ (see Eq. (2.39)). Those asymmetries give access to explicit parton transverse momentum dependent (TMD) parton distribution functions (PDFs); the fundamental constituents of the TMD QCD framework describing different correlations between quark intrinsic transverse momentum and quark and nucleon spins. In general, the TMD PDFs are expected to be universal and process-independent. The universality concept turns to be conditional when it applies to the T-odd PDFs; they are expected to have same functional form and magnitude, but opposite sign when accessed via semi-inclusive deep inelastic scattering (SIDIS) reaction and Drell-Yan process. The sign-change prediction is a direct consequence of QCD gauge invariance and its verification is one of the major challenges in hadron physics. The study of TMD PDFs via measurements of relevant SIDIS and in Drell-Yan asymmetries is among the main objectives of the scientific programme of the COMPASS experiment at CERN.

The focus of the present work was set on the extraction and study of transverse spin dependent and unpolarized asymmetries from COMPASS dimuon-production data collected in 2015 and 2018 with 190 GeV/c π^- beam impinging on a transversely polarized NH_3 and unpolarized tungsten targets. The study of transverse spin dependent asymmetries (TSAs) was performed using events originating from NH_3 polarized target cells. The analysis was done for two physics channels, which were defined by the corresponding dimuon mass selection intervals: the J/ψ

¹⁵In this work the same framework has been applied also to the case of J/ψ -production.

production ($2.85 < M_{\mu^+\mu^-}/(\text{GeV}/c^2) < 3.4$) and the Drell-Yan process in the so-called “high mass” range ($4.3 < M_{\mu^+\mu^-}/(\text{GeV}/c^2) < 8.5$). The study was carried out on the full sample of events collected by COMPASS in 2015 and 2018. The Drell-Yan asymmetries from the target-polarization-independent part of the cross-section were extracted only for the 2018 sample, using events produced in NH_3 target and in first 20 cm of the tungsten beam plug ¹⁶.

The Drell–Yan TSA analysis presented in this Thesis is a continuation of the COMPASS study published in Ref. [84]. While the published results were based on first productions of COMPASS 2015 data, this work is carried out on the full data-set, which comprises a recent re-production of 2015 sample and “new” 2018 set. The data of both years have been recently re-processed using final detector calibrations and alignment and most updated reconstruction software, which was characterized by several technical improvements. Compared to the COMPASS published data [84], presented in this Thesis Drell-Yan TSA results have considerably better statistical accuracy.

In Fig. 5.77 the TSA results obtained in this Thesis are compared to a recent set of model predictions calculated for COMPASS kinematics [136]. In general, for all TSAs the theory curves appear to be in a good agreement with obtained experimental points. Achieved precision of the measurement is not enough for any conclusive study of possible kinematic trends, and the data cannot be used to favor one or the other of the presented model predictions. However, obtained results will serve as a unique input for global SIDIS-DY cross-analyses and TMD fits and can be used to impose global upper limits on DY TSAs, involved PDFs and their scale dependence. The TSA results presented in Fig. 5.77 can be summarized as follows.

- Presented Siverts asymmetry $A_{UT}^{\sin(\varphi_S)}$ appears to be slightly positive and does not exhibit any clear kinematic trends. The effect is relatively small compared to some early theoretical estimations predicting large, up to $\sim 15\%$ amplitudes [190]. As discussed in the following, obtained results for the $A_{UT}^{\sin(\varphi_S)}$ asymmetry serve as a first Drell-Yan input for Siverts sign change study.
- The transversity asymmetry $A_{UT}^{\sin(2\varphi_{CS}-\varphi_S)}$ is found to be at about one standard deviation below zero. The experimental points are found to be in a good agreement with the

¹⁶The analysis of tungsten data was performed for the reduced dimuon mass range of $4.7 < M_{\mu^+\mu^-}/(\text{GeV}/c^2) < 8.5$ in order to cope with higher background conditions w.r.t. the NH_3 case.

model predictions from Ref. [18, 136]. This result serves as a unique input to study the universality of the nucleon transversity TMD PDF when accessed in SIDIS and Drell-Yan channels.

- The pretzelosity asymmetry $A_{UT}^{\sin(2\varphi_{CS}+\varphi_S)}$, is found to be slightly negative and compatible with zero within the total uncertainties, which can be attributed to the small size of pretzelosity TMD PDF. Together with the transversity asymmetry $A_{UT}^{\sin(2\varphi_{CS}-\varphi_S)}$, it is related to the pion Boer-Mulders PDFs.
- The results for $A_{UT}^{\sin(\varphi_{CS}-\varphi_S)}$ and $A_{UT}^{\sin(\varphi_{CS}+\varphi_S)}$ asymmetries presented in this Thesis are not included in the figure, since there are no prediction available for these TSAs. These amplitudes are related to twist-3 mechanisms and can be useful for future higher-twist phenomenological studies. No significant effect was observed for these asymmetries.

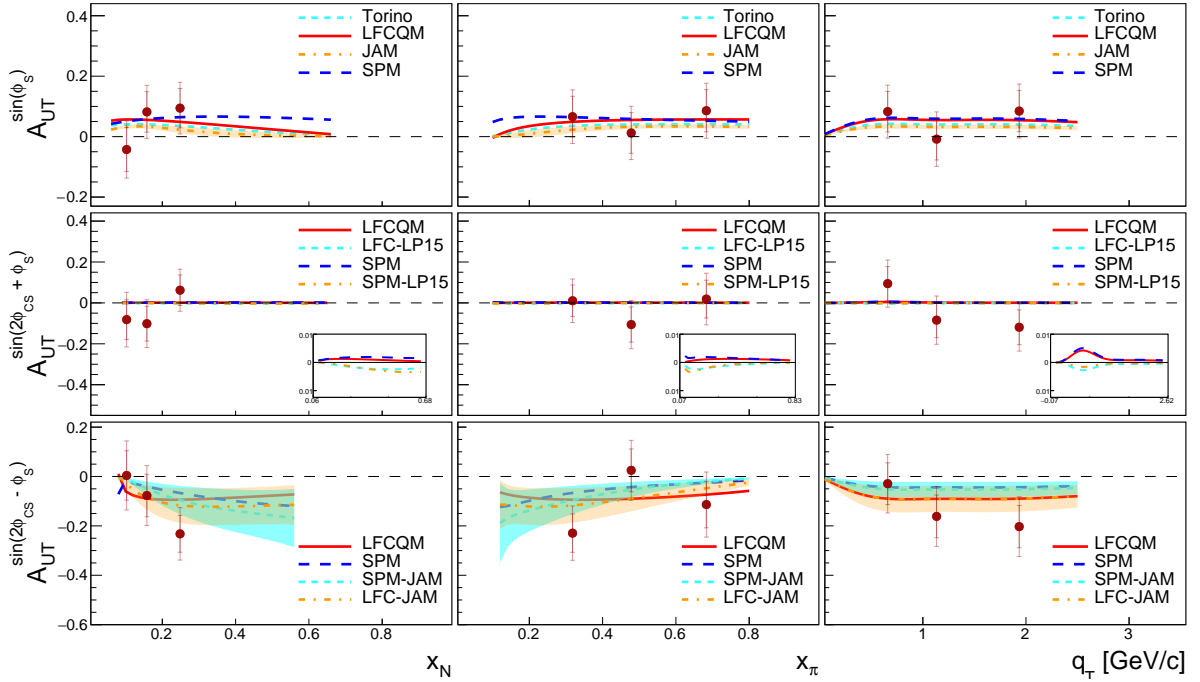


Figure 5.77: Predictions from various models for the Sivers, transversity and pretzelosity asymmetries in the COMPASS kinematic region. The model labels are according to Fig. 1.9 and to Ref. [136].

In Fig. 5.78 the measured high-mass Drell-Yan Sivers asymmetry is compared with selected theoretical predictions that are based on standard DGLAP [86] and two different TMD evolution approaches labeled as “TMD-1” [87] and “TMD-2” [88]. The parameterizations used to evaluate the Sivers functions in these models were based on a fit of COMPASS and HERMES

experimental SIDIS data for the Siverts TSA [73, 78, 115]. Note, that “TMD-2” predictions in Fig 5.78 have been updated to better match the COMPASS kinematics, compared to the earlier curves quoted in the COMPASS paper [84]. Positive predictions for Drell-Yan Siverts asymmetry were obtained applying the sign change hypothesis for the Siverts TMD PDFs. Presented COMPASS averaged point for the Drell-Yan Siverts asymmetry is found to be above zero at about half standard deviation and is in agreement with “sign change” model predictions. The obtained result is in tension with negative (mirrored) curves that correspond to “no sign change” hypothesis. Hence, one can conclude that COMPASS data is consistent with the predicted change of sign for the Siverts function and slightly favors it.

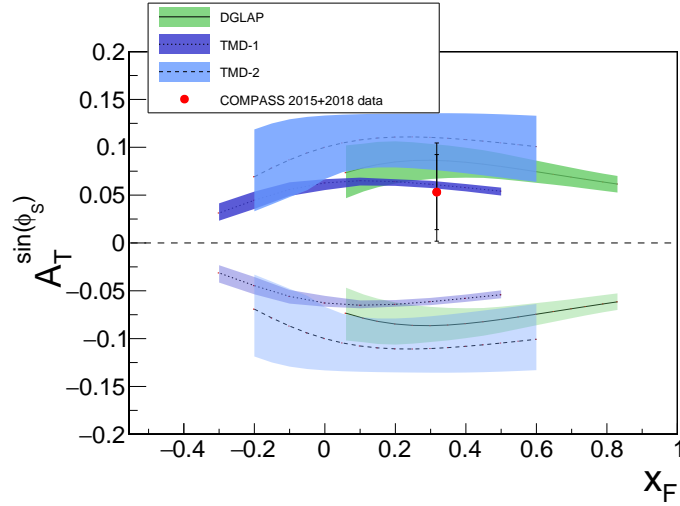


Figure 5.78: The measured mean Siverts asymmetry and the theoretical predictions for different Q^2 evolution schemes from [86] (DGLAP), [87] (TMD-1) and [88] (TMD-2). The dark-shaded (light-shaded) predictions are evaluated with (without) the sign-change hypothesis.

COMPASS was the first ever experiment that performed polarized Drell-Yan measurements. Beside that, COMPASS is the only experiment having the unique capability to explore the transverse-spin structure of the nucleon in a similar kinematic region by two alternative and complementary experimental approaches, *i.e.* SIDIS and Drell-Yan. This offered the opportunity of minimizing uncertainties of TMD evolution in the comparison of Siverts and other TMD PDFs when extracted from these two measurements. Such comparison is a fundamental test of the universal and conditionally-universal features of TMD PDFs, which includes opposite-sign prediction for T-odd PDFs by QCD.

A dedicated analysis aiming to provide SIDIS inputs for universality studies of TMD PDFs

was performed by the collaboration and is reported in Ref. [79]. It was the first multi-differential study of the Sivers and other transverse asymmetries that were extracted from SIDIS data at four different hard scales. The scales were generally chosen to match those adopted in the COMPASS Drell-Yan programme, the highest one being defined as: $4 \text{ GeV}/c < Q < 9 \text{ GeV}/c$, which is very similar to the DY HM range ($4.3 < M_{\mu^+\mu^-}/(\text{GeV}/c^2) < 8.5$). In Fig. 5.79 averaged over all kinematic dependences Drell-Yan TSAs from high mass range are confronted to their SIDIS counterparts. In the SIDIS analysis the Sivers asymmetry $A_{UT}^{\sin(\phi_h - \phi_S)}$ for positive hadrons was found to be above zero by 3.2σ of the total experimental accuracy. Under the sign-change hypothesis it is expected to turn into a positive effect also in DY case [86]. The transversity asymmetry $A_{UT}^{\sin(\phi_h + \phi_S - \pi)}$ from the SIDIS proton data shows a clear non-zero signal for both positive and negative hadrons, which should result in a negative transversity TSA amplitude in Drell-Yan case [136]. Finally, the pretzelosity asymmetry $A_{UT}^{\sin(3\phi_h - \phi_S)}$ is found to be compatible with zero in both SIDIS and Drell-Yan, which matches the theory expectations [136]. Hence, the overall SIDIS picture appears to be consistent with the above discussed Drell-Yan observations and universality considerations for TMD PDFs.

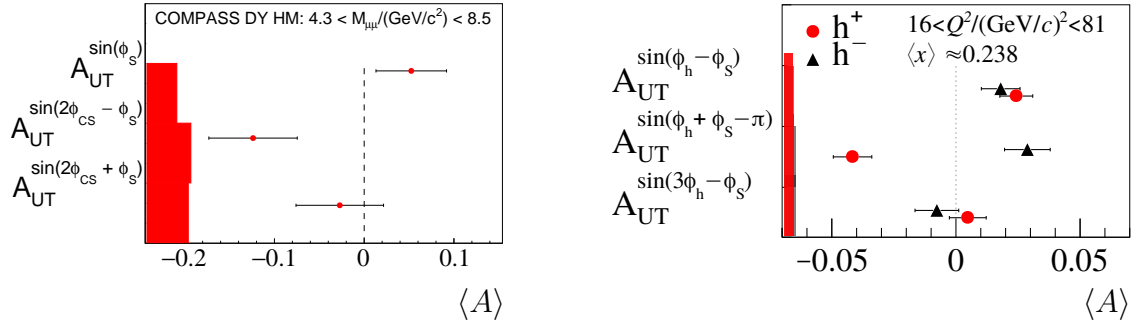


Figure 5.79: COMPASS SIDIS-DY “bridge” results. Left: Sivers, Pretzelosity, Transversity asymmetries extracted in this Thesis from DY data (2015+2018) in the HM range. Right: same asymmetries extracted from COMPASS 2010 SIDIS data [79] at mostly the same hard scale. Note that angles are differently defined in SIDIS and DY, thus the same sign for the Sivers asymmetry implies the opposite sign for the corresponding TMD PDF.

In this Thesis, in addition to the Drell-Yan channel in “high mass” range, the study of transverse spin effects has also been carried out for the J/ψ mass range.

Assuming the $q\bar{q}$ annihilation being the dominant channel for J/ψ -production in COMPASS kinematics (neglecting the contribution of gluon-gluon (gg) fusion process) the study of J/ψ

TSAAs can be considered as an alternative way to access quark TMD PDFs. In particular, this approach has been adopted in Ref. [166] where it was assumed that the gluon Sivvers contribution, as well as the contribution from J/ψ mesons originating from feed-down decays, are small and that related dilution effects can be neglected. As a result, the authors conjectured that the $q\bar{q}$ -driven Sivvers asymmetry in the J/ψ -peak region can be quite significant at COMPASS kinematics. Hence, within this approach the J/ψ channel can be considered as a particularly promising way to test *e.g.* the sign change of the quark Sivvers function with high accuracy.

However, recent studies carried out within the framework of the color evaporation model suggested, that at COMPASS kinematics the gg fusion contribution can be significantly high and can even play a dominant role [167]. This point makes more elaborate the interpretation of the TSAAs in J/ψ -production in pion-nucleon collisions at COMPASS. In particular, the asymmetries may serve as a unique and complementary source of information about J/ψ -production mechanisms and gluon PDFs. While there is quite some knowledge accumulated about quark TMD PDFs, information about gluon PDFs is rather scarce. The Sivvers asymmetry for gluons was extracted by COMPASS studying high- p_T hadron pair production in SIDIS data collected transversely polarized deuterons and protons [221]. The asymmetry was found to be negative and away from zero by more than two standard deviations, which could hint to a non-zero gluon Sivvers effect. On the other hand, in recent gluon-Sivvers sensitive measurements performed at PHENIX, the transverse single-spin asymmetries in π^0 and η meson productions in polarized $p + p$ collisions (pseudorapidity range $|\eta| < 0.35$, center-of-mass energy of 200 GeV) were found to be consistent with zero [222]. The seeming tension between COMPASS and PHENIX results is not straightforward to interpret. Direct comparison of the results is not justified, as the centre of mass energy and kinematic coverage of two experiments are quite different.

The analysis performed in the scope of this Thesis has demonstrated that the TSAAs in J/ψ channel are rather small and compatible with zero within the statistical accuracy. It is the first ever measurement of J/ψ TSAAs in pion-nucleon scattering and it clearly does not confirm expectations of large spin-effects from model predictions based on the $q\bar{q}$ -dominance hypothesis. Whether observed zero asymmetries are conditioned by small gluon Sivvers PDF effect, or certain cancellation of quark and gluon contributions, requires more complementary inputs (*e.g.* future COMPASS J/ψ polarization and cross-sections results) and is still to be understood.

The last analysis section of this Thesis is dedicated to the study of target spin-independent asymmetries in dimuon-production from COMPASS 2018 run. The asymmetries have been extracted for the “high mass” Drell-Yan range from both NH_3 and W targets data. The experimental results on DY spin-independent azimuthal asymmetries, including COMPASS data presented in this work, are in slight tension with available perturbative calculations [16,149]. In Fig. 5.80 tungsten results obtained in this Thesis are confronted with results from past fixed-target experiments: NA10 at CERN [144] and E615 at Fermilab [128] and with perturbative NLO calculations from Ref. [149].

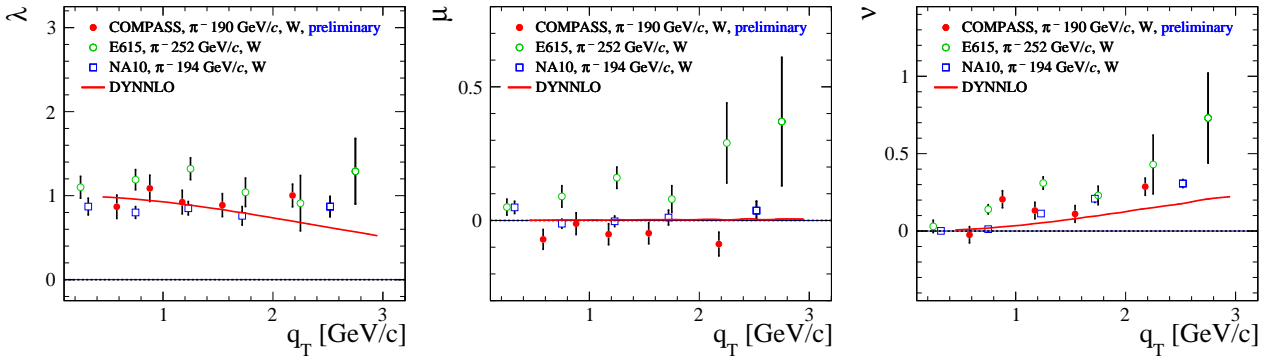


Figure 5.80: Results on λ , μ , ν asymmetries from the W target (red) in comparison with the pQCD DYNNLO curve [149] (red) and other experiments: E615 [128] (green), NA10 [144] (blue).

One can see that, extracted amplitudes for the spin-independent ν asymmetry are non-zero both in NH_3 and tungsten data. This observation is in a qualitative agreement with perturbative NLO predictions [16]. Experimental points are, however, systematically above pQCD curves and the discrepancy is statistically significant. The discrepancy between NLO calculations and data vanishes at higher q_T regimes accessible *e.g.* by the LHC experiments [148]. In the fixed-target regime with relatively small range of $q_T \sim 1$ GeV, fixed-order perturbation theory does not provide reliable results for cross sections, even in case of relatively large hard scale [148]. On the other hand, in fixed target kinematics, the intrinsic transverse momenta of the initial partons may become relevant and observed offset can be interpreted as a hint pointing to existence of predicted non-perturbative TMD effects. Possible non-perturbative interpretation of ν asymmetry is associated with the Boer–Mulders effect and respective TMD PDFs [136]. In Fig. 5.81 COMPASS data points, in addition to NLO pQCD curves, are confronted with non-perturbative predictions for Boer–Mulders TMD effect from selected models discussed in

Ref. [136]. Note that presented TMD model predictions do not account for pQCD effects and in reality perturbative and non-perturbative components should supplement each other or interfere in some form.

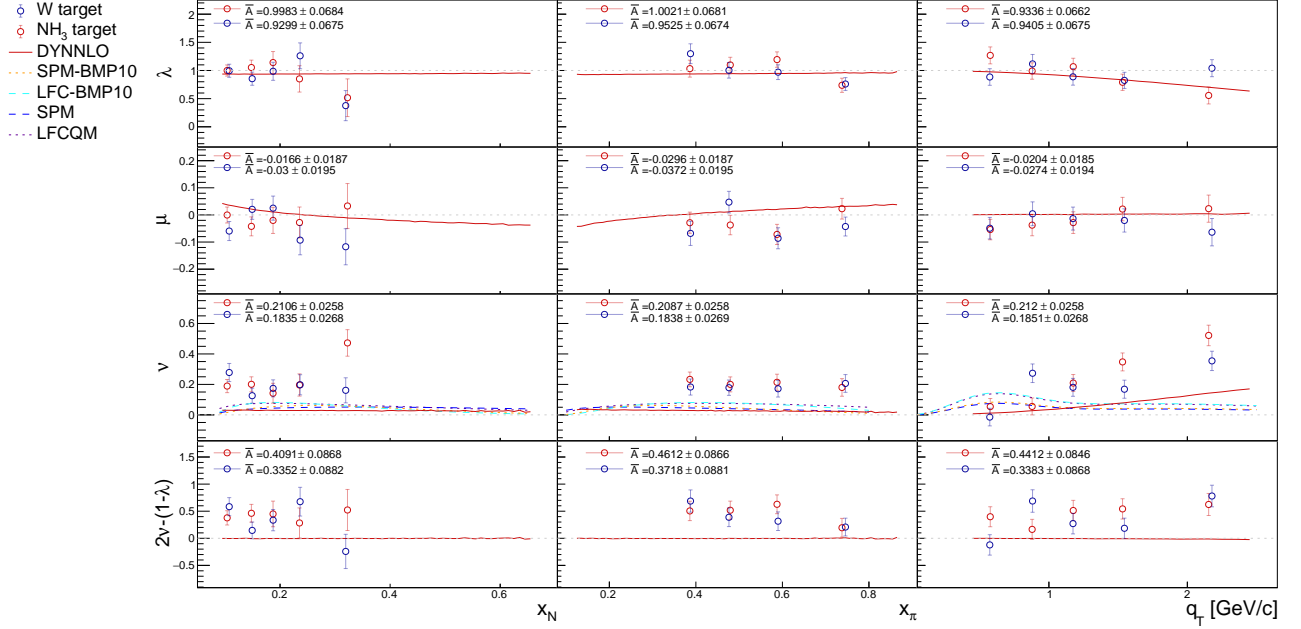


Figure 5.81: Results on λ , μ , ν asymmetries from the W target (blue open circle) and NH_3 target (red open circle) in comparison with the pQCD DYNNLO curve [149] (red curve) and with available model predictions for the ν asymmetry (dashed curves) according to the Ref. [136].

In the bottom panel of Fig. 5.81 the NH_3 and tungsten results obtained in this Thesis for the so-called Lam-Tung relation are confronted with NLO calculations from Ref. [149]. The Lam-Tung sum rule, $2\nu = 1 - \lambda$, is derived from the fermion nature of quarks. It is expected to hold at lowest order of the Drell-Yan process, while at NLO it is expected to be slightly violated towards negative values, $2\nu < 1 - \lambda$ (see Ref. [149]). Presented COMPASS results demonstrate violation of this sum rule with a clear positive trend. In Fig. 5.82 COMPASS data on Lam-Tung relation are confronted with experimental points coming from pion-tungsten measurements performed at NA10 [144] and E615 [128] experiments. The data from the other two experiments appear to be in qualitative agreement with COMPASS points and thus confirm the violation of the sum rule with a positive (opposite of the NLO predictions) trend.

On the other hand, the proton-induced Drell-Yan measurements from the E866 experiment at Fermilab [145] and the results from proton-proton collisions by CDF [146], CMS [147] and

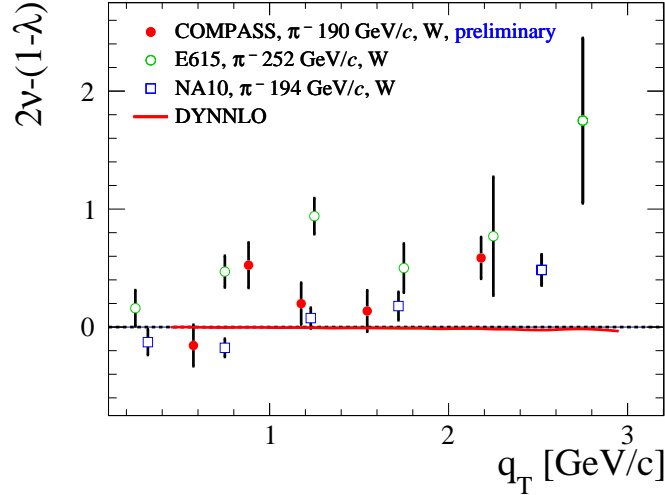


Figure 5.82: Results on Lam-Tung relation from the W target (red) in comparison with the pQCD DYNNLO curve [149] (red) and other experiments: E615 (green), NA10 (blue).

ATLAS [223] confirm the expected negative tendency from NLO QCD. It might be that the positive trend of the violation, observed in fixed target pion-induced Drell-Yan measurements, is driven by the non-perturbative TMD contributions to the amplitude, which vanish at higher energies.

The same set of target spin-independent asymmetries were estimated in one period from COMPASS J/ψ production data. The measurements of the UAs in J/ψ production can provide information on the direction of the spin-alignment of the decaying J/ψ meson and, therefore, on the topological properties of the dominant production mechanism [168–170]. The preliminary results obtained in different dilepton rest frames (Collins-Soper, Gottfried-Jackson, and Helicity frame) do not show an univocal indication for the direction of J/ψ polarization, since *e.g.* the λ asymmetry was found positive in the Collins-Soper and in the Helicity frame, as well. However, as it was shown in Ref. [168], there are quantities $\tilde{\lambda}$ and F , which are invariant w.r.t. the choice of the dilepton rest frame. In terms of $\tilde{\lambda}$, contributing processes to J/ψ production are transversely polarized if $\tilde{\lambda} = +1$. Otherwise, in case of $\tilde{\lambda} = -1$, all contributing polarizations are longitudinal. The estimated invariant $\tilde{\lambda}$ is positive (about +0.25), but less than one by about 3σ of statistical uncertainty. As a result, the extracted $\tilde{\lambda}$ value indicates predominant transverse polarization with an admixture of the longitudinal component for the J/ψ production mechanism at COMPASS kinematics.

The results obtained in this Thesis, combined with COMPASS SIDIS measurements, can be used for various QCD studies including: the quest of QCD universality of TMD PDFs, understanding of non-perturbative TMD dynamics in hadrons, constraining of TMD evolution aspects in theoretical models and global fits of TMD PDFs. Given all that, presented COMPASS Drell-Yan asymmetries will serve as a unique and valuable input to explore the spin structure of the nucleon.

Appendix A. Details on the DY cross-section

Here we present the details on the DY cross section $d\sigma/d\Omega d^4q$ introduced in Eq. (2.1) in the Chapter 2. The $d\sigma/d\Omega d^4q$ is proportional to convolution of the leptonic and hadronic tensors:

$$\frac{d\sigma}{d\Omega d^4q} = \frac{\alpha_{em}^2}{2Fq^4} L_{\mu\nu} W^{\mu\nu}, \quad F = 4\sqrt{(P_a \cdot P_b)^2 - M_a^2 M_b^2}. \quad (5.35)$$

In this Appendix, we will reproduce the calculation, mainly following to formalism described in Ref. [176], in order to establish a relation between the formula (5.35) writing down from the first principles and the hadronic structure functions, which are related to parton distributions and asymmetries.

The leptonic tensor $L^{\mu\nu}$ from (5.35) in case of the DY reaction induced by a photon can be explicitly calculated by QED:

$$L^{\mu\nu} = \sum_{\lambda, \lambda'} (\bar{u}(l, \lambda) \gamma^\mu v(l', \lambda')) (\bar{u}(l, \lambda) \gamma^\nu v(l', \lambda'))^* = 4 \left(l^\mu l'^\nu + l^\nu l'^\mu - \frac{q^2}{2} g^{\mu\nu} \right), \quad (5.36)$$

while $W^{\mu\nu}$ is a hadronic tensor:

$$W^{\mu\nu}(P_a, S_a; P_b, S_b; q) = \frac{1}{(2\pi)^4} \int d^4x e^{iq \cdot x} \langle P_a, S_a; P_b, S_b | J_{em}^\mu(0) J_{em}^\nu(x) | P_a, S_a; P_b, S_b \rangle \quad (5.37)$$

which is determined by the electromagnetic current operator J_{em}^μ . The tensor $W^{\mu\nu}$ contains the information on the hadron structure but it is difficult to explicitly calculate it from the first principles. In this case one uses decomposition and parameterization of the unknown expression. Due to electromagnetic gauge invariance, parity, and hermiticity the tensor has to satisfy the

following constraints:¹⁷

$$q_\mu W^{\mu\nu}(P_a, S_a; P_b, S_b; q) = q_\nu W^{\mu\nu}(P_a, S_a; P_b, S_b; q) = 0, \quad (5.38)$$

$$W^{\mu\nu}(P_a, S_a; P_b, S_b; q) = W_{\mu\nu}(\bar{P}_a, -\bar{S}_a; \bar{P}_b, -\bar{S}_b; \bar{q}), \quad (5.39)$$

$$W^{\mu\nu}(P_a, S_a; P_b, S_b; q) = [W^{\nu\mu}(P_a, S_a; P_b, S_b; q)]^*. \quad (5.40)$$

Since a tensor can be decomposed in symmetric and antisymmetric parts, we can write down spin independent part (unpolarized $W_u^{\mu\nu}$) and part with dependence on spin of the first hadron H_a (term $W_a^{\mu\nu}$), of the second hadron H_b (term $W_b^{\mu\nu}$), and with spin dependence on both of them (double polarized $W_{ab}^{\mu\nu}$)

$$W^{\mu\nu} = W_u^{\mu\nu} + W_a^{\mu\nu} + W_b^{\mu\nu} + W_{ab}^{\mu\nu}. \quad (5.41)$$

These four tensors can be decomposed on a basis. The functions arising at basis tensors are called *structure functions*.

For example, we will treat unpolarized hadron tensor $W_u^{\mu\nu}$. In general, Lorentz tensor structure in $W^{\mu\nu}$ must come from the combination of four objects of the process: Minkowski metric tensor $g^{\mu\nu}$, 4-momentum of virtual photon q^μ , and 4-momenta of hadrons P_a^μ and P_b^μ . Thus, basis shell can be presented as

$$\{h_{u,i}^{\mu\nu}\}_{i=1}^7 = \{g^{\mu\nu}, q^\mu q^\nu, P_a^\mu P_a^\nu, P_b^\mu P_b^\nu, q^\nu P_a^\mu + q^\mu P_a^\nu, q^\nu P_b^\mu + q^\mu P_b^\nu, P_a^\mu P_b^\nu + P_a^\nu P_b^\mu\}, \quad (5.42)$$

and in terms of structure functions V_u (which depend on invariants $q^2, (P_a \cdot q), (P_b \cdot q)$) one can write

$$W_u^{\mu\nu} = \sum_{i=1}^7 h_{u,i}^{\mu\nu} V_{u,i}(q^2, (P_a \cdot q), (P_b \cdot q)). \quad (5.43)$$

However, due to gauge invariance (Eq. 5.38) we have

$$\begin{aligned} & q^\nu V_{u,1} + q^2 q^\nu V_{u,2} + (q \cdot P_a) P_a^\nu V_{u,3} + (q \cdot P_b) P_b^\nu V_{u,4} \\ & + (q^2 P_a^\nu + (q \cdot P_a) q^\nu) V_{u,5} + (q^2 P_b^\nu + (q \cdot P_b) q^\nu) V_{u,6} \\ & + ((q \cdot P_a) P_b^\nu + (q \cdot P_b) P_a^\nu) V_{u,7} = 0. \end{aligned} \quad (5.44)$$

¹⁷The notation $\bar{v}^\mu = v_\mu$ for a generic 4-vector v is used.

Since q^ν, P_b^ν, P_b^ν are not generally equal zero, the condition (5.44) can result zero only if the sum at their similar terms is equal to zero

$$\begin{aligned} V_{u,1} + q^2 V_{u,2} + P_a \cdot q V_{u,5} + P_b \cdot q V_{u,6} &= 0, \\ P_a \cdot q V_{u,3} + q^2 V_{u,5} + P_b \cdot q V_{u,7} &= 0, \\ P_b \cdot q V_{u,4} + q^2 V_{u,6} + P_a \cdot q V_{u,7} &= 0. \end{aligned} \quad (5.45)$$

These three constraints yield a subspace with dimension of 4. So we can decrease the number of basis tensors and, consequently, the number of structure functions by choosing a new basis in this subspace. The choice of basis is a matter of taste but, following [224], we hold one of the most used and convenient notations, introducing the new basis in terms of projection operators

$$P^{\mu\nu} = g^{\mu\nu} - \frac{q^\mu q^\nu}{q^2}. \quad (5.46)$$

One can obtain new basis $\{t_{u,i}^{\mu\nu}\}_{i=1}^4$ from basis (5.42) acting on basis tensors by operator (5.46) by following way $P_\rho^\mu h_{u,i}^{\rho\sigma} P_\sigma^\nu$. This results

$$\begin{aligned} P_\rho^\mu h_{u,1}^{\rho\sigma} P_\sigma^\nu &= \left(g_\rho^\mu - \frac{q^\mu q_\rho}{q^2}\right) g^{\rho\sigma} \left(g_\sigma^\nu - \frac{q^\nu q_\sigma}{q^2}\right) = \left(g_\rho^\mu - \frac{q^\mu q_\rho}{q^2}\right) \left(g^{\nu\rho} - \frac{q^\nu q^\rho}{q^2}\right) \\ &= g^{\mu\nu} - \frac{q^\mu q^\nu}{q^2} - \frac{q^\nu q^\mu}{q^2} + \frac{q^\mu q^\nu q^2}{q^4} = g^{\mu\nu} - \frac{q^\mu q^\nu}{q^2} = t_{u,1}^{\mu\nu}, \end{aligned} \quad (5.47)$$

$$\begin{aligned} P_\rho^\mu h_{u,2}^{\rho\sigma} P_\sigma^\nu &= \left(g_\rho^\mu - \frac{q^\mu q_\rho}{q^2}\right) q^\rho q^\sigma \left(g_\sigma^\nu - \frac{q^\nu q_\sigma}{q^2}\right) \\ &= \left(g_\rho^\mu - \frac{q^\mu q_\rho}{q^2}\right) (q^\rho q^\nu - q^\rho q^\nu) \equiv 0, \end{aligned} \quad (5.48)$$

and introducing a notation $\tilde{P}_a^\mu = P_a^\mu - \frac{q^\mu (P_a \cdot q)}{q^2}$, the rest basis tensors reduce

$$\begin{aligned} P_\rho^\mu h_{u,3}^{\rho\sigma} P_\sigma^\nu &= \left(g_\rho^\mu - \frac{q^\mu q_\rho}{q^2}\right) P_a^\rho P_a^\sigma \left(g_\sigma^\nu - \frac{q^\nu q_\sigma}{q^2}\right) = \left(g_\rho^\mu - \frac{q^\mu q_\rho}{q^2}\right) \\ &\times \left(P_a^\rho P_a^\nu - \frac{P_a^\rho q^\nu (P_a \cdot q)}{q^2}\right) = \left(P_a^\mu - \frac{q^\mu (P_a \cdot q)}{q^2}\right) \left(P_a^\nu - \frac{q^\nu (P_a \cdot q)}{q^2}\right) \\ &= \tilde{P}_a^\mu \tilde{P}_a^\nu = t_{u,2}^{\mu\nu}, \end{aligned} \quad (5.49)$$

$$P_\rho^\mu h_{u,4}^{\rho\sigma} P_\sigma^\nu = \left(g_\rho^\mu - \frac{q^\mu q_\rho}{q^2}\right) P_b^\rho P_b^\sigma \left(g_\sigma^\nu - \frac{q^\nu q_\sigma}{q^2}\right) = \tilde{P}_b^\mu \tilde{P}_b^\nu = t_{u,3}^{\mu\nu}, \quad (5.50)$$

$$P_\rho^\mu h_{u,5}^{\rho\sigma} P_\sigma^\nu = \left(g_\rho^\mu - \frac{q^\mu q_\rho}{q^2} \right) (q^\rho P_a^\sigma + q^\sigma P_a^\rho) \left(g_\sigma^\nu - \frac{q^\nu q_\sigma}{q^2} \right) = \left(g_\rho^\mu - \frac{q^\mu q_\rho}{q^2} \right) \quad (5.51)$$

$$\begin{aligned} & \times \left(q^\rho P_a^\nu + q^\nu P_a^\rho - q^\rho q^\nu \frac{(P_a \cdot q)}{q^2} - q^\nu P_a^\rho \right) \\ & = q^\mu P_a^\nu + q^\nu P_a^\mu - q^\mu q^\nu \frac{(P_a \cdot q)}{q^2} - q^\nu P_a^\mu \\ & - q^\mu P_a^\nu - q^\mu q^\nu \frac{(P_a \cdot q)}{q^2} + q^\mu q^\nu \frac{(P_a \cdot q)}{q^2} + q^\mu q^\nu \frac{(P_a \cdot q)}{q^2} \equiv 0, \end{aligned}$$

$$P_\rho^\mu h_{u,6}^{\rho\sigma} P_\sigma^\nu = \left(g_\rho^\mu - \frac{q^\mu q_\rho}{q^2} \right) (q^\rho P_b^\sigma + q^\sigma P_b^\rho) \left(g_\sigma^\nu - \frac{q^\nu q_\sigma}{q^2} \right) \equiv 0, \quad (5.52)$$

$$P_\rho^\mu h_{u,7}^{\rho\sigma} P_\sigma^\nu = \left(g_\rho^\mu - \frac{q^\mu q_\rho}{q^2} \right) (P_a^\rho P_b^\sigma + P_a^\sigma P_b^\rho) \left(g_\sigma^\nu - \frac{q^\nu q_\sigma}{q^2} \right) = \left(g_\rho^\mu - \frac{q^\mu q_\rho}{q^2} \right) \quad (5.53)$$

$$\begin{aligned} & \times \left(P_a^\rho P_b^\nu - P_a^\rho q^\nu \frac{(P_b \cdot q)}{q^2} + P_a^\nu P_b^\rho - P_b^\rho q^\nu \frac{(P_a \cdot q)}{q^2} \right) \\ & = P_a^\mu P_b^\nu - P_a^\mu q^\nu \frac{(P_b \cdot q)}{q^2} + P_a^\nu P_b^\mu - P_b^\mu q^\nu \frac{(P_a \cdot q)}{q^2} \\ & - q^\mu P_b^\nu \frac{(P_a \cdot q)}{q^2} + q^\mu q^\nu \frac{(P_a \cdot q)}{q^2} \frac{(P_b \cdot q)}{q^2} - q^\mu P_a^\nu \frac{(P_b \cdot q)}{q^2} \\ & + q^\mu q^\nu \frac{(P_a \cdot q)}{q^2} \frac{(P_b \cdot q)}{q^2} = \tilde{P}_a^\mu \left(P_b^\nu - q^\nu \frac{(P_b \cdot q)}{q^2} \right) + (\mu \longleftrightarrow \nu) \\ & = \tilde{P}_a^\mu \tilde{P}_b^\nu + \tilde{P}_a^\nu \tilde{P}_b^\mu = t_{u,4}^{\mu\nu}. \end{aligned}$$

Thereby we have new decomposition of unpolarized part of hadronic tensor with four structure functions $U_u(q^2, (P_a \cdot q), (P_b \cdot q))$

$$W_u^{\mu\nu} = \sum_{i=1}^4 t_{u,i}^{\mu\nu} U_{u,i}(q^2, (P_a \cdot q), (P_b \cdot q)). \quad (5.54)$$

Now it was explicitly demonstrated the general way (frame independent) to obtain a basis with structure functions for unpolarized case. It includes consideration the linear combination of possible Lorentz structures of the process and reduce dimension of this tensor space due to constraints (5.38), (5.39), (5.40) and another relations between Lorentz tensor (*e.g.* relation between Minkowski metric and antisymmetric Levi-Civita tensor). Below we will briefly discuss polarized cases without technical treatment of all mathematical transformations due to cumbersome. We follow the paper [176] and more details can be found therein.

In case of single polarization ($W_a^{\mu\nu}$ or $W_b^{\mu\nu}$), the decomposition on basis tensors includes 4-vector of spin S^μ of polarized hadron and Levi-Civita antisymmetric tensor $\varepsilon^{\mu\nu\rho\sigma}$. There are 23 possible candidates for basis tensors which are symmetric under the exchange μ, ν Lorenz

indices. Using gauge invariance and the Schouten identity [225–227]

$$T^{\beta[\alpha\mu\nu\rho\sigma]} = g^{\alpha\beta}\varepsilon^{\mu\nu\rho\sigma} + g^{\mu\beta}\varepsilon^{\nu\alpha\rho\sigma} + g^{\nu\beta}\varepsilon^{\alpha\mu\rho\sigma} + g^{\rho\beta}\varepsilon^{\mu\nu\sigma\alpha} + g^{\sigma\beta}\varepsilon^{\mu\nu\alpha\rho} = 0. \quad (5.55)$$

one can decrease the number of linear-independent Lorenz tensors to 8. In particular, Gauge invariance eliminates two tensor structure candidates, while the Schouten identity eliminates 13 tensor structures. Note, that the Schouten identity (5.55) is a tensor of 6th rank, which is fully antisymmetric over 5 Lorenz indices $\alpha, \mu, \nu, \rho, \sigma$. Physical meaning of this identity is that it is impossible in 4 dimensional theory to place four Lorenz indices in an antisymmetric 5th rank tensor.

Finally, the hadronic tensor is expanded through the basis of 8 linear-independent Lorenz tensor structures as:

$$W_a^{\mu\nu} = \sum_{i=1}^8 t_{a,i}^{\mu\nu} U_{a,i}, \quad (5.56)$$

where basis tensors read

$$\begin{aligned} t_{a,1}^{\mu\nu}, \dots, t_{a,4}^{\mu\nu} &= \varepsilon^{S_a q P_a P_b} \left\{ g^{\mu\nu} - \frac{q^\mu q^\nu}{q^2}, \tilde{P}_a^\mu \tilde{P}_a^\nu, \tilde{P}_b^\mu \tilde{P}_b^\nu, \tilde{P}_a^\mu \tilde{P}_b^\nu + \tilde{P}_a^\nu \tilde{P}_b^\mu \right\}, \\ t_{a,5}^{\mu\nu}, t_{a,6}^{\mu\nu} &= \left\{ S_a \cdot q, S_a \cdot P_b \right\} (\varepsilon^{\mu q P_a P_b} \tilde{P}_a^\nu + \varepsilon^{\nu q P_a P_b} \tilde{P}_a^\mu), \\ t_{a,7}^{\mu\nu}, t_{a,8}^{\mu\nu} &= \left\{ S_a \cdot q, S_a \cdot P_b \right\} (\varepsilon^{\mu q P_a P_b} \tilde{P}_b^\nu + \varepsilon^{\nu q P_a P_b} \tilde{P}_b^\mu). \end{aligned} \quad (5.57)$$

Similarly, one can derive the basis for polarized of hadron H_b ($W_b^{\mu\nu}$ part of the hadronic tensor)

$$W_b^{\mu\nu} = \sum_{i=1}^8 t_{b,i}^{\mu\nu} U_{b,i}, \quad (5.58)$$

with the the basis tensors

$$\begin{aligned} t_{b,1}^{\mu\nu}, \dots, t_{b,4}^{\mu\nu} &= \varepsilon^{S_b q P_b P_a} \left\{ g^{\mu\nu} - \frac{q^\mu q^\nu}{q^2}, \tilde{P}_a^\mu \tilde{P}_a^\nu, \tilde{P}_b^\mu \tilde{P}_b^\nu, \tilde{P}_a^\mu \tilde{P}_b^\nu + \tilde{P}_a^\nu \tilde{P}_b^\mu \right\}, \\ t_{b,5}^{\mu\nu}, t_{b,6}^{\mu\nu} &= \left\{ S_b \cdot q, S_b \cdot P_a \right\} (\varepsilon^{\mu q P_b P_a} \tilde{P}_a^\nu + \varepsilon^{\nu q P_b P_a} \tilde{P}_a^\mu), \\ t_{b,7}^{\mu\nu}, t_{b,8}^{\mu\nu} &= \left\{ S_b \cdot q, S_b \cdot P_a \right\} (\varepsilon^{\mu q P_b P_a} \tilde{P}_b^\nu + \varepsilon^{\nu q P_b P_a} \tilde{P}_b^\mu). \end{aligned} \quad (5.59)$$

And for the double polarized part $W_{ab}^{\mu\nu}$ there are 48 combination of 4-vector of states (spin and momentum), Minkowski, and Levi-Civita tensors which satisfy parity property (5.39) and are being symmetric under the exchange μ, ν Lorenz indices. Applying of gauge invariance and

the following identity

$$\begin{vmatrix} g^{\mu\nu} & g^{\mu\bar{\alpha}} & g^{\mu\bar{\beta}} & g^{\mu\bar{\gamma}} & g^{\mu\bar{\delta}} \\ g^{\alpha\nu} & g^{\alpha\bar{\alpha}} & g^{\alpha\bar{\beta}} & g^{\alpha\bar{\gamma}} & g^{\alpha\bar{\delta}} \\ g^{\beta\nu} & g^{\beta\bar{\alpha}} & g^{\beta\bar{\beta}} & g^{\beta\bar{\gamma}} & g^{\beta\bar{\delta}} \\ g^{\gamma\nu} & g^{\gamma\bar{\alpha}} & g^{\gamma\bar{\beta}} & g^{\gamma\bar{\gamma}} & g^{\gamma\bar{\delta}} \\ g^{\delta\nu} & g^{\delta\bar{\alpha}} & g^{\delta\bar{\beta}} & g^{\delta\bar{\gamma}} & g^{\delta\bar{\delta}} \end{vmatrix} = 0, \quad (5.60)$$

remains 28 non-vanishing terms. Note, the identity (5.60) directly follows from the Schouten identity (5.55) after multiplying of $T^{\beta[\alpha\mu\nu\rho\sigma]}$ with Levi-Civita tensor $\varepsilon^{\bar{\alpha}\bar{\beta}\bar{\rho}\bar{\sigma}}$.

Thus, the final form of the hadronic tensor for the case of polarization of both hadrons reads

$$W_{ab}^{\mu\nu} = \sum_{i=1}^{28} t_{ab,i}^{\mu\nu} U_{ab,i}, \quad (5.61)$$

with the 28 structure functions $U_{ab,i}$, and the basis tensors

$$\begin{aligned} t_{ab,1}^{\mu\nu}, \dots, t_{ab,4}^{\mu\nu} &= S_a \cdot S_b \left\{ g^{\mu\nu} - \frac{q^\mu q^\nu}{q^2}, \tilde{P}_a^\mu \tilde{P}_a^\nu, \tilde{P}_b^\mu \tilde{P}_b^\nu, \tilde{P}_a^\mu \tilde{P}_b^\nu + \tilde{P}_a^\nu \tilde{P}_b^\mu \right\}, \\ t_{ab,5}^{\mu\nu}, \dots, t_{ab,8}^{\mu\nu} &= S_a \cdot q S_b \cdot q \left\{ g^{\mu\nu} - \frac{q^\mu q^\nu}{q^2}, \tilde{P}_a^\mu \tilde{P}_a^\nu, \tilde{P}_b^\mu \tilde{P}_b^\nu, \tilde{P}_a^\mu \tilde{P}_b^\nu + \tilde{P}_a^\nu \tilde{P}_b^\mu \right\}, \\ t_{ab,9}^{\mu\nu}, \dots, t_{ab,12}^{\mu\nu} &= S_a \cdot q S_b \cdot P_a \left\{ g^{\mu\nu} - \frac{q^\mu q^\nu}{q^2}, \tilde{P}_a^\mu \tilde{P}_a^\nu, \tilde{P}_b^\mu \tilde{P}_b^\nu, \tilde{P}_a^\mu \tilde{P}_b^\nu + \tilde{P}_a^\nu \tilde{P}_b^\mu \right\}, \\ t_{ab,13}^{\mu\nu}, \dots, t_{ab,16}^{\mu\nu} &= S_b \cdot q S_a \cdot P_b \left\{ g^{\mu\nu} - \frac{q^\mu q^\nu}{q^2}, \tilde{P}_a^\mu \tilde{P}_a^\nu, \tilde{P}_b^\mu \tilde{P}_b^\nu, \tilde{P}_a^\mu \tilde{P}_b^\nu + \tilde{P}_a^\nu \tilde{P}_b^\mu \right\}, \\ t_{ab,17}^{\mu\nu}, \dots, t_{ab,20}^{\mu\nu} &= S_a \cdot P_b S_b \cdot P_a \left\{ g^{\mu\nu} - \frac{q^\mu q^\nu}{q^2}, \tilde{P}_a^\mu \tilde{P}_a^\nu, \tilde{P}_b^\mu \tilde{P}_b^\nu, \tilde{P}_a^\mu \tilde{P}_b^\nu + \tilde{P}_a^\nu \tilde{P}_b^\mu \right\}, \\ t_{ab,21}^{\mu\nu}, t_{ab,22}^{\mu\nu} &= S_a \cdot q \left\{ \tilde{S}_b^\mu \tilde{P}_a^\nu + \tilde{S}_b^\nu \tilde{P}_a^\mu, \tilde{S}_b^\mu \tilde{P}_b^\nu + \tilde{S}_b^\nu \tilde{P}_b^\mu \right\}, \\ t_{ab,23}^{\mu\nu}, t_{ab,24}^{\mu\nu} &= S_b \cdot q \left\{ \tilde{S}_a^\mu \tilde{P}_a^\nu + \tilde{S}_a^\nu \tilde{P}_a^\mu, \tilde{S}_a^\mu \tilde{P}_b^\nu + \tilde{S}_a^\nu \tilde{P}_b^\mu \right\}, \\ t_{ab,25}^{\mu\nu}, t_{ab,26}^{\mu\nu} &= S_a \cdot P_b \left\{ \tilde{S}_b^\mu \tilde{P}_a^\nu + \tilde{S}_b^\nu \tilde{P}_a^\mu, \tilde{S}_b^\mu \tilde{P}_b^\nu + \tilde{S}_b^\nu \tilde{P}_b^\mu \right\}, \\ t_{ab,27}^{\mu\nu}, t_{ab,28}^{\mu\nu} &= S_b \cdot P_a \left\{ \tilde{S}_a^\mu \tilde{P}_a^\nu + \tilde{S}_a^\nu \tilde{P}_a^\mu, \tilde{S}_a^\mu \tilde{P}_b^\nu + \tilde{S}_a^\nu \tilde{P}_b^\mu \right\}. \end{aligned} \quad (5.62)$$

As a result one has the following final decomposition of the hadronic tensor with 48 structure functions

$$\begin{aligned} W^{\mu\nu} &= \sum_{i=1}^{48} t_{pol,i}^{\mu\nu} U_{pol,i} = \\ &= \sum_{i=1}^4 t_{u,i}^{\mu\nu} U_{u,i} + \sum_{i=1}^8 t_{a,i}^{\mu\nu} U_{a,i} + \sum_{i=1}^8 t_{b,i}^{\mu\nu} U_{b,i} + \sum_{i=1}^{28} t_{ab,i}^{\mu\nu} U_{ab,i}. \end{aligned} \quad (5.63)$$

Appendix B. Structure functions in parton model

5.8 DY case

The notation for unit vector \vec{h} is used (Tab. 2.1). Expansion of the structure functions through TMDs reads:

$$F_{UU}^1 = \mathcal{C} [f_1 \bar{f}_1], \quad (5.64)$$

$$F_{UU}^{\cos 2\varphi} = \mathcal{C} \left[\frac{2(\vec{h} \cdot \vec{k}_{aT})(\vec{h} \cdot \vec{k}_{bT}) - \vec{k}_{aT} \cdot \vec{k}_{bT}}{M_a M_b} h_1^\perp \bar{h}_1^\perp \right], \quad (5.65)$$

$$F_{LU}^{\sin 2\varphi} = \mathcal{C} \left[\frac{2(\vec{h} \cdot \vec{k}_{aT})(\vec{h} \cdot \vec{k}_{bT}) - \vec{k}_{aT} \cdot \vec{k}_{bT}}{M_a M_b} h_{1L}^\perp \bar{h}_1^\perp \right], \quad (5.66)$$

$$F_{UL}^{\sin 2\varphi} = -\mathcal{C} \left[\frac{2(\vec{h} \cdot \vec{k}_{aT})(\vec{h} \cdot \vec{k}_{bT}) - \vec{k}_{aT} \cdot \vec{k}_{bT}}{M_a M_b} h_1^\perp \bar{h}_{1L}^\perp \right], \quad (5.67)$$

$$F_{TU}^1 = -\mathcal{C} \left[\frac{\vec{h} \cdot \vec{k}_{aT}}{M_a} f_{1T}^\perp \bar{f}_1 \right], \quad (5.68)$$

$$F_{TU}^{\sin(2\varphi - \varphi_a)} = \mathcal{C} \left[\frac{\vec{h} \cdot \vec{k}_{bT}}{M_b} h_1 \bar{h}_1^\perp \right], \quad (5.69)$$

$$F_{TU}^{\sin(2\varphi + \varphi_a)} = \mathcal{C} \left[\frac{1}{2M_a^2 M_b} \left(2(\vec{h} \cdot \vec{k}_{aT}) [2(\vec{h} \cdot \vec{k}_{aT})(\vec{h} \cdot \vec{k}_{bT}) - \vec{k}_{aT} \cdot \vec{k}_{bT}] - \vec{k}_{aT}^2 (\vec{h} \cdot \vec{k}_{bT}) \right) h_{1T}^\perp \bar{h}_1^\perp \right], \quad (5.70)$$

$$F_{UT}^1 = \mathcal{C} \left[\frac{\vec{h} \cdot \vec{k}_{bT}}{M_b} f_1 \bar{f}_{1T}^\perp \right], \quad (5.71)$$

$$F_{UT}^{\sin(2\varphi-\varphi_b)} = -\mathcal{C} \left[\frac{\vec{h} \cdot \vec{k}_{aT}}{M_a} h_1^\perp \bar{h}_1 \right], \quad (5.72)$$

$$F_{UT}^{\sin(2\varphi+\varphi_b)} = -\mathcal{C} \left[\frac{1}{2M_a M_b^2} \left(2(\vec{h} \cdot \vec{k}_{bT}) [2(\vec{h} \cdot \vec{k}_{aT})(\vec{h} \cdot \vec{k}_{bT}) - \vec{k}_{aT} \cdot \vec{k}_{bT}] \right. \right. \\ \left. \left. - \vec{k}_{bT}^2 (\vec{h} \cdot \vec{k}_{aT}) \right) h_1^\perp \bar{h}_{1T} \right]. \quad (5.73)$$

$$F_{LL}^1 = -\mathcal{C} [g_{1L} \bar{g}_{1L}], \quad (5.74)$$

$$F_{LL}^{\cos 2\varphi} = \mathcal{C} \left[\frac{2(\vec{h} \cdot \vec{k}_{aT})(\vec{h} \cdot \vec{k}_{bT}) - \vec{k}_{aT} \cdot \vec{k}_{bT}}{M_a M_b} h_{1L}^\perp \bar{h}_{1L}^\perp \right], \quad (5.75)$$

$$F_{LT}^1 = -\mathcal{C} \left[\frac{\vec{h} \cdot \vec{k}_{bT}}{M_b} g_{1L} \bar{g}_{1T} \right], \quad (5.76)$$

$$F_{LT}^{\cos(2\varphi-\varphi_b)} = \mathcal{C} \left[\frac{\vec{h} \cdot \vec{k}_{aT}}{M_a} h_{1L}^\perp \bar{h}_1 \right], \quad (5.77)$$

$$F_{LT}^{\cos(2\varphi+\varphi_b)} = \mathcal{C} \left[\frac{2(\vec{h} \cdot \vec{k}_{bT}) [2(\vec{h} \cdot \vec{k}_{aT})(\vec{h} \cdot \vec{k}_{bT}) - \vec{k}_{aT} \cdot \vec{k}_{bT}] - \vec{k}_{bT}^2 (\vec{h} \cdot \vec{k}_{aT})}{2M_a M_b^2} h_{1L}^\perp \bar{h}_{1T}^\perp \right], \quad (5.78)$$

$$F_{TL}^1 = -\mathcal{C} \left[\frac{\vec{h} \cdot \vec{k}_{aT}}{M_a} g_{1T} \bar{g}_{1L} \right], \quad (5.79)$$

$$F_{TL}^{\cos(2\varphi-\varphi_a)} = \mathcal{C} \left[\frac{\vec{h} \cdot \vec{k}_{bT}}{M_b} h_1 \bar{h}_{1L}^\perp \right], \quad (5.80)$$

$$F_{TL}^{\cos(2\varphi+\varphi_a)} = \mathcal{C} \left[\frac{2(\vec{h} \cdot \vec{k}_{aT}) [2(\vec{h} \cdot \vec{k}_{aT})(\vec{h} \cdot \vec{k}_{bT}) - \vec{k}_{aT} \cdot \vec{k}_{bT}] - \vec{k}_{aT}^2 (\vec{h} \cdot \vec{k}_{bT})}{2M_a^2 M_b} h_{1T}^\perp \bar{h}_{1L}^\perp \right], \quad (5.81)$$

$$F_{TT}^1 = \mathcal{C} \left[\frac{2(\vec{h} \cdot \vec{k}_{aT})(\vec{h} \cdot \vec{k}_{bT}) - \vec{k}_{aT} \cdot \vec{k}_{bT}}{2M_a M_b} (f_{1T}^\perp \bar{f}_{1T}^\perp - g_{1T} \bar{g}_{1T}) \right], \quad (5.82)$$

$$\bar{F}_{TT}^1 = -\mathcal{C} \left[\frac{\vec{k}_{aT} \cdot \vec{k}_{bT}}{2M_a M_b} (f_{1T}^\perp \bar{f}_{1T}^\perp + g_{1T} \bar{g}_{1T}) \right], \quad (5.83)$$

$$F_{TT}^{\cos(2\varphi-\varphi_a-\varphi_b)} = \mathcal{C} [h_1 \bar{h}_1], \quad (5.84)$$

$$F_{TT}^{\cos(2\varphi-\varphi_a+\varphi_b)} = \mathcal{C} \left[\frac{2(\vec{h} \cdot \vec{k}_{bT})^2 - \vec{k}_{bT}^2}{2M_b^2} h_1 \bar{h}_{1T}^\perp \right], \quad (5.85)$$

$$F_{TT}^{\cos(2\varphi+\varphi_a-\varphi_b)} = \mathcal{C} \left[\frac{2(\vec{h} \cdot \vec{k}_{aT})^2 - \vec{k}_{aT}^2}{2M_a^2} h_{1T}^\perp \bar{h}_1 \right], \quad (5.86)$$

$$F_{TT}^{\cos(2\varphi+\varphi_a+\varphi_b)} = \mathcal{C} \left[\left(\frac{4(\vec{h} \cdot \vec{k}_{aT})(\vec{h} \cdot \vec{k}_{bT})[2(\vec{h} \cdot \vec{k}_{aT})(\vec{h} \cdot \vec{k}_{bT}) - \vec{k}_{aT} \cdot \vec{k}_{bT}]}{4M_a^2 M_b^2} + \frac{\vec{k}_{aT}^2 \vec{k}_{bT}^2 - 2\vec{k}_{aT}^2(\vec{h} \cdot \vec{k}_{bT})^2 - 2\vec{k}_{bT}^2(\vec{h} \cdot \vec{k}_{aT})^2}{4M_a^2 M_b^2} \right) h_{1T}^\perp \bar{h}_{1T}^\perp \right]. \quad (5.87)$$

5.9 SIDIS case

Expansion of the structure functions through TMDs reads:

$$F_{UU,T} = \mathcal{C}[f_1 D_1], \quad F_{UU,L} = 0, \quad (5.88)$$

$$F_{UU}^{\cos \phi_h} = \frac{2M}{Q} \mathcal{C} \left[-\frac{\hat{h} \cdot \vec{k}_T}{M_h} \left(xh H_1^\perp + \frac{M_h}{M} f_1 \frac{\tilde{D}^\perp}{z} \right) - \frac{\hat{h} \cdot \vec{p}_T}{M} \left(x f^\perp D_1 + \frac{M_h}{M} h_1^\perp \frac{\tilde{H}}{z} \right) \right], \quad (5.89)$$

$$F_{UU}^{\cos 2\phi_h} = \mathcal{C} \left[-\frac{2(\hat{h} \cdot \vec{k}_T)(\hat{h} \cdot \vec{p}_T) - \vec{k}_T \cdot \vec{p}_T}{MM_h} h_1^\perp H_1^\perp \right], \quad (5.90)$$

$$F_{LU}^{\sin \phi_h} = \frac{2M}{Q} \mathcal{C} \left[-\frac{\hat{h} \cdot \vec{k}_T}{M_h} \left(xe H_1^\perp + \frac{M_h}{M} f_1 \frac{\tilde{G}^\perp}{z} \right) + \frac{\hat{h} \cdot \vec{p}_T}{M} \left(xg^\perp D_1 + \frac{M_h}{M} h_1^\perp \frac{\tilde{E}}{z} \right) \right], \quad (5.91)$$

$$F_{UL}^{\sin \phi_h} = \frac{2M}{Q} \mathcal{C} \left[-\frac{\hat{h} \cdot \vec{k}_T}{M_h} \left(xh_L H_1^\perp + \frac{M_h}{M} g_{1L} \frac{\tilde{G}^\perp}{z} \right) + \frac{\hat{h} \cdot \vec{p}_T}{M} \left(x f_L^\perp D_1 - \frac{M_h}{M} h_{1L}^\perp \frac{\tilde{H}}{z} \right) \right], \quad (5.92)$$

$$F_{UL}^{\sin 2\phi_h} = \mathcal{C} \left[-\frac{2(\hat{h} \cdot \vec{k}_T)(\hat{h} \cdot \vec{p}_T) - \vec{k}_T \cdot \vec{p}_T}{MM_h} h_{1L}^\perp H_1^\perp \right], \quad (5.93)$$

$$F_{LL} = \mathcal{C}[g_{1L} D_1], \quad (5.94)$$

$$F_{LL}^{\cos \phi_h} = \frac{2M}{Q} \mathcal{C} \left[\frac{\hat{h} \cdot \vec{k}_T}{M_h} \left(xe_L H_1^\perp - \frac{M_h}{M} g_{1L} \frac{\tilde{D}^\perp}{z} \right) - \frac{\hat{h} \cdot \vec{p}_T}{M} \left(xg_L^\perp D_1 + \frac{M_h}{M} h_{1L}^\perp \frac{\tilde{E}}{z} \right) \right], \quad (5.95)$$

$$F_{UT,T}^{\sin(\phi_h - \phi_S)} = \mathcal{C} \left[-\frac{\hat{\vec{h}} \cdot \vec{p}_T}{M} f_{1T}^\perp D_1 \right], \quad (5.96)$$

$$F_{UT,L}^{\sin(\phi_h - \phi_S)} = 0, \quad (5.97)$$

$$F_{UT}^{\sin(\phi_h + \phi_S)} = \mathcal{C} \left[-\frac{\hat{\vec{h}} \cdot \vec{k}_T}{M_h} h_1 H_1^\perp \right], \quad (5.98)$$

$$F_{UT}^{\sin(3\phi_h - \phi_S)} = \mathcal{C} \left[\frac{1}{2M^2 M_h} \left(2(\hat{\vec{h}} \cdot \vec{p}_T)(\vec{p}_T \cdot \vec{k}_T) + \vec{p}_T^2 (\hat{\vec{h}} \cdot \vec{k}_T) - 4(\hat{\vec{h}} \cdot \vec{p}_T)^2 (\hat{\vec{h}} \cdot \vec{k}_T) \right) h_{1T}^\perp H_1^\perp \right], \quad (5.99)$$

$$F_{UT}^{\sin \phi_S} = \frac{2M}{Q} \mathcal{C} \left\{ \left(x f_T D_1 - \frac{M_h}{M} h_1 \frac{\tilde{H}}{z} \right) - \frac{\vec{k}_T \cdot \vec{p}_T}{2MM_h} \times \left[\left(x h_T H_1^\perp + \frac{M_h}{M} g_{1T} \frac{\tilde{G}^\perp}{z} \right) - \left(x h_T^\perp H_1^\perp - \frac{M_h}{M} f_{1T}^\perp \frac{\tilde{D}^\perp}{z} \right) \right] \right\}, \quad (5.100)$$

$$F_{UT}^{\sin(2\phi_h - \phi_S)} = \frac{2M}{Q} \mathcal{C} \left\{ \frac{2(\hat{\vec{h}} \cdot \vec{p}_T)^2 - \vec{p}_T^2}{2M^2} \left(x f_T^\perp D_1 - \frac{M_h}{M} h_{1T}^\perp \frac{\tilde{H}}{z} \right) - \frac{2(\hat{\vec{h}} \cdot \vec{k}_T)(\hat{\vec{h}} \cdot \vec{p}_T) - \vec{k}_T \cdot \vec{p}_T}{2MM_h} \left[\left(x h_T H_1^\perp + \frac{M_h}{M} g_{1T} \frac{\tilde{G}^\perp}{z} \right) + \left(x h_T^\perp H_1^\perp - \frac{M_h}{M} f_{1T}^\perp \frac{\tilde{D}^\perp}{z} \right) \right] \right\}, \quad (5.101)$$

$$F_{LT}^{\cos(\phi_h - \phi_S)} = \mathcal{C} \left[\frac{\hat{\vec{h}} \cdot \vec{p}_T}{M} g_{1T} D_1 \right], \quad (5.102)$$

$$F_{LT}^{\cos \phi_S} = \frac{2M}{Q} \mathcal{C} \left\{ -\left(x g_T D_1 + \frac{M_h}{M} h_1 \frac{\tilde{E}}{z} \right) + \frac{\vec{k}_T \cdot \vec{p}_T}{2MM_h} \times \left[\left(x e_T H_1^\perp - \frac{M_h}{M} g_{1T} \frac{\tilde{D}^\perp}{z} \right) + \left(x e_T^\perp H_1^\perp + \frac{M_h}{M} f_{1T}^\perp \frac{\tilde{G}^\perp}{z} \right) \right] \right\}, \quad (5.103)$$

$$F_{LT}^{\cos(2\phi_h - \phi_S)} = \frac{2M}{Q} \mathcal{C} \left\{ -\frac{2(\hat{\vec{h}} \cdot \vec{p}_T)^2 - \vec{p}_T^2}{2M^2} \left(x g_T^\perp D_1 + \frac{M_h}{M} h_{1T}^\perp \frac{\tilde{E}}{z} \right) + \frac{2(\hat{\vec{h}} \cdot \vec{k}_T)(\hat{\vec{h}} \cdot \vec{p}_T) - \vec{k}_T \cdot \vec{p}_T}{2MM_h} \left[\left(x e_T H_1^\perp - \frac{M_h}{M} g_{1T} \frac{\tilde{D}^\perp}{z} \right) - \left(x e_T^\perp H_1^\perp + \frac{M_h}{M} f_{1T}^\perp \frac{\tilde{G}^\perp}{z} \right) \right] \right\}. \quad (5.104)$$

Appendix C. Statistics summary

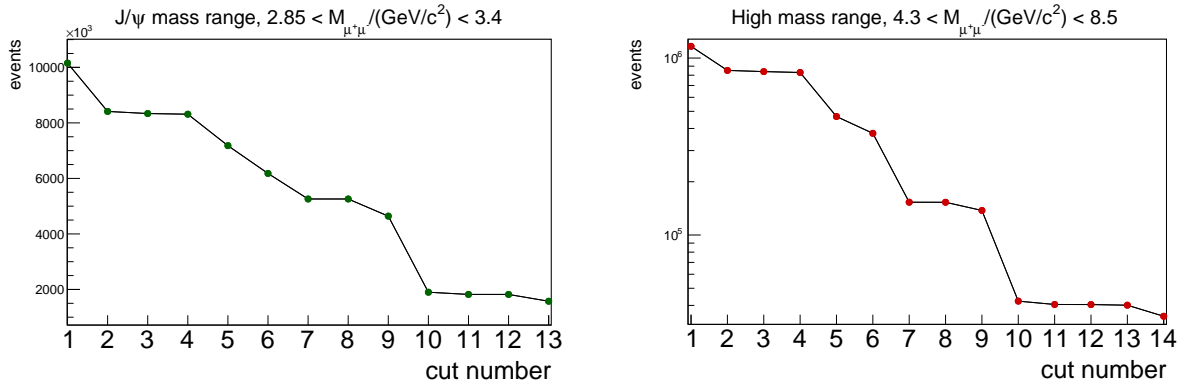


Figure 5.83: Impact of cuts in slot2 production of 2015.

	P01 (W07)	P02 (W08)	P03 (W09)	P04 (W10)	P05 (W11)	P06 (W12)	P07 (W13)	P08 (W14)	P09 (W15)	Total
1	136734	138619	125576	128471	198930	150381	139527	94602	52105	1164945
2	102576	103484	91961	94244	145081	108766	99975	68197	37207	851491
3	101398	102201	90807	93125	142890	106364	98179	66964	36544	838472
4	100035	100656	90116	92426	141699	105437	96649	65790	35989	828797
5	52421	50765	51101	53551	81586	61392	57159	38066	21246	467287
6	45682	43528	36906	42126	62170	45426	49154	32761	17767	375520
7	18157	17298	15571	17960	26260	19266	19361	12392	6937	153202
8	18143	17287	15555	17954	26239	19248	19344	12389	6929	153088
9	16364	15559	13949	16188	23589	17277	17372	11121	6211	137630
10	4849	4763	4345	4828	7393	5474	5351	3334	1956	42293
11	4636	4533	4155	4623	7078	5242	5152	3198	1876	40493
12	4626	4526	4152	4619	7071	5239	5151	3193	1872	40449
13	4581	4480	4116	4587	7021	5187	5112	3169	1858	40111
14	3907	3803	3716	3943	5125	4916	4626	2897	1796	34729

Table 5.18: Cut-by-cut event flow by periods in the HM range of 2015 s2-production

	P01 (W07)	P02 (W08)	P03 (W09)	P04 (W10)	P05 (W11)	P06 (W12)	P07 (W13)	P08 (W14)	P09 (W15)	Total
1	1140578	1121855	1130396	1164685	1797954	1360372	1197228	789498	450883	10153449
2	952578	933661	939584	969567	1491880	1126261	982781	646706	369719	8412737
3	944461	925992	929831	962044	1478890	1114153	974178	640740	366526	8336815
4	941382	922572	927915	960059	1475868	1111511	970500	638041	365156	8313004
5	794438	770717	803337	836769	1287812	970940	845736	550833	319305	7179887
6	726105	696109	634060	716169	1069005	782119	770980	501436	282977	6178960
7	616125	590346	540980	611842	914608	667044	653761	422954	240832	5258492
8	616123	590344	540977	611841	914607	667043	653760	422953	240832	5258480
9	544465	521516	477321	540014	807548	588470	576490	373306	212313	4641443
10	218193	210372	200802	218033	333249	245154	235073	152346	87206	1900428
11	208778	201331	192715	208944	319378	235032	225646	145262	83703	1820789
12	208754	201306	192687	208914	319327	234999	225606	145238	83691	1820522
13	178234	171575	173630	178988	230817	223036	204066	133609	81039	1574994

Table 5.19: Cut-by-cut event flow by periods in the J/ψ mass range of 2015 s2-production

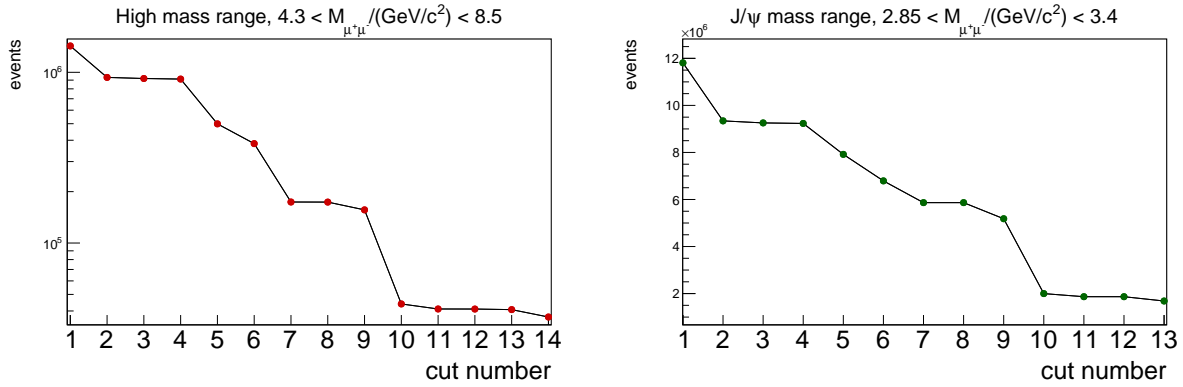


Figure 5.84: Impact of cuts in t8-production of 2018.

	P01	P02	P03	P04	P05	P06	P07	P08	Total
1	157552	286710	220059	209140	123480	135083	207200	87834	1427058
2	105624	188567	144561	136078	80260	87348	134409	56755	933602
3	104362	185810	142481	134044	78984	86027	132429	55686	919823
4	103588	184436	141438	133057	78347	85370	131422	55218	912876
5	55331	100485	78486	73074	42226	47340	71557	30457	498956
6	42218	77980	62412	55542	32359	36099	53517	22035	382162
7	17526	35335	27173	24983	15041	17475	25555	10800	173888
8	17508	35293	27150	24954	15033	17458	25523	10784	173703
9	15814	31792	24459	22459	13482	15640	23019	9721	156386
10	4467	8845	6965	6469	3821	4296	6432	2677	43972
11	4171	8280	6493	6042	3548	4039	6002	2508	41083
12	4167	8273	6492	6036	3546	4033	5997	2507	41051
13	4133	8206	6439	5984	3523	4010	5954	2479	40728
14	3663	7339	5862	5244	3355	3741	5482	2183	36869

Table 5.20: Cut-by-cut event flow by periods in the HM range of 2018 t8-production

	P01	P02	P03	P04	P05	P06	P07	P08	Total
1	1223500	2369506	1781524	1719929	1016748	1167575	1773867	755545	11808194
2	970962	1876630	1409733	1359447	802195	923531	1403901	595402	9341801
3	963502	1859089	1396772	1345478	792498	915576	1392661	589658	9255234
4	961284	1854940	1393622	1342369	790561	913248	1389349	588181	9233554
5	812322	1586690	1193827	1151590	676265	790972	1198563	508374	7918603
6	687711	1376347	1056510	984870	578975	675919	1012271	418421	6791024
7	583618	1189186	907887	849439	503115	590341	877042	365073	5865701
8	583618	1189184	907885	849437	503115	590340	877042	365071	5865692
9	515733	1051301	801795	750364	444072	521215	774551	322356	5181387
10	199020	404813	310124	295068	173326	198581	294933	122679	1998544
11	185925	378428	289208	275213	161996	185869	275433	114888	1866960
12	185898	378377	289167	275174	161967	185841	275404	114873	1866701
13	165608	336198	263736	241243	153343	172076	252312	99404	1683920

Table 5.21: Cut-by-cut event flow by periods in the J/ψ mass range of 2018 t8-production

List of Figures

1.1	Interrelations between distribution functions.	4
1.2	The eight leading 2-twist TMD PDFs.	6
1.3	Results on Drell-Yan TSAs as functions of x_N , x_π , x_F , q_T , $M_{\mu\mu}$ extracted by COMPASS collaboration from 2015 data.	9
1.4	Sivers sign-change test from the COMPASS Drell-Yan data [84] compared to the theoretical predictions for different Q^2 evolution schemes from [86] (DGLAP), [87] (TMD-1) and [88] (TMD-2). The dark-shaded (light-shaded) predictions are evaluated with (without) the sign-change hypothesis.	10
1.5	Results on the Sivers asymmetry for pions, protons (upper plot) and antiprotons (lower plot) from the HERMES experiment at DESY [85].	10
1.6	Results from the STAR collaboration at BNL [82], the plots show the Sivers asymmetry as a function of rapidity y^W and transverse momentum P_T^W from the W^\pm -boson production compared to the KQ [89] and to the EIKV [87] models; the Sivers asymmetry as a function of rapidity of the Z^0 -boson from DY process is shown on the bottom right panel.	11
1.7	New preliminary results from the STAR collaboration given at the PANIC conference in 2021 [83]. Two left plots: the Sivers asymmetry as a function of rapidity y^W from the W^\pm -boson production compared to the previous results [82] (gray points) and a theoretical prediction from Ref. [90] (in green). Right plot: the Sivers asymmetry from the DY-like $Z^0 \rightarrow l^+l^-$ production as a function of rapidity y^{Z^0} compared to the previous results [82] (blue point) and to a theoretical prediction from Ref. [91] (in green).	11

1.8	TMDs in a light-front quark model multiplied with x (left: up quark distributions; right: for down quark distributions). Plots are taken from [130].	13
1.9	The proton TMDs of u and d quarks in LFCQM [137–139] and SPM [142] at the scale $Q_0^2 = 2.4 \text{ GeV}^2$ compared to phenomenological fits for $f_{1,p}(x)$ from MSTW2008(LO) [95], $f_{1T,p}^{\perp(1)a}(x)$ from JAM20 [105] and Torino [103], $h_{1,p}^a(x)$ from JAM20 [105] and Torino [104], $h_{1,p}^{\perp(1)a}(x)$ from BMP10 [114], $h_{1T,p}^{\perp(2)a}(x)$ from LP15 [113]. Sivers and Boer-Mulders TMDs are shown with the sign for DY process. The error bands show the $1\text{-}\sigma$ uncertainty of the JAM20 extractions [105]. Plots are taken from Ref. [136].	14
1.10	Left: $f_{1,\pi^-}^{\bar{u}}(x)$ from LFCQM [143] and SPM [140] LO-evolved to the scale $Q_0^2 = 2.4 \text{ GeV}^2$ in comparison to MRSS parameterization [108]. Right: Predictions from LFCQM [143] and SPM [140] for the pion Boer-Mulders function (with the sign for DY) for which no parameterizations are currently available. Plots are taken from Ref. [136].	15
1.11	Leading-twist TSAs as a function of x_p (left), x_π (middle) and q_T (right) compared to COMPASS results [84]. Plots are taken from Ref. [136].	15
1.12	Results on λ , ν , μ asymmetries from CERN (NA10 [144]) and FermiLab (E615 [128], E866 [145]) experiments. The asymmetries are presented in the CS frame and only statistical uncertainties are drawn.	17
1.13	Results on λ and ν asymmetries from CDF (left) and CMS (right) experiments with a comparison to LO (line) and NLO (histogram) pQCD calculations [148]. Plots are taken from Ref. [148].	18
1.14	Results on spin-independent azimuthal asymmetries λ , ν , μ experiments with a comparison to NLO (red line) and NNLO (blue line) pQCD calculations [149]. Plots are taken from Ref. [149].	18
1.15	Results on phenomenological extractions of the ν asymmetry. Two left plots: extracted results from the Ref. [153] based on data of the E866 experiments, the red solid line is the fit curve, while the dotted red lines represent the corresponding errors. Right plot: extracted results from Ref. [152].	19

1.16	Predictions in the COMPASS kinematics for the asymmetry as a function of q_T related to the non-perturbative Boer-Mulders effect. Left: a prediction from Ref. [160]. Right: model predictions for the $A_{UU}^{\cos(2\varphi_{CS})} = \nu/2$ from Ref. [136].	20
1.17	Experimental results on gluon Sivers asymmetry. Left: COMPASS results at high- p_T in hadron pair production in SIDIS data collected transversely polarized deuterons and protons [221]. Right: PHENIX results in π^0 and η meson productions in polarized $p+p$ collisions (pseudorapidity range $ \eta < 0.35$, center-of-mass energy of 200 GeV) compared to theoretical predictions (see details and references in Ref. [222]).	21
1.18	The Sivers asymmetry from J/ψ production predicted in Ref. [166] at COMPASS kinematics.	22
1.19	Results on the λ asymmetry in J/ψ production from various fixed target experiments [174]. The data are presented in the Collins-Soper frame.	23
1.20	Results on the λ asymmetry in J/ψ production from collider experiments [168, 175]. The data are presented in Helicity frame.	23
2.1	Diagram of the DY process at tree level.	26
2.2	Target rest frame definition for proton-pion interaction where the proton belongs to the target and has zero 3-momentum. S_T — target (proton) spin vector.	27
2.3	Collins-Soper frame definition for a proton-pion interaction.	27
2.4	Diagrams of DIS and SIDIS processes.	36
2.5	Lepton and hadron planes in semi-inclusive deep inelastic scattering.	37
2.6	Left: charged hadron SIDIS 2010 two-dimensional phase space (Q^2, x) distribution for $z > 0.1$. Right: dimuon pairs DY 2015 two-dimensional phase space (Q^2, x_N) . The SIDIS sub- Q^2 ranges correspond to four DY Q^2 ranges.	41
3.1	COMPASS location in CERN.	43
3.2	Scheme of previous collaborations on which COMPASS was founded.	44
3.3	Scheme of the COMPASS setup.	46
3.4	The scheme of the experimental Hall North 1 and 2 (EHN1, EHN2) and Experimental Cavern North 3 (ECN3).	47
3.5	The SPS PAGE 1 monitoring.	47

3.6	The SPS spill structure.	48
3.7	Beamline part.	48
3.8	The principle of operation of CEDAR [68].	49
3.9	The COMPASS polarized target.	50
3.10	The COMPASS hadron absorber. Side view left. 3D view right.	51
3.11	The principle of operation of the scintillating fibers.	53
3.12	A principle of operation of the COMPASS Micromegas detector.	54
3.13	Sketch of pixelized Micromegas detector (right). Zoom of the pixel area (left).	54
3.14	The COMPASS GEM detector.	55
3.15	The COMPASS Rich Wall detector.	56
3.16	Module of the COMPASS Rich and Muon walls.	56
3.17	Principle of operation of the COMPASS MWPC detector.	57
3.18	Principle of operation of the COMPASS Drift Chamber.	58
3.19	Scheme of the cross section of Straw tubes.	59
3.20	Sketch of the COMPASS Straw detector.	59
3.21	A sketch of cross-sectional side view of MW1.	61
3.22	Structure of the HCAL1 module: 1, scintillators; 2, iron plates; 3, light guide; 4, container; 5, PMT; 6, PMT magnetic shielding; 7, Cockcroft–Walton divider; 8, optical connector for LED control. Dimensions are in mm.	62
3.23	Schematic view (not in scale) of the location of the components relevant to the trigger system.	63
3.24	Principle of operation of the veto trigger. Muons passing the veto detector are removed (red) while other muons (which are probably produced in the target) are taken into account (green).	64
3.25	The COMPASS FPGA-based DAQ architecture.	66
3.26	Scheme of the COMPASS network.	67
4.1	CORAL operations.	70

4.2	Misalignment impact on the track reconstruction: a) ideal case of absence of misalignment — the reconstructed track coincides to the real track; b) some position is shifted by α , which is larger than typical spatial resolution of the detector; c) the wrong reconstructed due to misalignment track is demonstrated; d) the reconstruction taking into account a misalignment correction.	72
4.3	Alignment procedure flowchart.	76
4.4	Scheme of the CORAL coordinate reference frames: global in black and local associated with a certain detector plane in blue.	76
4.5	Δu distributions for the 4 th GEM station before the alignment procedure performed. The misalignment is clearly seen as asymmetric shapes of the distributions.	78
4.6	Δu distributions for the 4 th GEM station after performing 5 iterations of the alignment procedure.	78
4.7	Run-by-run comparison of the angle value. It is seen that V1 of FI55 was rotated between 2012 and 2016 runs.	79
4.8	Run-by-run comparison of the center coordinates. One can see a displacement correction in P09 for FI03.	80
4.9	Δu versus v distribution before alignment procedure (GM01 station, alignment run 278902 with magnetic field, $\mu+$ beam).	82
4.10	Δu versus v distribution after 5 iterations without angle constraint for GEMs (GM01 station, alignment run 278902 with magnetic field, $\mu+$ beam).	83
4.11	Δu versus v distribution after 5 iterations with angle constraint for GEMs (GM01 station, alignment run 278902 with magnetic field, $\mu+$ beam).	83
4.12	χ^2 -distributions of the track reconstruction: left – before alignment; middle – after 5 iterations of standard alignment; right – after 5 iterations of constrained alignment.	84
5.1	Performed physics data collection schedule for 2015 run. The $+-$ and $-+$ polarization configurations are indicated by red and blue boxes, correspondingly.	86
5.2	Performed physics data collection schedule for 2018 run. The $+-$ and $-+$ polarization configurations are indicated by red and blue boxes correspondingly.	88

5.3	Impact of trigger time difference cut (based on P02 period of 2015 t8-production data). Events without trigger validation cut (left), events passed by trigger validation (right). Red color represents the applied time window.	91
5.4	Impact of Z-coordinate cut for the NH ₃ target cells (in blue) target and a part of the W target used for unpolarized analysis (in yellow). Left HM range, right J/ψ mass range.	92
5.5	Impact of radial cut for NH ₃ target (based on P06 slot1 2015 data). Left before the cut, right the result of the cut.	93
5.6	Dimuon invariant mass distribution cut-by-cut, events with $M_{\mu\mu} > 2.0$ GeV (based on all periods of slot1 2015 data).	94
5.7	Distributions of x -variables and Q^2 in the HM range (based on all periods of slot1 2015 data).	95
5.8	Distributions of x -variables and Q^2 in the J/ψ mass range (based on all periods of slot1 2015 data).	96
5.9	Kinematic maps for the HM range (2015 slot1 data). The values are shifted horizontally for a better visibility. U-cell in red, D-cell in green, both cells of the NH ₃ target in blue.	96
5.10	Kinematic maps for the J/ψ range (2015 slot1 data). The values are shifted horizontally for a better visibility. U-cell in red, D-cell in green, both cells of the NH ₃ target in blue.	97
5.11	An example of instabilities indication among spills.	99
5.12	Examples of instabilities indication among runs.	99
5.13	Dimuon invariant mass distribution between two data productions.	101
5.14	Distributions of invariant dimuon mass differences for events that are in common between the two data productions are shown for three mass ranges.	101
5.15	Primary vertex Z-coordinate distributions and their ratio for the two productions in one period (P02): J/ψ mass range is on the left, HM range is on the right. Same distributions for the NH ₃ cells data are shown in the bottom panels. . . .	102

5.16	Distributions for X and Y coordinates of the primary vertex and their ratio for two productions in one period (P02). Results for J/ψ mass range are on the left, HM range is on the right. Same distributions for the NH_3 cells data are shown in the bottom panels	103
5.17	Distributions of the difference of the primary vertex Z-coordinate for events that are in common between the two data productions.	103
5.18	Muon momenta distributions in the laboratory frame and their ratio two productions in one period (P02). Muons on the left, anti-muon on the right.	104
5.19	Muon polar angle distributions in the laboratory frame and their ratio for two productions in one period (P02). Muons on the left, anti-muons on the right.	104
5.20	Muon azimuthal angle distributions in the laboratory frame for two productions in one period (P02). Muons on the left, anti-muons on the right.	104
5.21	Distributions of ϕ_S differences for events that are in common between the two data productions are shown for three mass ranges.	105
5.22	Distributions of θ_{CS} differences for events that are in common between the two data productions are shown for three mass ranges.	105
5.23	Distributions of ϕ_{CS} differences for events that are in common between the two data productions are shown for three mass ranges.	105
5.24	Dimuon invariant mass distributions for common and uncommon events from two productions in one period (P02).	106
5.25	Position (top plot) and resolution (bottom plot) of the J/ψ by sub-periods.	106
5.26	Position (top plot) and resolution (bottom plot) of the J/ψ by runs in 2015 from slot1 production.	107
5.27	An example of J/ψ -peak fit by periods (2018 t8-production data).	107
5.28	q_T dependence of the ϕ_S (left) and ϕ_{CS} (right) angular resolutions.	109
5.29	Left panel: decomposition of the dimuon mass spectrum using CB estimated from real data like-sign pairs, and physics contributions evaluated by MC. Right panel: independent estimation of the background fraction in the HM range.	109
5.30	Z-vertex distribution of the events originating from different materials in the NH_3 target region.	111

5.31	NH ₃ Z-vertex distribution of the events originating from upstream and downstream cells and unpolarized medium in different kinematic bins in high mass (top panel) and J/ψ (bottom panel) regions. The plots are based on MC simulations done with 2018(t2) configuration.	112
5.32	Average polarization values along the time (top - coil by coil, bottom -integrated).	114
5.33	Target polarization in 2015 and 2018 as a function of kinematic variables.	115
5.34	Dilution factor calculated for COMPASS dimuon pairs. Top plots: DY dilution factor in HM range x_N (left) and dilution factor for J/ψ production versus x_N (right). Two different sub-samples corresponding to the target cells are visible. Bottom plot: Average Drell-Yan dilution factor in 2015 and 2018 as a function of kinematic variables. Target compositions in 2015 and 2018 were slightly different, which causes small differences at the level of the dilution factor.	115
5.35	Depolarization factors shown as function of kinematic variables. Top plot: impact of different “ λ -value” hypotheses ($\lambda = 1.0, 0.8, 0.5$) is shown. Bottom plot: relative impact of different “ λ -value” hypotheses w.r.t. to the case $\lambda = 1.0$	117
5.36	The φ_S distribution in the first x_N bin is shown as extracted for u/d cells and $\uparrow\downarrow$ polarization states (2015-P06 data, slot1 production).	118
5.37	Results of 1DDR fit for Sivers asymmetry (based on HM 2015 data from all periods of slot1).	119
5.38	Period-wise LO asymmetries in the HM (top) and J/ψ mass (bottom) ranges (2018 data, t8 production).	125
5.39	TSA’s in the HM range by periods from two years averaged over kinematic bins. Red points represent asymmetries from 2015 (s2) while blue ones correspond to 2018 (t8).	126
5.40	TSA’s in the J/ψ mass range by periods from two years averaged over kinematic bins. Red points represent asymmetries from 2015 (s2) while blue ones correspond to 2018 (t8).	126
5.41	Pull-histograms for period compatibilty check.	127
5.42	Acceptance sub-division scheme over ϕ_{μ^+} used for RLTB-test.	128

5.43	Asymmetries extracted from the Right-, Left- (red points) and Top-, Bottom- (blue points) segments of the target cells in the HM range (2015 data, s2 production).	129
5.44	Asymmetries extracted from the Right-, Left- (red points) and Top-, Bottom- (blue points) segments of the target cells in the HM range from 2018 data (t8 production).	130
5.45	An example of the point-by-point estimation of the systematic uncertainties in terms of statistical ones from RLTB-test (HM range, 2015 data, s2 production).	131
5.46	“Fake-cells” configuration with respect to real ones.	133
5.47	Three types of false-asymmetries extracted for LO modulations in the HM range from 2015 (top) and 2018 (bottom) data.	134
5.48	TSA’s in the HM range as functions of kinematic variables. Available model predictions for twist-2 TSA’s from Ref. [136] are shown as functions of x_N , x_π , q_T (top plot).	139
5.49	TSA’s in the J/ψ mass range as functions of kinematic variables.	140
5.50	COMPASS published TSA’s from 2015-t3 data [84] compared to the 2015-s2 and joint 2015-s2+2018-t8 results.	141
5.51	5 TSA’s extracted from 2015 (red points) and 2018 data (blue points) with the joint results (green points).	141
5.52	The principle of determination of coincidence matrix.	145
5.53	The digit pattern of coincidence matrices. For each matrix, the x axis corresponds to the slab number of downstream hodoscope of each hodoscope pair, and the y axis corresponds to the slab number of upstream hodoscope. Each pixel corresponds to a combination of paired signal from two slabs.	146
5.54	The efficiencies of coincidence matrices.	146
5.55	The 2D hodoscope efficiencies for period P03 of 2018. For each hodoscope plane, the X axis corresponds to the x position in laboratory frame, and the Y axis corresponds to the y position in laboratory frame.	147
5.56	Illustration of agreement between RD and MC data as a function of x_F , for the NH_3 target on the top and for the W target on the bottom.	148

5.57 Kinematic maps for the NH_3 target. RD in blue, MC data in green. The values are shifted horizontally for a better visibility.	149
5.58 Kinematic maps for the W target. RD in blue, MC data in green. The values are shifted horizontally for a better visibility.	149
5.59 An example of a two-dimensional $\cos(\theta) \times \varphi$ histogram built for reconstructed MC data.	153
5.60 From left to right: reconstructed, generated distributions and reconstructed to generated ratio for φ_{CS} angle.	154
5.61 From left to right: reconstructed, generated distributions and reconstructed to generated ratio for $\cos(\theta_{CS})$	154
5.62 An example of the extended 16x8 histograms used in the acceptance estimation in case of HBL Three-dimensional simultaneous fit (P02, reconstructed MC). . .	156
5.63 Pull-histograms and their fit from different periods for the NH_3 target.	158
5.64 Pull-histograms and their fit from different periods for the W target.	159
5.65 Pull-histograms and their fit from two target cells of the NH_3 target.	160
5.66 Pull-histograms and their fit from two target halves of the W target.	161
5.67 Invariant $\tilde{\lambda}$ and F extracted from three dilepton rest frames for the NH_3 target (2018 data, t8 production).	162
5.68 Invariant $\tilde{\lambda}$ and F extracted from three dilepton rest frames for the W target (2018 data, t8 production).	162
5.69 UAs by periods for the NH_3 (top panels) and W (bottom panels) targets in the Collins-Soper frame (2018 data, t8 production).	165
5.70 NH_3 (red points) and W (blue points) UAs and Lam-Tung relation in the HM range in the Collins-Soper frame (2018 data, t8 production).	166
5.71 NH_3 (red points) and W (blue points) UAs and Lam-Tung relation in the HM range (2018 data, t8 production). Top panel: Gottfried-Jackson frame, Bottom panel: Helicity frame.	167
5.72 NH_3 (red points) and W (blue points) UAs and Lam-Tung relation in the Collins-Soper frame from J/ψ production (2018 data, only P03 period).	168

5.73	NH ₃ (red points) and W (blue points) UAs and Lam-Tung relation from J/ψ production (2018 data, only P03 period). Top panel: Gottfried-Jackson frame, Bottom panel: Helicity frame.	169
5.74	Invariant $\tilde{\lambda}$ and F extracted from three dilepton rest frames for the NH ₃ target from J/ψ production ($3.0 < M_{\mu\mu}/(\text{GeV}/c^2) < 3.3$). Top panel: NH ₃ target, Bottom panel: tungsten target.	170
5.75	Comparison of NH ₃ and tungsten results in the same high mass range. Top panel: standard cuts. Bottom panel: idem but with an additional cut $x_\pi > 0.34$	171
5.76	Comparison of NH ₃ and tungsten results in the same J/ψ mass range ($3.0 < M_{\mu\mu}/(\text{GeV}/c^2) < 3.3$) with an additional cut $x_\pi > 0.25$	172
5.77	Predictions from various models for the Sivers, transversity and pretzelosity asymmetries in the COMPASS kinematic region. The model labels are according to Fig. 1.9 and to Ref. [136].	175
5.78	The measured mean Sivers asymmetry and the theoretical predictions for different Q^2 evolution schemes from [86] (DGLAP), [87] (TMD-1) and [88] (TMD-2). The dark-shaded (light-shaded) predictions are evaluated with (without) the sign-change hypothesis.	176
5.79	COMPASS SIDIS-DY “bridge” results. Left: Sivers, Pretzelosity, Transversity asymmetries extracted in this Thesis from DY data (2015+2018) in the HM range. Right: same asymmetries extracted from COMPASS 2010 SIDIS data [79] at mostly the same hard scale. Note that angles are differently defined in SIDIS and DY, thus the same sign for the Sivers asymmetry implies the opposite sign for the corresponding TMD PDF.	177
5.80	Results on λ , μ , ν asymmetries from the W target (red) in comparison with the pQCD DYNNLO curve [149] (red) and other experiments: E615 [128] (green), NA10 [144] (blue).	179
5.81	Results on λ , μ , ν asymmetries from the W target (blue open circle) and NH ₃ target (red open circle) in comparison with the pQCD DYNNLO curve [149] (red curve) and with available model predictions for the ν asymmetry (dashed curves) according to the Ref. [136].	180

5.82 Results on Lam-Tung relation from the W target (red) in comparison with the pQCD DYNNLO curve [149] (red) and other experiments: E615 (green), NA10 (blue).	181
5.83 Impact of cuts in slot2 production of 2015.	193
5.84 Impact of cuts in t8-production of 2018.	194

List of Tables

1.1	World-wide results and extraction of a part of TMD PDFs. The table concerns only observables, which are related to an TSAs analyses of pion-induced DY data from COMPASS, and, therefore here the helicity $g_1^a(x, k_T)$, the Kotzinian-Mulders (transerve worm-gear) $g_{1T}^{\perp a}(x, k_T)$ and the longitudinal worm-gear $h_{1L}^{\perp a}(x, k_T)$ functions are skipped.	12
1.2	Mean value results on spin-independent azimuthal asymmetries from the NA10, E615 and E866 experiments.	16
2.1	Common used notations in kinematics of the DY process	28
2.2	Commonly used notations in kinematics of the SIDIS process.	37
2.3	Relations in measurements between the SIDIS and DY processes.	40
3.1	The COMPASS data taking by years.	45
3.2	List of triggers used during DY runs.	65
4.1	Output of the alignment procedure (“ <i>align.out</i> ”) after 5 iterations with and without angle constraints for the GEM detectors (alignment run 278902 with magnetic field, $\mu+$ beam).	84
4.2	Result values in the “ <i>detectors.dat</i> ” file after 5 iterations with and without angle constraints for the GEM detectors (alignment run 278902 with magnetic field, $\mu+$ beam).	84
5.1	2015 data taking periods.	87
5.2	2018 data taking periods.	89
5.3	Target cells positions in cm along Z-axis in the DY data-taking runs.	92

5.4	Kinematic bins for TSAs analysis in the HM range.	95
5.5	Kinematic bins for TSAs analysis in the J/ψ mass range.	95
5.6	Total statistics after the event selection from the data productions used for the TSAs extraction in the Thesis.	100
5.7	Resolutions for main kinematic and angular variables.	108
5.8	Composition of the events reconstructed in the polarized target cells.	111
5.9	Additional dilution factors due to cell-to-cell event migration in each kinematic bin.	116
5.10	Estimations of the systematic uncertainties in the HM range for analysis of 2015 data in units of $\sigma_{sys}/\sigma_{stat}$	135
5.11	Estimations of the systematic uncertainties in the HM range for analysis of 2018 data in units of $\sigma_{sys}/\sigma_{stat}$	135
5.12	Estimations of the systematic uncertainties in the J/ψ mass range for analysis of 2015 data in units of $\sigma_{sys}/\sigma_{stat}$	136
5.13	Estimations of the systematic uncertainties in the J/ψ mass range for analysis of 2018 data in units of $\sigma_{sys}/\sigma_{stat}$	136
5.14	Main part of the Pythia 8 settings used in the MC for the DY process.	144
5.15	Cut-by-cut event flow by periods in t8 production of 2018 for UAs analysis.	152
5.16	Kinematic bin limits for UAs analysis in the HM range for data from the NH_3 target.	152
5.17	Kinematic bin limits for UAs analysis in the HM range for data from the W target.	153
5.18	Cut-by-cut event flow by periods in the HM range of 2015 s2-production	193
5.19	Cut-by-cut event flow by periods in the J/ψ mass range of 2015 s2-production	194
5.20	Cut-by-cut event flow by periods in the HM range of 2018 t8-production	194
5.21	Cut-by-cut event flow by periods in the J/ψ mass range of 2018 t8-production	195

List of Abbreviations

1DDR	one-dimensional double ratio
BDM	beam decay muons
BMS	beam momentum station
CASTOR	CERN advanced storage
COMPASS	Common muon and proton apparatus for structure and spectroscopy
CORAL	COMPASS reconstruction and analysis
CS	Collins-Soper
DAQ	data acquisition
DCS	detector control system
DDD	DAQ data decoding
DGLAP	Dokshitzer–Gribov–Lipatov–Altarelli–Parisi equations
DIM	Distributed information management
DIS	deep inelastic scattering
DNP	dynamic nuclear polarization
DPS	detector pseudo-performance study
DVCS	deep virtual compton scattering
DY	Drell–Yan
EMC	European muon collaboration
EWUML	extended weighted unbinned maximum likelihood
JAM	Jefferson Lab angular momentum
FA	false asymmetry
FF	fragmentation function
FNAL	Fermi national accelerator laboratory
FPGA	field-programmable gate arrays

GEM	gas electron multiplier
GJ	Gottfried-Jackson
HBL	histogram binned likelihood
HERA	Hadron–electron ring accelerator
HM	high mass
LAS	large angle spectrometer
LAST	large angle spectrometer trigger
LFCQM	light-front constituent quark model
LHAPDF	Les Houches accord PDFs
LHC	Large hadron collider
LO	leading order
mDST	mini data summary trees
MC	Monte Carlo
MF	Muon Filter
MT	middle trigger
MWPC	multi-wire proportional chamber
NLO	next-to-leading order
NMR	nuclear magnetic resonance
NRQCD	non-relativistic QCD
OT	outer trigger
PDF	parton distribution functions
PHAST	PHysics Analysis Software Tools
PHENIX	Pioneering high energy nuclear interaction eXperiment
pQCD	perturbative quantum chromodynamics
QED	quantum electrodynamics
QCD	quantum chromodynamics
RHIC	Relativistic heavy ion collider
RICH	ring imaging Cherenkov
RLTB	right-left-top-bottom
SAS	small angle spectrometer
SIDIS	semi-inclusive deep inelastic scattering

SLAC	Stanford linear accelerator center
SM	standard model / solenoid magnet
SP	sub-period
SPM	spectator model
SPS	super proton synchrotron
STAR	Solenoidal tracker at RHIC
TMD	transverse momentum dependent
TSA	transverse spin asymmetries
UA	unpolarized asymmetries
UK	unbinned Kolmogorov
UML	unbinned maximum likelihood
WW	Wandzura-Wilczek

Bibliography

- [1] Murray Gell-Mann. A Schematic Model of Baryons and Mesons. *Phys. Lett.*, 8:214–215, 1964.
- [2] G. Zweig. An $SU(3)$ model for strong interaction symmetry and its breaking. Version 1. 1 1964.
- [3] G. Zweig. *An $SU(3)$ model for strong interaction symmetry and its breaking. Version 2.* 2 1964.
- [4] R. P. Feynman. The behavior of hadron collisions at extreme energies. *Conf. Proc.*, C690905:237–258, 1969.
- [5] J. D. Bjorken and E. A. Paschos. Inelastic electron-proton and γ -proton scattering and the structure of the nucleon. *Phys. Rev.*, 185:1975–1982, Sep 1969.
- [6] Elliott D. Bloom et al. High-Energy Inelastic e p Scattering at 6-Degrees and 10-Degrees. *Phys. Rev. Lett.*, 23:930–934, 1969.
- [7] Martin Breidenbach, Jerome I. Friedman, Henry W. Kendall, Elliott D. Bloom, D. H. Coward, H. C. DeStaebler, J. Drees, Luke W. Mo, and Richard E. Taylor. Observed behavior of highly inelastic electron-proton scattering. *Phys. Rev. Lett.*, 23:935–939, 1969.
- [8] G. Peter Lepage and Stanley J. Brodsky. Exclusive Processes in Quantum Chromodynamics: Evolution Equations for Hadronic Wave Functions and the Form-Factors of Mesons. *Phys. Lett.*, 87B:359–365, 1979.
- [9] A.V. Efremov and A.V. Radyushkin. Factorization and asymptotic behaviour of pion form factor in qcd. *Physics Letters B*, 94(2):245 – 250, 1980.

- [10] John C. Collins, Davison E. Soper, and George F. Sterman. Factorization of Hard Processes in QCD. *Adv. Ser. Direct. High Energy Phys.*, 5:1–91, 1989.
- [11] Xiangdong Ji. Viewing the proton through “color” filters. *Phys. Rev. Lett.*, 91:062001, Aug 2003.
- [12] A.V. Belitsky, Xiangdong Ji, and Feng Yuan. Quark imaging in the proton via quantum phase-space distributions. *Phys. Rev. D*, 69:074014, Apr 2004.
- [13] C. Lorce and B. Pasquini. Quark Wigner Distributions and Orbital Angular Momentum. *Phys. Rev.*, D84:014015, 2011.
- [14] S. D. Drell and Tung-Mow Yan. Massive Lepton Pair Production in Hadron-Hadron Collisions at High-Energies. *Phys. Rev. Lett.*, 25:316–320, 1970. [Erratum: *Phys. Rev. Lett.*25,902(1970)].
- [15] John C. Collins and Davison E. Soper. Angular distribution of dileptons in high-energy hadron collisions. *Phys. Rev. D*, 16:2219–2225, Oct 1977.
- [16] C. S. Lam and Wu-Ki Tung. Systematic approach to inclusive lepton pair production in hadronic collisions. *Phys. Rev. D*, 18:2447–2461, Oct 1978.
- [17] C. S. Lam and Wu-Ki Tung. Parton-model relation without quantum-chromodynamic modifications in lepton pair production. *Phys. Rev. D*, 21:2712–2715, May 1980.
- [18] A. N. Sissakian, O. Yu. Shevchenko, A. P. Nagaitsev, and O. N. Ivanov. Polarization effects in drell-yan processes. *Physics of Particles and Nuclei*, 41(1):64–100, Jan 2010.
- [19] Jen-Chieh Peng and Jian-Wei Qiu. Novel phenomenology of parton distributions from the Drell–Yan process. *Prog. Part. Nucl. Phys.*, 76:43–75, 2014.
- [20] R. D. Field and R. P. Feynman. Quark Elastic Scattering as a Source of High Transverse Momentum Mesons. *Phys. Rev. D*, 15:2590–2616, 1977.
- [21] P. Renton and W. S. C. Williams. Hadron Production in Lepton - Nucleon Scattering. *Ann. Rev. Nucl. Part. Sci.*, 31:193–230, 1981.

-
- [22] M. Anselmino, A. Efremov, and E. Leader. The Theory and phenomenology of polarized deep inelastic scattering. *Phys. Rept.*, 261:1–124, 1995. [Erratum: *Phys. Rept.*281,399(1997)].
- [23] John C. Collins. Leading twist single transverse-spin asymmetries: Drell-Yan and deep inelastic scattering. *Phys. Lett.*, B536:43–48, 2002.
- [24] Stanley J. Brodsky, Dae Sung Hwang, Yuri V. Kovchegov, Ivan Schmidt, and Matthew D. Sievert. Single-Spin Asymmetries in Semi-inclusive Deep Inelastic Scattering and Drell-Yan Processes. *Phys. Rev. D*, 88(1):014032, 2013.
- [25] Yuri L. Dokshitzer. Calculation of the Structure Functions for Deep Inelastic Scattering and $e+e-$ Annihilation by Perturbation Theory in Quantum Chromodynamics. *Sov. Phys. JETP*, 46:641–653, 1977. [*Zh. Eksp. Teor. Fiz.*73,1216(1977)].
- [26] Guido Altarelli and G. Parisi. Asymptotic Freedom in Parton Language. *Nucl. Phys.*, B126:298–318, 1977.
- [27] V. N. Gribov and L. N. Lipatov. Deep inelastic $e p$ scattering in perturbation theory. *Sov. J. Nucl. Phys.*, 15:438–450, 1972. [*Yad. Fiz.*15,781(1972)].
- [28] John C. Collins and Davison E. Soper. Back-To-Back Jets in QCD. *Nucl. Phys.*, B193:381, 1981. [Erratum: *Nucl. Phys.*B213,545(1983)].
- [29] R. D. Klem, J. E. Bowers, H. W. Courant, H. Kagan, M. L. Marshak, E. A. Peterson, K. Ruddick, W. H. Dragoset, and J. B. Roberts. Measurement of Asymmetries of Inclusive Pion Production in Proton Proton Interactions at 6-GeV/c and 11.8-GeV/c. *Phys. Rev. Lett.*, 36:929–931, 1976.
- [30] W. H. Dragoset, J. B. Roberts, J. E. Bowers, H. W. Courant, H. Kagan, M. L. Marshak, E. A. Peterson, K. Ruddick, and R. D. Klem. Asymmetries in Inclusive Proton-Nucleon Scattering at 11.75-GeV/c. *Phys. Rev. D*, 18:3939–3954, 1978.
- [31] G. Baum, M. R. Bergström, J. E. Clendenin, R. D. Ehrlich, V. W. Hughes, K. Kondo, M. S. Lubell, S. Miyashita, R. H. Miller, D. A. Palmer, W. Raith, N. Sasao, K. P. Schüller, and P. A. Souder. Measurement of asymmetry in spin-dependent $e - p$ resonance-region scattering. *Phys. Rev. Lett.*, 45:2000–2003, Dec 1980.

- [32] Guenter Baum et al. Measurement of Asymmetry in Spin Dependent e p Resonance Region Scattering. *Phys. Rev. Lett.*, 45:2000, 1980.
- [33] M. J. Alguard et al. Deep Inelastic Scattering of Polarized Electrons by Polarized Protons. *Phys. Rev. Lett.*, 37:1261, 1976.
- [34] M. J. Alguard et al. Deep Inelastic e p Asymmetry Measurements and Comparison with the Bjorken Sum Rule and Models of Proton Spin Structure. *Phys. Rev. Lett.*, 41:70, 1978.
- [35] P. L. Anthony et al. Deep inelastic scattering of polarized electrons by polarized He-3 and the study of the neutron spin structure. *Phys. Rev. D*, 54:6620–6650, 1996.
- [36] K. Abe et al. Measurements of the proton and deuteron spin structure function g_2 and asymmetry A_2 . *Phys. Rev. Lett.*, 76:587–591, 1996.
- [37] K. Abe et al. Precision determination of the neutron spin structure function $g_1(n)$. *Phys. Rev. Lett.*, 79:26–30, 1997.
- [38] P. L. Anthony et al. Measurement of the deuteron spin structure function $g_1(d)(x)$ for $1-(\text{GeV}/c)^{**2} < Q^{**2} < 40-(\text{GeV}/c)^{**2}$. *Phys. Lett. B*, 463:339–345, 1999.
- [39] P. L. Anthony et al. Measurements of the Q^{**2} dependence of the proton and neutron spin structure functions $g(1)^{**p}$ and $g(1)^{**n}$. *Phys. Lett. B*, 493:19–28, 2000.
- [40] J. Ashman et al. A Measurement of the Spin Asymmetry and Determination of the Structure Function $g(1)$ in Deep Inelastic Muon-Proton Scattering. *Phys. Lett.*, B206:364, 1988. [,340(1987)].
- [41] V. Papavassiliou. A Proposal to measure the spin dependent structure functions g_1 of the neutron and proton in the CERN muon beam by the Spin Muon Collaboration. In *24th Rencontres de Moriond: New Results in Hadronic Interactions*, 1989.
- [42] B. Adeva et al. Polarization of valence and nonstrange sea quarks in the nucleon from semiinclusive spin asymmetries. *Phys. Lett. B*, 369:93–100, 1996.
- [43] B. Adeva et al. Polarized quark distributions in the nucleon from semiinclusive spin asymmetries. *Phys. Lett. B*, 420:180–190, 1998.

- [44] HERMES technical design report. 7 1993.
- [45] A. Airapetian et al. Precise determination of the spin structure function $g(1)$ of the proton, deuteron and neutron. *Phys. Rev. D*, 75:012007, 2007.
- [46] A. Airapetian et al. Measurement of Parton Distributions of Strange Quarks in the Nucleon from Charged-Kaon Production in Deep-Inelastic Scattering on the Deuteron. *Phys. Lett. B*, 666:446–450, 2008.
- [47] A. Airapetian et al. Quark helicity distributions in the nucleon for up, down, and strange quarks from semi-inclusive deep-inelastic scattering. *Phys. Rev. D*, 71:012003, 2005.
- [48] Guenter Baum et al. COMPASS: A Proposal for a Common Muon and Proton Apparatus for Structure and Spectroscopy. 3 1996.
- [49] G. Cates, E. Cisbani, G. Franklin, A. Puckett, and Wojtsekhowsky B. Measurement of semi - inclusive pion and kaon electroproduction in the dis regime on a transversely polarized ^3He target using the super bigbite and bigbite spectrometers in hall a. *JLab Experiment E12-09-018*, 2009.
- [50] Haiyan Gao, Qian X., and Peng J.-C. Pr12-11-007 asymmetries in semi - inclusive deep - inelastic electro - production of charged pion on a transversely polarized ^3He target at 8.8 and 11 gev. *JLab Experiment E12-11-007*, 2008.
- [51] Jian-Ping Chen, Jin Huang, Yi Qiang, and Yan Wenbiao. Pr12-11-007 asymmetries in semi - inclusive deep - inelastic electro - production of charged pion on a longitudinally polarized ^3He target at 8.8 and 11 gev. *JLab Experiment E12-11-007*, 2008.
- [52] H. Avakian et al. Probing the proton's quark dynamics in sidis at 12 gev. *JLab Experiment E12-06-112*, 2006.
- [53] H. Avakian et al. Studies of spin-orbit correlations in pion electroproduction in dis with polarized hydrogen and deuterium targets. *JLab Experiment E12-07-107*, 2007.
- [54] R. Ent et al. Measurement of the ratio $r=\text{signal}/\text{sigmat}$ in semi-inclusive deep-inelastic scattering. *JLab Experiment E12-06-104*, 2006.

- [55] R. Ent et al. Transverse momentum dependence of semi-inclusive pion production. *JLab Experiment E12-09-017*, 2009.
- [56] R. Ent et al. Measurement of semi-inclusive pi0 production as validation of factorization. *JLab Experiment E12-09-017*, 2013.
- [57] F. Videbaek. The BRAHMS experiment at RHIC. *Nucl. Phys. A*, 566:299C–304C, 1994.
- [58] J. C. Gregory et al. PHENIX experiment at RHIC. *Nucl. Phys. A*, 566:287C–298C, 1994.
- [59] K. Kadija et al. Update to the RHIC Letter of Intent for an experiment on particle and jet production at mid-rapidity. 7 1991.
- [60] John W. Harris. Physics of the STAR experiment at the relativistic heavy ion collider. In *8th Winter Workshop on Nuclear Dynamics*, 1 1992.
- [61] B. Adams et al. Letter of Intent: A New QCD facility at the M2 beam line of the CERN SPS (COMPASS++/AMBER). 8 2018.
- [62] B. Adams et al. COMPASS++/AMBER: Proposal for Measurements at the M2 beam line of the CERN SPS Phase-1: 2022-2024. May 2019.
- [63] V. M. Abazov et al. Conceptual design of the Spin Physics Detector. 1 2021.
- [64] C. A. Aidala et al. The LHCSpin Project. 1 2019.
- [65] M. Santimaria, V. Carassiti, G. Ciullo, P. Di Nezza, P. Lenisa, S. Mariani, L. L. Pappalardo, and E. Steffens. The LHCspin project. In *28th International Workshop on Deep Inelastic Scattering and Related Subjects*, 5 2021.
- [66] John Skaritka, Erdong Wang, Ferdinand Willeke, Robert Lambiase, Wei Lui, Vadim Ptitsyn, and Omer Rahman. Conceptual design of a Polarized Electron Ion Collider at Brookhaven National Laboratory. *PoS, PSTP2017:015*, 2018.
- [67] A. Accardi et al. Electron Ion Collider: The Next QCD Frontier: Understanding the glue that binds us all. *Eur. Phys. J. A*, 52(9):268, 2016.
- [68] Ph. Abbon et al. The COMPASS Setup for Physics with Hadron Beams. *Nucl. Instrum. Meth.*, A779:69–115, 2015.

- [69] A. Airapetian et al. Single-spin asymmetries in semi-inclusive deep-inelastic scattering on a transversely polarized hydrogen target. *Phys. Rev. Lett.*, 94:012002, 2005.
- [70] A. Airapetian et al. Effects of transversity in deep-inelastic scattering by polarized protons. *Phys. Lett.*, B693:11–16, 2010.
- [71] V. Yu. Alexakhin et al. First measurement of the transverse spin asymmetries of the deuteron in semi-inclusive deep inelastic scattering. *Phys. Rev. Lett.*, 94:202002, 2005.
- [72] E. S. Ageev et al. A New measurement of the Collins and Sivers asymmetries on a transversely polarised deuteron target. *Nucl. Phys. B*, 765:31–70, 2007.
- [73] M. Alekseev et al. Collins and Sivers asymmetries for pions and kaons in muon-deuteron DIS. *Phys. Lett. B*, 673:127–135, 2009.
- [74] C. Adolph et al. Collins and Sivers asymmetries in muonproduction of pions and kaons off transversely polarised protons. *Phys. Lett.*, B744:250–259, 2015.
- [75] M. G. Alekseev et al. Measurement of the Collins and Sivers asymmetries on transversely polarised protons. *Phys. Lett.*, B692:240–246, 2010.
- [76] M. G. Alekseev et al. Azimuthal asymmetries of charged hadrons produced by high-energy muons scattered off longitudinally polarised deuterons. *Eur. Phys. J.*, C70:39–49, 2010.
- [77] C. Adolph et al. Transverse spin effects in hadron-pair production from semi-inclusive deep inelastic scattering. *Phys.Lett.*, B713:10–16, 2012.
- [78] C. Adolph et al. II – Experimental investigation of transverse spin asymmetries in μ -p SIDIS processes: Sivers asymmetries. *Phys. Lett. B*, 717:383–389, 2012.
- [79] C Adolph et al. Sivers asymmetry extracted in SIDIS at the hard scales of the Drell–Yan process at COMPASS. *Phys. Lett. B*, 770:138–145, 2017.
- [80] X. Qian et al. Single Spin Asymmetries in Charged Pion Production from Semi-Inclusive Deep Inelastic Scattering on a Transversely Polarized ^3He Target. *Phys. Rev. Lett.*, 107:072003, 2011.

- [81] Y. X. Zhao et al. Single spin asymmetries in charged kaon production from semi-inclusive deep inelastic scattering on a transversely polarized ${}^3\text{He}$ target. *Phys. Rev. C*, 90(5):055201, 2014.
- [82] L. Adamczyk et al. Measurement of the transverse single-spin asymmetry in $p^\uparrow + p \rightarrow W^\pm/Z^0$ at RHIC. *Phys. Rev. Lett.*, 116(13):132301, 2016.
- [83] Oleg Eyser. Transverse Single-Spin Asymmetries and Cross Section of Weak Bosons in p+p collisions at $\sqrt{s} = 510$ GeV. *Talk given at 22nd Particles and Nuclei International Conference PANIC2021*, 2021.
- [84] M. Aghasyan et al. First measurement of transverse-spin-dependent azimuthal asymmetries in the Drell-Yan process. *Phys. Rev. Lett.*, 119(11):112002, 2017.
- [85] A. Airapetian et al. Azimuthal single- and double-spin asymmetries in semi-inclusive deep-inelastic lepton scattering by transversely polarized protons. *JHEP*, 12:010, 2020.
- [86] M. Anselmino, M. Boglione, U. D'Alesio, F. Murgia, and A. Prokudin. Study of the sign change of the Sivers function from STAR Collaboration W/Z production data. *JHEP*, 04:046, 2017.
- [87] Miguel G. Echevarria, Ahmad Idilbi, Zhong-Bo Kang, and Ivan Vitev. QCD Evolution of the Sivers Asymmetry. *Phys. Rev. D*, 89:074013, 2014.
- [88] Peng Sun and Feng Yuan. Transverse momentum dependent evolution: Matching semi-inclusive deep inelastic scattering processes to Drell-Yan and W/Z boson production. *Phys. Rev. D*, 88(11):114012, 2013.
- [89] Zhong-Bo Kang and Jian-Wei Qiu. Testing the Time-Reversal Modified Universality of the Sivers Function. *Phys. Rev. Lett.*, 103:172001, 2009.
- [90] Marcin Bury, Alexei Prokudin, and Alexey Vladimirov. Extraction of the Sivers Function from SIDIS, Drell-Yan, and W^\pm/Z Data at Next-to-Next-to-Next-to Leading Order. *Phys. Rev. Lett.*, 126(11):112002, 2021.

- [91] Marcin Bury, Alexei Prokudin, and Alexey Vladimirov. Extraction of the Sivers function from SIDIS, Drell-Yan, and W^\pm/Z boson production data with TMD evolution. *JHEP*, 05:151, 2021.
- [92] M. Gluck, E. Reya, and A. Vogt. Parton distributions for high-energy collisions. *Z. Phys.*, C53:651–656, 1992.
- [93] M. Gluck, E. Reya, and A. Vogt. Dynamical parton distributions of the proton and small x physics. *Z. Phys.*, C67:433–448, 1995.
- [94] M. Glück, E. Reya, and A. Vogt. Dynamical parton distributions revisited. *Eur. Phys. J.*, C5:461–470, 1998.
- [95] A. D. Martin, W. J. Stirling, R. S. Thorne, and G. Watt. Parton distributions for the LHC. *Eur. Phys. J.*, C63:189–285, 2009.
- [96] L.A. Harland-Lang, A.D. Martin, P. Motylinski, and R.S. Thorne. Parton distributions in the LHC era: MMHT 2014 PDFs. *Eur. Phys. J. C*, 75(5):204, 2015.
- [97] Sayipjamal Dulat, Tie-Jiun Hou, Jun Gao, Marco Guzzi, Joey Huston, Pavel Nadolsky, Jon Pumplin, Carl Schmidt, Daniel Stump, and C.P. Yuan. New parton distribution functions from a global analysis of quantum chromodynamics. *Phys. Rev. D*, 93(3):033006, 2016.
- [98] F. Landry, R. Brock, Pavel M. Nadolsky, and C.P. Yuan. Tevatron Run-1 Z boson data and Collins-Soper-Sterman resummation formalism. *Phys. Rev. D*, 67:073016, 2003.
- [99] M. Anselmino, M. Boglione, J.O. Gonzalez Hernandez, S. Melis, and A. Prokudin. Unpolarised Transverse Momentum Dependent Distribution and Fragmentation Functions from SIDIS Multiplicities. *JHEP*, 04:005, 2014.
- [100] Andrea Signori, Alessandro Bacchetta, Marco Radici, and Gunar Schnell. Investigations into the flavor dependence of partonic transverse momentum. *JHEP*, 11:194, 2013.
- [101] Alessandro Bacchetta, Valerio Bertone, Chiara Bissolotti, Giuseppe Bozzi, Filippo Delcarro, Fulvio Piacenza, and Marco Radici. Transverse-momentum-dependent parton distributions up to N³LL from Drell-Yan data. *JHEP*, 07:117, 2020.

- [102] Ignazio Scimemi and Alexey Vladimirov. Non-perturbative structure of semi-inclusive deep-inelastic and Drell-Yan scattering at small transverse momentum. *JHEP*, 06:137, 2020.
- [103] M. Anselmino, M. Boglione, U. D’Alesio, S. Melis, F. Murgia, and A. Prokudin. Sivers Distribution Functions and the Latest SIDIS Data. In *19th International Workshop on Deep-Inelastic Scattering and Related Subjects (DIS 2011) Newport News, Virginia, April 11-15, 2011*, 2011.
- [104] M. Anselmino, M. Boglione, U. D’Alesio, S. Melis, F. Murgia, and A. Prokudin. Simultaneous extraction of transversity and Collins functions from new SIDIS and e+e- data. *Phys. Rev.*, D87:094019, 2013.
- [105] Justin Cammarota, Leonard Gamberg, Zhong-Bo Kang, Joshua A. Miller, Daniel Pitonyak, Alexei Prokudin, Ted C. Rogers, and Nobuo Sato. Origin of single transverse-spin asymmetries in high-energy collisions. *Phys. Rev. D*, 102(5):054002, 2020.
- [106] Miguel G. Echevarria, Zhong-Bo Kang, and John Terry. Global analysis of the Sivers functions at NLO+NNLL in QCD. *JHEP*, 01:126, 2021.
- [107] M. Glück, E. Reya, and A. Vogt. Pionic parton distributions. *Z. Phys. C*, 53:651–656, 1992.
- [108] P. J. Sutton, Alan D. Martin, R. G. Roberts, and W. James Stirling. Parton distributions for the pion extracted from Drell-Yan and prompt photon experiments. *Phys. Rev.*, D45:2349–2359, 1992.
- [109] M. Glück, E. Reya, and I. Schienbein. Pionic parton distributions revisited. *Eur. Phys. J. C*, 10:313–317, 1999.
- [110] Matthias Aicher, Andreas Schafer, and Werner Vogelsang. Soft-gluon resummation and the valence parton distribution function of the pion. *Phys. Rev. Lett.*, 105:252003, 2010.
- [111] P.C. Barry, N. Sato, W. Melnitchouk, and Chueng-Ryong Ji. First Monte Carlo Global QCD Analysis of Pion Parton Distributions. *Phys. Rev. Lett.*, 121(15):152001, 2018.

- [112] Ivan Novikov et al. Parton Distribution Functions of the Charged Pion Within The xFitter Framework. *Phys. Rev. D*, 102(1):014040, 2020.
- [113] Christopher Lefky and Alexei Prokudin. Extraction of the distribution function h_{1T}^\perp from experimental data. *Phys. Rev.*, D91(3):034010, 2015.
- [114] Vincenzo Barone, Stefano Melis, and Alexei Prokudin. The Boer-Mulders effect in unpolarized SIDIS: An Analysis of the COMPASS and HERMES data on the $\cos 2\phi$ asymmetry. *Phys. Rev.*, D81:114026, 2010.
- [115] A. Airapetian et al. Observation of the Naive-T-odd Sivers Effect in Deep-Inelastic Scattering. *Phys. Rev. Lett.*, 103:152002, 2009.
- [116] Marco Radici and Alessandro Bacchetta. First Extraction of Transversity from a Global Analysis of Electron-Proton and Proton-Proton Data. *Phys. Rev. Lett.*, 120(19):192001, 2018.
- [117] V. Barone, F. Bradamante, A. Bressan, A. Kerbizi, A. Martin, A. Moretti, J. Matousek, and G. Sbrizzai. Transversity distributions from difference asymmetries in semi-inclusive DIS. *Phys. Rev. D*, 99(11):114004, 2019.
- [118] L. L. Pappalardo. Accessing TMDs at HERMES. *AIP Conf. Proc.*, 1441(1):229–232, 2012.
- [119] Aram Kotzinian. Beyond Collins and Sivers: Further measurements of the target transverse spin-dependent azimuthal asymmetries in semi-inclusive DIS from COMPASS. *15th International Workshop on Deep-Inelastic Scattering and Related Subjects*, 5 2007.
- [120] Bakur Parsamyan. Six 'beyond Collins and Sivers' transverse spin asymmetries at COMPASS. *Phys. Part. Nucl.*, 45:158–162, 2014.
- [121] Bakur Parsamyan. Transverse spin asymmetries at COMPASS: beyond Collins and Sivers effects. *PoS*, DIS2013:231, 2013.
- [122] Y. Zhang et al. Measurement of pretzelosity asymmetry of charged pion production in Semi-Inclusive Deep Inelastic Scattering on a polarized ^3He target. *Phys. Rev. C*, 90(5):055209, 2014.

- [123] C. Adolph et al. Measurement of azimuthal hadron asymmetries in semi-inclusive deep inelastic scattering off unpolarised nucleons. *Nucl. Phys. B*, 886:1046–1077, 2014.
- [124] A. Moretti. TMD observables in unpolarised Semi-Inclusive DIS at COMPASS. *Contribution to DIS2021 conference*, April 2021.
- [125] A. Airapetian et al. Azimuthal distributions of charged hadrons, pions, and kaons produced in deep-inelastic scattering off unpolarized protons and deuterons. *Phys. Rev. D*, 87(1):012010, 2013.
- [126] M. Osipenko et al. Measurement of unpolarized semi-inclusive pi+ electroproduction off the proton. *Phys. Rev. D*, 80:032004, 2009.
- [127] L. Anderson et al. A High Resolution Spectrometer for the Study of High Mass Muon Pairs Produced by Intense Hadron Beams. *Nucl. Instrum. Meth. A*, 223:26, 1984.
- [128] J. S. Conway et al. Experimental Study of Muon Pairs Produced by 252-GeV Pions on Tungsten. *Phys. Rev. D*, 39:92–122, 1989.
- [129] A. Chumakov Y.-Sh. Lian. Measurement of target spin (in)dependent asymmetries in dimuon production in pion-nucleon collisions at compass. *Contribution to DIS2021 conference*, April 2021.
- [130] Thomas Gutsche, Valery E. Lyubovitskij, and Ivan Schmidt. Nucleon parton distributions in a light-front quark model. *Eur. Phys. J. C*, 77(2):86, 2017.
- [131] Stanley J. Brodsky and Glennys R. Farrar. Scaling Laws at Large Transverse Momentum. *Phys. Rev. Lett.*, 31:1153–1156, 1973.
- [132] V. A. Matveev, R. M. Muradian, and A. N. Tavkhelidze. Automodellism in the large - angle elastic scattering and structure of hadrons. *Lett. Nuovo Cim.*, 7:719–723, 1973.
- [133] S. D. Drell and Tung-Mow Yan. Connection of Elastic Electromagnetic Nucleon Form-Factors at Large Q^{*2} and Deep Inelastic Structure Functions Near Threshold. *Phys. Rev. Lett.*, 24:181–185, 1970.
- [134] Geoffrey B. West. Phenomenological model for the electromagnetic structure of the proton. *Phys. Rev. Lett.*, 24:1206–1209, 1970.

- [135] Thomas Gutsche, Valery E. Lyubovitskij, Ivan Schmidt, and Alfredo Vega. Light-front quark model consistent with Drell-Yan-West duality and quark counting rules. *Phys. Rev. D*, 89(5):054033, 2014. [Erratum: *Phys.Rev.D* 92, 019902 (2015)].
- [136] S. Bastami, L. Gamberg, B. Parsamyan, B. Pasquini, A. Prokudin, and P. Schweitzer. The Drell-Yan process with pions and polarized nucleons. *JHEP*, 02:166, 2021.
- [137] B. Pasquini, S. Cazzaniga, and S. Boffi. Transverse momentum dependent parton distributions in a light-cone quark model. *Phys. Rev.*, D78:034025, 2008.
- [138] S. Boffi, A. V. Efremov, B. Pasquini, and P. Schweitzer. Azimuthal spin asymmetries in light-cone constituent quark models. *Phys. Rev.*, D79:094012, 2009.
- [139] B. Pasquini and P. Schweitzer. Naive time-reversal odd phenomena in semi-inclusive deep-inelastic scattering from light-cone constituent quark models. *Phys. Rev.*, D83:114044, 2011.
- [140] Leonard Gamberg and Marc Schlegel. Final state interactions and the transverse structure of the pion using non-perturbative eikonal methods. *Phys. Lett. B*, 685:95–103, 2010.
- [141] Jefferson lab angular momentum collaboration. <https://www.jlab.org/theory/jam>. Accessed: 2021-04-16.
- [142] Leonard P. Gamberg, Gary R. Goldstein, and Marc Schlegel. Transverse Quark Spin Effects and the Flavor Dependence of the Boer-Mulders Function. *Phys. Rev.*, D77:094016, 2008.
- [143] B. Pasquini and P. Schweitzer. Pion transverse momentum dependent parton distributions in a light-front constituent approach, and the Boer-Mulders effect in the pion-induced Drell-Yan process. *Phys. Rev.*, D90(1):014050, 2014.
- [144] NA10 Collaboration, S. Falciano, M. Guanziroli, H. Hofer, P. Lecomte, P. Le Coultre, H. Suter, V. L. Telegdi, G. Viertel, B. Betev, K. Freudenreich, A. Ereditato, E. Gorini, P. Strolin, P. Bordalo, L. Cerrito, L. Kluberg, A. Romana, R. Salmeron, J. Varela, J. J. Blaising, A. Degré, P. Juillot, R. Morand, B. Mours, and M. Winter. Angular distributions of muon pairs produced by 194 gev/c negative pions. *Zeitschrift für Physik C Particles and Fields*, 31(4):513–526, Dec 1986.

- [145] L. Y. Zhu et al. Measurement of Angular Distributions of Drell-Yan Dimuons in $p + p$ Interactions at 800-GeV/c. *Phys. Rev. Lett.*, 102:182001, 2009.
- [146] T. Aaltonen et al. First Measurement of the Angular Coefficients of Drell-Yan e^+e^- pairs in the Z Mass Region from $p\bar{p}$ Collisions at $\sqrt{s} = 1.96$ TeV. *Phys. Rev. Lett.*, 106:241801, 2011.
- [147] Vardan Khachatryan et al. Angular coefficients of Z bosons produced in pp collisions at $\sqrt{s} = 8$ TeV and decaying to $\mu^+\mu^-$ as a function of transverse momentum and rapidity. *Phys. Lett. B*, 750:154–175, 2015.
- [148] Martin Lambertsen and Werner Vogelsang. Drell-Yan lepton angular distributions in perturbative QCD. *Phys. Rev. D*, 93(11):114013, 2016.
- [149] Wen-Chen Chang, Randall Evan McClellan, Jen-Chieh Peng, and Oleg Teryaev. Lepton Angular Distributions of Fixed-target Drell-Yan Experiments in Perturbative QCD and a Geometric Approach. *Phys. Rev. D*, 99(1):014032, 2019.
- [150] Daniel Boer. Investigating the origins of transverse spin asymmetries at RHIC. *Phys. Rev. D*, 60:014012, 1999.
- [151] Jen-Chieh Peng. Transverse Spin Effects in Future Drell-Yan Experiments. *EPJ Web Conf.*, 85:01009, 2015.
- [152] L. Y. Zhu et al. Measurement of Angular Distributions of Drell-Yan Dimuons in $p + d$ Interaction at 800-GeV/c. *Phys. Rev. Lett.*, 99:082301, 2007.
- [153] Zhun Lu and Ivan Schmidt. Updating Boer-Mulders functions from unpolarized pd and pp Drell-Yan data. *Phys. Rev. D*, 81:034023, 2010.
- [154] Vincenzo Barone, Zhun Lu, and Bo-Qiang Ma. The $\cos 2\phi$ asymmetry of Drell-Yan and J/psi production in unpolarized p anti-p scattering. *Eur. Phys. J. C*, 49:967–971, 2007.
- [155] Matthias Burkardt and Brian Hannafious. Are all Boer-Mulders functions alike? *Phys. Lett. B*, 658:130–137, 2008.

- [156] J. J. Aubert et al. Measurement of Hadronic Azimuthal Distributions in Deep Inelastic Muon Proton Scattering. *Phys. Lett. B*, 130:118–122, 1983.
- [157] M. Arneodo et al. Measurement of Hadron Azimuthal Distributions in Deep Inelastic Muon Proton Scattering. *Z. Phys. C*, 34:277, 1987.
- [158] M. R. Adams et al. Perturbative QCD effects observed in 490-GeV deep inelastic muon scattering. *Phys. Rev. D*, 48:5057–5066, 1993.
- [159] J. Breitweg et al. Measurement of azimuthal asymmetries in deep inelastic scattering. *Phys. Lett. B*, 481:199–212, 2000.
- [160] Xiaoyu Wang, Wenjuan Mao, and Zhun Lu. Boer-Mulders effect in the unpolarized pion induced Drell–Yan process at COMPASS within TMD factorization. *Eur. Phys. J. C*, 78(8):643, 2018.
- [161] Harald Fritzsch. Producing Heavy Quark Flavors in Hadronic Collisions: A Test of Quantum Chromodynamics. *Phys. Lett. B*, 67:217–221, 1977.
- [162] F. Halzen. Cvc for Gluons and Hadroproduction of Quark Flavors. *Phys. Lett. B*, 69:105–108, 1977.
- [163] C. E. Carlson and R. Suaya. Hadronic Production of ψ/J Mesons. *Phys. Rev. D*, 14:3115, 1976.
- [164] Chao-Hsi Chang. Hadronic Production of J/ψ Associated With a Gluon. *Nucl. Phys. B*, 172:425–434, 1980.
- [165] Geoffrey T. Bodwin, Eric Braaten, and G. Peter Lepage. Rigorous QCD analysis of inclusive annihilation and production of heavy quarkonium. *Phys. Rev. D*, 51:1125–1171, 1995. [Erratum: *Phys.Rev.D* 55, 5853 (1997)].
- [166] M. Anselmino, V. Barone, and M. Boglione. The Sivers asymmetry in Drell–Yan production at the J/Ψ peak at COMPASS. *Phys. Lett. B*, 770:302–306, 2017.
- [167] Wen-Chen Chang, Jen-Chieh Peng, Stephane Platchkov, and Takahiro Sawada. Constraining gluon density of pions at large x by pion-induced J/ψ production. *Phys. Rev. D*, 102(5):054024, 2020.

- [168] Pietro Faccioli, Carlos Lourenco, Joao Seixas, and Hermine K. Wohri. Towards the experimental clarification of quarkonium polarization. *Eur. Phys. J. C*, 69:657–673, 2010.
- [169] Mathias Butenschoen and Bernd A. Kniehl. J/ψ production in NRQCD: A global analysis of yield and polarization. *Nucl. Phys. B Proc. Suppl.*, 222-224:151–161, 2012.
- [170] Vincent Cheung and Ramona Vogt. Production and polarization of prompt J/ψ in the improved color evaporation model using the k_T -factorization approach. *Phys. Rev. D*, 98(11):114029, 2018.
- [171] Peter L. Cho and Mark B. Wise. Spin symmetry predictions for heavy quarkonia alignment. *Phys. Lett. B*, 346:129–136, 1995.
- [172] Eric Braaten, Bernd A. Kniehl, and Jungil Lee. Polarization of prompt J/ψ at the Tevatron. *Phys. Rev. D*, 62:094005, 2000.
- [173] An-Ping Chen, Yan-Qing Ma, and Hong Zhang. A short theoretical review of charmonium production. 9 2021.
- [174] P. Faccioli. Quarkonium polarization from high to low p_T . *COMPASS Seminar given at AM, May 2018*, 2018.
- [175] Eric Braaten and James Russ. J/ψ and Υ Polarization in Hadronic Production Processes. *Ann. Rev. Nucl. Part. Sci.*, 64:221–246, 2014.
- [176] S Arnold, A Metz, and Marc Schlegel. Dilepton production from polarized hadron hadron collisions. *Physical Review D*, 79, 09 2008.
- [177] K. Gottfried and J. D. Jackson. On the connection between production mechanism and decay of resonances at high energies. *Il Nuovo Cimento (1955-1965)*, 33(2):309–330, Jul 1964.
- [178] NA10 Collaboration, S. Falciano, M. Guanziroli, H. Hofer, P. Lecomte, P. Le Coultre, H. Suter, V. L. Telegdi, G. Viertel, B. Betev, K. Freudenreich, A. Ereditato, E. Gorini, P. Strolin, P. Bordalo, L. Cerrito, L. Kluberg, A. Romana, R. Salmeron, J. Varela, J. J. Blaising, A. Degré, P. Juillot, R. Morand, B. Mours, and M. Winter. Angular distributions

- of muon pairs produced by 194 gev/c negative pions. *Zeitschrift für Physik C Particles and Fields*, 31(4):513–526, Dec 1986.
- [179] J. T. Donohue and S. A. Gottlieb. . *Phys. Rev. D*, 23:2577, 1983.
- [180] K. Goeke, A. Metz, and M. Schlegel. Parameterization of the quark-quark correlator of a spin-1/2 hadron. *Phys. Lett.*, B618:90–96, 2005.
- [181] John P. Ralston and Davidson E. Soper. Production of dimuons from high-energy polarized proton-proton collisions. *Nuclear Physics B*, 152(1):109 – 124, 1979.
- [182] P. J. Mulders and R. D. Tangerman. The Complete tree level result up to order $1/Q$ for polarized deep inelastic leptonproduction. *Nucl. Phys.*, B461:197–237, 1996. [Erratum: *Nucl. Phys.*B484,538(1997)].
- [183] D. Boer and P. J. Mulders. Time-reversal odd distribution functions in leptonproduction. *Phys. Rev. D*, 57:5780–5786, May 1998.
- [184] R. D. Tangerman and P. J. Mulders. Intrinsic transverse momentum and the polarized drell-yan process. *Phys. Rev. D*, 51:3357–3372, Apr 1995.
- [185] A. Bacchetta, M. Diehl, K. Goeke, A. Metz, P. J. Mulders, and M. Schlegel. Semi-inclusive deep inelastic scattering at small transverse momentum. *Journal of High Energy Physics*, 2007(02):093–093, feb 2007.
- [186] A. Kotzinian. Description of polarized pi- N Drell-Yan processes. *COMPASS note*, 2010.
- [187] Alessandro Bacchetta, Umberto D’Alesio, Markus Diehl, and C. Andy Miller. Single-spin asymmetries: The Trento conventions. *Phys. Rev. D*, 70:117504, 2004.
- [188] Aram Kotzinian. New quark distributions and semiinclusive electroproduction on the polarized nucleons. *Nucl. Phys. B*, 441:234–248, 1995.
- [189] Alessandro Bacchetta, Markus Diehl, Klaus Goeke, Andreas Metz, Piet J. Mulders, and Marc Schlegel. Semi-inclusive deep inelastic scattering at small transverse momentum. *JHEP*, 02:093, 2007.
- [190] F Gautheron et al. COMPASS-II Proposal. 5 2010.

- [191] A Abragam and M Goldman. Principles of dynamic nuclear polarisation. *Reports on Progress in Physics*, 41(3):395–467, mar 1978.
- [192] J. Bisplinghoff et al. A scintillating fibre hodoscope for high rate applications. *Nucl. Instrum. Meth.*, A490:101–111, 2002.
- [193] D Thers, Ph Abbon, J Ball, Y Bedfer, C Bernet, C Carasco, E Delagnes, D Durand, J.-C Faivre, H Fonvieille, A Giganon, F Kunne, J.-M. Le Goff, F Lehar, A Magnon, D Neyret, E Pasquetto, H Pereira, S Platchkov, E Poisson, and Ph Rebourgeard. Micromegas as a large microstrip detector for the compass experiment. *Nuclear Instruments and Methods in Physics Research Section A: Accelerators, Spectrometers, Detectors and Associated Equipment*, 469(2):133 – 146, 2001.
- [194] D Neyret, M Anfreville, Y Bedfer, E Burtin, N d'Hose, A Giganon, B Ketzer, I Konorov, F Kunne, A Magnon, C Marchand, B Paul, S Platchkov, and M Vandenbroucke. New pixelized micromegas detector for the COMPASS experiment. *Journal of Instrumentation*, 4(12):P12004–P12004, dec 2009.
- [195] S. Bachmann et al. Performance of GEM detectors in high intensity particle beams. *Nucl. Instrum. Meth.*, A470:548–561, 2001.
- [196] N. V. Vlasov, O. P. Gavrishchuk, N. A. Kuz'min, V. V. Kukhtin, A. N. Maksimov, P. K. Man'yakov, Yu. V. Mikhailov, I. A. Savin, V. K. Semenov, A. B. Shalygin, and A. I. Yukaev. A calorimeter for detecting hadrons with energies of 10–100 gev. *Instruments and Experimental Techniques*, 49(1):41–55, Jan 2006.
- [197] Development of new data acquisition system for compass experiment. *Nuclear and Particle Physics Proceedings*, 273-275:976 – 981, 2016. 37th International Conference on High Energy Physics (ICHEP).
- [198] B. Adams et al. Letter of Intent: A New QCD facility at the M2 beam line of the CERN SPS (COMPASS++/AMBER). 2018.
- [199] R. Fruhwirth. Application of Kalman filtering to track and vertex fitting. *Nucl. Instrum. Meth.*, A262:444–450, 1987.

- [200] E. J. Wolin and L. L. Ho. Covariance matrices for track fitting with the Kalman filter. *Nucl. Instrum. Meth.*, A329:493–500, 1993.
- [201] Volker Blobel and Claus Kleinwort. A New method for the high precision alignment of track detectors. In *Advanced Statistical Techniques in Particle Physics. Proceedings, Conference, Durham, UK, March 18-22, 2002*, 2002.
- [202] A. M. Kotzinian and P. J. Mulders. Longitudinal quark polarization in transversely polarized nucleons. *Phys. Rev.*, D54:1229–1232, 1996.
- [203] M. G. Alexeev et al. Measurement of P_T -weighted Sivers asymmetries in lepton production of hadrons. *Nucl. Phys.*, B940:34–53, 2019.
- [204] B. Parsamyan. Drell-Yan 2015: status of the analysis and proposal for a paper (Sivers in DY). *COMPASS Analysis Meeting*, 2016.
- [205] M. Quaresma for the DY-group R. Longo, B. Parsamyan. Preliminary results for the transverse-spin-dependent azimuthal Drell-Yan asymmetries extracted from COMPASS 2018 data. *COMPASS Release note*, 2019.
- [206] Radja Boughezal, John M. Campbell, R. Keith Ellis, Christfried Focke, Walter Giele, Xiaohui Liu, Frank Petriello, and Ciaran Williams. Color singlet production at NNLO in MCFM. *Eur. Phys. J. C*, 77(1):7, 2017.
- [207] K. J. Eskola, V. J. Kolhinen, and C. A. Salgado. The Scale dependent nuclear effects in parton distributions for practical applications. *Eur. Phys. J. C*, 9:61–68, 1999.
- [208] K. Kovarik et al. nCTEQ15 - Global analysis of nuclear parton distributions with uncertainties in the CTEQ framework. *Phys. Rev. D*, 93(8):085037, 2016.
- [209] Bradamante et al. Azimuthal asymmetries of hadrons produced in muon SIDIS off longitudinally polarized deuterons. *COMPASS note*, 2014.
- [210] Roger Barlow. Extended maximum likelihood. *Nuclear Instruments and Methods in Physics Research Section A: Accelerators, Spectrometers, Detectors and Associated Equipment*, 297(3):496 – 506, 1990.

- [211] Jay Orear. Notes on statistics for physicists, revised. Report CLNS 82/511, Laboratory for Nuclear Studies, Cornell University, Ithaca, NY 14853, USA, July 1982.
- [212] Nelson Harry. Guide to Unbinned Maximum Likelihood Fits. *CBX*, pages 98–61, 1998.
- [213] M. Guanziroli et al. Angular Distributions of Muon Pairs Produced by Negative Pions on Deuterium and Tungsten. *Z. Phys. C*, 37:545, 1988.
- [214] C. Adolph et al. Experimental investigation of transverse spin asymmetries in muon-p SIDIS processes: Collins asymmetries. *Phys. Lett. B*, 717:376–382, 2012.
- [215] Torbjorn Sjostrand, Stephen Mrenna, and Peter Z. Skands. A Brief Introduction to PYTHIA 8.1. *Comput. Phys. Commun.*, 178:852–867, 2008.
- [216] S. Agostinelli et al. GEANT4—a simulation toolkit. *Nucl. Instrum. Meth. A*, 506:250–303, 2003.
- [217] Richard D. Ball et al. Parton distributions for the LHC Run II. *JHEP*, 04:040, 2015.
- [218] B. Parsamyan R. Longo, Y.-S. Lian. Unpolarized azimuthal asymmetries in Drell-Yan (2015 data). *Presentation given at AM, July 2018*.
- [219] Margarita Gavrilova and Oleg Teryaev. Rotation-invariant observables as Density Matrix invariants. *Phys. Rev. D*, 99(7):076013, 2019.
- [220] Pietro Faccioli, Carlos Lourenco, Joao Seixas, and Hermine K. Wohri. Model-independent constraints on the shape parameters of dilepton angular distributions. *Phys. Rev. D*, 83:056008, 2011.
- [221] C. Adolph et al. First measurement of the Sivers asymmetry for gluons using SIDIS data. *Phys. Lett. B*, 772:854–864, 2017.
- [222] U. A. Acharya et al. Transverse single-spin asymmetries of midrapidity π^0 and η mesons in polarized $p + p$ collisions at $\sqrt{s} = 200$ GeV. *Phys. Rev. D*, 103(5):052009, 2021.
- [223] Georges Aad et al. Measurement of the angular coefficients in Z -boson events using electron and muon pairs from data taken at $\sqrt{s} = 8$ TeV with the ATLAS detector. *JHEP*, 08:159, 2016.

- [224] W. A. Bardeen and Wu-Ki Tung. Invariant amplitudes for photon processes. *Phys. Rev.*, 173:1423–1433, Sep 1968.
- [225] A.L. Bondarev. A New identity in Minkowski space and some applications of it. *Theor. Math. Phys.*, 101:1376–1379, 1994.
- [226] J.G. Korner and M.C. Mauser. One loop corrections to polarization observables. *Lect. Notes Phys.*, 647:212–244, 2004.
- [227] Ettore Remiddi and Lorenzo Tancredi. Schouten identities for Feynman graph amplitudes; The Master Integrals for the two-loop massive sunrise graph. *Nucl. Phys. B*, 880:343–377, 2014.